Experimental pore scale analysis and mechanical modeling of cement-based materials submitted to delayed ettringite formation and external sulfate attacks

Yushan Gu

UNIVERSITÉ PARIS-EST

IFSTTAR

ECOLE DOCTORALE : SCIENCES, INGENIERIE ET ENVIRONNEMENT

Thèse présentée pour obtenir le grade de

Docteur de l'Université Paris-Est

Spécialité : Structures et Matériaux

Par

Yushan GU

Experimental pore scale analysis and mechanical modeling of cement-based materials submitted to delayed ettringite formation and external sulfate attacks

---

Soutenance prévue le 11 décembre 2018 devant le jury composé de :

M. Benoit Bary	Ingénieur - Chercheur	Rapporteur
M. Kefei Li	Professeur des universités	Rapporteur
M. Karim Aït-Mokhtar	Professeur des universités	Examinateur
M. Yves Berthaud	Professeur des universités	Examinateur
M. Ahmed Loukili	Professeur des universités	Examinateur
M. Patrick Dangla	Ingénieur - Chercheur	Directeur de thèse
M. Teddy Fen-Chong	Directeur de recherche	Co-Directeur de thèse
M. Renaud-Pierre Martin	Ingénieur - Chercheur	Co-Encadrant de thèse
M. Othman Omikrine Metalssi	Chargé de recherche	Co-Encadrant de thèse

Acknowledgement

First of all, I am deeply grateful to all members of the jury for agreeing to read the manuscript and to participate in the defense of this thesis.

Then, I would like to express my sincere gratitude to my supervisor Patrick DANGLA for the continuous support of my Ph.D study and related research, for his patience, motivation, and immense knowledge. His guidance helped me open a new door to modeling work, which will affect my career in whole life. And, I would like to thank my second supervisor Teddy FEN-CHONG who gave me the opportunity to work in IFSTTAR and advised my work.

Further, I would like to thank my advisor Renaud-Pierre MARTIN for his advice on experimental work and his patience and effort to help me get analyses of better quality. His guidance helped me in the time of research and writing of this thesis. His loyal attitude to science and truth will always motivate me further in my career. Moreover, I would like to thank my second advisor Othman OMIKRINE METALSSI for his guidance on experimental work and correction of my thesis. His knowledge inspired me to investigate some new aspect of our project.

I would like to thank all the people who helped me finish the lab work: I thank to the technicians in the department of FM2D: Jean Daniel Simitambe for the aid the specimens' fabrication; Jean-François Bouteloup for the preparation and organization of samples; Baraka Mohamed for the preparation of samples and water accessible porosity test; Pauline Huart for her aide to all the administrative files.

And I thank to the technicians in the department of EMGCU: Jean-Claud Renaude, Lenaïc Baron, Franck Guirado, Joel Saint-Ange Billo, Amandine Bonnet, and Damien Suray-Faure, who helped me prepare the DEF specimens.

Besides, I would like to thank previous members of FM2D, Aiman, Sylvain and Matthieu, who treated me like a family when I just came to France. I am also grateful to the members of our department, Mike, Baptiste, Veronique, Ingrid, Assia, Marie for their support in overcoming numerous obstacles I have been facing through my research.

Also I thank my friends who helped me during these three years. In particular, I am grateful to Antoine and Xiaoxiong BBao, who encouraged and motivated me

always.

Last but not the least, this thesis is dedicated to my mom for her love, endless support and encouragement.

Abstract

This work aims to study cement-based materials subjected to sulfate attacks in three different conditions: External Sulfate Attack (ESA), Delayed Ettringite Formation (DEF) and the Coupling effect of both, and to propose a common damage mechanism for all of them. Based on the proposed mechanism, a poromechanical model is established to simulate the expansion induced by expansive crystals during the degradation. The study includes the following three parts.

In the first part, the degradation of cement paste specimens with two kinds of cement type (CEM I and CEM III) and two dimensions ($2 \times 2 \times 12$ cm^3 and $11 \times 11 \times 22$ cm^3) exposed to three sulfate attack conditions (ESA, DEF, and Coupling effect) are studied and compared, including the length variation, mass variations, and observations. The specimens exposed to the coupling effect show the fastest kinetics and the most serious degree of degradation compared to the other cases.

Then, the pore structure of cement pastes before and after sulfate attacks is characterized via different techniques: mercury intrusion porosimetry, dynamic vapor sorption, water accessible tests and heat-based dissolution tests. By comparing the variation of pore size distribution of cement pastes exposed to different conditions, the generated crystals are found to be precipitated both in capillary and gel pores. In addition to the evolution of pore size distribution during DEF, a damage mechanism is proposed based on the experimental results: the generated crystals (ettringite) precipitate in the big pores without inducing an obvious expansion, and then penetrate into capillary and gel pores, which leads to a swelling. Finally, some tests have been performed to investigate the pore volume occupied by DEF induced products. A heat-based dissolution test procedure has been developed during this project; it intends to "remove" ettringite crystals from the material to investigate the modification of pore structure due to the reactions. This part of the program further confirms the formation of expansive products in the pore range described above.

Finally, based on the experimental conclusion that ettringite forms through the large to small pores in all cases, a poromechanical model is proposed to simulate the expansion of cement-based materials submitted to sulfate attacks. The model is based on the surface-controlled growth and physicochemical properties both for ESA and DEF, despite the different source of sulfate ions. Two independent constants, a_i and a_p, are proposed to represent the kinetics of crystal invasion and deformation.

Moreover, the model could be coupled with any mechanical theories, e.g. elasticity, plasticity, damage theory or any other. The model well illustrates the crystallization process and well predicts the corresponding expansion both in ESA and DEF through some limitations that are shown.

Keywords: Sulfate attack, ESA, DEF, Coupling effect of ESA and DEF, cement pastes, pore size distribution, ettringite formation, poromechanical modeling

Résumé

Ce travail de recherche a pour but d'étudier des matériaux cimentaires soumis à des attaques sulfatiques selon trois différentes conditions : attaques sulfatiques externes (ASE), formation différée d'ettringite communément appelée réaction sulfatique interne et l'effect couplé des deux réactions. L'objectif est également de proposer un mécanisme commun pour les dégradations causées par ces réactions. En se basant sur le mécanisme proposé, un modèle poro-mécanique est développé pour simuler l'expansion induite par les produits expansifs néoformés pendant la dégradation.

Cette étude inclut trois parties : dans la première partie, les dégradations des éprouvettes de pâte de ciment coulées à l'aide de deux types de liant (CEM I et CEM III) et deux dimensions ($2 \times 2 \times 12$ cm^3 et $11 \times 11 \times 22$ cm^3) exposées à trois différents types d'attaques sulfatiques (ASE, ASI, et le couplage des deux réactions), sont étudiées et comparés : variations de longueur, de masse, ainsi que des observations visuelles. Les éprouvettes exposées au couplage ASE-RSI montrent la cinétique d'expansion la plus rapide et le degré de dégradation le plus important, comparé aux autres cas.

Ensuite, la structure poreuse des pâtes de ciment avant et après les attaques sulfatiques est caractérisée en utilisant différentes techniques : porosimétrie à mercure (MIP), sorption dynamique de vapeur (DVS), porosité accessible à l'eau ou technique de dissolution d'ettringite par traitement thermique. En comparant les variations de la distribution de la taille des pores des pâtes de ciment exposées à différentes conditions, il a été mis en évidence que les cristaux néoformés précipitent à la fois dans les pores capillaires et les pores des C-S-H. Sur la base de l'analyse expérimentale de l'évolution de la distribution de la taille des pores pendant la RSI, un mécanisme de dégradation est proposé : il est suggéré que les cristaux néoformés (l'ettringite) précipitent dans les grands pores, sans provoquer une expansion manifeste, puis se forment dans les pores capillaires et les pores des C-S-H, ce qui induit un gonflement. Par ailleurs, le volume des pores occupé par les produits de la RSI sont analysés après des essais de dissolution par traitement thermique : développée dans le cadre de ce projet, cette technique a pour vocation à dissoudre les cristaux d'ettringite issus des réactions pathologiques et permettre d'analyser l'évolution de la structure poreuse sous l'effet des expansions. Ces investigations ont confirmé la formation de produits d'expansion dans la gamme de pores discutée ci-dessus.

Enfin, en se basant sur les résultats expérimentaux montrant que l'ettringite se

forme en allant des grands pores vers les plus petits, un modèle poro-mécanique est proposé pour simuler l'expansion des matériaux cimentaires soumis à des attaques sulfatiques. Le modèle est basé sur la croissance contrôlée en surface et les propriétés physico-chimiques pour l'ASE et la RSI, malgré les différences entre ces deux réactions. Deux constantes indépendantes, a_i et a_p, sont proposées pour représenter la cinétique de l'invasion des cristaux et la déformation. De plus, le modèle peut être couplé avec toutes les théories mécaniques, par exemple : l'élasticité, la plasticité, la théorie de l'endommagement etc. Le modèle illustre bien le processus de cristallisation et il prédit l'expansion correspondante à la fois à l'ASE et la RSI bien que certaines limites de notre approche aient pu être mises en évidence.

Mots clés : attaque sulfatique externe (ASE), réaction sulfatique interne (RSI), effet du couplage de l'ASE et la RSI, pâtes de ciment, distribution de la taille des pores, ettringite, modélisation poromécanique.

Contents

Glossary

C_3A	$3CaO \cdot Al_2O_3$, Tricalcium aluminate.
CH	$Ca(OH)_2$, Portlandite.
CSH	$CaO \cdot SiO_2 \cdot H_2O$, Calcium silicate hydrate.
$C\bar{S}H_2$	$CaSO_4 \cdot 2H_2O$, Gypsum.
Na_2SO_4	Thenardite.
$Na_2SO_4 \cdot 10H_2O$	Mirabilite.
NaCl	Halite.
C_3S	$3CaO \cdot SiO_2$, Tricalcium silicate.
C_2S	$2CaO \cdot SiO_2$, Dicalcium silicate.
C_4AF	$4CaO \cdot Al_2O_3 \cdot Fe_2O_3$, Tetracalcium aluminoferrite.
$C_4A\bar{S}H_{12}$	$3CaO \cdot Al_2O_3 \cdot CaSO_4 \cdot 12H_2O$, AFm/Monosulfate aluminate.
$C_6A\bar{S}H_{32}$	$3CaO \cdot Al_2O_3 \cdot 3CaSO_4 \cdot 32H_2O$, AFt/Sulfoaluminate.
C_3AH_6	$3CaO \cdot Al_2O_3 \cdot 6H_2O$, Tricalcium aluminate hydrate.
$K_2Ca(SO_4)_2H_2O$	Syngenite.
$Mg(OH)_2$	Brucite.
$C_3A(CaCl_2)H_{10}$	$3CaO \cdot Al_2O_3 \cdot CaCl_2 \cdot 10H_2O$, Friedel's salt.
$C_4A_3\bar{S}$	$4CaO \cdot 3Al_2O_3 \cdot CaSO_4$, Anhydrous calcium sulfoaluminate.
P_C	Crystallization pressure.
P_L	Liquid pressure.
R	Ideal gas constant.
T	Temperature.
V_C	Molar volume of the crystal.
β_p	Saturation index of the crystal at the crystal-solid interface.
ϵ	Expansion of a material.
σ'	Effective stress of a material.
σ	Stress of a material.
b	Biot's coefficient.

S_C	Volume fraction of pore space saturated with crystals in the pore invasion process.
E	Bulk modulus.
Φ_C	Volume fraction of the crystal phase.
Φ_0	The initial porosity in the material.
φ_C	Porosity change due to deformation of the pores.
n_i	The crystal content formed in the pore invasion process.
n_p	The crystal content formed in the pore deformation process.
ϵ_s	Volumetric strain of solid part.
φ	Deformation of pores.
$E(d)$	Modulus with considering the damage.
ϵ_0	The maximum elastic strain.
ϵ_f	A damage parameter.
β	Saturation index of the crystal in the solution.
γ_{CL}	The surface energy of crystals.
r_{eq}	The mean radius of curvature of the crystal-liquid interface at equilibrium.
β_i	Saturation index of the crystal at the crystal-liquid interface.
ΔG_r	The reaction Gibbs energy of the crystal dissolution reaction.
a_i	A kinetic constant for crystallization in the pore invasion process.
a_p	A kinetic constant for crystallization in the pore deformation process.
$n_{\mathrm{SiO_2}}$	Initial mass content of SiO_2 in the cement.
n_{CaO}	Initial mass content of CaO in the cement.
$n_{\mathrm{Al_2O_3}}$	Initial mass content of Al_2O_3 in the cement.
$n_{\mathrm{SO_3}}$	Initial mass content of SO_3 in the cement.
n_{CSH}	The content of CSH in the material.
n_{CH}	The content of CH in the material.
$n_{\mathrm{C_3A}}$	The content of C_3A in the material.
n_{AFt}	The content of AFt in the material.
n_{AFm}	The content of AFm in the material.
$n_{\mathrm{SO_4^{2-}}}$	The free sulfate ions in pore solution.
$n_{\mathrm{SO_4}}^{ads}$	The sulfate ions adsorbed on C-S-H.
$c_{\mathrm{Ca^{2+}}}$	Concentration of Ca^{2+} in the solution.
$c_{\mathrm{Al^{3+}}}$	Concentration of Al^{3+} in the solution.
$c_{\mathrm{SO_4^{2-}}}$	Concentration of sulfate ions in the solution.

c_{OH^-}	Concentration of OH^- in the solution.
β_{AFt}	Saturation index of Aft in the solution.
β_{CH}	Saturation index of CH in the solution.
$\beta_{C_3AH_6}$	Saturation index of C_3AH_6 in the solution.
β_{AFm}	Saturation index of AFm in the solution.

List of Figures

List of Tables

Introduction

Concrete is the most widely used building material in the world. Many of the destructive and corrosive processes affecting mortar and concrete involving chemical reactions can be attributed to the aggressive action of sulfate in solution. Sulfate attacks have been considered as potentially affecting the durability of cement-based materials, which is a problem perplexing the researchers. It has been a concern to concrete technologists since the early years of the 19th century, and thus the subject of sulfate attacks has been studied extensively.

Sulfate ions, commonly present in sulfate-containing environments (marine environment or groundwater) or construction materials, are indispensable in the engineering field. The different source of sulfate ions distinguishes sulfate attacks from External Sulfate Attack (ESA) to Internal Sulfate Attack (ISA). Delayed Ettringite Formation (DEF), as a form of ISA, is observed in cementitious materials which experienced elevated temperatures during curing, either from a heating treatment or from an internal high temperature due to the heat released by hydration in massive concrete. A great number of studies have been conducted on ESA and DEF separately, which includes aspects of chemical reactions, ettringite formation, expansion mechanisms, affecting factor analyses and modeling simulations.

However, there are quite a lot in common between ESA and DEF. For example, cement-based specimens exposed either to ESA or DEF show expansions and crackings, which are due to the formation of ettringite. Moreover, the hypotheses proposed to explain the expansion induced by ettringite formation include volume increase theory, colloidal dimension theory, topochemical reaction theory and the crystallization pressure induced theory. Furthermore, the material mix has a similar effect on expansion, e.g. the high content of C_3A and C_3S have a positive role on ettringite formation, higher W/C ratio leads to a higher porosity and results in a higher permeability and more space to accommodate expansive products, and so on.

In addition, few studies have been performed to study the coupling effect of ESA and DEF, though it may happen when a massive structure is exposed to a sulfate environment.

Therefore, in this work, experimental studies on cement pastes exposed to different sulfate attack conditions (ESA, DEF, and the coupling effect of ESA and DEF) are performed to figure out a uniform expansion mechanism. The main objectives of the

experiments are to characterize the pore structure of cement-based materials before and after sulfate attacks via experimental techniques: MIP and DVS. To figure out the exact pore position where ettringite forms is the main goal. Based on the experimental results, a poromechanical model based on the mechanism of ettringite crystallization and other physicochemical properties will be proposed. The model will take into account the chemical reactions involved, dissolution, the precipitation of solid phases, the crystallization of ettringite and corresponding induced strain.

This dissertation includes four chapters. After this introduction, the first chapter will be the Literature Review. A general review of the studies on ESA and DEF are presented in this chapter, as well as the potential for the occurrence of the coupling effect of ESA and DEF. The studies include the experimentations that have been performed to find out the mode of deterioration, the reason for the expansion, the mechanism for expansion, the affecting factors (concrete mix, curing conditions, exposure environment) and so on. Meanwhile, studies on modeling to simulate the expansion of cement-based materials are presented in this chapter as well.

Then, the second chapter introduces the Experimental Programs, in which the design of the specimens, and the experimental procedures are presented. The experimentations include the measurements of length and mass variations, Mercury Intrusion Porosimetry (MIP), Dynamic Vapor Sorption (DVS) and Water Accessible Porosity Technique (WAPT). Furthermore, a heat-based dissolution test is proposed to release the pore volume in the pore range occupied during sulfate attacks, which aims to further confirm the formation of ettringite.

The experimental results are presented and analyzed in the third chapter: Experimental Results. In this chapter, the degradation of the specimens is demonstrated from observations, length and mass variations. Then, the pore structure of cement pastes is illustrated by the pore size distribution, the variation of which provides a clue to figure out the pore location where ettringite forms. By comparing the variations of pore size distribution of $2 \times 2 \times 12$ cm^3 specimens before and after the sulfate attacks and investigating the evolution of pore size distribution of $11 \times 11 \times 22$ cm^3 specimens during DEF, an expansion mechanism is proposed.

Based on the expansion mechanism investigated in chapter 3, a model is proposed in the fourth chapter: Poromechanical Modeling. The proposed model is established on the surface-controlled growth and physicochemical properties for both ESA and DEF, despite the differences between them. Then, the model is used to illustrate

the crystallization process and to predict the expansion of cement-based materials induced by sulfate attacks.

Finally, this dissertation ends with a summary of the conclusions and perspectives for studies in the future.

1 Literature review

1.1 Introduction

A sulfate attack is a degradation phenomenon that can occur in cement-based materials. It is defined as the "loss of strength or visible deterioration accompanied by a high sulfate content in the material" [1]. It encompasses a series of chemical and physical interactions that occur between hardened cement pastes and sulfates. A sulfate attack mainly is the result of the chemical reactions between the tricalcium aluminate (C_3A) contained in Portland cement and sulfate ions supplied by different sources, which separate sulfate attacks into external sulfate attacks (ESA) and internal sulfate attacks (ISA). In ESA, the sulfate ions come from the exterior environment, while for ISA, the sulfate ions come from sulfate-containing materials present in the material by the time of casting. Three forms of ISA are mentioned in [2]: the contamination of the aggregates by sulfates; over addition of sulfates in cement and delayed ettringite formation (DEF). The last form is observed in cementitious materials that experienced elevated temperatures during curing, either from heating treatment or from internal high temperature due to heat released by hydration in massive concrete members. DEF is the form of ISA that is studied only in this dissertation. Due to different sources of sulfate ions, ESA and DEF are generally studied separately. However, the physics are similar, such as the degradation modes of the cement-based materials, the mechanism of expansion... The literature will be examined in order to provide a comprehensive understanding of the current research concerning sulfate attacks.

In the following sections, a literature review will be presented from ESA and DEF studies, and a potential occurrence of the coupling of ESA and DEF will be described. The mechanisms of these swelling phenomena as well as the different parameters influencing them will be discussed. In the conclusion part, the similarities and differences between ESA and DEF will be summarized and analyzed. Finally, a synthesis of the existing models will be presented for both phenomena, which will be analyzed to justify the objectives of this thesis.

1.2 Chemo-physical features of the reactions

1.2.1 Pore structure of cementitious materials

The pore structure of cement-based materials is an important characteristic which affects their physical and mechanical properties. The typical dimensions of the voids in hydrated cement paste are shown in Fig. 1.1. The interlayer spacing in C-S-H sheets, which is simplified as gel pore, has a pore size between 1 nm to several nm. Capillary pores are originally water filled spaces which are not filled by the solid hydration products of cement. In well-hydrated, low w/c ratio pastes, the capillary pores may range from 10 to 50 nm, while in high w/c ratio, the capillary voids may be as large as 3–5 mm.

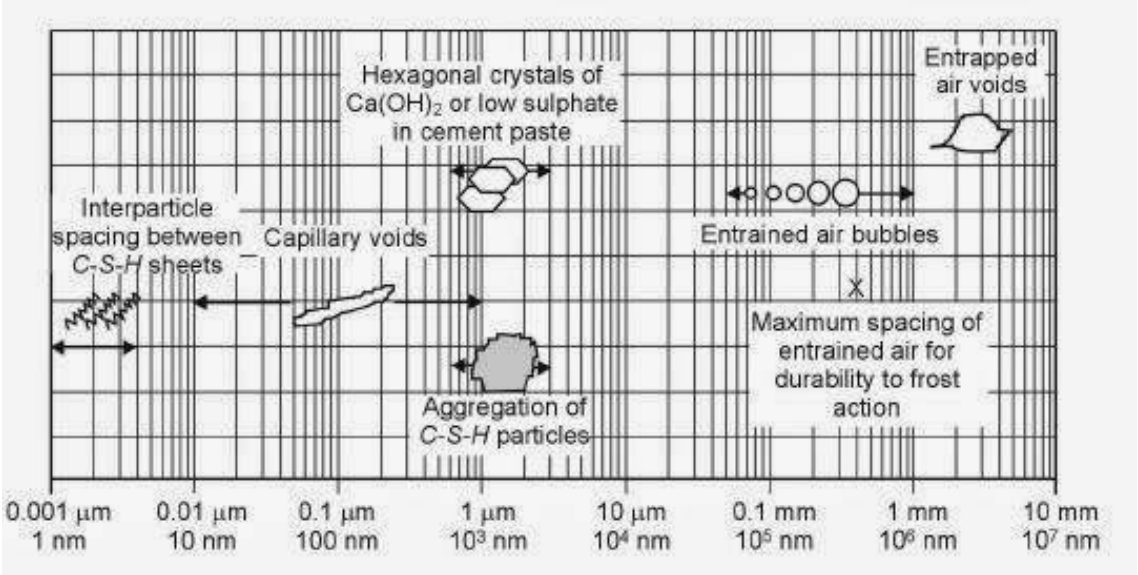

Figure 1.1 – Pore classification in hydrated cement paste [3].

1.2.2 External Sulfate Attack

It is well known that cements undergo deterioration in sulfate-rich environments. Loss of strength of concrete structures in a wet sulfate-bearing environment, such as ground water, rivers and seawater, has been widely reported. For example, Lei et al. report the damage of tunnel structures suffering from sulfate attack [4]. As shown in Fig. 1.2, a surface spalling is observed on the side wall of a tunnel when it is exposed to a sulfate-rich environment. Wang et al. [5] show that many buildings, ground conduits, and bridges are exposed to sulfate-rich soils in western

China, especially those lying in the upper-middle beaches of the Yellow River. ESA typically occurs where water containing dissolved sulfates penetrates concrete, such as groundwater, seawater [6], sulfuric acid formed from bacterial action in sewers [7] and so on. The ESA damage is determined by the chemical interaction of a sulfate-rich soil or water with the cement paste. These phenomena are the coupled effect of calcium leaching including dissolution of the CH and sophisticated decalcification of the CSH [8]. It results in changes in the microstructure, loss of strength, a propagation of microcracking, softening, decohesion, expansion or even spalling [9]. The degradation is present both due to the expansion and the decalcification of C-S-H, with the latter ensuring for the binding capacity of the cement [10]. The loss of mechanical performance has been attributed to the formation of secondary sulfate-bearing phases, the sulfate ions of which penetrate from outside solutions, such as the sodium sulfate, potassium sulfate, magnesium sulfate and so on [6]. Expansion is attributed to the formation of expansive compounds like ettringite in the case of sodium sulfate solutions [11]. Some other theories are also proposed, they attribute the damage to the formation of gypsum ($C\bar{S}H_2$) crystals [12]. Despite many research efforts, this process is still poorly understood and explained.

Figure 1.2 – Surface concrete spalling exposed to sulfate-rich environment [4].

The microstructure changes occur when sulfate ions penetrate into cementitious materials, which are caused by some chemical reactions. First the C_3A is converted to ettringite, which may modify the microstructure. In parallel leaching of calcium and of other ions occurs close to the surface leading to a weakened decalcified zone [13, 14, 15], which changes the pore size distribution of the material as well. A representative system explaining the development of ESA and the progress of the expansion in previous studies is not fully complete, and needs continuation.

Even though explanations and theories concerning sulfate attacks are still insufficient, many studies are able to show the precautions and the steps needed in order

to reduce the effect of sulfate attacks. The most important and known of them is the need to reduce the concentration of tricalcium aluminate (C_3A) content in the cement. Other theories propose the reduction of calcium hydroxide (CH) in concrete since it reacts with sulfates ions to produce gypsum, considered along with ettringite to be one of the main components affecting the strength and performance of concrete.

The following conditions are required in order for ESA to occur: a high permeability of cement-based material, sulfate-rich environment, and the presence of water [16]. Several factors affect the damage to cement-based materials due to ESA: the transport of ions inward and outward through the pore system, chemical reactions between sulfates and the solid hydration products of cement, the formation of expansive products, the internal stress caused by the crystallization, and the mechanical response of the bulk material resulting from the internal stress. In general, two types of study methods have been conducted:
1. experimental studies to observe the deterioration of specimens, to measure the length and mass variations, to analyze the impact of the different factors including material compositions and exposure solutions, to analyze the distribution of the crystals formed and so on;
2. modelings of the durability of specimens taking into account chemical reactions, mass balance, crystal formation and the mechanical response of the specimens.

A general study of ESA in the literature will be presented from the definition of sulfate attacks (physical and chemical), the damage modes of the cement-based materials, the mechanisms of expansion, impact factors analysis and the different approaches for modeling.

1.2.2.1 Physical sulfate attacks

Physical sulfate attacks are damages caused by physical actions without any chemical reactions [17]. It may occur when dissolved salts diffuse through concrete and precipitate in pores, causing damage [18, 19, 20, 21]. The idea of crystallization pressure was put forward in [22]. Large pressure may occur if crystallization happens in the pores of the concrete. A form of physical sulfate attacks is the change of thenardite (Na_2SO_4) into mirabilite ($Na_2SO_4 \cdot 10H_2O$) [23]. A solution of thenardite is supersaturated with respect to mirabilite at temperatures below 32 °C and humidity above 75%; the precipitation of mirabilite can then cause damage [24, 25, 26].

Table 1.1 – Properties of sodium and magnesium sulfate salts [27]

					Crystallization pressure [MPa]					
					C/Cs = 2		C/Cs = 10		C/Cs = 50	
Salt	Formula	Density [g/cm³]	Molecular weight [g/mol]	Molar volume [cm³/mol]	0 °C	50 °C	0 °C	50 °C	0 °C	50 °C
Mirabilite	$Na_2SO_4 \cdot 10H_2O$	1.46	322.19	220	7.2	8.3	23.4	27.7	39.7	47.3
Thenardite	Na_2SO_4	2.69	142.04	93	29.2	34.5	97.0	115.0	165.0	196.5
Epsomite	$MgSO_4 \cdot 7H_2O$	1.68	246.40	147	10.5	12.5	35.0	41.5	59.5	70.8
Hexahydrate	$MgSO_4 \cdot 6H_2O$	1.75	228.45	130	11.8	14.1	39.5	46.9	67.1	30.0
Kieserite	$MgSO_4 \cdot H_2O$	2.45	138.39	57	27.2	32.4	91.0	107.9	154.3	184.0

C solute concentration in bulk solution (supersaturation) [mol/cm³];
C_S solute concentration at equilibrium [mol/cm³].

Experimental studies of the crystallization of salts from sodium sulfate solutions in porous materials were performed [21, 24, 27, 28]. It was observed that the stress is high enough to overcome the tensile strength of normal porous material when crystallization takes place within the pores. The salt pressure of sodium and magnesium sulfate solutions are calculated in [27], which is shown in Table 1.1. The crystallization pressures are presented at different saturation index C/C_S, where C and C_S correspond to the solubility product of the considered salt at the actual and equilibrium states of the solution. This saturation index signifies the saturation state of crystal solution. $C/C_S > 1$ means the solution is supersaturated and tends to crystallize. As shown in Table 1.1, when the mirabilite saturation index (C/C_S) equals 2 at temperature of 0 °C, the crystallization pressure is up to 7.2 MPa, which is bigger than the tensile stress for normal cement materials. Several damage mechanisms due to salt crystallization have been proposed and have been previously summarised [21].

Hime [29] proposed a damage mechanism of solid volume change during the transformation of anhydrous salt to its hydrous form. But this mechanism could not explain the expansion when the salt has no hydrous form, such as halite (NaCl), where there is no solid volume change. The salt hydration pressure hypothesis is also proposed to explain the damage. The hydration process producing pressure is believed to cause distress in the porous material [29]. However, the solid-state hydration of thenardite to mirabilite does not occur in [30]. The most popular mechanism is the crystallization pressure mechanism. The salt crystallization pressure is described as the driving force for damage in literature [19, 27, 30], which will be explained in detail later.

1.2.2.2 Chemical sulfate attacks

Ettringite formation Hydration of concrete is an exothermic reaction of cement anhydrous elements (C_3S, C_2S, C_3A, and C_4AF) with water forming hydrates (CSH, CH, $C_4A\bar{S}H_{12}$, and $C_6A\bar{S}H_{32}$...). Ettringite (AFt), which is the product responsible for the swelling due to sulfate attack, corresponds to the formula ($3CaO \cdot Al_2O_3 \cdot 3CaSO_4 \cdot 32H_2O$) [31]. This chemical process is well described in Fig. 1.3. As the most common type of external sulfate attacks, sodium sulfate attacks are caused by the reaction of gypsum with monosulfate and the other alumina-bearing phases to form ettringite. With the sulfate ions penetrated from the outside solution, the gypsum and ettringite form near the surface. The ettringite formation in ESA is governed by the transfer of sulfate ions into the cement matrix and the consumption of portlandite, as well as the decalcification of C-S-H. Ragoug [32] pointed out that the sulfate ions transfer with concentration gradient firstly, and then tend to be stable when the sulfates can react with the cement hydrates.

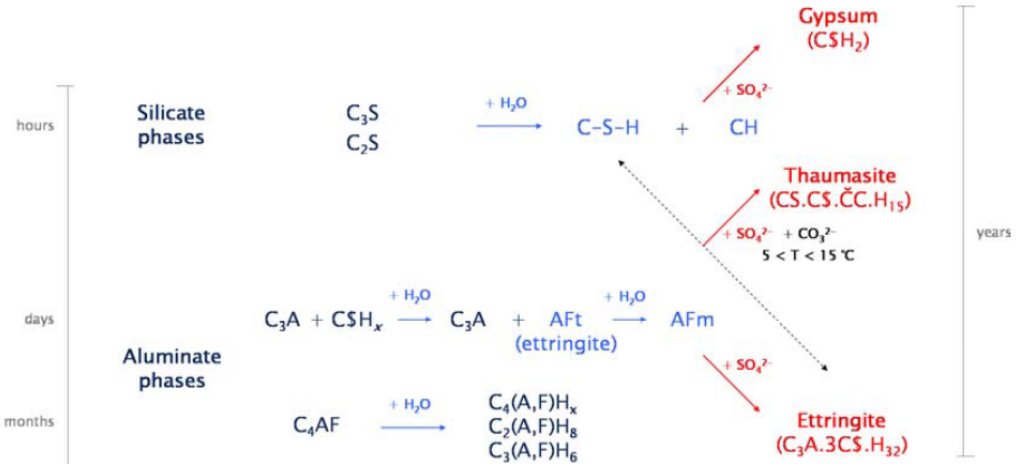

Figure 1.3 – Chemical mechanism during sulfate attacks [33].

Portland cements with more than 5% of tricalcium aluminate (C_3A) will contain most of its alumina in the form of monosulfate hydrate $C_3A \cdot C\bar{S} \cdot H_{18}$ or $C_3A \cdot C\bar{S} \cdot H_{12}$ [34]. The hydrogarnet (C_3AH_6) will also appear in the hydration products. Alumina-containing hydrates are converted to ettringite when the cement paste comes into contact with sulfate ions, as shown in Eq. 1:

$$\begin{aligned} CH + N\bar{S} + 2H &\rightarrow C\bar{S}H_2 + NH \\ C_3A + 3C\bar{S}H_2 + 26H &\rightarrow C_6A\bar{S}_3H_{32} \\ C_4A\bar{S}H_{12} + 2C\bar{S}H_2 + 16H &\rightarrow C_6A\bar{S}_3H_{32} \\ C_4AH_{13} + 3C\bar{S}H_2 + 14H &\rightarrow C_6A\bar{S}_3H_{32} + CH \end{aligned} \tag{1}$$

where $N = Na_2O, H = H_2O$.

Gypsum formation In addition to the precipitation of ettringite, the precipitation of gypsum is also observed when the concentration of sulfates in the aggressive solution is high [35, 36, 37] or the pH of the surrounding environment is low [32]. It is debated whether gypsum formation is the cause of the expansion. Metha supports that the gypsum formation is expansive based on his experimental study on alite paste [10]. However, no obvious expansion was observed, especially for the long-term results. Wang considered that gypsum formation plays a more important role in the physical damage than ettringite formation via analyzing the results of X-ray diffraction (XRD) examination of the solid phases present at different depths in Portland cement paste exposed to sodium sulfate solution [8]. Yang et al [38] studied the role of the interfacial zone during sulfate attacks, and concluded that sulfate reacts with CH and AFm in the interfacial zone, which leads to expansion and cracking. However, Santhanam pointed out that the most degraded zone of the material, such as microcrack spaces and aggregate/paste interfaces, provide the most suitable sites for the precipitation of gypsum [39]. It is believed that gypsum forms after the cracks. Once the crack appears, the penetration of sulfate ions increases, and the formation of gypsum is observed [11]. This clearly shows that gypsum forms after the development of the microcracks, without contributing to the macroscopic expansion [36, 40]. Mather [41] believes that gypsum formation during sulfate attack on cement paste causes no expansion. He claims that gypsum forms from the supersaturated solution by evaporation and subsequent precipitation, which leads to no expansion. Therefore the extensive gypsum formation occurs only after cracking and the main cause of expansion is ettringite formation according to this author.

1.2.2.3 Damage modes

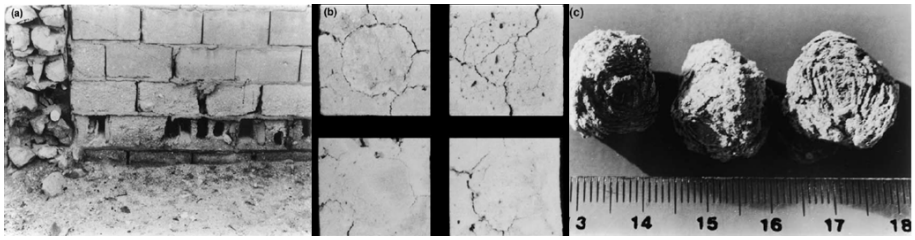

Figure 1.4 – Damage modes of external sulfate attack: (a) acidic type; (b) expansive type; (c) onion-peeling type [42].

The ESA-related damage manifests itself in several forms including acidic type, expansive type (cracking) and onion-peeling type [42], which are shown in Fig. 1.4. The first one, the acidic type, may lead to a reduction in the cross-sectional area of the structural component and a decrease in strength, which was believed to be attributed mainly to the formation of gypsum [43]. However, whether the gypsum is the reason for the expansion is in controversy, and has been discussed in the section 1.2.2.2. The second mode, the expansive type with cracking, is the most common phenomenon occurring in sulfate attacks. It takes place when the reactive hydrated aluminate phases are present in sulfate-rich conditions. The expansion is generally attributed to ettringite formation, as ettringite forms from cement hydrates when SO_4^{2-} is supplied. Observations from scanning electron microscope (SEM) studies [39] clearly show three distinct zones in Fig. 1.5: a cracked and highly deteriorated surface zone, a zone of deposition of attack products and a chemically unaltered zone (corresponding respectively to zones number 1, 2 and 3 in Fig. 1.5). The last mode is the onion-peeling type, which is characterized by a scaling or shelling of the surface in successive layers in the form of delamination [44]. It is observed in plain and fly ash-blended cement paste specimens exposed to mixed sulfate environments.

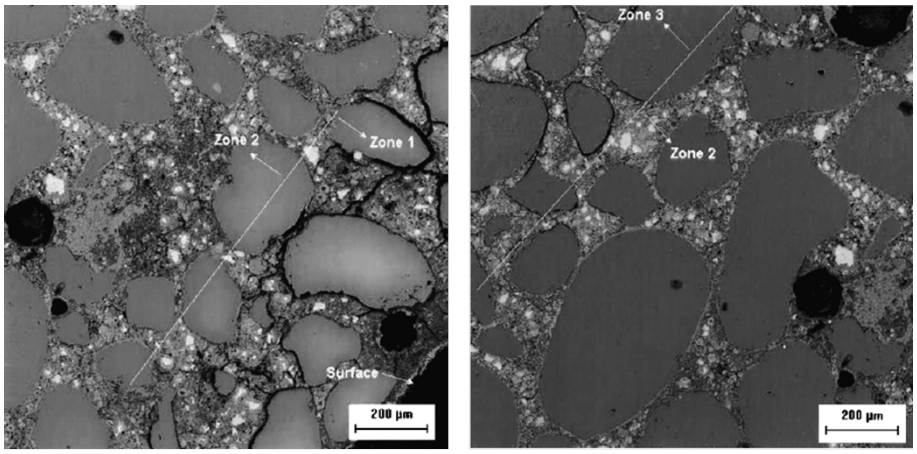

Figure 1.5 – Microstructural observations by SEM for Portland cement mortar specimen stored in sodium sulfate solution for 12 weeks [39].

When exposed to a sodium sulfate solution, the attack process can be described in six steps [45], see Fig. 1.6. As the sample is immersed in a sodium sulfate solution with a pH of 7 in this study, gypsum and ettringite start to form when sulfate ions penetrate into the material. The presence of crystals at this stage allows the expansion of the surface zone. Then, the expansion is induced by the bulk of the

mortar with creating tensile forces. The cracks start to appear when the tensile forces reach the tensile strength of material. During this process, the degraded zone goes further into the center of the material due to the accumulation of gypsum inside pores and voids. This process leads to the creation of new ettringite and gypsum inside the cracks. In the end, various layers in the concrete specimens are developed which are "disintegrated surface, mineral deposition area and the new cracked but chemically unaltered area further inside the specimen". In addition, the expansion of cement-based materials exposed to sodium sulfate solution, as shown in Fig. 1.7, occurs in two stages [39]. In the first stage, the expansion increases slowly, which is called the "induction period". It was proposed that in the first stage, ettringite forms in the large pores, leading to no expansion in the paste [11]. In the second stage, the expansion increases at a fast and constant rate until the breaking of samples. When the solution concentration reaches a critical level, the ettringite precipitates in small pores. The force is exerted when the crystal touches the pore walls. And when the force exceeds the tensile strength of the specimen, microcracks appear inside. Afterwards, gypsum and ettringite deposit in the cracks and voids due to the penetrated sulfate ions. This two-stage expansion for sodium sulfate attacks is observed in various studies [12, 39, 46].

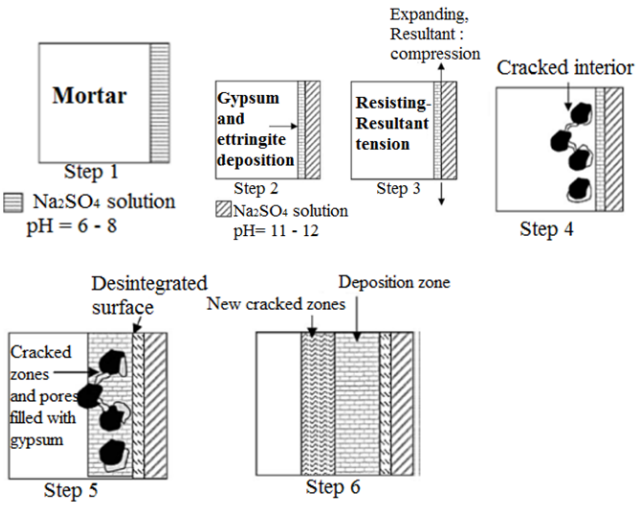

Figure 1.6 – Six steps of the sulfate attack process in a sodium sulfate solution [39].

1.2.2.4 Factors affecting ESA

Impact of the exposure solution The effect of existing cations in the solution is very important and it affects the development of sulfate attacks. In fact, the

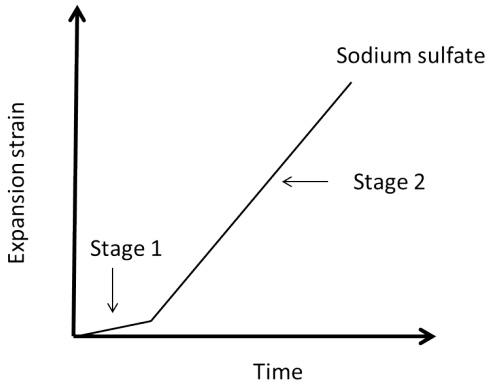

Figure 1.7 – Expansion curve of cement-based materials exposed to sodium sulfate solution [39].

more cations are present, the more various types of reactions will take place. External sulfate attacks on cement-based materials is primarily attributed to sodium, magnesium and calcium sulfate salts. However, in laboratory studies, the sulfate attack is normally induced by the sodium sulfate or magnesium sulfate due to the limited solubility of calcium sulfate in water at normal temperature (approximately 1400 mg/l) [47]. Sodium sulfate is the most widely used salt for assessing sulfate attack, due to its high solubility. Little work is available on the use of potassium sulfate. It is predicted that ettringite would precipitate when cement material is immersed in potassium sulfate solutions, possibly accompanying with syngenite ($K_2Ca(SO_4)_2H_2O$) [48].

Magnesium sulfate appears to be the most detrimental of all the sulfates [49], especially to Portland-cement concrete containing silica fume. The mechanism of the magnesium sulfate attacks is different from the one of sodium sulfate attacks. The magnesium sulfate attacks result in the formation of brucite ($Mg(OH)_2$) and gypsum layers, accompanied with the decalcification of the C-S-H gel, and the loss of the cementitious structure. The chemical reactions happening in magnesium sulfate attacks have been studied in [50]. Magnesium sulfate reacts with the hydrated cement paste to form gypsum, ettringite and brucite ($Mg(OH)_2$). The corresponding chemical reactions are shown in Eq. 2. The formation of ettringite leads to an expansion. But the brucite layer that forms on the surface has a function of protection to the concrete due to its low solubility. The formation of brucite continues until the $Ca(OH)_2$ is depleted. The consumption of $Ca(OH)_2$ leads to a gradual decrease of pH, which renders the calcium silicate hydrate (C-S-H) gel unstable and liberate more Ca^{2+} into the surrounding solution to increase the pH. This can once again go

into reaction with the attacking solutions.

$$\begin{aligned} M\bar{S} + CH + 2H &\rightarrow C\bar{S}H_2 + MH \\ C_4AH_{13} + 3C\bar{S}H_2 + 14H &\rightarrow C_6A\bar{S}_3H_{32} + CH \\ C_4A\bar{S}H_{12-18} + 2C\bar{S}H_2 + (10-16)H &\rightarrow C_6A\bar{S}_3H_{32} \\ C_3A + 3C\bar{S}H_2 + 26H &\rightarrow C_6A\bar{S}_3H_{32} \end{aligned} \tag{2}$$

where M = MgO.

ESA is slowed down for low solution concentrations. Indeed, this reaction is closely related to the sulfate content in solution. As the sulfate concentration increases, the kinetics of the attack increase also. It is noted that for high levels of sulfate, the precipitation of gypsum is favored over the precipitation of AFt [11], which is consistent with the stability domain of the sulfated phases with respect to the sulfate concentration in solution.

Table 1.2 – Molar composition of the sulfate solutions tested [51]

Sulfate salt	Na_2SO_4 (mol/l)	$MgSO_4$ (mol/l)	Low $MgSO_4$ (mol/l)	Mixture (mol/l)
Na_2SO_4	0.35			0.132
$MgSO_4$		0.35	0.035	0.088
$CaSO_4$				0.088
K_2SO_4				0.044

The degradation of mortar prisms exposed to various sulfate solutions is studied in [48, 51], including sodium sulfate (0.35 mol/l), magnesium sulfate (0.35 mol/l), low magnesium sulfate (0.035 mol/l) and a mixture of sodium, magnesium, calcium, and potassium (for detailed composition, see Table 1.2). The expansion curves are presented in Fig. 1.8. The expansion of CEM I mortar prism exposed to the sodium sulfate is the fastest and highest, followed by the exposure to magnesium sulfate solution. The expansions of CEM I mortar prisms exposed to a mixed-cation solution and a dilute magnesium sulfate solution are compared: the expansion of the two samples are comparable, even when the overall sulfate content is much greater in the mixed-cation solution.

The presence of chloride and sulfate ions leads respectively to the reinforcement corrosion and sulfate attacks in a marine environment. It is reported that the C_3A tends to react with sulfate ions to form ettringite and monosulfate [52, 53, 54].

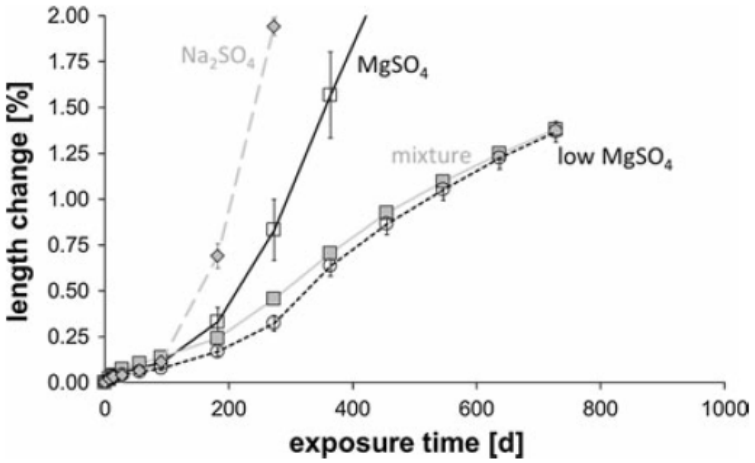

Figure 1.8 – Length changes of CEM I mortar bars exposed to different sulfate solutions [51].

An increase is also reported in the sulfate concentration in the pore solution of specimens contaminated with sodium chloride plus sodium sulfate in comparison with only sodium sulfate [55]. However, the expansion due to ESA in the seawater is for example very low compared to an exposure only to sodium sulfate. It is due to the reaction of C_3A and Cl^- forming Friedel's salt ($C_3A(CaCl_2)H_{10}$) which slows down the penetration of sulfate ions inside the material [56].

The concentration of the sulfate solution is an important factor. The use of highly concentrated solution [11, 36, 57, 58] usually accelerates the attack, because the higher concentration gradient leads to a higher penetration. The expansion of mortar specimens immersed in different sulfate solutions (3 g/L, 10 g/L and 30 g/L) is studied in [11], see Fig. 1.9. It shows similar swelling at the initial 120 days, but the expansion for concentration of 30g/L increases rapidly later. An increase in the concentration of the solution leads to an increase of the rate of expansion during the accelerated phase for the mortars stored in sodium sulfate solution [39]. Based on the crystallization pressure mechanism, it is concluded [11] that the sulfate concentration in the solution has a large impact on the supersaturation with respect to ettringite, and thus also on the expansive force which is generated. Since the microstructure is changed by the presence of microcracks around and between the aggregates [36, 39, 59], the microstructure is affected by the sulfate concentration in the solution in an indirect way.

On the other hand, the pH of the solution plays a major role in sulfate attacks since it controls the leaching effect and the solubility of the phases. In the practical field, the

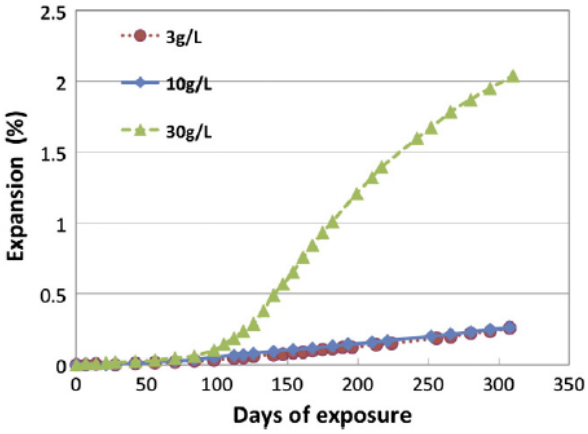

Figure 1.9 – Expansion of mortar specimens immersed in sodium sulfate solutions with different concentrations: 3g/L, 10g/L and 30g/L [11].

concentration variation of the sulfate ions caused by ESA is small compared to the volume of the sulfate ions in the field, indicating that the pH of the solution should be controlled constantly. Monitoring the pH of the solution during the test is proposed [32, 60, 61]. Comparison between the controlled and uncontrolled pH conditions shows that the time to reach a certain level of expansion for the uncontrolled pH condition was twice as much as for the controlled pH condition [62, 63]. The leaching appears to be prevented when the solution is not renewed [33]. A reduction in expansion is found [33, 64, 65, 66] when the pH is reduced. However, reducing the pH contributes to a faster onset of the expansion [62]. A cycling pH rise from 7 to 12-13 is observed owing to the solution renewal frequency in [33]. Though a constant pH is not obtained from renewal of the solution, an unlimited source of the sulfate ions is simulated.

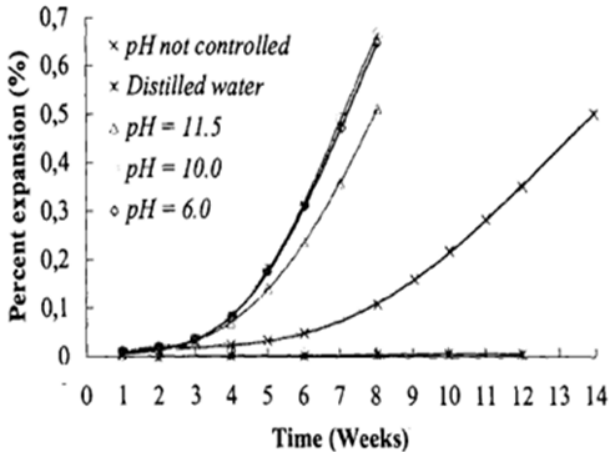

Figure 1.10 – Effect of pH on the durability of cement pastes [67].

The study of Revertegat et al. [67] confirms the accelerated effect of ESA for pH values below 11.5 for both Portland and slag cement pastes, see Fig. 1.10. This degradation results in an increase of the surface porosity, a larger quantity of leached calcium and, in the long term, surface cracks in the sample, which favors a deeper sulfate penetration in the cement matrix.

Impact of the mix design The intensity and rate of the ESA depend on the mix design of the materials. The type of cement significantly affects all types of sulfate attacks on concrete. To be more specific, it is the content of C_3A that affects the degradation degree. Studies indicate [68] that the type of cement significantly affects the resistance of concrete to sodium sulfate solutions. The standard composition requirements for cement are different in ASTM C150 and EN-197. For example, for cement I in ASTM C150, the maximum content of SO_3% that could be added is 3.0% when C_3A % is less than 8 %, and is 3.5% when C_3A % is more than 8%. However, in EN-197, the maximum sulfate content SO_3 % that could be added in cement I depends on the strength class: 4.0% for 32.5N, 32.5R, 42.5N and 4.5% for 42.5R, 52.5N, and 52.5R.

ASTM C 150 type I cement with $C_3A = 8\%$ shows a significant deterioration compared to ASTM C 150 type V cement with $C_3A = 3.5\%$ and blended cements. As a reactant, the content of C_3A plays an important role in the resistance to sodium sulfate attacks. Al-Amoudi proposed that when the C_3A content is less than 5%, the cement will be sulfate-resistant [69], and it is possible to observe sodium sulfate attacks if the C_3A content ranges from 5% to 8%. It is also recommended in [7] that the use of cement with C_3A should not be greater than 7%. Moreover, according to Neville [17], decreasing the amount of C_3A in the cement mix will lead to a lower ettringite formation since there will only be a small amount left to react with calcium sulfates. In addition to the C_3A content, the C_3S/C_2S has a significant influence on sulfate resistance as well [70]. The sulfate deterioration for a Type I Portland cement ($C_3A = 11.9$ %) with a C_3S/C_2S ratio of 7.88 was found to be 2.5 times the deterioration for another Type I Portland cement ($C_3A = 9.3$ %) with a C_3S/C_2S ratio of 2.57 after 150 days of exposure to an accelerated sulfate test. However, the C_3A content has little effect on the magnesium sulfate attack due to the formation of brucite as a layer on the surface of the specimens. It reduces the penetration of sulfate ions and results in less chemical reactions of C_3A and sulfate ions.

In order to obtain a good durability performance of cement pastes, a low water to

cement ratio is recommended. The effect of different water to cement ratios (w/c = 0.485 or 0.435) on the expansion of cement pastes is studied by Naik et al [71]. As shown in Fig. 1.11, the w/c = 0.435 shows four times less expansion compared to w/c = 0.485. It is believed that the deterioration phenomena are related to the permeability of concrete which is proportional to the water to cement ratio [72]. The reduction of the water to cement ratio contributes to small pore size and thus to a decrease in the diffusion of sulfate ions into the matrix [42, 73]. However, a small porosity provides a low capacity to accommodate the ettringite formed later, which leads to a greater expansion.

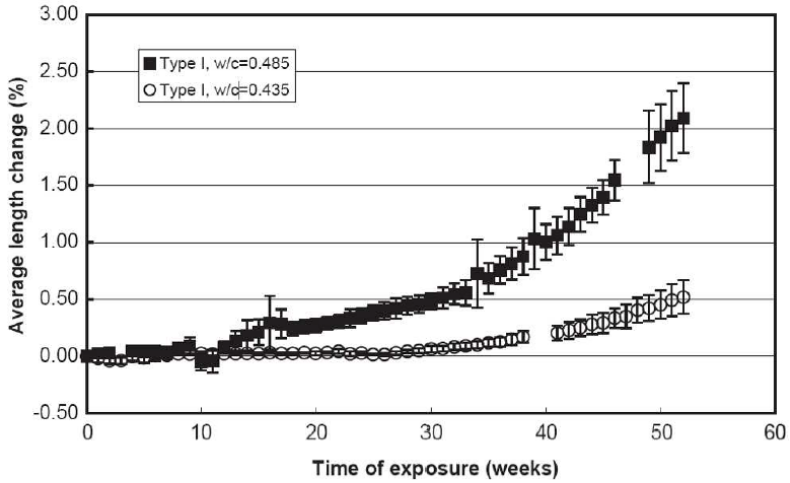

Figure 1.11 – Influence of the w/c ratio on cement paste exposed to a sodium sulfate solution [71].

Supplementary cementitious materials have been used to mitigate sulfate attacks, reducing the ettringite and gypsum formation [74, 75, 76]. It is found [69] that the use of blends leads to a reduction of the reaction of tricalcium aluminate and tricalcium silicate with the sulfates. A finer pore structure is presented with the addition of blends, which reduces the permeability [77], and thereby restrains the formation of ettringite. A good resistance upon exposure to sodium sulfate solutions is shown with a blend of up to 15% silica fume [78]. This is a result of denser microstructure provided by the hydration of the finer silica fume particles [79]. Low expansion is shown for silica fume blended cements in all sulfate solutions [64]. Similarly to fly ash blended cements, silica fume blended cements show no accelerating expansion even after 1 year of immersion in a variety of sulfate solutions. It is unaffected by changes in pH of the sulfate solution.

On the other hand, some studies [11, 48] show that clinker substitution by slag

improves the resistance of concretes in sulfate-rich media or that silica fume improves the resistance of the mortar exposed to a sodium sulfate solution. This is explained by the non-coexistence of gypsum and AFt in these types of binders.

1.2.2.5 Ions transport

The main factor that affects the concrete degradation resulting from external sulfate attacks is the penetration of the ions. In a full immersion the concrete structure is saturated. Ions may diffuse either outwards or inwards. The contact with pure or deionized water creates concentration gradients between the pore solution and the aggressive environment of the materials. The concentration gradients disturb the initial thermodynamic equilibrium between the pore solution and the solid hydrates, which leads to the ions transport. The pore solution of cementitious material consists of K^+, Na^+, and is saturated with $Ca(OH)_2$. Consequently, the K^+, Na^+ and Ca^{2+} ions in the pore solution diffuse outwards into the exterior solution. During the Ca^{2+} leaching process, Ca^{2+} ions continue to dissolve in the pore solution, mainly from $Ca(OH)_2$ and/or C-S-H gel, and diffuse outwards into exterior solutions. According to the investigations in the literature, the calcium leaching of the cementitious material is accompanied with dissolution of different hydrates [80, 81]. Ragoug mentioned that two modes of transfer occur in ESA [32]. Sulfate ions transfer to the cement matrix and a leaching of calcium ions to the outer solution occurs. A coexistence of diffusion and physicochemical fixation of sulfate ions is observed in the cement matrix. Firstly, a concentration gradient transfer occurs. Then, the transfer of sulfate ions is rapidly stabilized and only a surface accumulation of sulfate ions is observed, suggesting that fixation occurs, causing self-deceleration of the ingress as long as the sulfates can react with the cement hydrates.

Furthermore, the physical and mechanical properties of cementitious materials subjected to leaching have been widely reported. The different zones at the cross section of leached specimens induced by the dissolution and precipitation were found [81]. The inner front is associated with the dissolution of CH, and the outer fronts are induced by the progressive decalcification of C-S-H gels as well as the dissolution or precipitation of AFm, ettringite, etc. As described in Fig. 1.12, the identification of the affected depth by ESA (combining leaching and the effect of external sulfate) and the characterization of this area in sub-zones as a function of the modification of the microstructure is a relevant method for identifying the different mechanisms of ESA. In the leaching process (at the surface of the material), the porosity increases due

to the dissolution of CH and the decalcification of C-S-H, and the microstructure is modified, which contributes to an increase in permeability. Studies on the relationship between leaching and porosity change were performed in [13, 14, 15]. Indeed, leaching leads to a significant reduction in bulk density, compressive strength and stiffness of the pastes and mortars, however, the ductility increases as a result of pore structure variation [82, 83, 84].

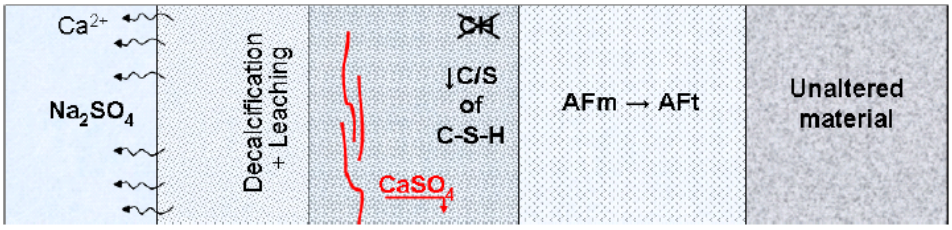

Figure 1.12 – Characterization of the affected depth by ESA and leaching [35].

1.2.2.6 The effect of the dissolution of CH and the decalcification of C-S-H on pore size distributions

Some studies [85, 86] have reported that C-S-H gel begins to dissolve only after complete dissolution of CH. However, other authors [31, 87] supposed that CH does not have to dissolve completely before the decalcification of C-S-H occurs, and that it depends on the mass or volume ratio of the leachant to the solid. In [88], Jain et al. separated the porosities created due to the dissolution of portlandite and the decalcification of C-S-H. For instance, it was found that 60% of the CH was leached out after 28 days of immersion in deionized water, and increased to 83% after 90 days of immersion. Meanwhile, leaching happened in 20% of the C-S-H after 28 days and increased to 28% after 90 days. This conclusion further confirms that the pore release comes both from CH and C-S-H. In addition, the pH of the pore solution of the cement paste is buffered by portlandite (pKa = 12.6). However, due to the presence of high concentration of alkalis in the solution, the pH may with (mostly) harmless effect exceed this known value. The pH of the renewed sodium sulfate solution with a concentration of 15g/L (in the case of ESA) remains around 8.0 (measured by Ragoug in [32]), which is below the pH of the equilibrium. In addition, the concentration of calcium ions has not reached the values of the stability domain of the CH (the solubility of the CH is about 1.1 g/L at 20 °C [32]). Therefore, these conditions further promote the dissolution of CH, as well as the

decalcification of C-S-H.

The effect of leaching on the pore structure has been studied in several researches. The change of pore structure of cementitious materials due to leaching was studied in [13]. Van Gerven showed that the effect of leaching on porosity is mainly on capillary pores with the range between 0.1-10 μm for one sample and 0.04-0.2 μm for another. Haga found that the pore volume became larger with a decrease in the quantity of CH [14], which results from the dissolution of CH. After leaching, pores of larger diameter than the ones of the initial samples were observed, and the pores with a diameter of less than 100 nm increased. The increased volume with a diameter of less than 100 nm is believed to be caused by the dissolution of C-S-H gel and the pores larger than a few microns are due to the dissolution of CH. In [89], it was determined that, in dissolution tests of alite hydrate, pores with a size of around 1 μm increased along with the progress of dissolution of the portlandite. Therefore, the author assumed that pores of 0.2 μm or smaller were attributable mainly to the C-S-H gel, while those larger than 0.2 μm were attributable mainly to the portlandite. The author questioned the reliability of this classification, but he was sure that there was a good correlation between the dissolution of portlandite and an increase in the volume of pores larger than 200 nm in leaching examinations of alite hydrate. However, Saito [15] pointed out that the increase of pore volume in the range of 50 to 500 nm in diameter can also be due to the dissolution of CH. To sum up, a table illustrating the results is shown in Table 1.3, and a corresponding figure with pore size range is shown in Fig. 1.13.

Table 1.3 – Literature studies on effect of leaching on pore size distribution

Studies	Pore release range	Explanations
Van Gerven [13]	0.1 - 10 μm or 0.04 - 0.2 μm	Calcium leaching
Haga [14]	>a few μm	dissolution of CH
	<100 nm	dissolution of C-S-H
Haga [89]	<200 nm	dissolution of CH
Saito [15]	50 - 500 nm	dissolution of CH

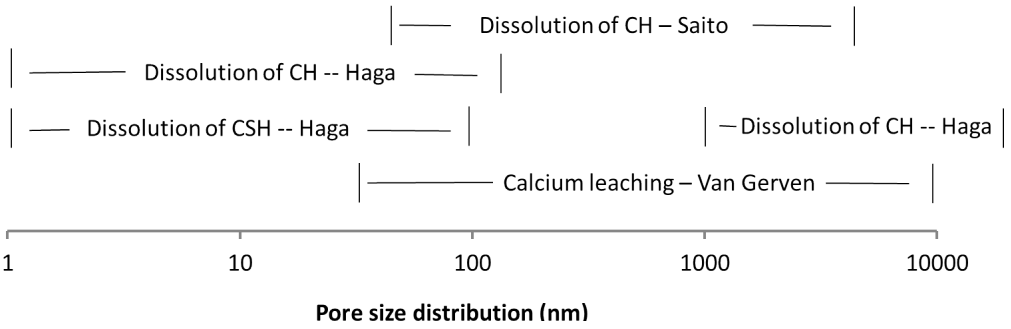

Figure 1.13 – Literature studies on effect of leaching on pore size distribution with pore size range.

1.2.3 Delayed Ettringite Formation

Internal sulfate attacks (ISA) are defined as the deterioration of cement-based materials due to ettringite formation, the sulfate source of which comes from the material itself. As one form of ISA, delayed ettringite formation (DEF) is an internal swelling reaction that can affect concrete when the material has experienced high temperatures (typically above a possible threshold value of 65 °C [90]). A great amount of studies have indicated that ettringite in hydrated Portland cement products can be fully or partially destroyed when the materials are cured at a temperature above about 65 °C [91, 92, 93]. This is why it is generally agreed that above this temperature the ettringite formed upon hydration is thermodynamically unstable and decomposes to hydrated calcium monosulphoaluminate, releasing sulfates in the pore solution. In addition, part of the released sulfates are adsorbed on CSH and the rest is available in the pore solution [94]. It is postulated that these available sulfate ions are trapped by physical adsorption on the surfaces of the calcium silicate hydrates (C-S-H gel) [95, 96], whose hydration has been accelerated due to the heat curing [97]. During the subsequent storage in cool water, ettringite forms over time. That is because at the ambient temperature, the C-S-H will start slowly releasing the trapped sulfates and making them available to the pore solution again. The released sulfate ions diffuse into the nearest microcrack and react with the Al-bearing materials (C_3A) and possibly C_4AF in the pores to form ettringite, which leads to the macroscopic local effects mainly consisting in material swelling, cracking and a decrease of the mechanical properties. This may cause large structural disorders due to unexpected deformations and additional stresses in concrete and reinforcement.

1.2.3.1 Observations

One of the common observations made on damaged cement-based material due to DEF is the occurrence of an expansion, accompanied by cracking. The normal experimental method to study the DEF is to measure the expansion considered as a degradation parameter for this phenomenon, and the corresponding results are presented as swelling curves. In [98], different forms of the swelling curves are summarized (Fig. 1.14). The first one is quick swelling, with a sigmoid form (curve 1). This kind of curve can be divided into three parts: latent period, accelerated period and the plateau period. At the first stage, the expansion is not obvious and normally smaller than 0.1%. It depends on the material composition and on the thermal history, amongst other parameters. The second period presents a marked acceleration at about 0.1% of expansion and stops at the inflection point. In the last stage, the rate of expansion decreases and stabilizes to a constant value. The second form of swelling curve corresponds to a slow swelling with a linear form (curve 2). This kind of swelling requires a long monitoring, and may have the same sigmoid shape as curve 1. The expansion increases with a constant rate during the observation time. The last form is called negligible swelling meaning that the specimens do not show any significant expansion. As the curve 3 in Fig. 1.14, the expansion does not reach 0.04% at 700 days.

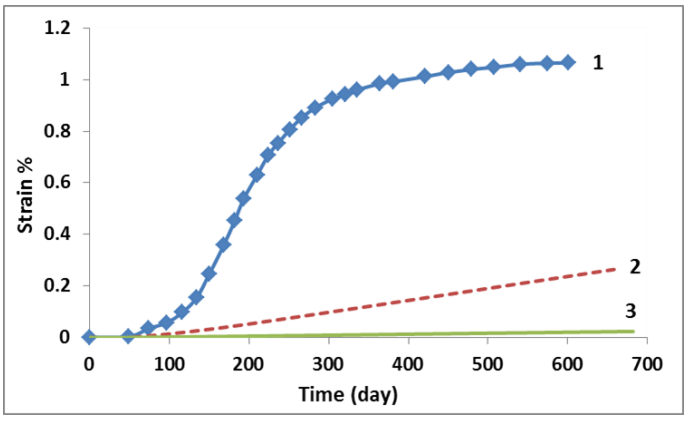

Figure 1.14 – Swelling curves of concrete specimens after DEF [98].

At a given temperature and moisture state, the rate and ultimate extent of the expansion of the concrete are mainly influenced by three factors (amongst others): cement chemistry, paste microstructure, and concrete or mortar microstructure [91]. The chemical properties of the component determine the amount of the expansion product that can be formed. The microstructure in small scale (e.g. in the paste) determines the stresses produced, while the microstructure in large scale (e.g. in the

mortar and concrete) determines the response of the material. Based on previous research, it can be summarized that the conditions necessary for the appearance of DEF are: an excessive rise of temperature during the casting of the cement-based materials; the presence of sulfates; the alkali content and a moist environment [99]. The kinetics of the reactions and the damage depend on environmental factors (species and concentration of sulfate, pH of the solution, humidity and temperature) and material properties (chemical composition of the cement paste, pore distribution and diffusive properties).

Not only an expansion, but also a weight gain is observed during DEF. The weight increases proportionally to the expansion when mortar specimens are immersed in water [100]. The observed weight gain is believed to be due to a combined effect of ettringite formation with the involvement of sulfate ions and the trapping of external water during the expansion process [101].

Several studies show that DEF leads to a degradation of mechanical properties. For example, Z. Zhang et al found that DEF-induced expansions were accompanied by significant and progressive reductions in dynamic elastic modulus, due to the progressive crack developed [101]. What's more, a degradation in flexural and compressive strength was observed when thermal treatments were applied [99].

1.2.3.2 Ettringite formation

The primary ettringite formation in the initial stage of the hydration is seen as a positive effect as the bulk is plastic during this period (within hours) and no stresses are produced [16], while a damaging role is shown in hardened concrete. Damaged concretes often show large amounts of ettringite even if they were not treated by preheating [102, 103] (e.g. pavement concrete). After DEF, the conspicuous formation of ettringite is observed in voids, cracks, and the contact zone between the aggregate and the hardened cement paste (see Fig. 1.15). Different hypotheses are proposed to explain the expansion observed. It is said that the formation mechanism [104] plays an important role in the damage. The authors found a good correlation between expansion and ettringite formation, even though no general relationship between the amount of ettringite formed and the extent of expansion appears to exist.

In a Portland cement, gypsum reacts with calcium aluminate to form ettringite.

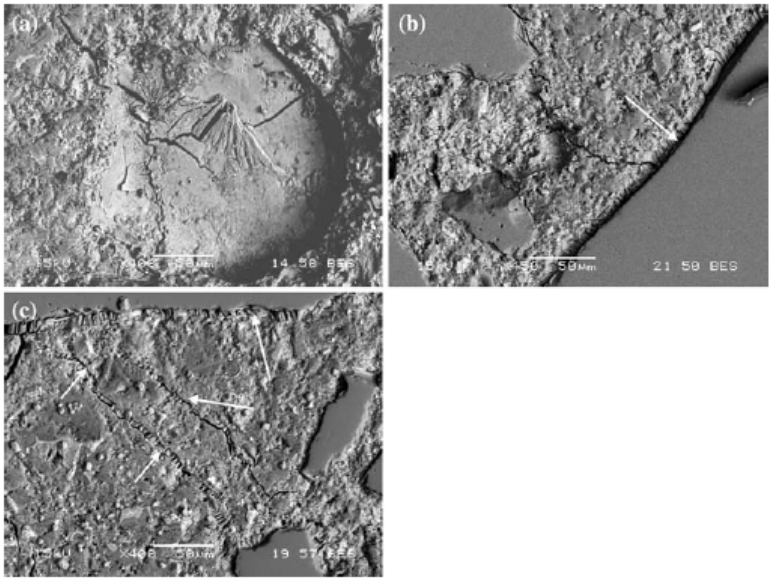

Figure 1.15 – BSE images showing the presence of ettringite at the paste/aggregate interface (a, b), and in cracks extending into the cement paste (c) [105].

X-ray peaks associated with ettringite are detectable within a few hours and the quantity increases during the first day. However, the ettringite peaks weaken in the next few days depending on the chemistry of the cement and the environmental conditions [106]. If all the gypsum is consumed through the ettringite reaction, ettringite converts to monosulphoaluminate (shown in Eq. 3 and 4):

$$C_3A + 3C\bar{S}H_2 + H_{26} \rightarrow C_6A\bar{S}_3H_{32} \tag{3}$$

$$2C_3A + C_6A\bar{S}_3H_{32} + H_4 \rightarrow 3C_4A\bar{S}H_{12} \tag{4}$$

Ettringite crystals are found in the pores and cracks of deteriorated concrete. However, it is not clearly proved that the cracks are connected with the crystallization of ettringite. It is still controversial whether the formation of ettringite in cracks is the cause of expansion or just a consequence after expansion. These crystals might precipitate in the voids when the sulfate ions transfer through the pore structure. The microstructure, the distribution and the quantity of ettringite formed in the Portland cement paste were studied in [94] by scanning electron microscope (SEM), X-ray microanalysis and quantitative X-ray diffraction analysis. For Portland cement paste specimens preheated at 100 °C for 3 hours, ettringite was found distributed in the prisms with large expansions, and more ettringite was distributed near the surface than in the central region where few cracks were observed. In the heat treated cement paste, lower total content of ettringite but greater areas of well

crystallized ettringite were observed, compared with the case of room temperature cured paste. It implied that the heated cement paste contained a smaller proportion of S and Al, owing to sorption on C-S-H gel [107] during the period of heat cure.

1.2.3.3 The stability of sulphoaluminates

Monosulfate is reported to be a metastable phase in hardened cement paste. At a temperature of 25 °C, the solubility product of ettringite (2.8×10^{-45}) is much lower than that for monosulfate (3.7×10^{-30}) [108], indicating that under ambient condition ettringite is more stable in a cement system than monosulfate. According to [109], the increase of temperature does not lead to precipitation of ettringite, which forms later until the system is cooled and results in internal crystallization pressure and expansion. However, the monosulfate is more stable than ettringite at high temperatures. It forms during steam curing at temperatures above 70 °C and transforms to ettringite after cooling [110].

Tepponen et al. report that ettringite is detectable by X-ray analysis after a few hours when curing at 25 °C [111]. Hekal points out that ettringite starts to form 15 minutes after the water and cement are mixed when curing at 60 °C, and the ettringite crystals formed at higher temperatures are larger than those developed at 25 °C [112]. However, at temperatures above 65 °C, ettringite starts to decompose. It is noted that the water content drops from 32 to 10 molecules at 70.5 °C [113]. Ettringite remains stable at the first-stage when it loses from 32 to 18 water molecules. However, when water drops from 18 to less molecules in the following stage, the crystal starts to disintegrate [114, 115]. The structure of ettringite is shown in Fig. 1.16. The octahedral alumina ($Al(OH)_6^{3+}$) is bound to adjacent CaO_8-polyhedra by sharing the hydroxyl (OH^-) ions, while the channels between the columns are occupied by tetrahedral sulfate (SO_4^{2-}) ions with water molecules around [100]. These loosely and disordered water molecules will be removed when ettringite is exposed to an elevated temperature.

1.2.3.4 Sulfate sorption

It is reported in [116] that sulfate ions can be linked to the C-S-H surface. Sulfates do not participate in the structure of C-S-H [117], since it is a specific physical adsorption phenomenon [118]. Sulfate sorption on C-S-H increases with sulfate con-

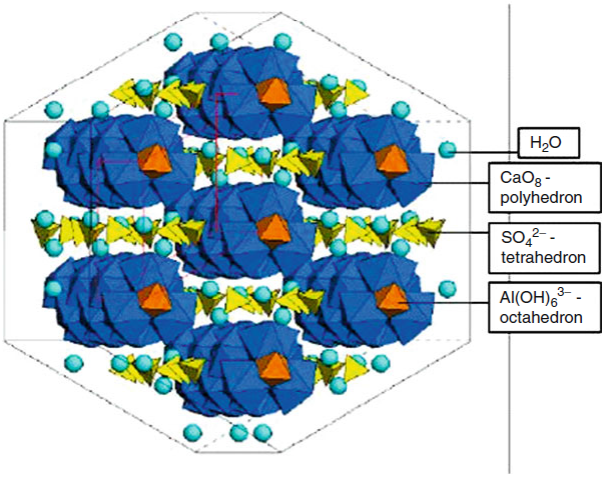

Figure 1.16 – The structure of ettringite (according to Dr. Neubauer/University Erlangen/Germany)

centration in solution, and follows a Langmuir law [97]. A true Langmuir isotherm is adopted to describe the SO_4^{2-} adsorption on C-S-H (Eq. 5) based on a well-defined condition (the adsorption is limited to a single layer, without side interactions, and the surface is homogeneous in terms of energy). A comparison of experimental data and simulation results is shown in Fig. 1.17, which proves that the adsorption isotherm of SO_4^{2-} ions on C-S-H samples is in fact governed by a Langmuir law:

$$\frac{1}{C_b} = \frac{1}{kC_{bm}}\frac{1}{C} + \frac{1}{C_{bm}} \tag{5}$$

where k is the affinity constant; C is the sulfate concentration at equilibrium in solution; C_b is the quantity adsorbed per gram of CSH; and C_{bm} is the quantity adsorbed when the surface is saturated.

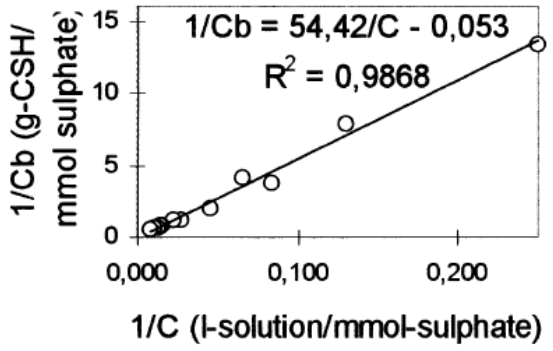

Figure 1.17 – Langmuir isotherm of SO_4^{2-} ions on C-S-H in 0.5 mol/L NaOH at T=25 °C [97]

However, the influence of the pH is also studied in [97]. Divet and Randriambololona find that the maximum quantity adsorbed and the affinity of the sulfates for the surface increases as the pH increases, which could be explained by the electrostatic contribution of the interaction between the sulfates and the surface.

The SO_4^{2-} ions are adsorbed on the C-S-H gel and balanced in terms of charge by calcium and alkali ions [119]. The impact of temperature and the concentration of Na^+ on sorption capacity of C-S-H is studied in [97], see Fig. 1.18. The amount of SO_4^{2-} increases with a higher alkali concentration in solution and higher temperatures. An equation based on the interpolation of these results is proposed in [120], and shown in Eq. 6:

$$SO_4^{2-} = 2.067 \times CSH \times (T)^{0.2124} \times [Na^+]^{0.2004} \times [SO_4^{2-}] \tag{6}$$

where CSH is the quantity of C-S-H formed in the concrete; T is the temperature; Na^+ and SO_4^{2-} are the concentration of Na^+ and SO_4^{2-} in solution.

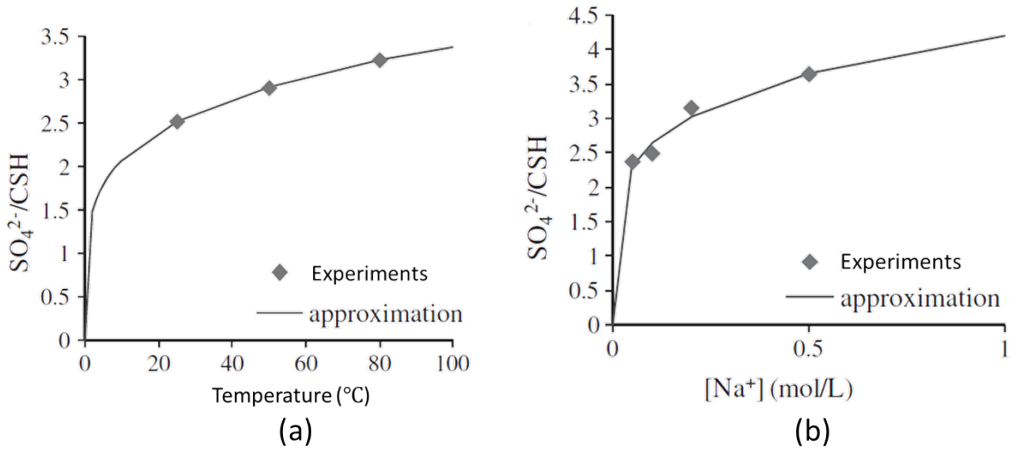

Figure 1.18 – Evolution of bound sulfates/C-S-H ratio relative to (a) temperatures with Na(OH) concentration of 0.1 mol/L; (b) Na(OH) concentrations at 25 °C [120].

The fact that the sulfate sorption capacity by C-S-H increases with temperature is confirmed by [121]. Barbarulo [117, 122] studied the sulfate sorption on C-S-H. He confirmed that the C-S-H has a capacity to adsorb sulfates, the quantity of which depends on the sulfate concentration in solution, on the Ca/Si ratio of the C-S-H but little on the temperature. He points out that the effect of the temperature on the sorption capacity comes from the Ca/Si ratio. For example, Fig. 1.19 shows the sulfate sorption capacity on C-S-H at a temperature of 20 and 85 °C. The amount of sulfate adsorbed in C-S-H increases with the ratio of Ca/Si for both temperatures.

The reason why the sulfate sorption capacity on C-S-H depends on the ratio of Ca/Si is that the surface of C-S-H is loaded negatively for low Ca/Si, vanishes when the ratio is around 1, and becomes positive for higher Ca/Si ratios [118]. The main effect of the temperature is a reduction in the total concentration of calcium in solution [117], which affects the sulfate sorption capacity indirectly. Based on the physical sorption of sulfate ions in C-S-H and the close dependence on the ratio of Ca/Si, Barbarulo proposes a model to study the adsorbed sulfate, which corresponds to the concentration of sulfate ions, calcium ions and the site of silicate tetrahedra susceptible to sulfate.

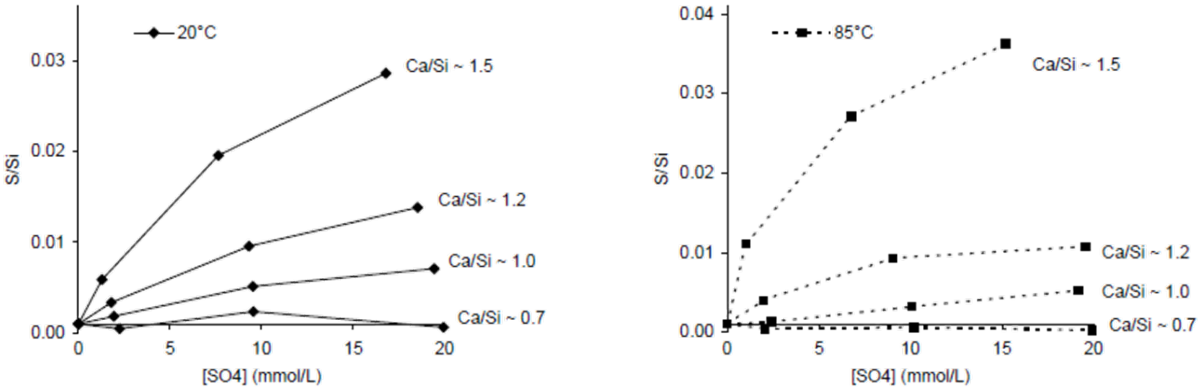

(a) The sulfate adsorbed in C-S-H with different Ca/Si at 20 °C

(b) The sulfate adsorbed in C-S-H with different Ca/Si at 85 °C

Figure 1.19 – The sulfate adsorbed in C-S-H with different ratios of Ca/Si at a temperature of 20 and 85 °C [117].

The presence of aluminates can modify the behavior of the system. Results from X-ray analyses [94, 123, 124] have shown that the ratio of Al/Si in C-S-H of cement pastes or mortars, which are moisturized at 20 °C or cured with steam, decreases from 1.3 to about 0.1 [117]. However, it is not indicated whether it is the consequence of the inclusion of aluminum in C-S-H or the result of a mixture of phases. This doubt is confirmed by Stade [125] and Faucon [126]. Both show that the substitution of silicon by aluminum occurred in octahedral sites.

1.2.3.5 Factors affecting DEF

Impact of the mix design High cement contents not only result in higher concrete temperatures during hydration, but also provide more source for ettringite formation, which increases the damage potential with more ettringite formation

(aluminates, sulfates, alkalis ...). The expansion increases together with the increasing cement content and high cement levels resulting in a higher damage rate in the presence of high content of C_3A [7] and probably C_4AF. Cement composition is also an important parameter for the expansion of the matrix. It is believed that there would be no expansion when the $(SO_3)^2/Al_2O_3$ is less than 2 [127]. Furthermore, the expansion caused by a high ratio depends on the heating duration as well [128]. In the later research, a pessimum value of the $(SO_3)^2/Al_2O_3$ is proposed [129, 130] between 0.8 and 1.4 [91]. Thus, the obtained experimental value of $(SO_3)^2/Al_2O_3$ varies with different test conditions and cement [91]. It is also reported that the expansion does not depend on $(SO_3)^2/Al_2O_3$ but on the contents of C_3A and SO_3 [129]. This idea is supported in [131] thinking that the higher ratio of $(SO_3)^2/Al_2O_3$ does not definitely result in an expansion, it depends on the duration of the heat treatment as well. Experimental studies [101] on mortars were performed with the addition of gypsum containing 1% SO_3 less than the optimum SO_3 content, optimum SO_3 content, and 1% greater than the optimum SO_3 content, see Fig. 1.20. The optimum cement sulfate content was defined as the total % SO_3 that produces the highest 24-h compressive strength at 23 °C. The specimens were heated with maximum temperature of 55 ° C and 85 °C, followed by long-term exposure at 100% RH over water. Both optimum and greater-than-optimum SO_3 content mortars show a clear expansion with a final value ranging from 0.2% to 1.7%. However, none of the lower-than-optimum SO_3 content mortars exhibited any expansion, and neither did the mortars cured at room temperature (23 °C) and 55 °C.

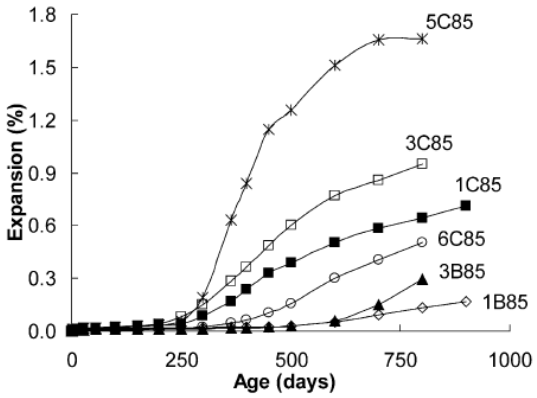

Figure 1.20 – Expansion-time plots for all 85 °C cured mortars. B stands for the optimum sulfate content, and C stands for the sulfate content 1% more than optimum. [101]

An index, see Eq. 7, based on sulfates, alkalis and aluminates amounts is proposed

in the literature [132]. However, this empirical relationship is only valid for specific experimental conditions: 85 °C (6h) and aging in 100% relative humidity:

$$\text{DEF Index} = (SO_3/Al_2O_3)_{molar} \times [(SO_3 + C_3A)/10] \times (\%Na_2O_{equiv})^{1/2} \qquad (7)$$

With a higher heating temperature, the cement composition plays a more important role. At a temperature of 90 °C, factors such as the fineness of cement, its content of alkali, C_3A, C_3S, MgO and SO_3 become very important [96]. The effect of mineral additions for controlling the expansion of mortars is studied as well. Class F fly ash and ground granulated blast furnace slag were found to be the most effective mineral additives for the elimination of the expansion of Portland cement mortars resulting from DEF. The silica fume has also similar effect, but the addition of silica fume is limited to 15% of cement by weight owing to its adverse effect on workability. The Class C fly ash is less effective in reducing the expansion than the aforementioned ones. Clinker with lower sulfate content can significantly reduce the risk of DEF-induced damage and portland cement with high C_3S and C_3A have more risk of DEF-related damage [133].

As one of the most important factors for ettringite formation, several studies have been done on porosity, especially microstructures, to locate the sites where ettringite can grow and produce damage. This microstructure depends on the w/c ratio. The pore volume has an effect on the damage in terms of transport of moisture and ions. The materials with a low porosity and a fine-pore microstructure are more sensitive than the less dense concretes of higher porosity and high-pored microstructure. The reason for this is that concretes with a fairly high porosity have a greater potential space for the formation of new products without expansion [91, 134].

Impact of storage conditions The potential for expansion due to DEF is related to the relative humidity. In general, the amount and rate of the swelling increase with increasing surrounding humidity of materials [129, 135, 136]. Some experimental results showed that the expansion occurred after a long period (600 days) when the specimens were stored at 98% RH, while no expansion was observed below 98% RH, which was explained by a combination of water availability and a leaching of alkalis out of the concrete pore solution [137] (shown in Fig. 1.21). An experimental study on the effect of different curing conditions [135] showed that: the expansion of

mortars heat-cured at 90 °C then stored in water increased the fastest and the most, followed by the ones stored in 100% relative humidity, KOH, KOH then in water. The author explained this phenomenon by alkali leaching. What's more, the Fig. 1.22 (b) shows that the expansion increases faster with less KOH concentration of the storage solution. No expansion was detected in the most concentrated [2P]KOH solutions, even after 540 days.

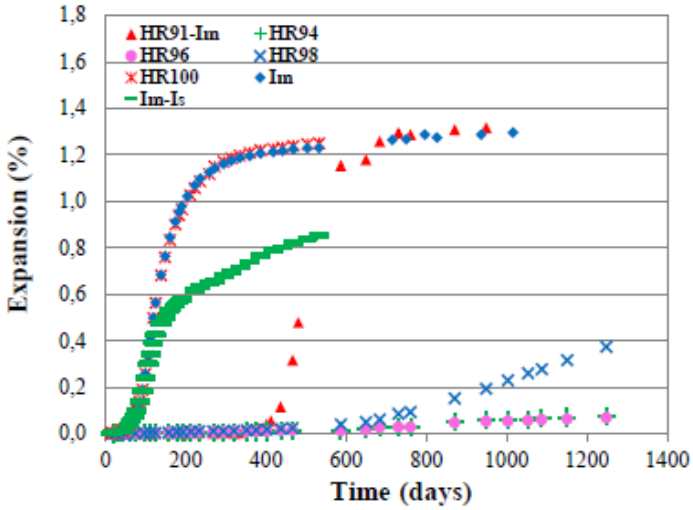

Figure 1.21 – Expansions of concrete specimens exposed to different relative humidity conditions [137].

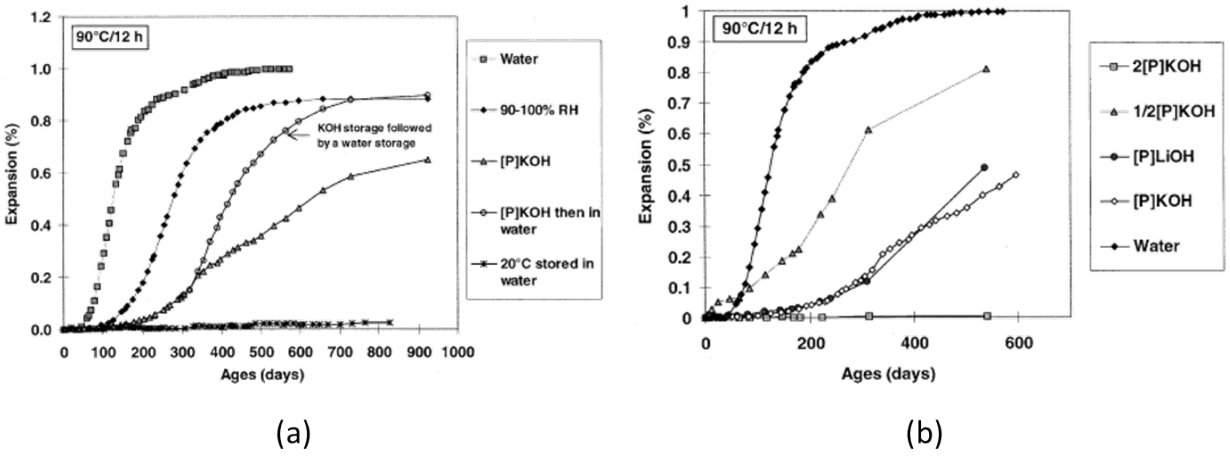

Figure 1.22 – (a) Effect of the storage conditions; and (b) Effect of the storage solutions' concentration on the expansion of mortars heated at 90 °C for 12h [135].

Impact of the thermal history The elevated-temperature heating treatment is a necessary condition for the phenomenon of DEF. It is generally admitted that a

curing temperature of above about 65 °C is essential to cause an expansion due to DEF when the concrete is subsequently stored in water [96, 129, 138, 139, 140]. As discussed previously, the thermodynamic stability of ettringite is reduced due to the rising temperature.

In general, the increase of the initial curing temperature is supposed to contribute to the increase of the DEF expansion [141, 142]. The maximum temperature influences expansion parameters, e.g, kinetics and magnitude [143, 144]. Specifically, the higher temperature leads to a faster kinetics and higher magnitudes of expansion. However, a pessimum effect of maximum temperature (combined with the duration of exposure) exists.

The heating duration is a significant factor for the development of DEF. Experimental studies [145, 146] were conducted to study the relationship between thermal history and the swelling characteristics (magnitude and kinetics). Different temperatures and heating durations (1 - 28 days) were adopted immediately after the casting. It was found that the coupling effect between the temperature and the heating duration was the most essential factor on DEF-related expansion. However, a pessimum effect has been highlighted. An experimental study trying to quantify the expansion due to different thermal histories and to identify the possible existence of a pessimum effect regarding the heating duration was conducted before [134]. Brunetaud [134] has shown that a heating at 85 °C for 2 days causes a significant swelling of about 1.2 %, while a heating at the same temperature (85 °C) for a period of 10 days produces significantly less swelling compared to treatment at the same temperature (Fig. 1.23). This pessimum effect was observed in [145] as well, see Fig. 1.24. The idea of "effective thermal energy" (ETE) was proposed [145]. It was assumed that only the thermal energy supplied beyond a threshold temperature T_{thresh} (calibrated at 65 °C for the concretes studied in [145]), is responsible for DEF expansions, see Eq. 8. In addition, there is a pessimum effect for the effective thermal energy (ETE). It means that the final expansion increases with the ETE provided up to a certain value, beyond which expansions decrease.

$$\text{EU} = \begin{cases} \int (T(t) - T_{thresh}) dt & \text{if } T(t) > T_{thresh} \\ 0 & \text{else} \end{cases} \tag{8}$$

where T_{thresh} is the threshold temperature, above which it contributes to the expansion.

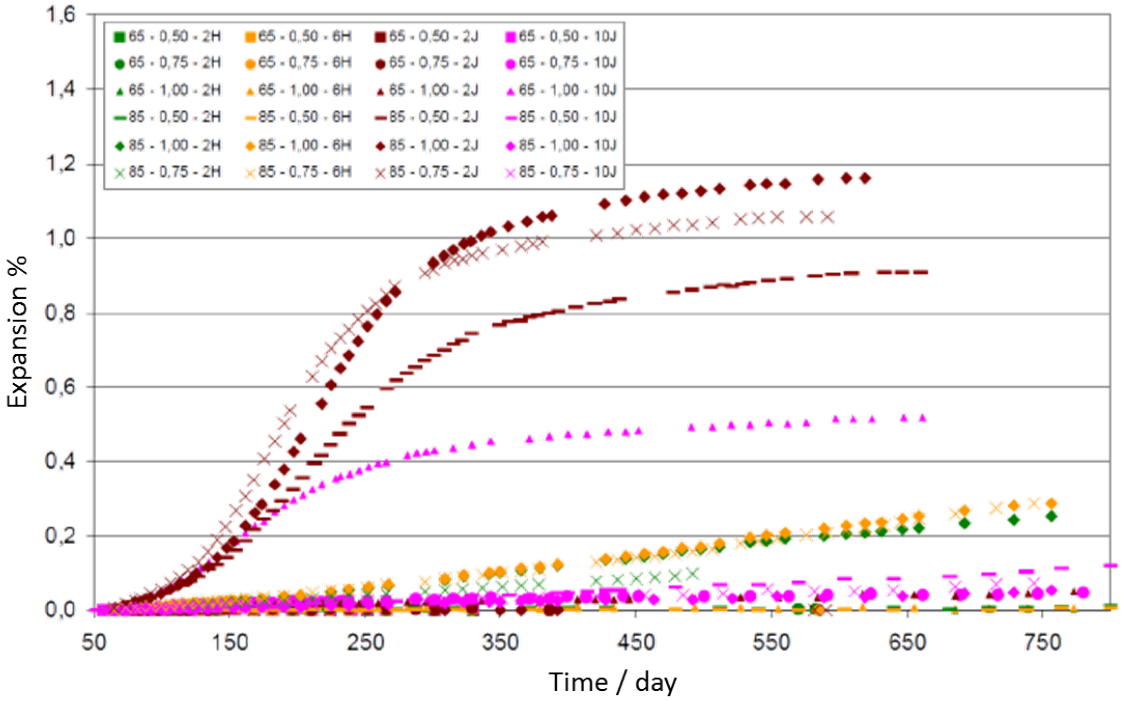

Figure 1.23 – Expansion results of the concrete specimens (maximum heating temperature - Alkali content % - Heat treatment duration) [134].

In addition, the heating has an effect on the C-S-H gel. Indeed, the heat treatment leads to a coarser pore structure [147, 148, 149] and the rims of C-S-H formed around the cement grains are brighter relative to pastes cured at lower temperatures [150, 151, 152, 153]. A lighter C-S-H rim formed at the temperature of 90 °C is observed, which is denser and contains much more sulfate than a darker C-S-H rim developed during subsequent storage at 20 °C [123, 153]. The composition of the inner C-S-H depends on the temperature and time at which the rims have developed. Kjellsen [151] studied the effect of heat curing and post-heat curing conditions on the microstructure and C-S-H composition of a high-performance concrete. The heat cured specimen which was stored outdoors, later showed a high hollow shell porosity and capillary porosity as revealed from backscattered electron images.

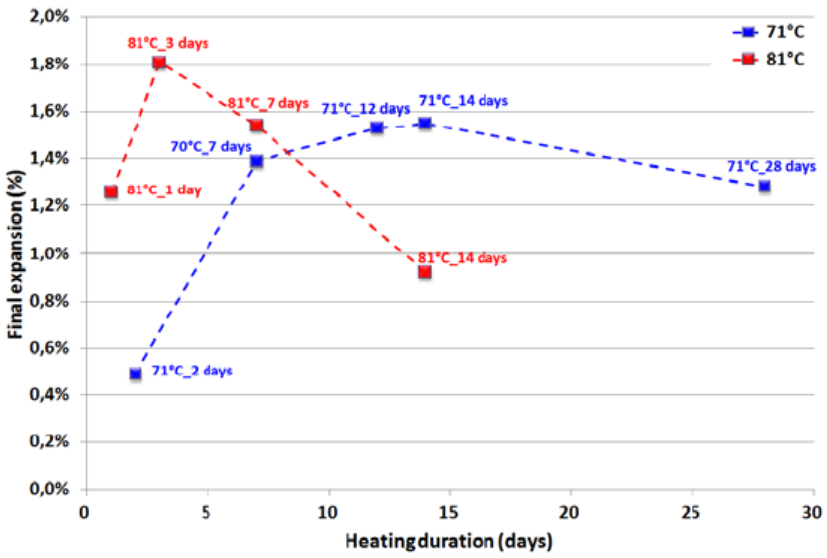

Figure 1.24 – Final expansion % evolution with heating durations [145].

1.2.4 Coupling of ESA and DEF

1.2.4.1 Mass concrete

Delayed ettringite formation does not only occur in heat-treated concrete but also in mass concrete structures. Mass concrete is defined by the ACI-116R (American Concrete Institute) [154] as "Any volume of concrete with dimensions large enough to require that measures be taken to cope with generation of heat from hydration of the cement and attendant volume change to minimize cracking." Mass concrete has been historically associated with large structures such as dams, bridge piers, and other large volume placements. In cast in-situ mass concrete elements, DEF can happen [155, 156]. Studies have shown that the long-term durability of certain mass concretes can be compromised if the maximum temperature after placement exceeds 65 °C. The maximum temperature is the sum of the placement temperature of concrete and of the temperature rise due to heat of hydration. The latter is affected by the mix design (cement content, type and source of cementitious materials), the structure design (section thickness), the ambient temperature and so on.

1.2.4.2 DEF in mass concrete

When cement is mixed with water, heat is liberated. This heat is called the heat of hydration, which results from the exothermic chemical reaction between cement and water. All concretes generate heat as the cementitious materials hydrate. The heat dissipates almost as quickly as it is generated for thin items, while heat dissipates more slowly if it is generated in mass concrete. Therefore, the heat generated by the hydration of cement raises the temperature of concrete, yielding significant temperature difference between the interior and the outside surface of the structures. The temperature induced by hydration in mass concrete may reach above 70 °C [156], which is high enough to induce DEF. In the field, for cast-in-place structures, DEF corresponds to the appearance of degradations in the most massive parts while the thinnest ones remain locally unaffected [157, 158].

DEF is encountered in concrete whose composition is particularly susceptible to it and which is subjected to appropriate long-term environmental conditions. It occurs in cast in-situ mass concrete elements. The first case that has been discovered was in 1998. Five bridges were studied [156] to determine the origin of the damage and identify the factors in all cases and that are necessary for the ettringite formation reaction to take place. Cements with higher contents of tricalcium silicate and tricalcium aluminate, as well as a higher fineness, have higher rates of heat generation than other cements. Tricalcium silicate and tricalcium aluminate chemically generate more heat, and at a faster rate, than dicalcium silicate or other cement compounds. Sulfate content, in its relation to the controlling of the hydration of calcium aluminate, contributes to the rate of heat liberation. In this case, DEF may occur in mass concrete.

1.2.4.3 Potential for coupling of ESA and DEF

Groundwater is a natural sulfate source to which buried concrete can be exposed. It typically has a low sulfate content. Sulfate ions can penetrate through the cement matrix, leading to damage. It contains different types and quantities of sulfate ions, depending on the flow of water. For example, it may contain calcium, magnesium, sodium and potassium with sulfate. According to instruction of concrete structures in Spain, a classification of potential damage related to the sulfate content in water or soils is presented in Table 1.4. As described before in this chapter, in fully

buried structures, the penetrated sulfates react with aluminate hydrates to produce ettringite and gypsum, which lead to an expansion, cracking and spalling. If the buried concrete is a mass concrete structure, the coupling of ESA and DEF may occur. In this way, the sulfate ions are provided not only from the exterior solutions, but also from internal sources, such as cement, aggregates and mixing components. The two sources of sulfate ions could increase the rate of the ettringite formation and result in a worst degradation.

Table 1.4 – Potential aggressiveness of water and soil relating to sulfate content [159].

		Aggressiveness of attack		
Aggressive medium	(SO_4^{2-}) content	Slight	Medium	High
Water	mg/l	200–600	600–3,000	>3,000
Soil	mg/kg	2,000–3,000	3,000–12,000	>12,000

Sea water is another possible source of external sulfate. It has a complex chemistry including magnesium, sulfate, sodium, chloride and dissolved CO_2 species [160]. The presence of chloride lowers the deterioration of the sulfate: precipitation of magnesium hydroxide (brucite) and calcium carbonate forms a semi-protective surface layer, which decreases the aggressiveness to a certain degree; this aggressiveness can be decreased also by Friedel's salts formed after the reaction between chloride ions and C_3A.

Even though there is high probability for coupling of ESA and DEF to occur, little research has been done in the literature. The coupling effect of ESA and DEF happens when sulfate ions are provided through the exterior solution and the material itself, meanwhile consuming the calcium- and aluminium-bearing products. A combined characterization of ESA and DEF should be presented in this case. First, the material mix should have a similar effect compared to ESA and DEF, such as the content of C_3A, C_3S, W/C and so on. Second, after the heating treatment, the material has a modified pore structure, which should be similar to the case of DEF. Moreover, the pore structure affects the mechanical response of the material to damage. Furthermore, the expansion plateau observed in DEF should not occur in the coupling effect of ESA and DEF due to an unlimited provision of sulfate ions from the exterior solution. In the end, a double source of sulfate ions contributes to more ettringite formation compared to a single effect either ESA or DEF on the one hand. On the other hand, it induces a higher crystallization pressure, which may force ettringite to form in smaller pores.

In this dissertation, a study aimed at the characterization of the pore size change in cement-based materials which are subjected to the coupling of ESA and DEF, will be performed. The experimental study on the coupling of ESA and DEF will be presented in Chap. 2 and the corresponding results will be presented in Chap. 3.

1.3 Mechanisms of expansion

1.3.1 General mechanisms due to ettringite formation

Over the years, several theories have been proposed to explain why an expansion occurs upon ettringite precipitation. The simplest hypothesis is that ettringite takes up more space than the AFm phases from which it forms. To be more specific, the molar volume of gypsum and ettringite formed in a hardened paste are higher than the molar volumes of the initial phases [161]. However, this theory is refuted since the cementitious materials have a large amount of porosity facilitating the formation of ettringite without leading to an expansion. It is observed in experimental studies that only about 1/20 of the ettringite formed causes expansion [162]. This implies that ettringite can form and grow in cracks as well as in pores with (mostly) harmless effect.

The second hypothesis is that expansion is the result of the swelling of ettringite colloidal particles [96], especially in the presence of lime [34]. These gel-like ettringite particles have a large specific surface area analogous to the C-S-H gel and adsorb water, resulting in an overall expansion. This theory was first proposed by Metha [163]. It was believed that the high surface area combined with the negative charge results in the attraction of large quantities of water. The relation between water gain and expansion of ettringite was studied. The amount of water adsorbed in the material increases with the relative humidity, and the specimen adsorbed 9.6 % of water when the relative humidity reached up to 95 %. What's more, the volumetric expansion increases when more water is adsorbed, see Fig. 1.25. In [164], the volume change of paste cylinders containing calcium sulfate or sodium sulfate additions is measured and the quantity of ettringite is determined by X-ray diffraction. A positive correlation exists between ettringite content and the volume increase in percent, which is shown in Fig. 1.26. However, it is shown that the expansion occurs only when ettringite content is greater than a certain value.

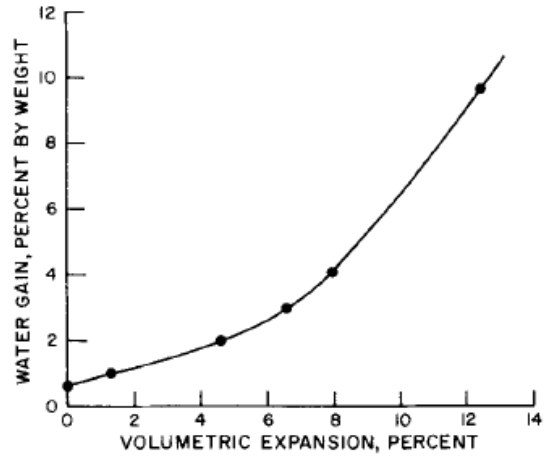

Figure 1.25 – Relation between water gain and the expansion of ettringite [163].

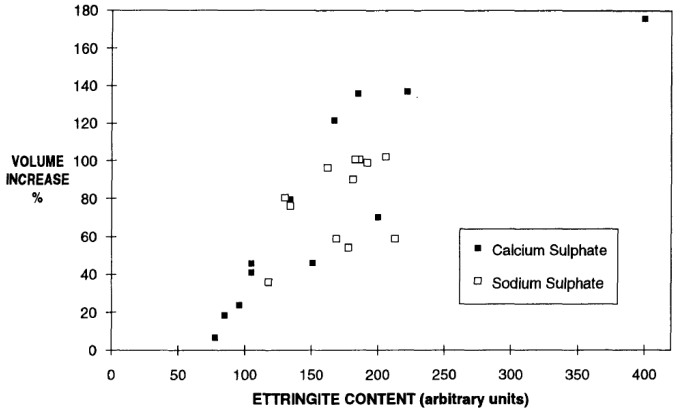

Figure 1.26 – Relation between ettringite content and volume increase [164].

It is also stated that ettringite grows topochemically [165]. A topochemical reaction is defined as a reaction between a solid particle and a surrounding solution in which the hydration product is formed on the surface of the particle. $C_4A_3\bar{S}$ is considered to be the only reactant. During the topochemical reaction, the length of ettringite crystals increase. The expansion starts when the length of these crystals becomes larger than the solution film thickness, as shown in Fig. 1.27, so that the crystals begin to exert pressure against the surrounding matrix. However, this theory is proposed based on the same crystal structures of tricalcium aluminate, AFm and ettringite.

The more recent and popular theory for the expansion mechanism is crystallization pressure theory. The precipitation is generally accompanied with internal pressures resulting from the interaction between the ettringite and the surrounding matrix of cement paste [11, 166], which may lead to significant free expansions of the speci-

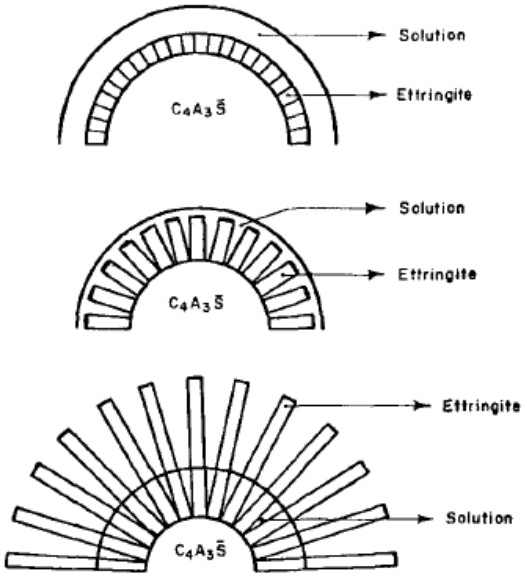

Figure 1.27 – Topomechanical mechanism for crystals growth: expansion begins when the crystals extend beyond the solution [165].

men and to damage. Although the origin of the pressure causing such macroscopic expansions is still controversial, ettringite precipitation is usually recognized as the major cause of the swelling observed [35].

1.3.2 Crystallization pressure theory

The crystallization process is well described by Scherer in [167]. As shown in Fig. 1.28, in a supersaturated solution, the crystal grows in a cylindrical pore with the radius of the tip $r_m = -\frac{r_p}{cos(\theta)}$ and the side radius of r_p. θ is the contact angle between the crystal and the pore wall. The chemical potential difference between the crystal and the liquid [168] drives the crystal to grow. The crystal stops growing toward the pore surface due to the interaction of large repulsive forces between the crystal and the surface of the pore. Direct contacts will not be possible [167] due to the need for large force to overcome the surface tension. At the interface of the crystal and the pore wall, a thin film of solution remains [22], where the concentration is not the same as the one in the rest of the pore. In this thin film, the concentration is not in equilibrium with the radius of the pore but with the tip of the crystal, which is free to grow into the area not in contact with the wall. Meanwhile, the tip of the crystal will keep growing until its surface reaches a curvature which is in equilibrium with the concentration of the solution. In this way, the chemical work is converted to the

mechanical one, with the driving forces being the activities of the reactants in the pore solution. At this point, the capillary pressure inside the crystal (Eq. 9) equals the hydrostatic pressure, P_h, (Eq. 10) from the solution.

$$P_C = P_L + \gamma_{cl}\kappa_{cl} \tag{9}$$

$$P_h = P_L + \frac{RT}{V_C}\ln(\beta_{cl}) \tag{10}$$

where P_L is the pressure in the liquid; V_C is the molar volume of the crystal; β_{cl} is the saturation index of the crystal at the crystal-liquid interface; γ_{cl} is the surface tension of crystal; and κ_{cl} is the mean curvature of the crystal-liquid interfaces.

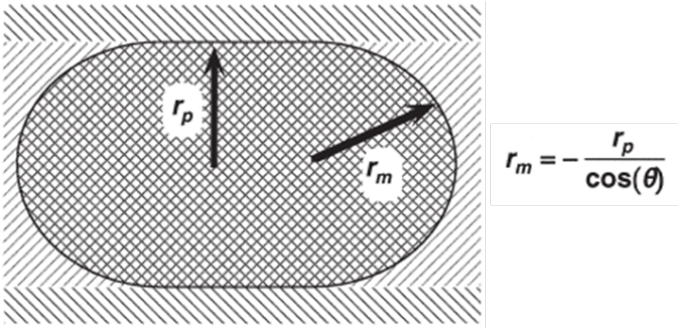

Figure 1.28 – Crystal in cylindrical pore with different curvatures [167]

The equilibrium state is described in Eq. 11. This equation shows that the solubility of a big crystal is less than a small one, that is the reason why crystal precipitates in big pores first, and then penetrates to smaller ones.

$$\gamma_{cl}\kappa_{cl} = \frac{RT}{V_C}\ln(\beta_{cl}) \tag{11}$$

A simple way to estimate the crystallization pressure is proposed by Correns [22] for monomolecular crystals. For more general cases, the original expression has been extended to include the number of ions in the crystal and ionic activities instead of the concentration in the form (Eq. 12 and 13) [45, 169, 170, 171, 172]:

$$P_C = \frac{RT}{V_C} ln(\frac{Q_{reac}}{K_{reac}}) \tag{12}$$

$$Q_{reac} = \prod_i a_i^{v_i} \tag{13}$$

where V_C is the molar volume (m^3/mol) of the growing crystal, R is the gas constant (8.314 J/(mol· K)), T is the temperature (K), a_i and v_i are the activity and the stoichiometric coefficient of species i in solution, respectively, and K_{reac} is the equilibrium constant of the chemical reaction. It is pointed out that the magnitude of crystallization pressure generally depends on both the size and the shape of the crystals [169], and on the kinetics of their formation [173].

1.3.2.1 ESA specificities

Once concrete is exposed to the ESA, the penetration of sulfate ions into the cementitious material generates a chemical reaction with the available monosulfate, which increases the amount of sulfate ions (SO_4^{2-}) inside pores. This will lead to the supersaturation of the solution and remaining monosulfate reacts with C-S-H which will lead to the formation of ettringite. Two conditions are required to get the crystallization pressure: confinement of the crystals and supersaturation of the solution [31].

1.3.2.2 DEF specificities

There are two main schools of thought concerning the crystallization pressure theory for DEF. The first proposed that the expansion is the result of the localized crystallization of ettringite. The ettringite is assumed to precipitate in the zones like cracks and paste-aggregate interfaces [138, 174] in this theory. This hypothesis is pretty reasonable, since these big voids provide more "comfortable" space for ettringite crystals. However, whether the precipitation of ettringite in these big voids is the reason for expansion has been debated in the literature. In the second school of thought, contrary to the local expansion hypothesis, a homogeneous crystallization of ettringite is supposed to be the reason for the swelling. The ettringite is assumed to form from the Al-bearing particles and in solution [91]. This idea is supported by [175] and it supposes that the expansion is caused by the homogeneous formation of ettringite in the C-S-H gel which leads to a swelling in the paste.

1.4 Modeling of sulfate attacks

1.4.1 ESA

1.4.1.1 Diffusive transport of ions

The two traditional approaches to simulate the diffusive transport of the ith ions are the empirical and the physical approaches. In the empirical way, the ions' transport is based on the Fick's law (Eq. 14). For example, the numerical studies on ionic transport are based on the simple Fick's law of diffusion without considering the chemical reaction [176, 177, 178]. This approach is reliable if the chemical reaction does not change the pore structure drastically and therefore the diffusion coefficient D is not affected. However, it is not the case for ESA where the sulfate ions diffuse into the material and react with the cement hydrates directly. The resulting damage will increase the parameter D.

$$j_i = -D \bigtriangledown c_i \tag{14}$$

where j is the flux; D is the effective diffusion coefficient; and c_i is the concentration of the ith ion.

In the physical approach, the transport of the ions is treated considering the chemical reactions, but in a separate way. In this way, the diffusion of any species can be modeled with two material parameters: the capillary porosity and the formation factor.

In the porous media, the cross section area available for diffusion is not the total cross section of the medium, and thus the diffusion coefficient is smaller than the bulk diffusion coefficient, which is proposed as effective diffusion coefficient. Carman has shown that the fluid moves on the average at about 45 ° to the direction of flow [179], as shown in Fig. 1.29. The real distance traveled by that fluid is actually $\sqrt{2}$ L, with a net distance of L. The effective diffusion coefficient is based on the average cross-sectional area open to diffusion and the distance traveled by the molecules in the porous media, thus it is linked to the bulk diffusion coefficient by porosity. However, the total porosity is not enough for assessing the diffusion parameter when dealing with different materials. The diffusive coefficient is found to be one order greater for cement paste with CEM I than with CEM V cement, though with the same water to

cement ratio [180]. A model based on the microstructure is proposed to estimate the diffusive properties of hardened cement pastes via a simplified multi-coated sphere assemblage model [181], which can predict the evolution of the effective diffusion coefficient due to calcium leaching or calcite formation.

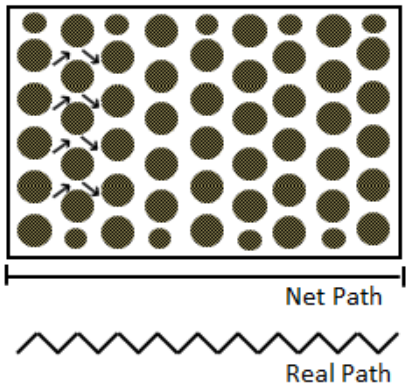

Figure 1.29 – Diffusion path in porous media [179].

1.4.1.2 Modeling of diffusion depth

With the diffusion of sulfate ions from an aggressive solution, several layered deterioration zones are created from the outside to the inside of the concrete [39, 45, 182]. The sulfate-induced damaged concrete section can thus be divided into three layers from the exposure surface to the core. The total thickness of the degraded layers is called the sulfate diffusion depth. The rate of diffusion reaction, depth of sulfate diffusion, and expansion stress due to the generation of the expansive products are the main important indexes that are used to quantitatively characterize the layered deterioration zones, which are influenced by both the external sulfate environment and concrete composition (e.g., concentration [183, 184], temperature [128, 185], dry-wet cycle and soaking [186], content of C_3A [7, 187]). According to the experimental results, a regression analysis is made and an empirical model (Eq. 15) is proposed for the prediction of diffusion depth [188]:

$$X = \frac{4.2}{5} \cdot \frac{C_{C_3A}}{8} \cdot \frac{(c_{Mg^{2+}} + c_{SO_4^{2-}})}{0.19} \cdot t \tag{15}$$

where X is the diffusion depth (cm); C_{C_3A} is the content of C_3A in cement (%); $c_{Mg^{2+}}$ or $c_{SO_4^{2-}}$ is the concentration of the aggressive solution (mol/l) and t is the time (year).

Atkinson's model (Eq. 15) is modified [189] by introducing the diffusion coefficient D as follows:

$$X = 1.86 \times 10^6 C_{C_3A}(c_{Mg^{2+}} + c_{SO_4^{2-}})D \cdot t \tag{16}$$

where D represents the initial diffusion coefficient of the sulfates in the concrete.

However, the diffusion coefficient is considered to be a constant, $3.4{\times}10^{-11}$ m^2/s, neglecting the fact that the pores of concrete would be gradually blocked by the reaction products. Moreover, this model has not been experimentally verified and needs further confirmation.

Afterwards, this deficiency of the constant diffusion coefficient is modified. A prediction model of diffusion depth depending on experimental analysis of the concrete with different C_3A content (9-13%) in the cements in different sodium sulfate solutions is proposed [6]:

$$X = [0.11\ c_{SO_4^{2-}}^{0.45}] \cdot [0.143\ t^{0.33}] \cdot [0.204\ e^{0.145\ C_{C_3A}}] \tag{17}$$

where t is the time of immersion (days) and C_{C_3A} is the C_3A content in the cement (%). The linear relationships among the diffusion depth, time and concentration of the external solution are modified. However, the effect of the diffusion coefficient on the rate of diffusion is not revealed, and the relationships between diffusion depth and diffusion reaction is not taken into account.

Based on Fick's first law, the prediction of the diffusion depth by theoretical derivation is proposed [190] as follows:

$$X = \sqrt{\frac{2D_0 c_{SO_4^{2-}} t}{a}} \tag{18}$$

where D_0 is the initial diffusion coefficient of the sulfates in the concrete; $c_{SO_4^{2-}}$ is the concentration of the sulfates on the concrete surface; t is the degradation time; and a is the capacity of the concrete to adsorb sulfates. However, this model has never been experimentally verified directly yet.

Considering the diffusion reaction, a similar model is derived [191] as follows:

$$X = \sqrt{\frac{2D_0 c_{SO_4^{2-}} t}{C_{C_3A}}} \tag{19}$$

A chemical-diffusion model for sulfate diffusion depth considering the chemical equilibrium reaction, the distribution of the sulfate ions and the time-varying diffusion coefficient is proposed [192] with a time-varying diffusion coefficient empirical equation:

$$X = \sqrt{\frac{2D_e(c_{SO_4^{2-}} - c^0_{SO_4^{2-}}) \cdot q}{C_{C_3A}}} \cdot \sqrt{t} \tag{20}$$

$$D_e = D_0(\frac{1}{t})^m \tag{21}$$

where $c_{SO_4^{2-}}$ is the concentration of the sulfates on the concrete surface; $c^0_{SO_4^{2-}}$ is the initial concentration of the sulfates in the concrete; and m is the attenuation coefficient of the diffusivity with time, related to the water/cement ratio of concrete.

1.4.1.3 Modeling for ESA-induced expansion

A volumetric expansion model is proposed [9] based on the concept of excluded volume, and the amount of expansion is assumed to be proportional to the difference between the net solid volume produced and the original capillary porosity. An expansion factor V (Eq. 22) is proposed to describe the potential for expansion when the volume of solid products is greater than that of the solid reactants ($V > 0$). However this expansion depends on the capacity of the cement pore structure to accommodate the ettringite and the ability of concrete to resist expansive stresses as well.

$$V = \frac{\text{solid product volume} - \text{solid reactant volume}}{\text{solid reactant volume}} \tag{22}$$

Following this model, a finite-element modeling approach is proposed to create a predictive model [63]. The volumetric change is caused by the reaction of sulfate ions and the various phases of the mortar, which induces stresses throughout the specimen. The stress is also calculated in an elastic theory (Eq. 23). The swelling theory induced by ettringite formation is adopted in this model.

$$\sigma_i = C_{ij}(\epsilon_j - \epsilon_j^0) \tag{23}$$

where C_{ij} is the elastic tensor; ϵ_j is the strain and ϵ_j^0 is the assumed intrinsic strain, which is not induced by the expansive products.

On the other hand, an empirical model of the expansion based on a long-term experiment is developed [46]. 114 concrete cylinders cast from 51 different mixtures are immersed in a 2.1% sodium sulfate solution at room temperature. A model to predict the concrete expansion due to a sulfate attack as a function of the cement (C_3A content) and the characteristics of the mixture (w/c) is proposed. However, only considering the content of C_3A and w/c in the model is not comprehensive enough.

Moreover, a simplified methodology is proposed to evaluate the external sulfate attack in concrete structures [193]. Only the monosulfate is considered as the hydrated aluminates in this model. Sulfate and aluminate concentrations are computed through a diffusion-reaction model based on Fick's second law. It is assumed that the expansions are caused by the volume increase, and the porosity percentage is estimated referring to [194].

Furthermore, a series of chemo-transport-mechanical models are developed to predict the behavior of cementitious materials under external sulfate attacks with controlled test conditions [194, 195, 196, 197, 198, 199, 200]. A full chemical-diffusive-mechanical model for the expansion is proposed based on the molar volumes of the different components of the cement paste and its microstructural parameters (degree of hydration, capillary porosity) [194]. It is assumed that no expansion occurs until the capillary pores are totally filled with ettringite. Hence, ettringite will fill the capillary pores first, and then the additional ettringite leads to the expansion. The model is developed with a continuum damage mechanics approach to evaluate structural damage. The diffusivity is modified with increasing damage. Based on the rule-mixtures, three components (C_3A, C_4AH_{13}, and $C_4A\bar{S}H_{12}$) are considered in the modeling of damage in cement-based materials under external sulfate attack [201]. A first-order reaction is established if only the sulfate ions are considered:

$$\frac{\partial U}{\partial T} = D\frac{\partial^2 U}{\partial X^2} - KU \tag{24}$$

where U is the sulfate concentration; D is the diffusion constant; and K is the rate of takeup of sulfates.

In addition, a second-order rate reaction is built depending on the depletion of calcium aluminates (C_3A) (Eq. 25) and the takeup of sulfate ions. In Eq. 26, the diffusion of calcium aluminate (C_3A) is not taken into account due to its immobilization. With the accumulated volumetric change and the assumption of the fraction of porosity being filled, the volumetric bulk strain is obtained. The main chemical reactions occurring between the C_3A, C_4AH_{13}, and $C_4A\bar{S}H_{12}$ and the sulfate ions are well expressed in this model, and the diffusion of the ions is coupled. However, the effect of the porosity change on the diffusion coefficient is not considered in this approach.

$$CA + q\bar{S} \rightarrow C_6A\bar{S}_3H_{32} \tag{25}$$

$$\frac{\partial U}{\partial T} = D\frac{\partial^2 U}{\partial X^2} - kUC \tag{26}$$

$$\frac{\partial C}{\partial T} = -\frac{kUC}{q} \tag{27}$$

where CA represents C_3A, C_4AH_{13}, and $C_4A\bar{S}H_{12}$; q corresponds to CA; U is the molar concentration of sulfate, and C is the molar concentration of calcium aluminate.

In most of the models, the cement-based materials are treated as homogeneous, which does not correspond to reality. Following the same idea in [202], the concrete is described as a two-phase material, with: the homogenized skeleton phase, including cement paste and aggregates, and the expansive phase of the products of the reaction. A fully coupled chemo-transfer-mechanical model is proposed [195]. The poroelasticity approach is adopted and used to describe concrete microcracking. The sulfate and calcium species are supposed to completely control the chemical system. Based on coupled models proposed in [194, 203], the sulfate molar concentration and the amount of formed ettringite and gypsum from a diffusive-reaction equation is calculated. The crystallization pressure generated from the interaction between growing AFm crystals and the surrounding C-S-H matrix is introduced in the model, and is supposed to generate the observed macroscopic swelling. In addition, a damage variable d is introduced into the mechanical model at macroscopic scale to simulate the cracking. The mechanical and diffusive properties are related to the degradation by application of the Mori-Tanaka (MT) scheme. This model well simulates the principal reactions occurring during the degradation processes in a simplified method, and the crystallization pressure adopted well explains the mechanism of the expansion. However, only considering the calcium and sulfate

concentrations in the model remains a limitation.

Moreover, a numerical methodology is proposed to simulate the cementitious materials' degradation under external sulfate attack, with considering the diffusion of the ions in and out of the structure, the chemical reactions, and the mechanical damage accumulation [198]. Some of the main hydration products are considered in the model: calcium silicate hydrate (C-S-H), calcium hydroxide or Portlandite (CH), ettringite ($C_6A\bar{S}_3H_{32}$), calcium monosulfoaluminate ($C_4A\bar{S}H_{12}$), hydrogarnet (C_3AH_6), and tetracalcium aluminate hydrate (C_4AH_{13}). These products may react with the sulfate ions and cause a volume change. The volumetric strain is calculated by the total volume change after the chemical reactions. The chemical reactions are modeled using the chemical equilibrium relationship, and the damages brought by the chemical reactions are also included in the model. The diffusion model is governed by Fick's second law [178] with a consideration of the chemical activity gradient. Due to the needle-shape structure of ettringite, it is assumed that not all the capillary pores are filled before the strain starts to develop. Thus, a parameter b, representing the fraction of porosity that is filled by ettringite is introduced in the model. Additionally, a tensile damage model is introduced in the model, considering the cracks. The advantage of this model is that the mechanical and diffusion properties are modified with the accumulated damage.

A coupled chemo-transport-mechanical model is proposed by Bary et al. in [204]. Firstly, the degradation of the cement paste and mortars is simulated by considering the decalcification of the hydrated phases, such as the leaching process, and the migration of sulfate ions. Then, the poroelasticity theory is adopted to simulate the macroscopic mechanical behavior of cement paste subjected to ESA, and the crystallization pressure is supposed to be the driving force for ettringite formation. The advantage of this model is that it focuses on the simulated microstructure of cement paste and mortars used to estimate the effective elastic and diffusive properties, as shown in Fig. 1.30. However, the elastic theory adopted in this model should be modified as the specimen is no longer in the elastic range when the cracks occur.

Finally, a comprehensive numerical model is proposed in [205] to evaluate the degradation of the cement-based materials under calcium leaching and external sulfate attack. Three main modules are adopted in the model: the ionic diffusion module, the chemical reaction module, and the damage quantification module. The diffusion of multiple ions is modeled based on the Poisson-Nernst-Planck model. The chemo-

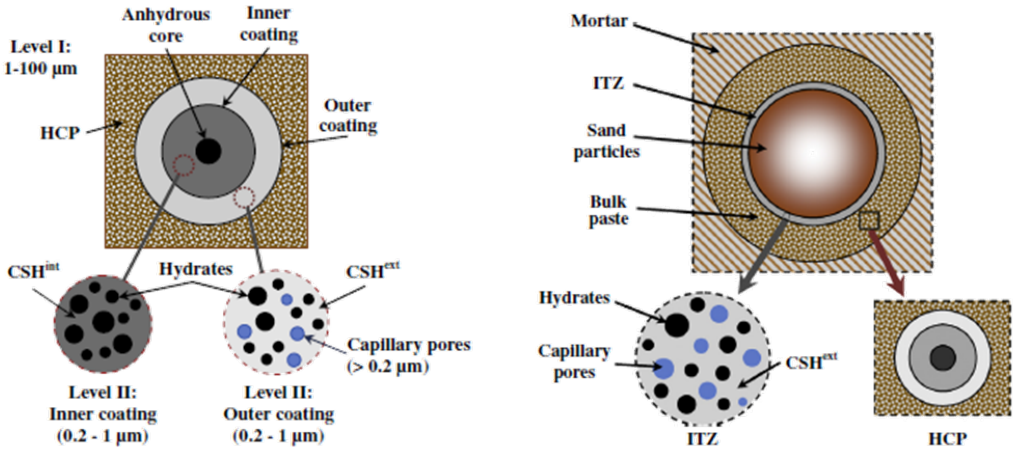

Figure 1.30 – 2D representation of the cement paste microstructure (a) and mortar microstructure (b) used to estimate the effective elastic and diffusive properties [204].

transport of the main species involved and the relevant reaction products formed are calculated and used to quantify the mechanical consequences of the degradation processes.

1.4.2 DEF

1.4.2.1 Modeling for thermodynamics

Flatt et al. propose a thermodynamic approach to evaluate the supersaturation which may result in ettringite formation and crystallization pressures [169]. The crystallization pressure which stops the crystal growth in a supersaturated solution can be estimated by Eq. 28 [22]:

$$\sigma_C = \frac{RT}{V_C} \ln(\frac{Q}{K}) \tag{28}$$

where R is the gas constant, T is the absolute temperature, V_C is the molar volume of the crystal, $\frac{Q}{K}$ is the supersaturation, Q is the ion activity product and K is the equilibrium constant.

The average hydrostatic tensile stress, σ_θ, is the one relevant to damage criterion, as shown in Eq. 29:

$$\sigma_\theta = \sigma_C g(\phi_C) \tag{29}$$

where $g(\phi_C)$ is a parameter as a function of ϕ_C (volume fraction of crystals exerting pressure in the sample) depending on pore shape. For a crystal in a cylindrical pore, $g(\phi_C)$ is given by:

$$g(\phi_C) = \frac{2}{3}(\frac{\phi_C}{1-\phi_C}) \tag{30}$$

and for a crystal in a spherical pore, it is given by:

$$g(\phi_C) = \frac{\phi_C}{1-\phi_C} \tag{31}$$

Furthermore, the crystallization pressure is estimated considering that the ettringite is at equilibrium with gypsum and monosulfate as follows:

$$\sigma_C = \frac{RT}{V_C} \ln(\frac{K_{\text{monosulfate}} K_{\text{gypsum}}^2}{K_{\text{ettringite}}} a_{\text{H}_2\text{O}}^{16}) \tag{32}$$

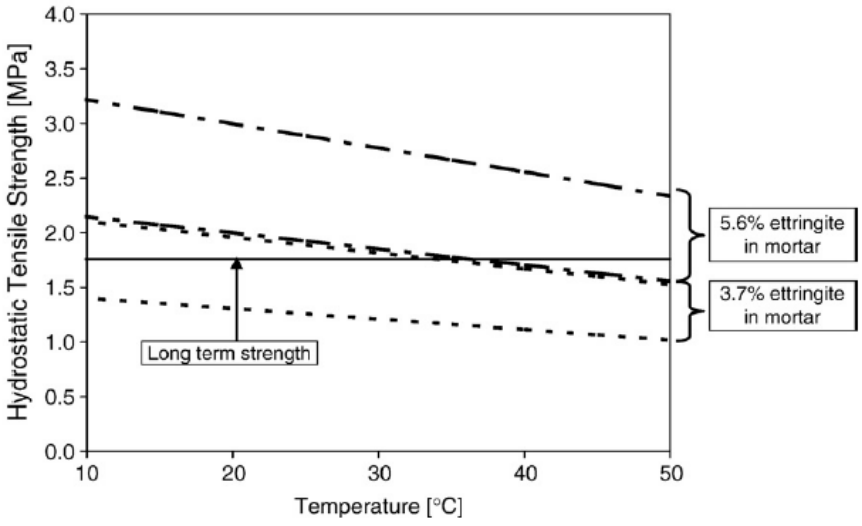

Figure 1.31 – Evolution of the estimated tensile stress as a function of temperature [169]

The evolution of the estimated tensile stress as a function of the temperature for two cases of ettringite content and pores shape is shown in Fig. 1.31. This approach well estimated the tensile stress induced by crystallization pressure of the tested samples.

However, the mechanical properties (such as sample strength) are not considered and the evolution of the whole expansion of the specimen is not simulated by this approach.

1.4.2.2 Modeling for evaluation of expansion magnitude

In [134], Brunetaud proposes a macroscopic model to estimate the DEF induced expansion. In order to simulate the sigmoid form of the expansion curve, five parameters $(\varepsilon_\infty, \tau_c, \tau_l, \varphi, \delta)$ are adopted to fit the expansion curves, which are on the conditions that: $\varphi \geq 0$ and $\varphi \leq \delta$ to avoid negative expansions.

$$\varepsilon_\chi = \varepsilon_\infty \frac{1 - \exp(-\frac{t}{\tau_c})}{1 + \exp(-\frac{t}{\tau_c} + \frac{\tau_l}{\tau_c})}(1 - \frac{\varphi}{\delta + t}) \tag{33}$$

where ε_∞ is the potential of expansion; τ_c is the characteristic time; τ_l is the latency time; φ and δ are correction coefficients taking into account a linear evolution of the last phase of swelling. A particular case of this equation taking $\varphi = mn\tau_c$ and $\delta = n\tau_l$, with m depending on water to cement ratio W/C equal to 0.0065 and n damping coefficient equal to 3.

Further, a relationship between the magnitude of expansion to the early-age thermal history was established, see Eq. 34 [92]. This model is based on the semi-empirical relationship which assumes that ettringite is no longer observed above a threshold temperature T_0. The expansion is predicted to increase with the temperature and heating duration. However, this model overestimates the expansion for the case with high temperatures and short durations, and it does not take into account a possible pessimum effect.

$$\varepsilon_\infty = \alpha_i \cdot \int_0^{t_m} \begin{cases} 0 & \text{if } T(t) < T_0 \\ \exp(-\frac{E_a}{R} \cdot \frac{1}{T(t) - T_0}) & \text{else} \end{cases} \cdot dt \tag{34}$$

where α_i is a constant depending on the mix-design and chemical characteristics; E_a is the activation energy; T_0 is the temperature threshold above which it contributes to DEF expansions; t_m is the mature time of concrete.

Therefore, a modified model (Eq. 35) for the potential expansion ε_∞ is proposed by [144] to decrease the impact of the temperature with the exposure duration based

on the Eq. 34. The time-dependent parameter $\alpha(t)$ is adopted to reduce the effect of the temperature and heating durations, which corrects the overestimation that occurred in the aforementioned model. It decreases with the exposure duration, which is explained by the drop of ability of CSH to trap the sulfates. The predicted expansion shows a good consistency with the experimental results, see Fig. 1.32. This figure shows the expansion of concrete cylinders with size of 11 cm in diameter and 22 cm in height preheated with different maximum temperatures (70, 80 and 85 °C) and different durations (1, 3 and 5 days).

$$\varepsilon_\infty = \int_0^{t_m} \alpha(t) \cdot \begin{cases} 0 & \text{if } T(t) < T_0 \\ exp(-\frac{E_a}{R} \cdot \frac{1}{T(t)-T_0}) & \text{else} \end{cases} \cdot dt \tag{35}$$

with

$$\alpha(t) = \lambda \cdot \beta \cdot t_{exp}(t)^{\beta-1}; \quad \lambda > 0; \beta \in [0,1] \tag{36}$$

$$t_{exp}(t) = \int_0^t \begin{cases} 0 & \text{if } T(u) < T_0 \\ 1 & \text{else} \end{cases} \cdot du \tag{37}$$

where λ, β are the material characteristic parameters, t_{exp} is the exposure time.

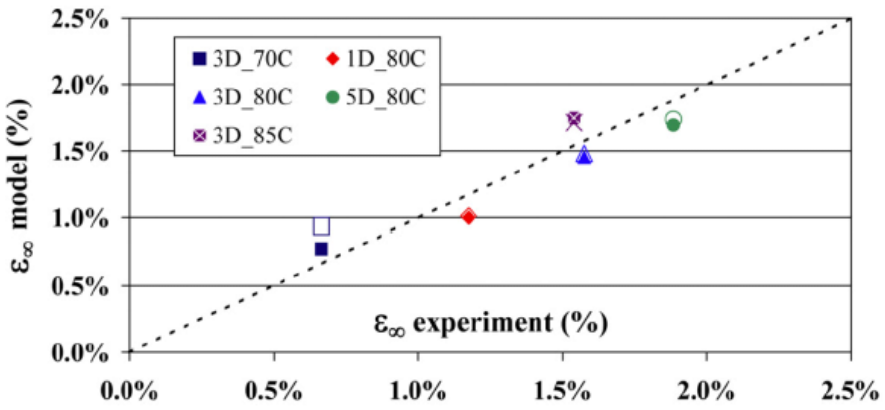

Figure 1.32 – Comparison between the predicted and the experimental results [144].

1.4.2.3 Modeling for mechanical calculations

A physicochemical model is proposed to link the characteristics of the concrete and the environmental conditions (temperature, moisture and leaching opportunity) for DEF [120]. The thermodynamic equilibrium of ettringite, monosulphoaluminate and portlandite, the sorption of ions into C-S-H and the mass balance equations

are considered in the model. The equilibrium of ettringite is dependent on the equilibrium conditions of monosulphoaluminate (AFm) and portlandite (CH), and the binding of ions into C-S-H as well. The binding and releasing of SO_4^{2-}, Na^+ and $Al(OH)_4^+$ in the C-S-H are also considered in the model. The Ca^{2+} was calculated by electroneutrality balance. The effect of the hydration temperature is reflected on a coefficient I_d, which is expressed as follows:

$$I_d = \int_0^t (A_{\frac{T}{R}} - 1)^+ \frac{\delta\alpha}{\delta t} dt \tag{38}$$

with $A_{\frac{T}{R}}$ the Arrhenius activation law:

$$A_{\frac{T}{R}} = exp(-\frac{E_{AR}}{R}(\frac{1}{T} - \frac{1}{T_0})) \tag{39}$$

where E_{AR} is the thermal activation energy for the hydration process [206].

This index, I_d, well expresses the pessimum effect of temperature. For example, if $T = T_0$ during hydration, $I_d = 0$. The higher the temperature during hydration, the higher the I_d, and more available aluminium can be bound in C-S-H. The swelling of the concrete is explained by the Oswald ripening phenomenon based on thermodynamic concepts [169], which assesses the homogenous pressure occurring in cement paste [119]. The amount of ettringite formed could be predicted by this model, which is converted into the volume, in order to integrate the deformation due to DEF. This model is validated on experimental results [93], as shown in Fig. 1.33.

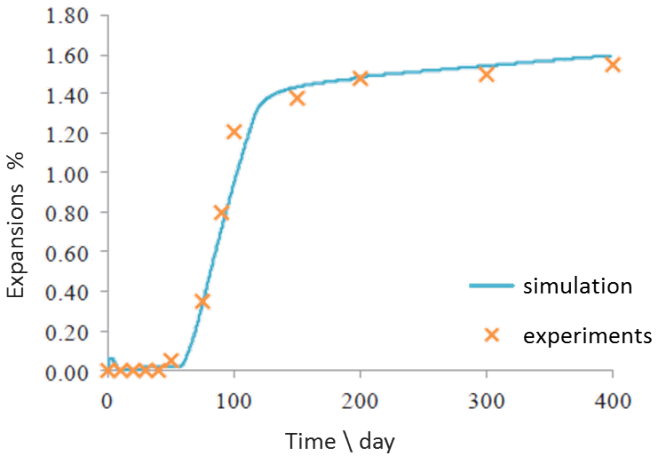

Figure 1.33 – Comparison between the predicted and experimental results [207].

A latest chemical-mechanical model is proposed in [208] to simulate the expansion due to DEF. According to the mass balance, the initial content of primary AFt (E_1), primary AFm (M_1), hydrogarnet, delayed AFt (E_2), the sulfates and aluminates adsorbed on C-S-H can be determined from the composition of cement materials. Three main processes: dissolution of primary sulfoaluminates, fixation of aluminates in hydrogarnet or carboaluminates, and the formation of delayed ettringite are considered in the model. The kinetics of these three processes are determined respectively by three characterization time: τ_d, τ_f, τ_p, which depend on temperature, moisture and chemical conditions. Then, the evolution of chemical species from studies in [93] is predicted, see Fig. 1.34 (a). With the output of the content of delayed AFt, the variation of the volume of ettringite ϕ_{DEF} could be predicted as (see Fig. 1.34 (b)):

$$\frac{\delta \phi_{DEF}}{\delta t} = V_{AFt} \frac{\delta E_2}{\delta t} - V_{AFm} \frac{\delta M_1}{\delta t} \tag{40}$$

where V_{AFt} and V_{AFm} are the molar volume of AFt and AFm.

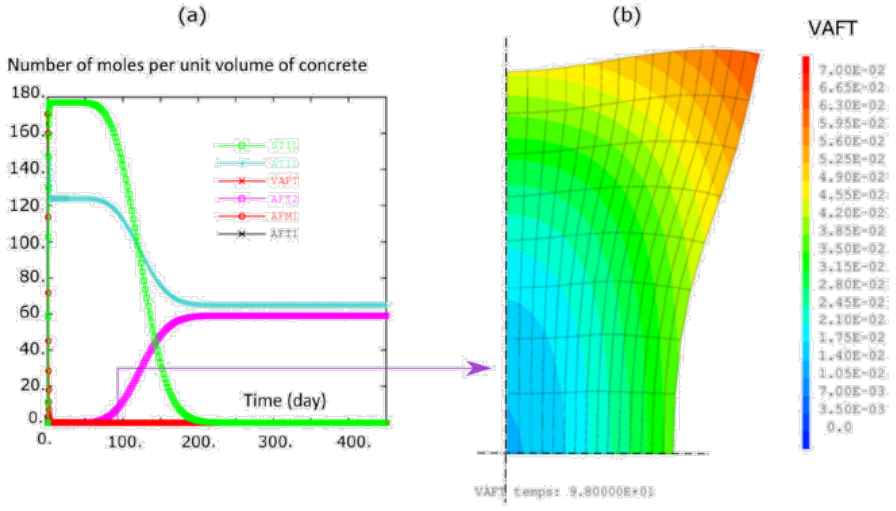

Figure 1.34 – Evolution of chemical species at the center of the specimen (a), and corresponding effective volume of DEF at 100 days (b) [208].

Then, the stress and strain is predicted through a nonlinear mechanical model [209], see Fig. 1.35. With considering the effect of temperature threshold and chemical conditions, this model provides a comprehensive evolution of chemical species, volume of ettringite and corresponding strain-stress state.

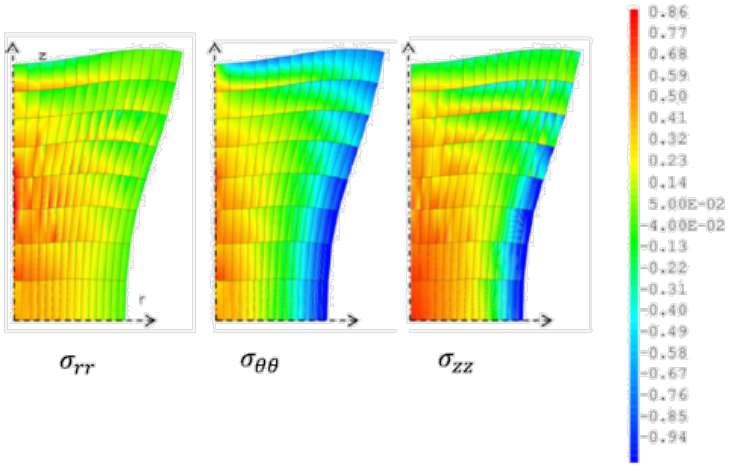

Figure 1.35 – Simulation of stress state during swelling [208].

1.5 Conclusions

Due to the different source of sulfate ions, the external sulfate attack (ESA) and the delayed ettringite formation (DEF) have been studied separately in the literature. The studies have been conducted on the aspects of chemical reactions, ettringite formation, the expansion mechanisms, the analysis of the affecting factors, and modeling simulation. However, a great amount of common between ESA and DEF have been summarized from the separate studies. The comparisons of ESA and DEF are summarized in Table 1.5.

Firstly, the most common degradation observations of cement-based materials subjected to ESA and DEF are expansion and cracking. In both situations, the expansion is attributed to the formation of ettringite, though the gypsum is considered as the reason for the ESA expansion by some authors. However, this hypothesis was invalidated by the observation of gypsum precipitation after the cracks occur [36, 40]. Several hypotheses were proposed to explain the expansion resulting from ettringite formation, including the volume increase theory, colloidal dimension theory, topochemical reaction theory, and crystallization pressure theory. The last one, crystallization pressure, is more recent and popular to explain the expansion. The expansion is assumed to be due to crystallization pressure resulting from the interaction between the ettringite and the surrounding matrix of the cement paste [11, 166]. A confined space for crystal growth, and a solubility product ratio greater than 1.0 are required for the production of crystallization pressure.

After summarizing the study on the impact of the material mix, it is concluded that

Table 1.5 – Comparisons of ESA and DEF

Sulfate attacks	Commons			
	Observations	Mechanisms for expansion		Impact of material mix on expansion
ESA	1. Expansion ; 2. Cracking.	1. Volume increase theory ; 2. Colloidal dimension theory; 3. Topochemical reaction theory; 4. Crystallization pressure theory.		1. C_3A ; 2. C_3S ; 3. W/C ; ...
DEF				
Sulfate attacks	Differences			
	Impact of material mix on expansion	Impact of temperature	Source of so_4^{2-}	Pore position where ettringite forms
ESA	W/C (effect on porosity which affects the penetration of so_4^{2-})	Solubility of sulfate solutions	Exposure solutions	Capillary pores
DEF	SO_3 (effect on source of so_4^{2-} in pore solution); Influence on the diffusion of the reactive species.	Ettringite decomposition; Kinetic and magnitude of chemical reactions.	Cement	C-S-H gel

the high content of C_3A and C_3S contributes to ettringite formation for both ESA and DEF [7, 68], which provide more calcium and aluminium source for ettringite. As a source of SO_4^{2-} ions, the SO_3 content of the material affects the degradation degree submitted to DEF. There would be no expansion if $(SO_3)^2/Al_2O_3$ were less than 2, and this relationship depends on the different test conditions and cement [91]. The water to cement ratio has the same effect on ESA and DEF. On the one hand, a higher w/c ratio leads to a higher porosity and results in a higher permeability, which leads to a faster SO_4^{2-} ions transport from the exterior solution for ESA. On the other hand, the higher porosity provides more space for ettringite accommodation, which is good for sulfate-resistance.

The temperature has a different effect on ESA and DEF. For ESA, the main effect of temperature is on the solubility of sulfate solutions, which affects the source of SO_4^{2-} for ettringite formation. It was found [39] that an increased temperature contributes to the decrease of the initial latent period for sulfate attacks, and has little effect on the accelerated period, while the increase in temperature leads to an increase of the rate of expansion of the mortars. For DEF, the temperature is more important. It is believed that (pre)heating at a temperature above about 65 °C causes the primary ettringite to become thermodynamically unstable and to decompose to hydrated calcium monosulphoaluminate, releasing sulfates to the pore solution. A great amount of experimental studies have shown that the increasing curing temperature leads to an increase of the DEF expansion, as well as the heating durations. However, a pessimum effect exists: for a given heat treatment temperature and above a certain threshold duration, the magnitude of expansion decreases with the heating durations.

Though both sulfate attacks result in the formation of ettringite, the source of the sulfate ions, the time of their availability to reaction and the position where ettringite forms are different. In the case of ESA, the sulfate ions must penetrate into the concrete to initiate the reaction. Any expansion caused by the penetration of these sulfates can cause cracking, which in turn accelerates the penetration of more sulfate ions. The rate of the external sulfate attack, namely the kinetic of ettringite formation, depends on the exposure solutions. On the other hand, in the case of DEF, the sulfate ions exist inside the cement-based material from the time of mixing. As the chemical reaction proceeds, the amount of sulfate ions decreases, which contributes to a decreasing rate of internal attack with time. However, the kinetic of the ettringite formation depends on the concentration of sulfate ions in the pore solution.

The ettringite formation when cementitious materials are exposed to sodium sulfate solution is found [11, 39] to occur in the large pores, and then penetrate into small pores. This process occurs in the capillary pores and is driven by the crystallization pressure, which is determined by the supersaturation index of expansive product in pore solution. For DEF, the high temperature decomposes the primary ettringite to hydrated calcium monosulphoaluminate, releasing sulfates to the pore solution. These available sulfate ions are trapped by physical adsorption on the surface of the calcium silicate hydrates (C-S-H gel) [95, 96]. In the following storage in cool water, the C-S-H releases the trapped sulfates, making them available to the pore solution again. The results of the X-ray microanalysis by Lewis et al. [100, 210] suggest that part of sulfate and aluminate ions may be desorbed by C-S-H after exposure to the ambient temperature. The sulfate content in the C-S-H gel decreases together with ettringite crystallization. Based on these observations, the ettringite is postulated [100] to initially form in C-S-H gel and then in cracks and voids, and ettringite crystallization in the C-S-H gel might be the reason for uniform expansion of the paste. This idea is further confirmed by Yang [138]. The presence of ettringite is detected by SEM X-ray microanalyses of the outer C-S-H gel [91] in a mortar directly after curing at 90 °C and after subsequent wet storage. Therefore, it is postulated that the ettringite forms in the gel pores. However, these conclusions are based only on the energy X-ray analysis and have to be confirmed by other investigation methods. In this study, the ettringite formation in gel pores in the case of DEF will be further studied by analyzing the pore size distribution change.

For the modeling, a great amount of models including chemical equations, diffusions, mass balance and mechanical properties are presented above. However, these models do not take into account the porous properties of the material, which is an important factor for crystallization. In addition, only the elastic theory is adopted in the models mentioned above, which does not correspond to reality as cracks are obviously observed in cementitious materials exposed to sulfate attacks. Therefore, in this PhD thesis, a poromechanical model is proposed, which is suitable to couple with elastic method, plastic method, damage theory and so on.

In this dissertation, a study of cement paste subjected to ESA, DEF and coupling effect of the two reactions will be presented. This study intends to characterize the pore size distribution via mercury intrusion porosimetry (MIP) and dynamic vapor sorption (DVS). By comparing the change of pore size distribution, the position of ettringite formation in capillary or gel pores will be confirmed, and a damage mechanism will be suggested. Then a uniform poromechanical model will be proposed

for both ESA and DEF, disregarding the difference.

2 Experimental programs

2.1 Introduction

As stated in the chapter 1, a great number of studies have focused on ESA or DEF separately. However, there are common features between ESA and DEF, including the macroscopic material effects (expansion and cracking), the mechanisms of expansion (volume increase theory, colloidal dimension theory, topochemical reaction theory and the crystallization pressure theory), and the impact of the material mix (content of C_3A, C_3S and W/C amongst others). According to the literature, the differences correspond to the source of SO_4^{2-} and the size of the pores where ettringite forms mainly (see section 1.5). For ESA, SO_4^{2-} ions penetrate from the aggressive outer solution and ettringite forms in the capillary pores [11, 39]. Whether gypsum formation is also a cause of the expansion has been a debated question. In some experimental studies, gypsum is observed in the microcrack spaces and aggregate/paste interfaces in the most degraded zones of the material, which provides the most suitable sites for the precipitation [45]. However, it is pointed out that gypsum forms after the cracks appear [11]. What's more, the sulfate concentration in seawater is actually low (0.2 - 30 mmol/L), which is hardly enough to stabilize the gypsum. Therefore, ettringite is believed to be the only cause for the expansion. For DEF, SO_4^{2-} ions are provided by the material mix, mainly from the cement. A high temperature (generally experienced at an early age due to a precast process or to the heat of hydration in a massive cast-in-place concrete part) decomposes the primary ettringite into hydrated calcium monosulphoaluminate, releasing sulfates to the pore solution [90]. Part of these available sulfate ions are trapped by physical adsorption on the surface of the calcium silicate hydrate (C-S-H gel) [95, 96]. Lewis et al. [100, 210] suggest that part of both sulfate and aluminate ions may be adsorbed by C-S-H after exposing to the ambient temperature. The sulfate content in the C-S-H gel decreases with ettringite crystallization progress, and thus the ettringite is postulated to initially occur in C-S-H gel pores and then in cracks and voids [210]. In addition, it is also pointed out that ettringite crystallization in C-S-H gel pores might be the reason explaining the uniform expansion of the paste.

In the present study, the ettringite formation in different cases will be further confirmed by analyzing the pore size distribution change during the degradation processes. With this goal, experiments were designed to figure out the pore location where ettringite forms via an analysis of the pore size distribution and the total

porosity in different cases. Furthermore, a similar experimental study method for ESA and DEF is performed to study the coupling effect of ESA and DEF. DEF occurs in mass concrete. When mass concrete is fully buried in groundwater, which contains different types and quantities of sulfate ions, the penetrating sulfates react with aluminate hydrates to produce ettringite which results in expansion, cracking and spalling. Even though the occurrence of coupling between ESA and DEF appears to be realistic, few studies have been conducted concerning this phenomenon. The coupling effect of ESA and DEF will be denoted as "coupling effect" in the following pages.

The pore structure of the cement-based material exerts a significant influence on their physical and mechanical properties. Studying the pore structure is helpful to understand and interpret the properties of the porous media. Some of the main pore structure parameters are porosity, pore size distribution, etc. The total porosity is a measure of the void volume fraction in a material, which can be expressed as a percentage of the bulk volume of the material (Eq. 41). To understand the characteristic of the microstructure, the pore size distribution has to be studied. There is no unique method that can adequately cover all scales. In addition, the porosity may be modified or changed by a variety of processes during the test including deformation, hydrothermal alteration and producing fracture porosity [211]. Finally, the pore shape and connection structure (open and closed) have a significant effect on the porosity, and this effect depends on the testing approach.

$$\phi = \frac{V_{\text{void}}}{V_{\text{bulk}}} \tag{41}$$

The methods to quantify porosity and pore size distribution can be classified into two categories: direct methods and indirect methods. For the first type, a broad range of imaging methods are available to describe the nature of the porosity. For example, using backscattered electron (BSE) images allows to obtain information about the surface topography of the sample and the composition of C-S-H with different grey levels depending on their composition [119]. Similar techniques are scanning electron microscope (SEM) and transmission electron microscopy (TEM), which can exhibit the structure of the crystals. Energy dispersive X-ray (EDS) can be adopted to analyze the elemental composition or chemical characterization of a sample. Besides the chemical composition, X-ray powder diffraction (XRD) provides the spatial arrangements of atoms in crystalline phases as well. Meanwhile, some methods can be employed to indirectly measure porosity, such as saturation

or imbibition, gas adsorption (DVS belongs to this technique - see below), mercury intrusion porosimetry (MIP) and so on. However, the different techniques are based on different principles and have different capability of measurement. Aligizaki summarized various methods used for characterization of pore structure in cement-based materials and the range of pore sizes where each technique is applicable [212], see Fig. 2.1. In order to capture the whole range of pore size distribution and total porosity, the combination of several techniques is indispensable. In the present study, mercury intrusion porosimetry (MIP), dynamic vapor sorption (DVS) and water accessible porosity test (WAPT) are combined. The possible pore ranges that could be investigated by those three techniques are shown in Table. 2.1, based on the devices used in this thesis. The MIP device provides a pore size range between 3.7 nm - 400 μm [213], and the deduced pore size range from DVS is between 0.2-20 nm. Therefore, the pore size distribution with a range of 0.2 nm to 400 μm could be obtained by combining the MIP and DVS techniques. Meanwhile, the comparison of pore volumes at the overlapped pore ranges, which were measured by different techniques, are made to analyze the advantages and limitations of the techniques.

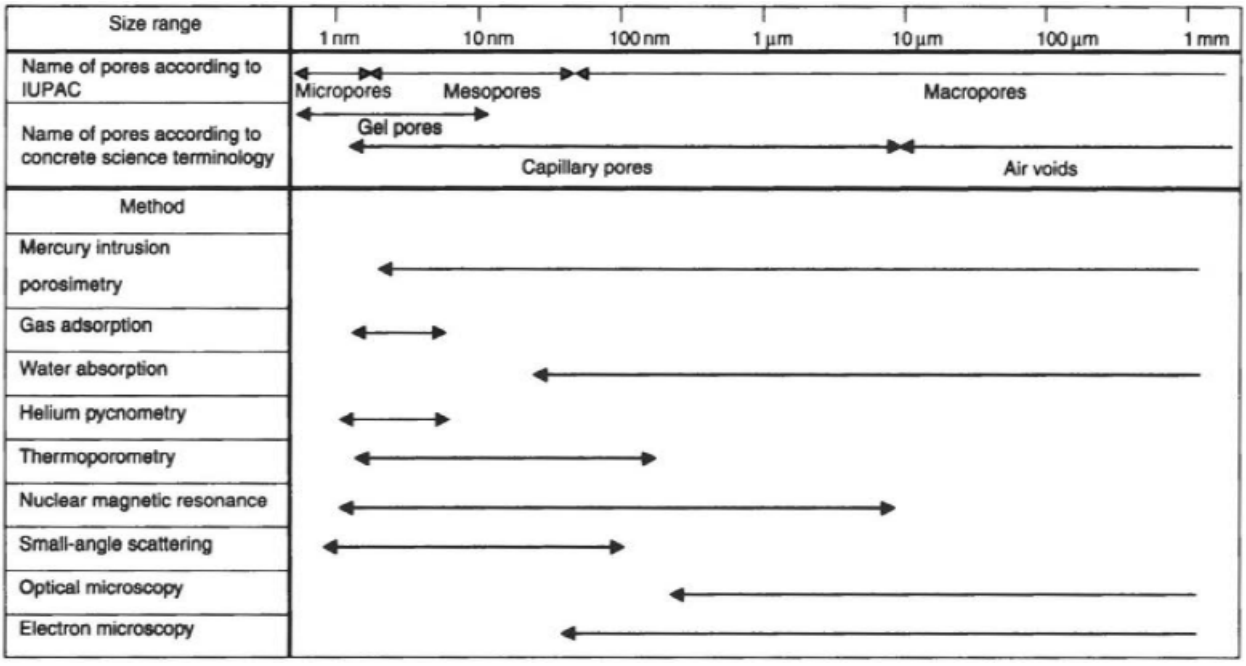

Figure 2.1 – Methods used to characterize pore structure in cement-based materials, including the range of pore sizes where they are applicable [212]

Table 2.1 – Techniques with the possible investigated pore range

Techniques	DVS	MIP	WAPT
Pore ranges in diameter	0.2-20 nm	3.7 nm - 400 μm [213]	>0.1 μm [214]

In this dissertation, the main objectives of the tests include:
1. The studies of deterioration phenomena of cement-based materials;
2. The determination of the pore position where ettringite forms during sulfate attacks in the microstructure;
3. The proposal of a uniform expansion mechanism (crystallization process in porous cement-based materials) despite the different exposure conditions: ESA, DEF, and coupling of ESA and DEF.

These goals are accomplished with three different techniques:

1. The measurements of mass and length variations, and the study of the relationship between these two parameters. In general, an increase of mass and an expansion are observed when cement-based materials are submitted to sulfate attacks [93, 100, 101]. These variations will be compared and analyzed according to different exposure conditions in the next chapter.

2. The characterization of the total porosity and pore size distribution. Three techniques (MIP, DVS, and water accessible porosity tests (WAPT)) are performed to capture the changes in pore size distribution and the total porosity before and after the sulfate attacks. Through an analysis of the measured pore size distribution, the position where ettringite forms could be detected. Meanwhile, the pore size distribution gradients in the specimens are analyzed for different exposure conditions as well.

3. Heat-based dissolution tests. During the degradation processes, some pores are filled by reaction products such as ettringite. Thus, the creation of new pores or the filling of existing ones might be hidden if reaction products are present in the corresponding spaces. The idea that the pore size changes are caused by ettringite formation after sulfate attacks will be confirmed by heat-based dissolution tests. Due to the unstable characteristics of ettringite at high temperature (above 65 °C [90]), the ettringite formed in degraded samples after the sulfate attacks will be heated and "washed" out, which results in the reversion of pore size distribution to the initial state in a certain pore range and further confirms the ettringite formation.

In the present chapter, the specimens design, the materials used, the experimental techniques adopted (MIP, DVS, and WAPT) and the heat-based dissolution tests will be presented in details. The experimental results and the corresponding discussions will be presented in the next chapter.

2.2 Specimens design

Six sets of small cement paste prisms ($2 \times 2 \times 12$ cm^3) and one set of big cement paste prisms ($11 \times 11 \times 22$ cm^3) were fabricated with CEM I [215], with a water cement ratio of 0.55, as shown in Table 2.2. Five sets of small cement paste prisms ($2 \times 2 \times 12$ cm^3) and one set of big cement paste prisms ($11 \times 11 \times 22$ cm^3) were fabricated with CEM III [215]. The small prisms were designed to accelerate the process of sulfate attacks. They were subjected to three different sulfate attack conditions (ESA, DEF and coupling effect of both reactions) and were tested at two states, initial and final state, see Fig. 2.2. The initial state is defined as the moment after the 28 days curing, right before exposing the specimens to their respective aging conditions. The final state is the time when the specimens are seriously degraded with an expansion of around 1% for ESA and the coupling effect of ESA and DEF, at which moment the material could not resist any more expansion. The final state for DEF is the plateau phase, which depends on the initial content of the chemical components amongst others. The small samples are named by:

- type of exposure (ESA, DEF, and Coup for coupled sulfate attack)
- type of cement (I or III)
- state of the specimen (before or after sulfate attack, "Ini" or "Fin" respectively).

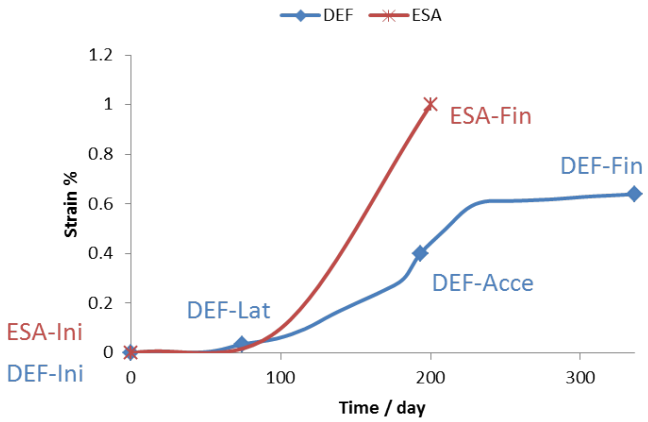

Figure 2.2 – Experimental measurements at different swelling states

The big prism samples ($11 \times 11 \times 22$ cm^3) were designed to be subjected only to DEF. The specimens were fabricated to characterize the pore size distribution at different states: the initial state (after the 28-day curing), the latent period, the accelerated period and the final plateau period. These four states are pointed out in Fig. 2.2

Table 2.2 – Samples design

Specimens	Cement type	Size	W/C	Expansion state	Techniques
ESA-I-Ini	CEM I	2×2×12 cm³	0.55	Initial	MIP; DVS.
ESA-I-Fin	CEM I			Final	
DEF-I-Ini	CEM I			Initial	
DEF-I-Fin	CEM I			Final	
Coup-I-Ini	CEM I			Initial	
Coup-I-Fin	CEM I			Final	
ESA-III-Ini	CEM III			Initial	
ESA-III-Fin	CEM III			Final	
DEF-III-Ini	CEM III			Initial	
DEF-III-Fin	CEM III			Final	
Coup-III-Fin	CEM III			Final	
DEF-I-Ini	CEM I	11×11×22 cm³		Initial	MIP, WAPT and heat-based dissolution test
DEF-I-Lat	CEM I			In the latent period with an expansion of 0.03%	MIP, and WAPT
DEF-I-Fin1	CEM I			At the plateau period with an expansion of 1.49%	MIP, WAPT and heat-based dissolution test
DEF-I-Fin2	CEM I			At the plateau period with an expansion of 1.22%	MIP and WAPT
DEF-III-Ini	CEM III			Initial	MIP and WAPT
DEF-III-Lat	CEM III			In the latent period	MIP and WAPT
DEF-III-Acce	CEM III			In the accelerated period	MIP and WAPT
DEF-III-Fin	CEM III			At the plateau period	MIP and WAPT

Notes: Initial state means the specimens after 28-day curing.
Final state is the moment when the material is worse degraded with an expansion degree around 1%.

and MIP tests were conducted to capture the evolution of pore size distribution during DEF at different depths. However, the specimen, which was designed to be measured at accelerated period, turned out to be at the plateau period. It means that two final specimens: DEF-I-Fin1 and DEF-I-Fin2 were obtained in the end.

The specimens DEF-I-Fin1 and DEF-I-Fin2 were fabricated at Ifsttar 1-year before the other two big specimens. These specimens were cast with the same cement mix and curing conditions. In addition, specimen DEF-I-Fin1 was selected for the heat-based dissolution test, the details of which are shown in the last part of this chapter.

2.3 Materials and casting

A cement CEM I 52.5 R CE CP2 NF. and a cement CEM III/A-LH CE PM ES CP1 NF. were used. The composition of the cement materials is shown in Table 2.3 and 2.4. The content of both cements used in the samples were calculated as:

$$V_{\text{cement paste}} = V_{\text{cement}} + V_{\text{water}} = C/d_C + W/C * C \quad (42)$$

where C is the mass content of cement, W/C is the water to cement ratio (0.55 in this study), and d_C is the density of cement.

Table 2.3 – Composition of the cement materials (CEM I composition measured at Ifsttar, CEM III provided by manufacturer)

Components%	CEM I	CEM III
CaO	62.79	49.46
SiO_2	20.38	29.58
Al_2O_3	4.30	8.93
TiO_2	0.24	0.60
Fe_2O_3	3.80	1.51
MgO	1.25	4.57
SO_3	3.46	1.46
S	Traces	0.58
K_2O	0.73	0.62
Na_2O	0.35	0.48
Cl	0.04	0.20
MnO	0.05	0.20
LOI (Loss on ignition)	2.04	1.12
Insoluble	0.54	0.60
Free lime	1.39	0

Table 2.4 – Composition of the cement I calculated by Bogue method based on information in Table 2.3 [93]

Components	Mass content from Bogue method %
C_3S	41.45
C_2S	27.15
C_3A	4.97
C_4AF	11.54
CSH_2	7.44

The content of Na_2O_{eq} was increased by adding KOH in the mixing water in addition to the alkalis brought by the cements. The quantity of K_2O needed in the mixing water was calculated from Eq. 43. Based on an alkali cement content of 0.83%

weight in cement I (see Table 2.3), KOH was added in the mix to reach a Na_2O_{eq} content of about 1% (precise calculation with a 0.83% Na_2O_{eq} content provides 1.065% weight cement with the KOH addition given in Table. 2.5). For cement III, KOH was added to the mix to obtain a total content of Na_2O_{eq} of about 1%, based on the K_2O content of 0.62% and Na_2O content of 0.48% in mass according to manufacturer data. The KOH was dissolved in mixing water one day before casting to avoid the heating of the solution due to the exothermic dissolution. As previously noted, the water to cement ratio w/c of 0.55 was adopted for all specimens, based on preliminary tests conducted at Ifsttar prior to the beginning of this Ph.D. thesis.

$$Na_2O_{eq}\% = Na_2O\% + 0.658\ K_2O\% \tag{43}$$

Table 2.5 – Materials mixes

	CEM I	CEM III	Unit
Cement	1.154	1.154	Kg/L
Water	0.635	0.635	L/L
KOH	4.912	2.79	g/L

Wooden formworks were used for small specimens, whereas stainless steel formworks were used for the big ones. Each formwork corresponded to 3 prisms, the inner faces of which were oiled before the casting to allow easy demolding operations. However, this was proved not working when demolding the big prisms with CEM III in the first fabrication, then the stainless steel plates of the formwork were wrapped in plastic foils in a second cast.

2.4 Curing of the specimens

All the specimens were protected during their moist cure with a curing textile on the top surfaces after casting to prevent excessive leaching. For the specimens dedicated to the ESA tests, an ambient temperature (around 20 °C) curing in water (to keep the same moist environment as DEF) was applied. Tanks were prepared with tap water for the moist cure of specimens dedicated to ESA, with water to solid ratio (volume of stored water / volume of specimens) of around 26. For the specimens dedicated to the DEF and the coupled effect tests, a heat treatment (Fig. 2.3) was applied in a tank containing water (see Fig. 2.4), with the temperature controlled by

the heating device and following the same preheating procedure adopted in [93]. The total duration of the heating process was 1 week. After casting, the formwork with the specimens was set aside for 2h (pre-curing time), and then the heat treatment started. The first step was to increase the temperature to 81 °C after 24 hours with a maximum rate of about 10 °C/h. Then, a constant temperature of 81 °C followed and was kept for 72 h. The heat treatment was completed by a cooling phase. The cooling rate was fixed at -1 °C/h to avoid a cracking of the bulk induced by a thermal effect. In the end, the heating was stopped at 25 °C. The objective of this temperature profile was to be representative of the curing conditions in the core of a massive structure.

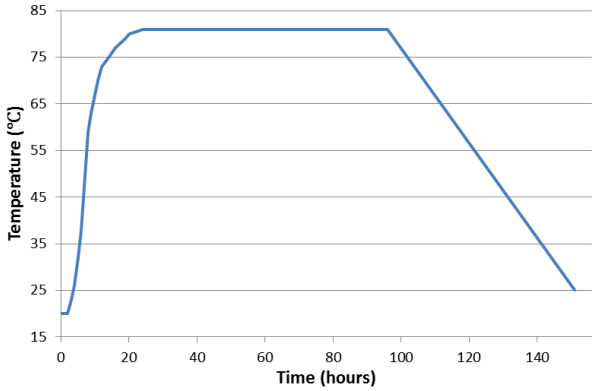

Figure 2.3 – Heating treatment for the samples subjected to DEF and the coupling effect

Figure 2.4 – The bath with a heating device used in the experiments [93]

All the prisms were demolded after 1 week and were equipped with stainless steel pins. The details will be shown in section 2.5.2. Then, the large prisms were kept under aluminium sealing until 28 days. It followed a usual procedure adopted at IFSTTAR [93] to keep the moisture in the specimens and limit the effect of leaching.

However, the small prisms were stored in tap water with water to solid ratio (volume of stored water / volume of specimens) of around 26 until the end of the curing period (28 days) due to a high probability of losing moisture in small-size specimens. Fig. 2.5 and 2.6 summarize the temperature and moisture history of all the specimens.

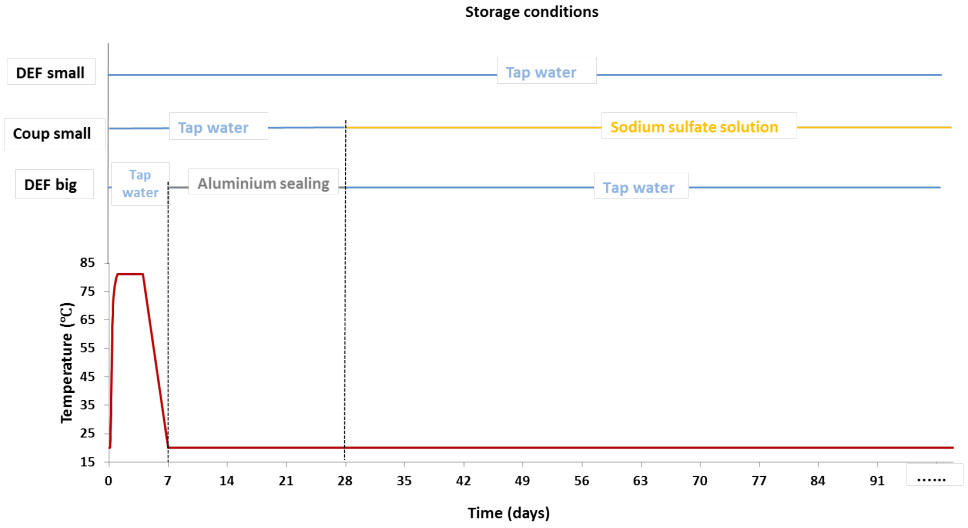

Figure 2.5 – Curing and storage conditions for DEF and Coup specimens

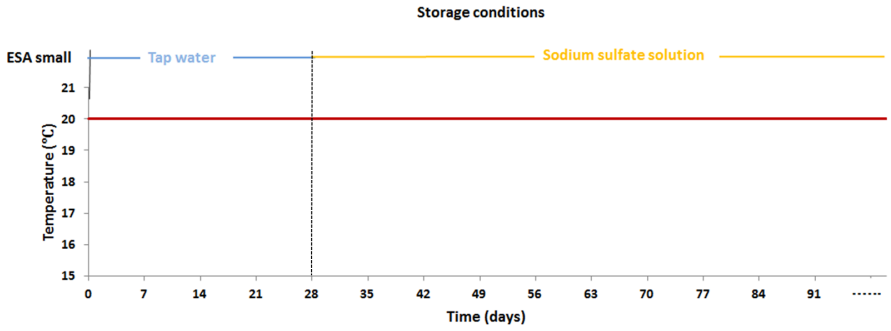

Figure 2.6 – Curing and storage conditions for ESA specimens

2.5 Length and mass measurements

2.5.1 Specimens storage

After the curing, the samples dedicated to DEF were stored in tap water, while the others were stored in a Na_2SO_4 solution with a sulfate concentration of 10 g/l. According to previous studies (see Table 2.6), this content seems to be an optimum concentration in triggering ESA.

Table 2.6 – Exposure conditions found in the study of ESA

References	Na_2SO_4 g/L	pH
[65]	3-10 and 30	7
[216]	6 and 34	7
[217]	30	7

The Na_2SO_4 solution was changed each week during the first month, and then every two weeks after in order to ensure a high concentration of sulfates ions during the ESA. The small specimens were immersed in a tank with two edges placed on the blocks to guarantee the bottom surface accessible to water or solution, see Fig. 2.7.

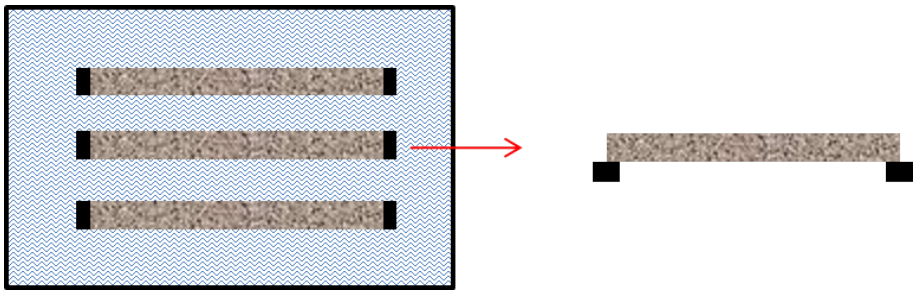

Figure 2.7 – Specimens curing in a tank with solution around

2.5.2 Instrumentation of the specimens

All the specimens subjected to sulfate attacks were equipped with stainless steel pins after demolding (1 week after casting) on faces to ensure the monitoring of axial dimension after demolding. The pins are designed with a small hole on one face, which matches with the needle on the reference length bar (Fig. 2.8 (a) on the right). Only three faces were equipped with stainless steel pins, because the

fourth face (non-formed face) was non-smooth due to the curing textile (shown in Fig. 2.8 (b)). However, the big prisms had them on the four surfaces (their bigger dimensions allowed a better surface preparation to glue the pins). The initial length of two pins was set as 107 mm for the small samples and 100 mm for the big ones (shown in Fig. 2.8(c) – two different measurement lengths due to the use of two different extensometers) along the geometric center axis with the help of the length reference bar.

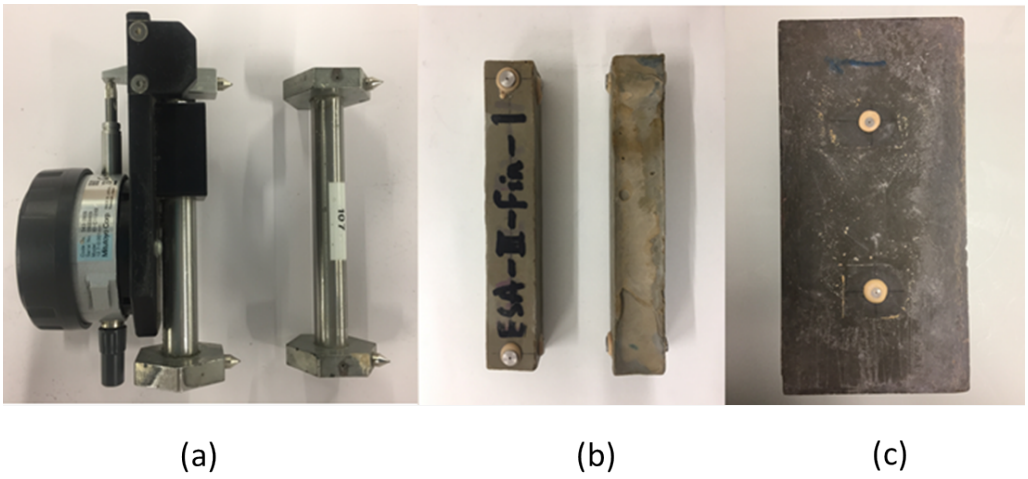

Figure 2.8 – Instrumentation of the specimens: (a) Extensometer with its reference bar; (b) $2 \times 2 \times 12$ cm^3 specimens; (c) $11 \times 11 \times 22$ cm^3 specimens.

For specimens exposed to sulfate attacks, the length and mass measurements were conducted every two weeks. After demolding and instrumentation with pins, the original mass of the sample with pins was recorded, which was named mass_{ori}. Due to the ingress of water from three exposure conditions and the penetration of sulfate ions from aggressive solutions for ESA and the coupling effect, the mass increases. The measurement at time t was recorded as "mass_{t}" and the variation was calculated referring to Eq. 44.

$$\text{relative mass variation} = \frac{\text{mass}_{\text{t}} - \text{mass}_{\text{ori}}}{\text{mass}_{\text{ori}}} \tag{44}$$

As explained before, the stainless pins were glued to the surfaces of the specimens. The distance between the two pins increased as expansion occurred. The measurement device used is shown in Fig. 2.8 (a). On the left of the picture, there is an extensometer with its measurement needles and its sensor showing the value of the measurement. On the right of the picture, there is a reference length bar with two

holes on the edges where the needles can be inserted. On the other side, there are two needles that are used to mark the reference length of pins on the specimens during the instrumentation process. For each measurement, the needles of the extensometer are inserted into the small holes on the reference length bar, and the length displayed on the screen is tared to 0 by pressing the initial setting button. Then the needles of the extensometer are placed on the holes of the pins fixed on the specimens. The length change was measured in this way after a 28-day curing, and the first measured result was named as "length change$_0$". Each measurement was performed three times and an average value was recorded. The measurement at time t was recorded as "length change$_t$". The length$_{ori}$ was 107 mm for small prisms and 100 mm for large ones. Then strain was calculated according to Eq. 45.

$$\text{strain} = \frac{\text{length change}_t - \text{length change}_0}{\text{length}_{ori}} \tag{45}$$

2.6 Sample preparation for pore size distribution characterization

(a) Small specimen 2×2×12 cm^3

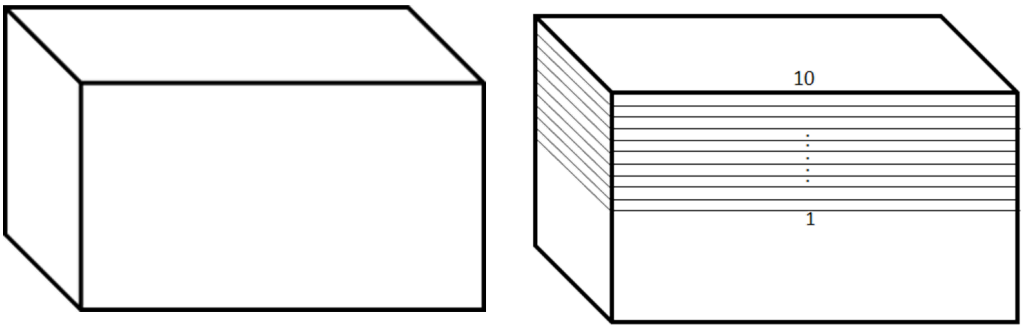

(b) Big specimen 11×11×22 cm^3

Figure 2.9 – Samples slicing plan

When the specimens were ready for the characterization of the pore size distribution, they were wet sawed, sliced, and prepared to be lyophilized. The small specimens were sliced from the top surface to bottom, and only the two top layers were se-

lected. With the aim of figuring out the pore size distribution along the depth of the specimens affected by ettringite formation, the big samples were sliced with a width of 0.55 cm (shown in Fig. 2.9) from surface to core, and samples were named as layer 10 to layer 1, respectively. The cutting device used is shown in Fig. 2.10, and the thickness of the blade used is 0.4 mm. It is a precise cutting and grinding machine. The sample was fixed with the specimen holder. The position of the specimen holder was adjustable and the coordinate was presented at the screen, which provided a high precision.

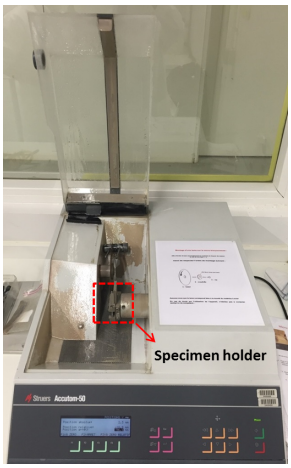

Figure 2.10 – Cutting equipment – Accutom-50

After slicing, the samples were put in a container filled with liquid nitrogen inside for approximately 5 minutes. At normal pressure, liquid nitrogen boils at -195.8 °C, which freezes the liquid water inside the material without changing the microstructure of the material [218]. Then, the samples were put in a freeze-dryer (Fig. 2.11) for 3 days. The lyophilization procedure was used to preserve a solid by withdrawing the water through sublimation under vacuum, after having frozen the product. By heating up water in a frozen state under very low air pressure conditions (0.07 mbar), the water is directly transformed into steam. The released steam is caught up in a cooling coil at a temperature of -57 °C and removed. This technology allows keeping the quality of the product unchanged. This is an efficient way of drying without changing the microstructure of the cement-based material. In this way, all the water within the material could be removed without having to heat the sample excessively. When the specimens were totally dried, they were roughly ground and stored in a desiccator with silica gel at a relative humidity of 3% to keep them dry.

Figure 2.11 – Freeze-dryer used in the study

2.7 Mercury Intrusion Porosimetry (MIP)

MIP is a simple and fast technique to measure the microstructure of materials. It is based on the premise that a non-wetting liquid (with contact angle greater than 90 °) will only intrude capillaries under pressure. MIP provides a wide range of information, e.g. the pore size distribution, the total pore volume (or porosity), the skeletal and apparent density, and the specific surface area of a sample. In this work, MIP is used to obtain the total porosity and the pore size distribution. The volume of mercury intruded at each pressure increment determines the pore size distribution of the material, while the total intruded volume determines the total porosity. A key assumption in MIP is the pore shape. All the pores are assumed as cylindrical pore geometry and fully accessible for mercury penetration from the surface of the specimen. However, in reality, the pores consist of large pores connected by smaller throats.

$$P = \gamma(\frac{1}{r_1} + \frac{1}{r_2}) = \frac{2\gamma \cos\theta}{r_p} \tag{46}$$

The Eq. 46 relates the pressure difference across the curved mercury interface (r_1 and r_2 describe the curvature of that interface) to the corresponding pore size r_p using the surface tension of mercury γ and the contact angle θ between the solid and mercury, see Fig. 2.12. For the contact angle θ, it is affected by the structure of

the solid surface, the age of the specimen, the drying method used for pretreatment, and the purity of the mercury [219]. In most practical situations, it is a fixed value irrespective of the specific sample material. In this work, the adopted value is 141.3 ° (angle adopted for cementitious materials) [220].

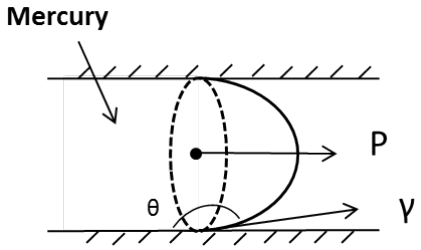

Figure 2.12 – Pressure applied on mercury for it to intrude inside a capillary pore

Initially, the sample is evacuated to remove air and residual moisture or other liquids from the pore system. The sample is then filled with mercury as the entire system is still under reduced pressure (0.1 MPa). Slowly increasing the overall pressure then allows mercury to penetrate the largest pores in the sample or any empty spaces between sample pieces. At the end of this "low pressure", the weight of the penetrometer, filled with mercury and the sample, is determined. The volume of intruded mercury is measured continuously through changes in the capacitance between the column of mercury in the capillary stem (capillary tube of known diameter connected to the sample cell) and a coaxial metal sheet surrounding the stem. Once transferred to the high-pressure system, the sample-cell is surrounded by a hydraulic fluid and pressures of up to 414 MPa are applied in an isostatic way. Intrusion pressure values are directly converted into the corresponding pore size by using the Young-Laplace and Washburn equation (Eq. 46). This is a straightforward calculation. The porosity is defined as the ratio of the cumulative intruded volume of mercury to the bulk volume of the samples. By measuring the volume of mercury that intrudes into the sample material with each pressure change, the volume of pores in the corresponding size class is known.

However, it also has limitations. For example, it measures the largest entrance towards a pore, but not the actual inner size of a pore (see Fig. 2.13(a)). Obviously, it can not be used to analyze closed pores as well, since the mercury has no way of entering. Therefore, the results from MIP always show a smaller pore size compared to other techniques, e.g. Scanning Electron Microscopy (SEM) or optical micrographs. Furthermore, the hysteresis exists, which is called ink-bottle effect (see Fig. 2.13). During mercury extrusion (similar to drying process), the partial pressure starts

Figure 2.13 – The ink-bottle effect in MIP

from the maximum to minimum, which means that mercury is removed from the narrowest to widest pores. Whereas during mercury intrusion (similar to wetting process) which starts from lowest partial pressure, mercury enters from the widest points in the pore cavity. As a result, the material at a given partial pressure retains more mercury while drying than it does in the wetting. Although MIP has several limitations, the pore structures determined by this technique have been related to the factors that control the characterization of materials [221], such as total porosity, and pore size distribution.

Figure 2.14 – Mercury intrusion porosimetry device

The instrument used in this study is a Micromeritics' AutoPore IV 9500 series Porosimeter (see Fig. 2.14), which is capable of exerting maximum pressure up to 414 MPa. The pore size range that could be investigated is between 3.7 nm to 400 μm. For each MIP test, about 1.0 g sample after lyophilization was selected. The low-pressure intrusion was performed first, followed by a high-pressure intrusion. A

typical pore size distribution obtained from this test is shown in Fig. 2.15, which illustrates the dV/dlogD pore volume (mL/g) on y axis and pore size diameter (nm) on x axis. This curve shows that the main porosity ranges between 3.7 nm to 100 nm with a peak around 90 nm, which means that pores around 90 nm are the majority of the total porosity. In this way, the characteristics of the pores in the materials could be captured.

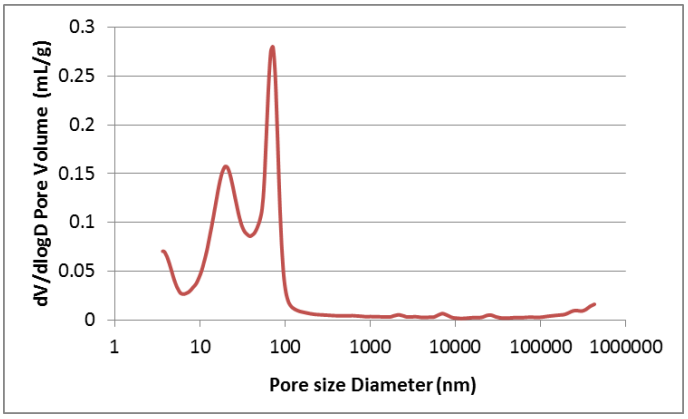

Figure 2.15 – Example of pore size distribution obtained from MIP

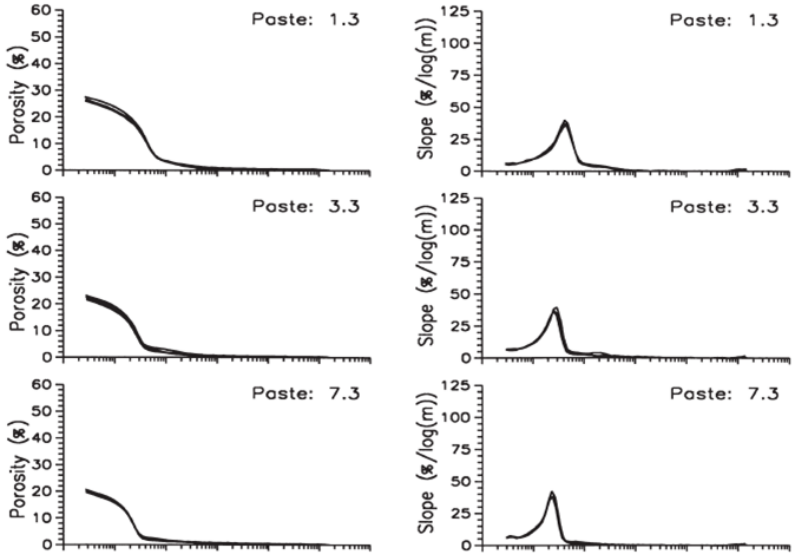

Figure 2.16 – Repeated MIP tests on cement pastes [222].

The MIP technique is precise and reproducible. It showed a relative variability of porosity measurements at 2% on two sets of samples (each conducts three times) [32]. The maximum relative difference between the highest and lowest total porosity for a given cement paste was 4% with an average standard error of 0.6% in [222], based on the measurement of 30 sets of specimens. The measured pore size distribution curves show a good consistency as well, see Fig. 2.16

2.8 Dynamic Vapor Sorption (DVS)

The water sorption isotherms show the equilibrium amount of vapor sorbed as a function of steady state relative humidity (RH) at a constant temperature. There are various methods that can be used to assess the water vapor sorption isotherms, such as the flow division method that mixes the dry and saturated air, the method with altering temperature or pressure or both, the volumetric method in a vacuum system with changing vapor pressure, and gravimetric methods [223].

DVS is a relatively new technique for water vapor sorption analysis in the field of cementitious materials. The equipment is placed in an incubator (see Fig. 2.17), allowing the temperature to be kept constant. The required RH is created by varying the water vapor concentration surrounding the sample. Each flow is controlled by thermal conductivity mass flow controllers. The relative humidity of the mixed gas flow can vary between 0 and 98%. The other main component of the DVS system is the microbalance, which continuously weighs the mass of the sample as a function of time. The test is accomplished by exposing the samples to a series of incremental changes in relative humidity (as shown in Fig. 2.18) and monitoring the mass change as a function of time. Isotherms are divided into two components: desorption for decreasing relative humidity steps and adsorption for increasing relative humidity steps. The sample mass must be allowed to reach gravimetric equilibrium at each step change in relative humidity before progressing to the next humidity level. The generated partial pressure (P/P_0) is within $\pm$ 1.5 % P/P_0 of the set point.

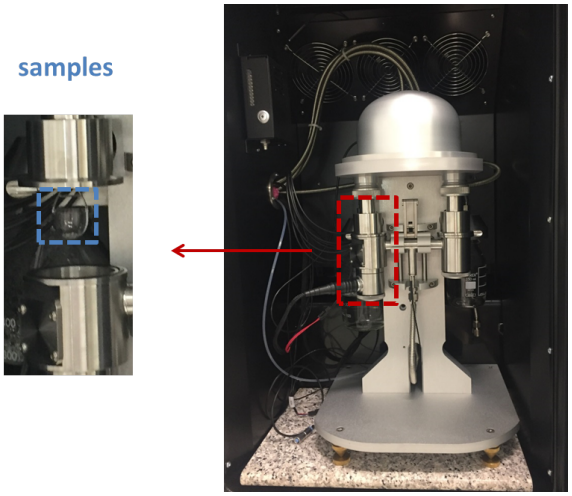

Figure 2.17 – The DVS equipment

The samples were firstly ground to obtain particle diameters between 1 and 1.25

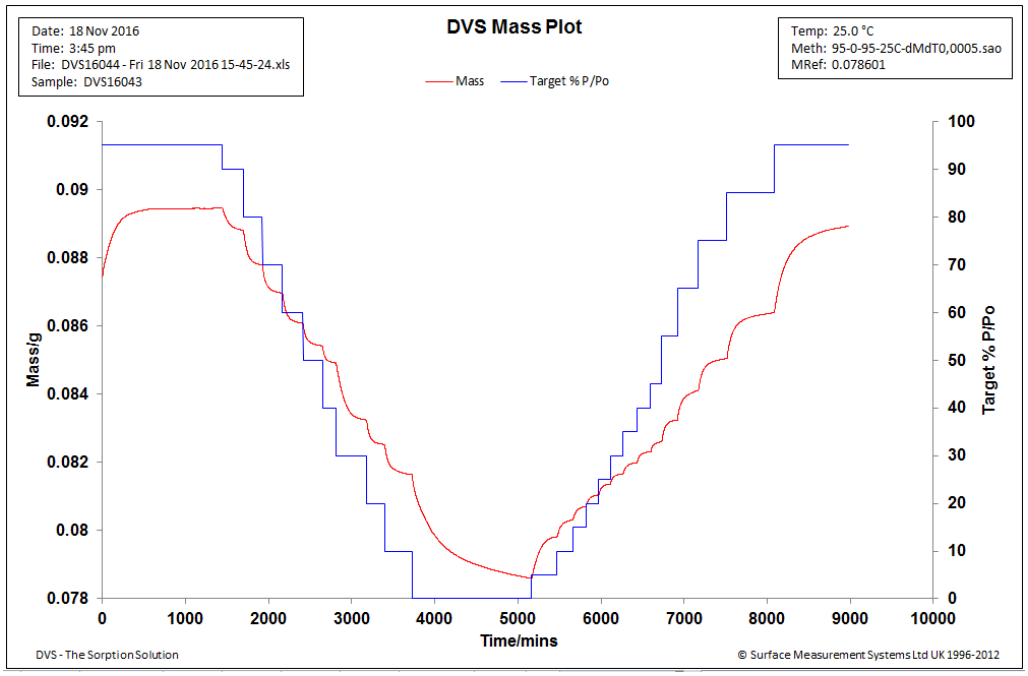

Figure 2.18 – The relative humidity changes method used in the DVS

mm. For each test, 80 to 100 mg materials were chosen. This amount is sufficient to be representative of the material and to have a fast test time [213]. The samples were kept over a saturated salt solution of K_2SO_4 in a desiccator laid in a thermo-regulated bath at T=23 °C to reach the relative humidity of 97 % [224]. The sample were mass monitored until the mass variation was less than 0.5%, then it was believed that the sample reached a relative humidity of 97 %. The sorption experiments started from a desorption process from RH=95% and continued stepwise to an RH=0. This order can avoid the pre-drying before the test, which might damage the microstructure of the material as well. After the step-by-step desorption process, the materials were submitted to a subsequent step-by-step adsorption process from 0% and stopped at RH=95%. Each point of the curve corresponded to an equilibrium state between the pore gaseous phase and the environmental conditions, including RHs and temperatures. In order to get a precise "equilibrium" mass state, a low variable rate and a long duration should be adopted for each step, taking into account the very slow kinetics of moisture transport in gel pores. However, a long-term exposure to a moist environment may lead to hydration of anhydrous materials, which changes the microstructure and is inevitable to avoid. After several trials conducted in this study, a rate of change of mass% with time of 0.0005 s^{-1} and a maximum duration of 2000 minutes were adopted to obtain the best balance. It means the following relative humidity will be imposed when the mass is stable or after 2000 minutes even if the mass of the sample has not reached the equilibrium.

2.8.1 Pore size distribution deduced from water vapor sorption isotherms

The Water Vapor Sorption Isotherms (WVSI) obtained from DVS shows the equilibrium mass at each relative humidity step. In order to obtain the pore size distribution from the dynamic water vapor sorption, the Brunauer-Emmett-Teller (BET) [225] surface area analysis theory and Barrett-Joyner-Halenda (BJH) [226] pore size and volume analysis theory were adopted. BET analysis provides a precise specific surface area evaluation of materials from the statistical thermodynamics of adsorption within the low RH range (11–35%). This technique determines the total specific surface area in m^2/g, namely the total surface area of a material per unit of mass. Based on the total specific surface area from BET theory, the BJH analysis was employed to determine the specific pore volume, that is to say, the total internal void volume per unit mass. The main assumption of this method is the coexistence of "capillary" and "adsorbed" (water) phases in cylindrical pores. The iterative computation is based on the step-by-step analysis of the desorption curve.

2.8.1.1 Determinations of the BET Surface Area (S_{BET}) using Sorption Isotherms

The BET constant C (unitless) was determined from the measured adsorption isotherms [227]. Data points in the low RH regime (RH=11-35%) were applied to generate a plot which noted the quantity $(1/m \times ((1/\mathrm{RH}) - 1))$ on the y-axis, and the RH (fraction) on the x-axis, where m was the amount of moisture adsorbed ($\mathrm{kg_{water}/kg_{solid}}$). The slope of the linear fit to the data revealed A (unitless), and the y-intercept revealed I (unitless). Both parameters can be applied to determine the BET constant and the monolayer capacity (v_m, $\mathrm{kg_{water}/kg_{solid}}$) of the material, to quantify the BET solid surface area as shown in Eq. 47 [228].

$$\begin{aligned} v_m &= \frac{1}{A+I} \\ C &= 1 + \frac{A}{I} \\ S_{\mathrm{BET}} &= \frac{v_m \times \mathrm{N_A} \times s_m}{V} \end{aligned} \tag{47}$$

where, S_{BET} is the BET surface area ($\mathrm{m^2 \cdot kg^{-1}}$), $\mathrm{N_A}$ is Avogadro's number ($6.022 \times 10^{23}\ \mathrm{mol^{-1}}$), V is the molar volume of water ($0.018\ \mathrm{kg \cdot mol^{-1}}$) and s_m is the surface coverage offered by a single water molecule ($0.114 \times 10^{-18}\ \mathrm{m^2}$).

2.8.1.2 Determinations of the t-Curve from the measured sorption response

The t-curve describes the statistical thickness (Å) or the numbers of layers (unitless) of vapor molecules adsorbed on the surface of an adsorbent as a function of the vapor pressure, or in the case of water vapor, the RH. The t-curve of porous materials as derived from Eq. 48 comprises both physically adsorbed water in multiple layers and condensed water [229, 230].

$$t_{RH} = \frac{V_m}{S_{\mathrm{BET}}} \tag{48}$$

where t_{RH} is the thickness of the water film (Å), V_m ($\mathrm{m^3 \cdot kg^{-1}}$) is the volume of water adsorbed per unit dry mass of the solid at a given RH.

2.8.1.3 Determinations of the pore size distribution via BJH method

A way to analyze the relationship between dynamic nitrogen vapor desorption isotherms and the distribution of pore volume with respect to pore radius was adopted in [226]. This method was followed and used in the water vapor desorption isotherms in this study. It is assumed that the equilibrium between the gas phase and the adsorbed phase during desorption is determined by two mechanisms: (1) physical adsorption on the pore walls, and (2) capillary condensation, with a radius of r_k which is related to relative pressure by classical Kelvin equation (Eq. 49).

$$\log(P/P_0) = \frac{-2\sigma V}{2.303 \times RT \times r_k} = \frac{-4.03}{r_k} \tag{49}$$

where P is the actual vapor pressure, P_0 is the saturated vapor pressure, σ is the surface tension of water (0.072 N/m) at 25 °C, V is the molar volume of water (18 $\mathrm{cm^3/mol}$), R is the gas constant and T is the temperature in K (T = 298.15 K in this study).

This method starts from the desorption curve (see Fig. 2.19). The assumed desorption mechanism is presented in Fig. 2.20. The first step of the partial pressure starts from $(P/P_0)_1$ to $(P/P_0)_2$, then goes further to $(P/P_0)_3$. At the first step $(P/P_0)_1$, the largest pore has a radius of r_{p1} with an inner capillary pore radius of r_{k1}. When the partial pressure decreases to $(P/P_0)_2$, it results in the desorption of

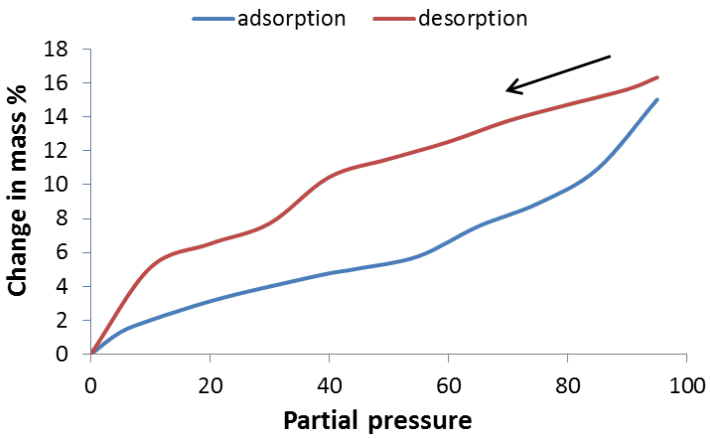

Figure 2.19 – Water vapor sorption isotherm from DVS.

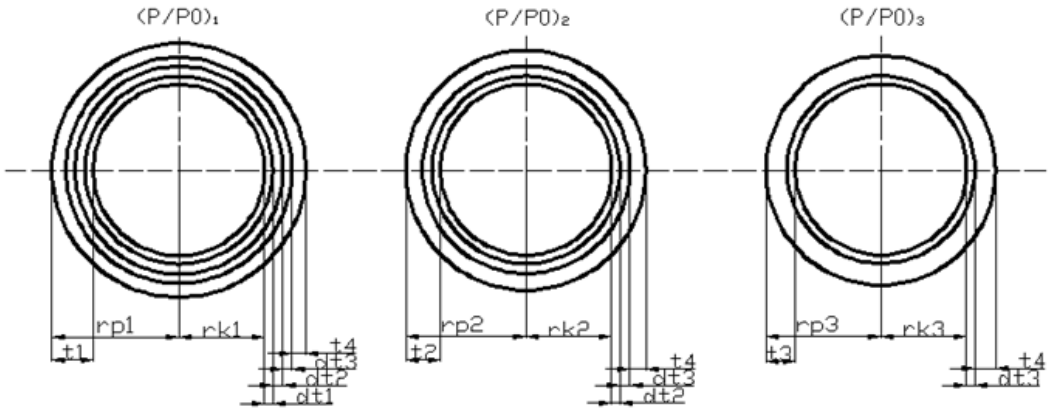

Figure 2.20 – Schematic representation of the assumed desorption mechanism [226]

adsorbed vapor with a volume ΔV_1, which is the loss of the mass measured in the water vapor sorption isotherms. The decrease in relative pressure results not only in the emptying the largest pore of its capillary condensate, but also in a reduction of the thickness of the physically adsorbed layer Δt_1. Then, the pore volume in this reduction range, V_{p1}, can be expressed by:

$$V_{p1} = R_1 \Delta V_1 = \frac{r_{p1}^2}{(r_{k1} + \Delta t_1)^2} \Delta V_1 \tag{50}$$

When the partial pressure decreases from $(P/P_0)_2$ to $(P/P_0)_3$, the situation is more complicated. At this step, the maximum pore radius is r_{p2}, with an inner capillary pore radius of r_{k2}. The volume of the liquid desorbed, ΔV_2, is not only from the

second largest pore but also from a second thinning of the physically adsorbed layer left behind after the first step, with a thickness reduction of Δt_2. The latter volume reduction can be calculated from $\Delta t_2 \times A_{C1}$, and A_{C1} is the average area from which the vapor is adsorbed. The average area is simplified as $\pi \bar{r_{p1}}^2$, with $\bar{r_{p1}}$ being the average radius between the radius corresponding to the upper and lower partial pressure $(P/P_0)_2$. Therefore, the pore volume in this range, V_{p2} is:

$$V_{p2} = \frac{r_{p2}^2}{(r_{k2} + \Delta t_2)^2}(\Delta V_2 - \Delta t_2 \cdot A_{C1}) \tag{51}$$

In this way, the pore volume at a certain pore range will be obtained by decreasing the RH step by step. In the end, the accumulated pore volume calculated should be comparable to the total volume of water vapor that was adsorbed in the material.

2.9 Water accessible porosity test

The water accessible porosity tests were carried out on big specimens ($11 \times 11 \times 22$ cm^3) to quantify the total porosity. The procedure followed here was proposed in [146], which was inspired from the one proposed by the AFPC-AFREM group [231]. The samples to be characterized in terms of porosity accessible to water were evacuated under a pressure of 30 mbar for 4 hours in order to remove the air present in the pores. Subsequently, the samples were immersed in water under a pressure of 30 mbar for 72 hours, in order to saturate all the porosity accessible to water. Under vacuum, water can penetrate into pores with a diameter larger than 100 nm [214]. Finally, the samples were placed in an oven at 105 °C and weighed at intervals of 24 hours until the mass variation was less than 0.05% between two successive weighings. The porosity accessible to water was obtained by comparing the saturated mass and the dry mass of the samples referring to Eq. 52.

$$\text{porosity}\% = \frac{\text{m}_{\text{air}} - \text{m}_{\text{dry}}}{\text{m}_{\text{air}} - \text{m}_{\text{water}}} \tag{52}$$

where m_{air} is the saturated mass in the air; m_{water} is the saturated mass in water and m_{dry} is the mass after drying at 105 °C.

2.10 Evaluation of the techniques

As explained at the beginning of this chapter, the combination of three different techniques (MIP, DVS, and WAPT) provides a way to study the microstructure of cement pastes in a wider pore range. However, each technique has its own limitations. For example, MIP has a limited ability to characterize pore structures in small ranges (the available pore range is between 3.7 nm - 400 μm in this study), and the high intrusion pressure may distort, compress and damage the pore structures [232]. Therefore, DVS was chosen to fill the blind-spot in the small pore range. The pore range that could be measured by DVS in this study is between 0.2-20 nm. The ranges of the two techniques present an overlap. However, the way to deduce the pore size distribution from DVS depends on several assumptions, such as the monolayer distribution of the water molecules, the cylinder shaped pores, etc. Then, the deduced pore size distribution may not be consistent with the real one. However, DVS is useful in the comparative studies. Therefore, it is meaningless to quantitatively compare the MIP and DVS results at the overlapped range. A qualitative comparison is however worth.

WAPT nevertheless also has its own limitations. On the one hand, it may overestimate the porosity in samples if they contain a significant amount of water soluble minerals. The dissolution of these minerals during saturation may increase the measured porosity. On the other hand, a porosity higher than the actual one may be induced by the creation of microcracks during the saturation process due to formation of needle-like crystals. However, this technique is popularly used in the industrial engineering, which provides an efficient and economic way to study concrete macroscopically. Therefore, WAPT is chosen in this study to provide an optional possibility to study the total porosity.

Even with its limitations, MIP may be closer to the actual values than the other techniques even if mercury pressures can collapse the small pores or break through to the isolated pores [233]. MIP is useful in comparative studies of similar materials [234], for example, this technique is found to illustrate the same shift in pore sizes as compared to image analyses [235]. The characterization and the comparison of the pore size distribution is one of the main objectives of the present study, which means MIP is an appropriate technique.

Based on the aforementioned evaluations of three techniques, MIP and DVS results will be used to study the pore size distribution of the samples separately, and WAPT

is employed as an optional choice to study the total porosity in a scientific way, with a comparison to results measured by MIP.

2.11 Heat-based dissolution test

The objective of the dissolution tests presented in this section is to "wash out" the crystal products formed in the pores due to DEF: the objective is to empty all the voids from crystalline products formed during the degradation processes to evaluate the new pores created by DEF, which results in the reversion of the pore size distribution. This goal will be accomplished by characterizing the porous structure before and after the heat-based dissolution test, and the details are shown in the following section: Validation of the heat-based dissolution tests. However, the "washed out" crystals may be not only the reason for expansion but also the consequence after the expansion. The expansive crystals could not be distinguished from the others in this test. Additionally, the results will further confirm that the decreased pore volume in a specific range during DEF is attributed to ettringite formation, including the ones that correspond to expansion and the ones may precipitate after the occurrence of cracks.

2.11.1 Samples

The specimen DEF-I-Fin1 ($11 \times 11 \times 22$ cm^3) was selected for the heat-based dissolution tests qualification. The specimen had been kept in water up to 1 year after the treatment and reached an expansion degree of 1.49%. Another big specimen, DEF-I-Ini, was selected as a reference. In order to limit the full effect of leaching during the dissolution test, sample at the core layer (with depth between 5-5.5 cm) was selected and submitted to a heat-based dissolution test.

2.11.2 Determinations of the heating process

Cement paste consists of different kinds of hydrate products, which may decompose and change phases at a certain range of high temperatures. A summary of temperatures at which cement hydrates may decompose or change phase was proposed by Collier in [236], see Table 2.7. This table helps to identify the change of phases due to high temperatures. At temperatures between 50-100 °C, ettringite and C-S-H

start to decompose or transform into other phases, which change the porous structure of the material. However, C-S-H porosity lies within the gel pores domain (less than 10 nm), while ettringite forms mainly in the capillary pores (this conclusion will be presented in the next chapter). This difference helps to distinguish C-S-H from ettringite at temperatures between 50 and 100 °C.

Table 2.7 – Summary of the main decomposition and phase change temperatures between 0 and 800 °C [236]

Formula	Nomenclature	Temperature (°C)	Reference
$CaSO_4 \cdot 2H_2O$	$C\bar{S}H_2$	70-200	[31]
		128	[237]
		120	[238]
		140	[239]
		140 and 170	[240]
$CaSO_4 \cdot 1/2H_2O$	$C\bar{S}H_{0.5}$	150	[239]
		173	[241]
		200-220	[242]
		>200	[31]
$CaSO_4^a$	$C\bar{S}^a$	380	[243]
$CaSO_4^b$	$C\bar{S}^b$	<1000	[244]
		1462[c]	[245]
-	C-S-H	$50 - 600^d$	[31]
		$100 - 125^e$	[31]
		111	[241]
		115-125	[246]
		130-140	[247]
		<200	[248]
$Ca_3Al_2O_6 \cdot 3CaSO_4 \cdot 32H_2O$	$C_3A \cdot 3C\bar{S} \cdot H_{32}$	$50 - 800^d$	[31]
		$90 - 120^{e,f}$	[31]
		125	[249]
		125-132	[241]
		130	[240]
		135-140	[246]
$Ca_3Al_2O_6 \cdot CaSO_4 \cdot 12H_2O$	$C_3A \cdot C\bar{S} \cdot H_{12}$	$75 - 800^d$	[31]
		185-200	[246]
		$200\&290^f$, $440\&480^g$	[31]

-	C-A-H	90-120	[250]
		100-120	[251]
$CaAl_2O_4 \cdot 10H_2O$	CAH_{10}	100-160	[250]
		$130 - 150^f, 290^g$	[31]
		140	[251]
$Ca_2Al_2O_5 \cdot 8H_2O$	C_2AH_8	140-200	[250]
		170-180	[251]
$Ca_4Al_2O_7 \cdot 13H_2O$	C_4AH_{13}	180-200	[250]
		195-200	[245]
$Ca_2Al_2SiO_7 \cdot 8H_2O$	C_2ASH_8	192	[250]
		200	[252]
		200-230	[253]
$Ca_3Al_2O_6 \cdot 6H_2O$	C_2AH_6	200-250	[31]
		$250 - 310^f, 450 - 550^g$	[254]
		315-330	[247]
		320	[251]
		330	[250]
$Al(OH)_3{}^h$	-	230	[250]
		$220 - 230^{g,i}, 310 - 325^{f,j}, 495 - 525^{g,k}$	[255, 256]
		320	[256]
$Mg(OH)_2$	MH	350	[237]
		400	[257]
		415-430	[247]
$Ca(OH)_2$	CH	$400 - 600^d$	[31]
		450	[257]
		$470^b, 450^m$	[258]
		480^e	[31]
		492-528	[241]
		<500	[240]
		500-600	[259]

$CaCO_3$	$C\bar{C}$	$500-600^n$ $500-700^n$ $>800^n$ $<800^n$	[31] [260] [259] [240]
$CaCO_3$	$C\bar{C}$	$650-660^n$ $720-740^n$	[257] [258]
$MgCO_3$	MC	617	[257]
$Mg_6Al_2O_9 \cdot CO_3 \cdot 12H_2O$	$M_6A\bar{C}H_{12}$	50-230 260-370 375-650	[261] [261] [261]

Notes: a-Soluble to insoluble anhydrite; b-in air; c-melting temperature; d-Total loss; e-highest rate of loss; f-major loss; g-minor loss; h-gibbsite; i-gibbsite to boehmite transition; j-gibbsite to alumina transition; k-boehmite to alumina transition; l-bayerite; m-in argon; n-calcite; o-vaterite; p-aragonite.

Table 2.8 – Temperatures and durations used in the heat-based dissolution tests

	1 day	3 days	5 days	7 days	11 days
68°C	√	√	√	√	√
78°C	√	√			
88°C	√	√			
98°C	√	√			

Generally, it is admitted that a curing temperature above 65°C is essential to decompose the ettringite formed in the cementitious material during the early-age hydration [91, 96, 109, 129, 138, 139, 140], which means that ettringite is unstable at a temperature above 65°C and that it provides a way to remove formed ettringite. Furthermore, a higher curing temperature (below the pessimum effect temperature) tends to decompose ettringite more and faster [135]. Therefore, a temperature range between 65–95 °C was chosen with a temperature step of 10 °C. However, the actual temperatures measured in the oven were 68, 78, 88 and 98 °C. Furthermore, the heating duration is a significant factor for the development of DEF, which has a positive role to decompose ettringite if it is below the pessimum effect [145, 146]. Therefore, different temperatures and durations were designed to perform the ettringite dissolution test: 4 temperature values (68, 78, 88, and 98 °C) and 5 heating durations (1, 3, 5, 7 and 11 days). The details are shown in Table 2.8. The samples were kept in the oven and immersed in the storage water of $11 \times 11 \times 22$ cm^3 DEF specimens (DEF-I-Fin1 and DEF-I-Fin2). After 1-year storage of $11 \times 11 \times 22$ cm^3 DEF specimens, the solution contains calcium ions, which can limit the leaching during the heat-based dissolution tests.

2.11.3 Validation of the heat-based dissolution tests

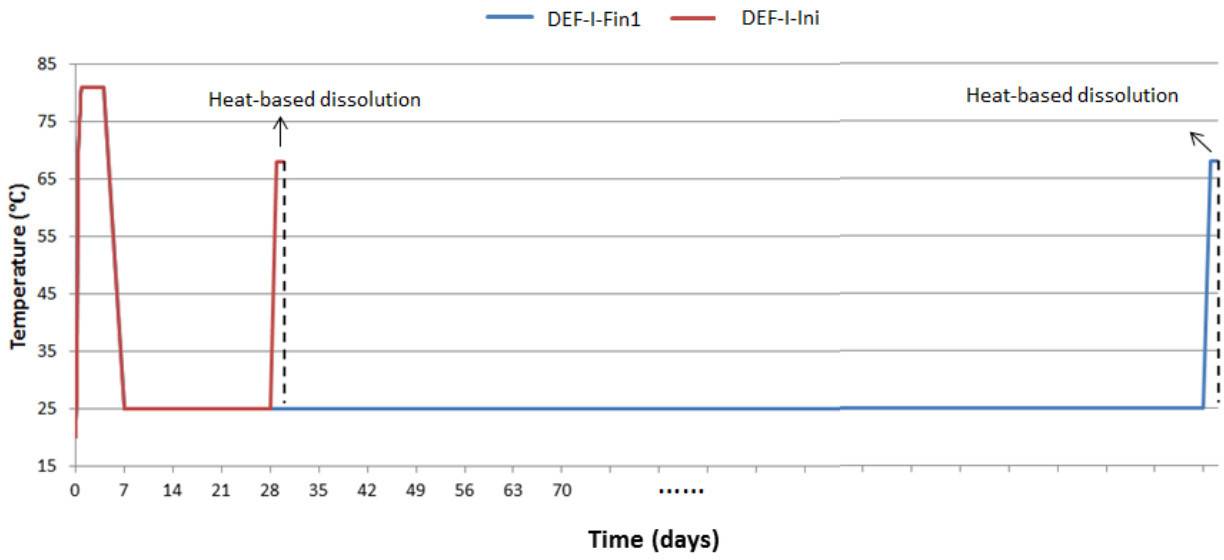

Figure 2.21 – Evolution of heating treatment with time

After the heat-based dissolution, the samples were lyophilized and prepared for MIP tests to obtain the pore size distribution. Firstly, the specimen DEF-I-Ini was heated at 68 °C for 1 day as a reference to study the effect of high temperature on

pore size distribution. Secondly, the DEF-I-Fin1 samples were heated with different temperatures and durations. The heating history of specimens are shown in Fig. 2.21. Then, the pore size distribution will be compared in the pore range where ettringite forms during DEF. As the later results will be analyzed in Chap. 3, the validation of this heat-based dissolution test will be presented in next chapter as well.

2.12 Conclusions

In this chapter, the material used, the specimens designed, and the experimental techniques adopted in this study have been presented. Two kinds of cement paste specimens (CEM I and CEM III) with two sizes ($2 \times 2 \times 12$ cm^3 and $11 \times 11 \times 22$ cm^3) were subjected to different sulfate attack conditions: ESA, DEF and coupling effect of ESA and DEF. The experimental studies included measurements (length and mass variation) and three techniques (MIP, DVS, and WAPT) to characterize the microstructure of cement paste. These techniques were adopted to capture the pore characterization before and after sulfate attacks. With a high reproducibility, MIP was used as a reliable technique to comparatively study the pore structure. Meanwhile, DVS was adopted as well to study the pore size distribution in nano pore range and WVPT was used to study the total porosity of the material. Then, heat-based dissolution tests have been conducted. Its final objective is to characterize how DEF alters the pore structure of the material.

All the experimental results and the corresponding analyses will be presented in the next chapter. The change of pore size distribution before and after sulfate attacks will provide the pore position where ettringite forms under different conditions. Based on these results, a uniform expansion mechanism will be suggested.

3 Experimental results and analyses

In this chapter, the experimental results of the studies on sulfate attacks conducted during this PhD project will be presented and summarized. For samples cast with CEM I, the experimental results include the measurements of mass and length variations, porosity, and pore size distributions deduced from MIP and DVS, porosity measured from water accessible tests, and the pore release after heat-based dissolution tests. All these techniques have been explained, qualified and compared in Chapter 2. The specimens submitted to different exposure conditions will be compared according to observations, mass and length variations, and pore size distributions. Furthermore, the evolution of microstructure will be investigated. Based on the proposed mechanism, a model will be established in Chap. 4 (Poromechanical modeling). As specimens fabricated with CEM III did not show obvious degradation as compared to CEM I specimens, length and mass monitoring, and pore size distribution will be presented only at the initial state.

3.1 Cement I samples

3.1.1 Observations

The specimens were monitored during the sulfate attacks. Fig. 3.1 illustrates a visual monitoring conducted on the specimens.

Firstly, in the case of ESA, a slight crack appeared at the bottom surface after only two months of contact with the sodium sulfate solution, which extended to the side faces later. After around 7 months of testing, the specimens were so damaged that they even could break when measuring the length variations. At that moment, it was supposed that the cement pastes had lost all cohesion and the damage was total. Furthermore, the bending of the specimen started with the appearance of cracks. This suggested that significant tensile stress was the cause for this degradation.

During the monitoring of the DEF specimens, firstly, a rancid odor similar to the smell of sulfur was detected when the specimens were removed from the bath. Secondly, the cracks were observed, but their appearance were much delayed in time, with a lower degree of deterioration compared to ESA. After immersion in water for up to 2 years, the monitoring of the DEF specimen was stopped due to the limited

Figure 3.1 – Observations of a selection of specimens under different sulfate attack conditions (for each attack, the same specimen is observed from different surfaces).

time of the experiment. The DEF specimens had an expansion around 0.5%, with slight cracks on the top and side surfaces. Finally, some whitish powdery material was observed coated on the surfaces of the specimens (not shown in the figure). The occurrence of the powder may be induced by leaching of lime compounds, which leads to the formation of calcium carbonate or calcium sulfate on the surface of the specimens. It may also be caused by sulfate efflorescence. A similar observation was found in the case of ESA with thaumasite formation [262], and the component of the powder was analyzed as either calcium and potassium sulfates or thenardite (Na_2SO_4).

For specimens exposed to the coupling effect of ESA and DEF, the degradation duration was short and the kinetic was fast compared to cases where ESA and DEF act separately. The first cracking appeared after approximately 1 month on the top surface. After immersion in sulfate solution for 2.5 months, the cement paste was totally damaged and the top surface of the specimen was separated into several sections because of the cracks. At the end of the monitoring, the crystals could be clearly seen in the material, especially in the cracks, see Fig. 3.2. Except for ettringite, this crystal formed in the cracks may also be gypsum [11]. From observations, specimens subjected to the coupling effect of ESA and DEF show a more aggressive degradation.

Figure 3.2 – Crystals observation in the cracks of Coupling specimens.

The degradation appeared in all cases, with different degrees of degradation at different ages. In this study, the greatest degree of cracking has been found in coupling specimens, while the DEF specimens showed the smallest degree for the duration of these experiments. The ESA specimens showed an intermediate level of degradation. The degree of cracking is linked to the degree of swelling, which will be presented in the next section. It is easy to understand that the coupling effect of ESA and DEF leads to the worst attacks and the fastest kinetic due to the multiple sources of sulfate ions. The presence of more sulfate ions results in a much larger swelling than in the other cases.

3.1.2 Mass and length variations

First of all, some information should be recalled here: pins were glued on three faces of $2 \times 2 \times 12$ cm^3 specimens as shown in Fig. 3.3, for the reason that the fourth face is not smooth. Fig. 3.4 shows the expansion of CEM I $2 \times 2 \times 12$ cm^3 specimens on each face, which illustrates that the strain on face 2 is very different compared to the other two faces, especially in the case of ESA. This is the consequence of the

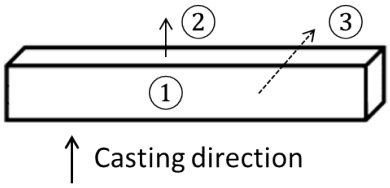

Figure 3.3 – Pins glued on $2 \times 2 \times 12$ cm^3 specimen.

bending of specimens observed above. Therefore, the expansion value on face 2 is not considered when calculating the average expansion of specimens; indeed, since the strain measurement on the fourth face is not available, there is no "balance" of the singular measurement of face 2 (e.g. in the ESA case in Fig. 3.4, strain of face 4 should show a high expansion that would balance the contraction of face 2). The reason for this difference will be discussed in the following section 3.1.3.1 and the expansion of each specimen on each face are shown in Appendix B.

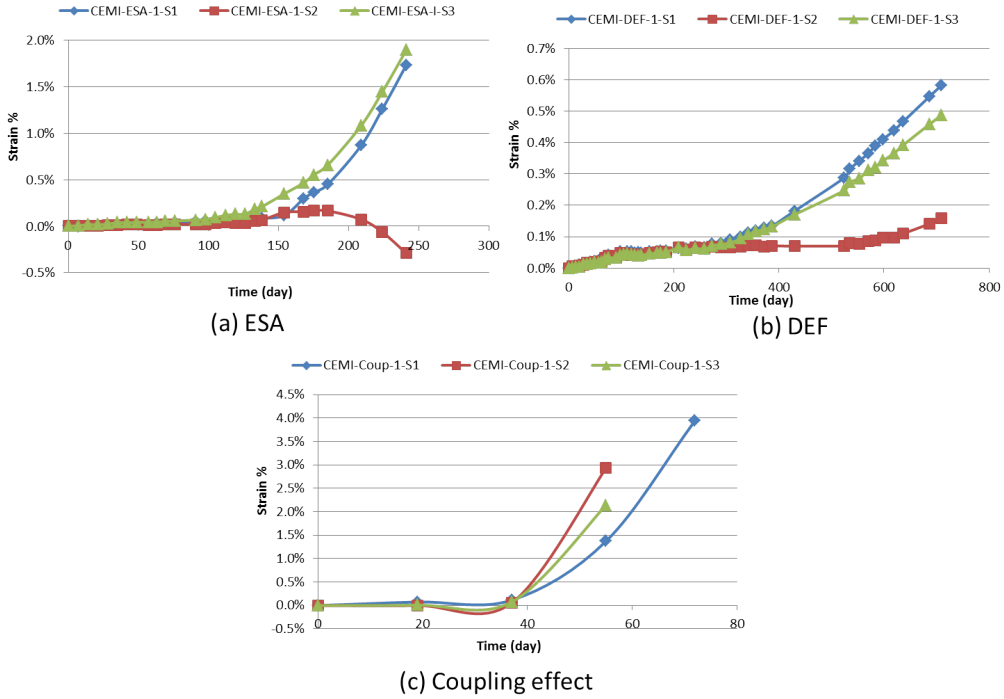

Figure 3.4 – Strain of CEM I $2 \times 2 \times 12$ cm^3 specimens on three faces due to ESA, DEF, and Coupling effect.

Fig. 3.5 shows the average strain of the $2 \times 2 \times 12$ cm^3 specimens under different cases of sulfate attacks. They represent the average values (measurements of faces 1 and 3 represented in Fig. 3.3) of the three specimens belonging to the same set. The error bars correspond to plus/minus the standard deviation. The Coup specimens show

a large standard deviation compared to the other ones, especially at high expansion level, which results from the variable response of materials to damage. The DEF specimens show an average final expansion of 0.5% after two years, which means that the specimens are in the accelerated stage. The coupling specimens show the highest expansion of around 2.7% after 2.5 months, and the DEF specimens show the smallest expansion of 0.5%. This order is consistent with the degree of crackings observed. These differences in kinetics and amplitudes can originate from a greater source of SO_4^{2-} for the coupling effect. In addition, the swelling kinetics of the ESA and Coup specimens tend to increase with time, due to a higher penetration speed of sulfate ions when cracks grow, see Fig. 3.6.

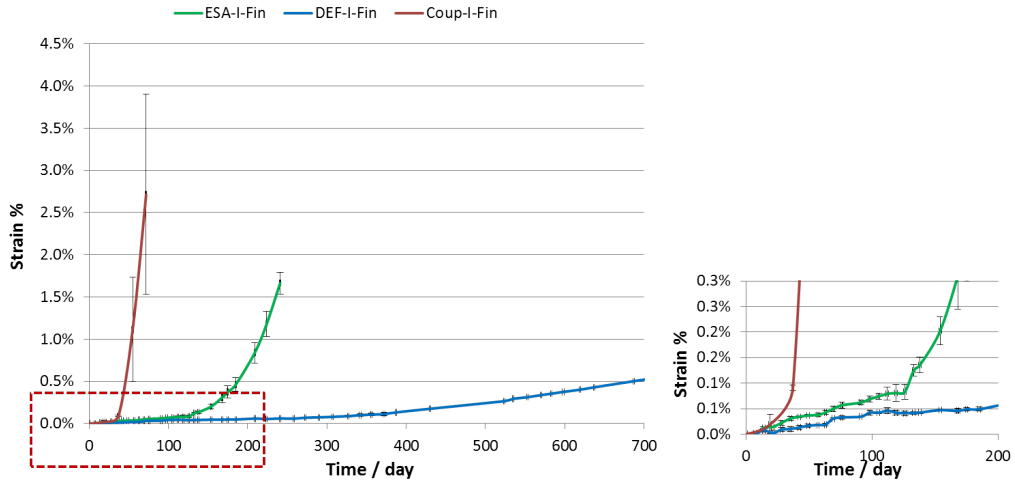

Figure 3.5 – Strain of the $2 \times 2 \times 12$ cm^3 specimens (left: general view; right: zoom).

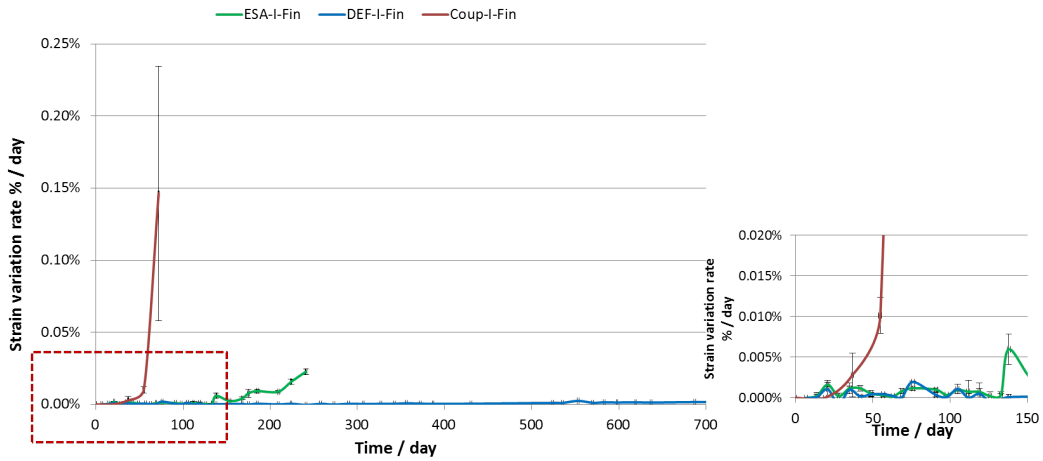

Figure 3.6 – Strain variation rate of the $2 \times 2 \times 12$ cm^3 specimens (left: general view; right: zoom).

As shown in Fig. 3.7, the mass increases with time, and this could be explained

by the penetration of SO_4^{2-}, forming ettringite for ESA and coupling specimens, in addition to water ingress happening for all attack cases considered in this work. The water appears in the pore solution on the one hand, and it interacts chemically to form new products on the other (e.g. a molecule of ettringite contains 32 water molecules).

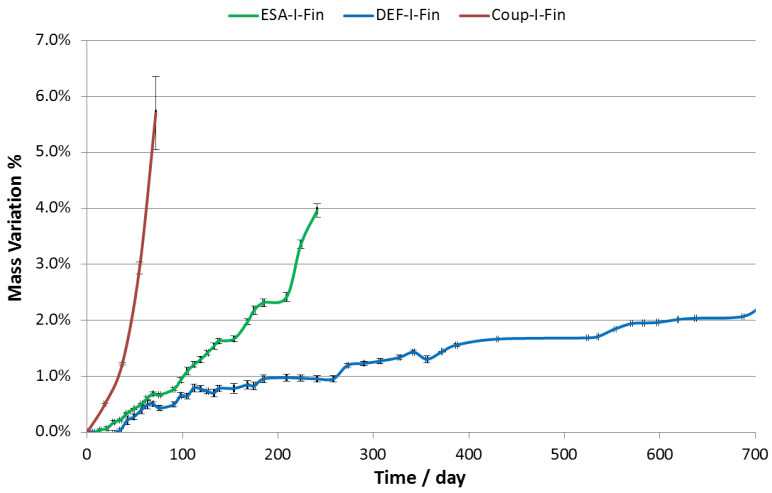

Figure 3.7 – Mass variations of the $2 \times 2 \times 12$ cm^3 specimens.

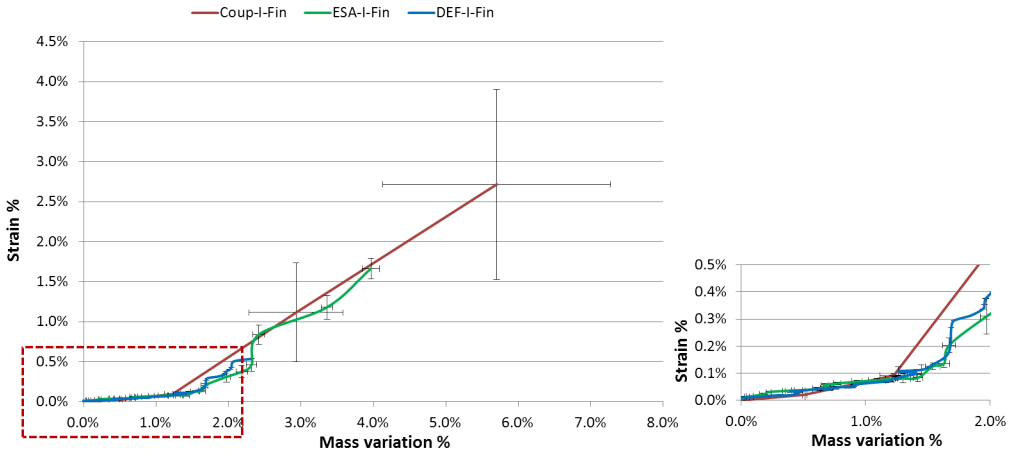

Figure 3.8 – Evolution of the strain as a function of the weight gain of the $2 \times 2 \times 12$ cm^3 specimens (left: general view; right: zoom).

The evolution of the strain as a function of the weight increase is presented in Fig. 3.8. It shows that the two variables are linked by a positive correlation. Within a strain threshold of 0.08%, the correlation showed a similar linear relationship with a slope of around 0.06 for the three cases, when materials were in the elastic stage (see Table 3.1). However, in the following period, this relationship was affected by the type of sulfate attacks. DEF and ESA specimens followed the same route, and

Coup specimen increased with a higher rate. As specimens are in the damaged range when the material is sensitive to the tensile stress, the content of the sulfate ions has a significant effect on the damage behavior of specimens.

Table 3.1 – Regression equations and R^2 coefficients of relationship between strain and mass variation of $2 \times 2 \times 12$ cm^3 within strain of 0.08%.

Specimens	Regression equations	R^2 coefficients
ESA-I-Fin	$y = 0.0574x + 1 \times 10^{-4}$	0.9589
DEF-I-Fin	$y = 0.0526x + 8 \times 10^{-5}$	0.9499
Coup-I-Fin	$y = 0.0627x - 4 \times 10^{-5}$	0.9556

The strain of the $11 \times 11 \times 22$ cm^3 DEF specimens is presented in Fig. 3.9. After 200-day immersion in water, specimen DEF-I-Lat shows an expansion of 0.03 %. Specimen DEF-I-Fin1 presents an expansion of 1.49% after 660 days, and DEF-I-Fin2 approaches to a swelling plateau of approximately 1.22% after 950 days. Some information should be recalled here about the $11 \times 11 \times 22$ cm^3 DEF specimens: the DEF-I-Fin1 and DEF-I-Fin2 were fabricated 1 year before the other two specimens (namely DEF-I-Ini and DEF-I-Lat), see section 2.2. These specimens showed a different swelling kinetic as compared to the newly fabricated DEF-I-Lat even though the materials and w/c were exactly the same. It may be caused by the slightly different fabrication procedures, which possibly led to different microstructures of the materials and resulted in a different response to the swelling. Indeed, DEF-I-Fin1 and DEF-I-Fin2 were cast with a 30-liters concrete mixer while DEF-I-Ini and DEF-I-Lat were cast with a specific mortar mixer; moreover, for each set of specimens, a different mixing procedure was used. This emphasizes the importance to have detailed and strict experimental procedures to ensure results as reproducible as possible.

The comparison of the strain between $2 \times 2 \times 12$ cm^3 and $11 \times 11 \times 22$ cm^3 DEF specimens is presented in Fig. 3.10. It is shown that the new fabricated $11 \times 11 \times 22$ cm^3 specimen (DEF-I-Lat) follows a similar swelling curve (at least at the beginning) as the $2 \times 2 \times 12$ cm^3 specimen. It further confirms that the different kinetics between the DEF $11 \times 11 \times 22$ cm^3 specimens could be induced by different fabrication procedures and not by the shape of the specimens. This excludes any explanation of the different swelling behavior based on different alkali and/or calcium leaching regimes.

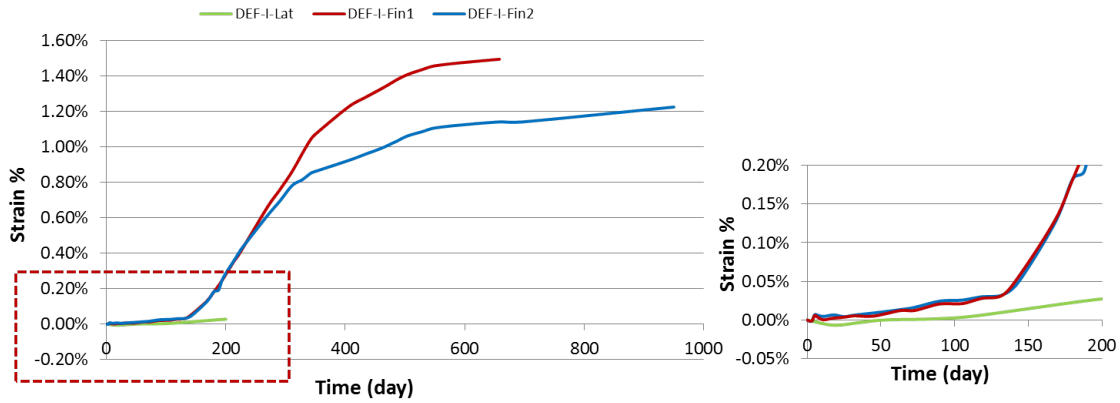

Figure 3.9 – Strain of the $11 \times 11 \times 22$ cm^3 DEF specimens.

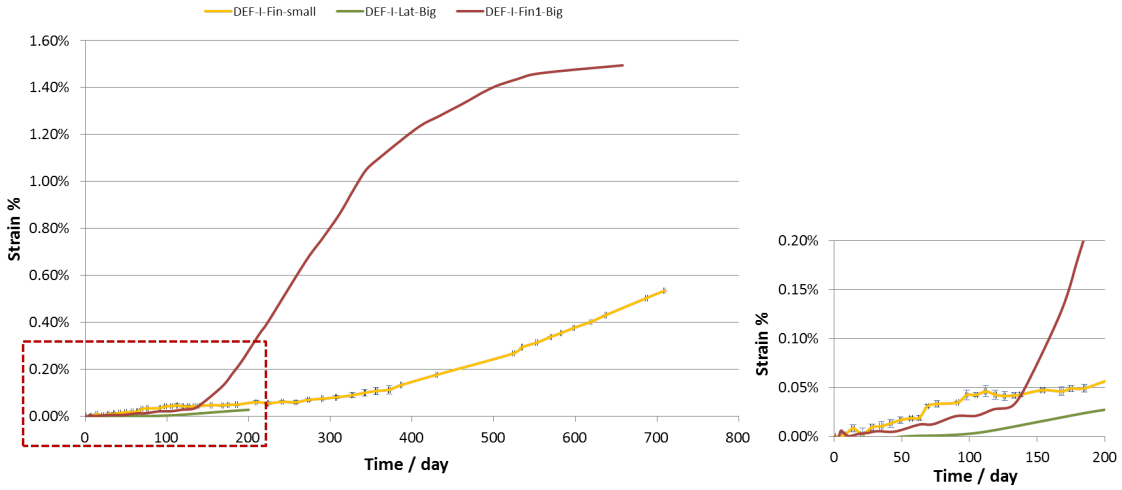

Figure 3.10 – Comparison of the strain between $2 \times 2 \times 12$ cm^3 and $11 \times 11 \times 22$ cm^3 DEF specimens (left: general view; right: zom).

3.1.3 Pore size distribution of $2 \times 2 \times 12$ cm^3 specimens

In portland cement, the main hydrate phases are portlandite and C-S-H which occupy different pore sizes. The pores in hardened cement paste are divided into gel and capillary pores, and the classification of the pores has been discussed in section 1.2.1. The dissolution of CH and the decalcification of C-S-H during the leaching leads to pore release, while pore ranges derived from CH or C-S-H are not identified by scholars, see 1.3. However, the change in pore size distribution caused by the dissolution of portlandite can be distinguished from the one in C-S-H. Therefore, it is assumed that the increase of pore volume with respect to pores between 10 nm and 1 μm is due to the dissolution of CH, and that the increase of pores with diameters less than 10 nm is related to the decalcification of C-S-H [13, 14, 15, 89].

During sulfate attacks, the generated crystals may be ettringite or gypsum, which could not be differentiated in this study. However, the formation of ettringite is believed to be the reason for expansion, which has been discussed in sections 1.2.2.2 and 1.2.3.2.

The evolution of the pore size distribution involves several processes, such as ettringite formation, dissolution of CH, decalcification of C-S-H, and growth of cracks. The resulting pore volume variation is determined by the kinetics/balance of these processes. For example, if the increased pore volume (δV_1) induced by cracks is higher than the absolutely decreased one (δV_2) due to ettringite formation, the accumulated pore volume ($\delta V_1 - \delta V_2$) shows an increase, which means that the total pore volume in this range increases. Conversely, the pore volume in a given range decreases if (δV_2) is higher than (δV_1). This is an important point that should be taken into account when analyzing the variation of pore size distribution in the following sections.

3.1.3.1 Pore size distribution of $2 \times 2 \times 12$ cm^3 specimens measured by MIP

First, the slicing scheme of $2 \times 2 \times 12$ cm^3 specimens is recalled here, see Fig. 3.11. The pore size distribution of the $2 \times 2 \times 12$ cm^3 specimens measured from MIP tests are presented in Fig. 3.12. It comprises a pore range between 3.7 nm to 400 μm. In this figure, the pore size distribution of the samples at different exposure conditions (ESA, DEF and coupling effect), different states (initial and final state), and different layers (surface and core layer) are presented.

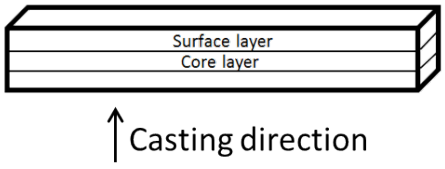

Figure 3.11 – Slicing scheme for $2 \times 2 \times 12$ cm^3 specimens.

Fig. 3.12(a) presents the pore size distribution of the $2 \times 2 \times 12$ cm^3 specimens exposed to ESA. First of all, the initial sample shows similar pore characteristics at different layers, which indicates a homogeneous material after the curing. Then, this figure shows that the pore volume with diameters between 3.7 and 50 nm decreases after the ESA. The ettringite which leads to expansion was found to form in the

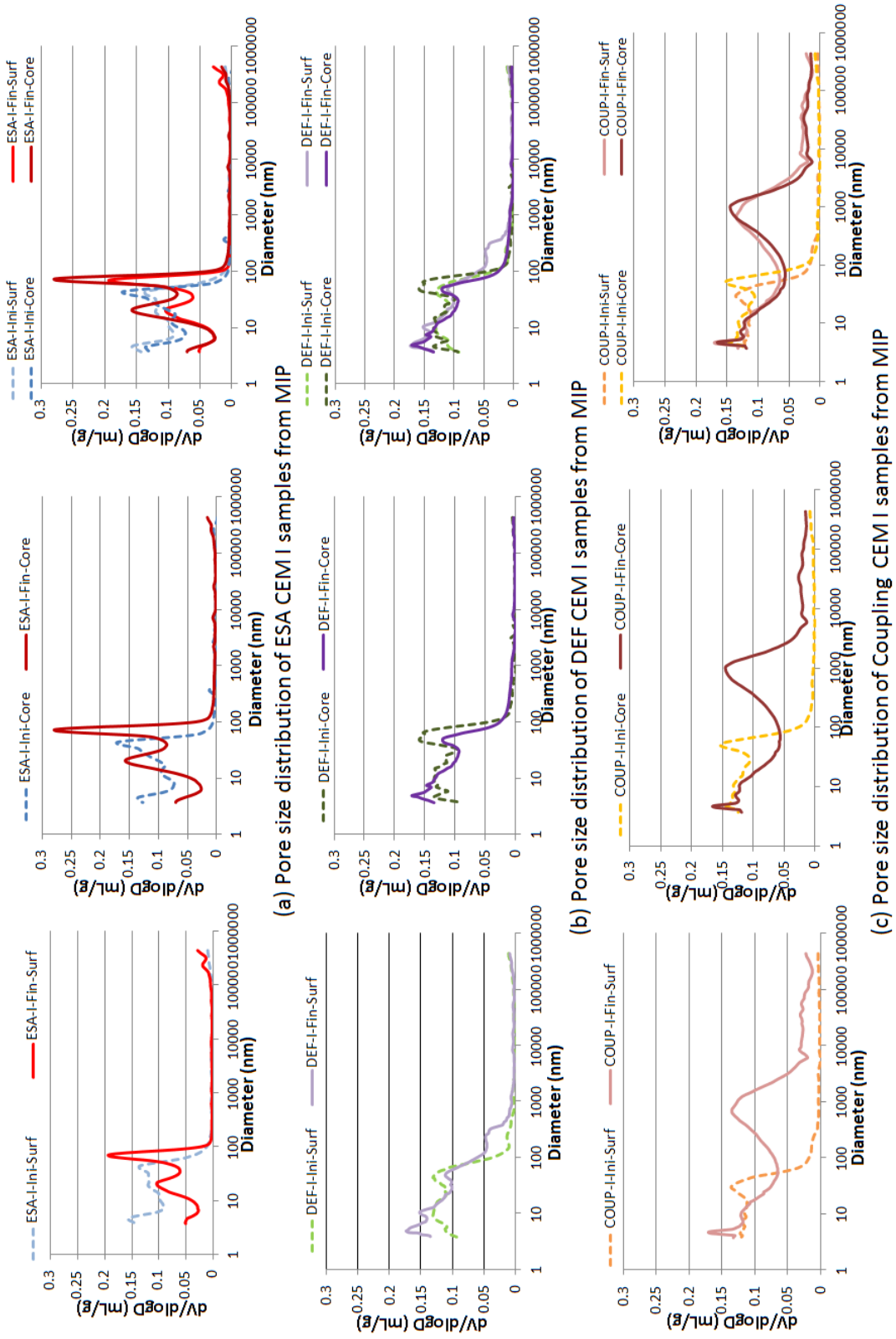

Figure 3.12 – Pore size distribution of (a) ESA-I samples; (b) DEF-I samples; and (c) Coup-I samples measured from MIP.

pores less than 0.1 μm in the literature [11]. This results in a decrease of pore volume which is consistent with the results illustrated in figure 3.12. Therefore, it is supposed that the main generated crystal is ettringite [36, 40, 41], which forms in the gel and capillary pores after the ESA. The decrease of pore volume with diameters between 3.7 and 50 nm is observed in the surface layer, and a smaller decrease with respect to pores in the range of 3.7-13 nm and 27-51 nm at the core layer. It is due to the fact that more sulfate ions penetrated from the exterior solution and results in formation of more ettringite in the surface layer. Yu found that almost all the AFm was transformed into ettringite at the surface layer, while the core layer was not sulfate attacked (specimen size $40 \times 40 \times 160$ mm^3) [11]. Furthermore, in the present work, an increase of pore volume at pores approximately 100 nm is observed. This can be explained by the dissolution of CH (see section 1.3), and the formation of microcracks due to expansion. The dissolution of CH provides a high source of calcium during the ESA [263]. Normally, microcracks focus in a pore range of a few microns, while the smallest size of a microcrack opening that could be detected is around 0.1 - 0.25 μm in [264].

Fig. 3.12(b) presents the pore size distribution of the $2 \times 2 \times 12$ cm^3 specimens exposed to DEF. First of all, the comparison of the initial pore size distribution at different layers shows that the curves are similar but the core layer shows a higher pore volume at the range of 40-100 nm. The pore volume in this range corresponds to the spaces where hydration products (mainly CH) exist [265]. Thereby, the higher pore volume at the core layer may be attributed to a lower degree of hydration. Further, a decrease of pore volume in the pore range of 9.7-100 nm is shown in the figure. It means that the pore volume filled by the generated crystals is larger than the one that may be created by the dissolution of CH. This indicates the formation of crystals in the pores between 9.7-100 nm. The crystals may form in smaller pores as well, while the corresponding decreased pore volume is balanced by the increased pore volume due to decalcification of C-S-H for example. As ettringite is believed to be the reason for expansion, then the precipitated crystal is supposed to be ettringite. However, the ettringite was postulated to initially occur in C-S-H gel corresponding to a pore size of 10 nm and then in cracks and voids [91, 100, 210], which is not consistent with the results obtained in this study. The results presented in Fig. 3.12(b) come from a $2 \times 2 \times 12$ cm^3 DEF specimen which has an expansion of 0.5%. Consequently, a question remains: will AFt continue to form in smaller pores when the expansion gets higher? This question will be answered in the next section while analyzing the experimental results of $11 \times 11 \times 22$ cm^3 DEF specimens. An

increase of pore volume between 3.7 and 9.7 nm is observed in this figure as well. This should be attributed to the decalcification of C-S-H. In addition, the surface layer shows an increase of pore volume between 100 nm and 1 μm, which is due to the dissolution of CH and to microcracks, as explained in the case of ESA.

Fig. 3.12(c) presents the pore size distribution of $2 \times 2 \times 12$ cm^3 specimens exposed to coupling effect of ESA and DEF. The initial state of the material at different layers show a similar pore size distribution except for a pore range between 40 and 100 nm. The core layer shows a larger pore volume around 100 nm, which should be attributed to a smaller degree of hydration. From the comparison of pore size distribution before and after degradation, it can be concluded that pore volume between 5.3 and 80 nm decreases. A huge space is released in pores with diameter larger than 80 nm. It is due to the dissolution of CH and the occurrence of microcracks, which is also seen in the pores of less than 5.3 nm induced by the decalcification of C-S-H. Compared to the other two cases, a much higher pore space is freed in the pores larger than 1 μm. This is related to the occurrence of cracks which results from a worst degradation. After the degradation, the coupling samples show a more homogeneous pore size distribution at different layers, which is attributed to the high diffusion [221] after a high degree of deteriorations.

The comparison of pore size distribution of samples among different exposure conditions is presented in Fig. 3.13. Firstly, in Fig. 3.13(a), the initial pore size distribution of DEF and Coup specimens show a larger pore volume between 5-19 nm at the surface layer and between 5-22 nm at the core layer compared to ESA specimens [151]. One reason is that the decomposition of primary ettringite during the preheating treatment [91, 92, 93] results in an increase of pore volume. Another reason is that the high temperature helps mineral ions (e.g. Al and Fe) to migrate from the reaction sites of anhydrous phases into the inner product in the C-S-H [151] chemically or physically, which further enhances the porosity in this range.

In addition, the porosity of initial $2 \times 2 \times 12$ cm^3 specimens (after curing) at the surface and core layers are summarized in Table 3.2. A porosity difference is found along the depths, even though in different trend when specimens were preheated or not. After the heating treatment, a lower porosity is observed at the surface layer, which was in contact with the bottom of the moulds during the heating treatment. A porosity gradient from the upper-water face to the lower was reported in [146], which was explained to be due to the higher effective W/C ratio at the upper-water surface and the vertical vibration process. Conversely, ESA-I-Ini shows a higher

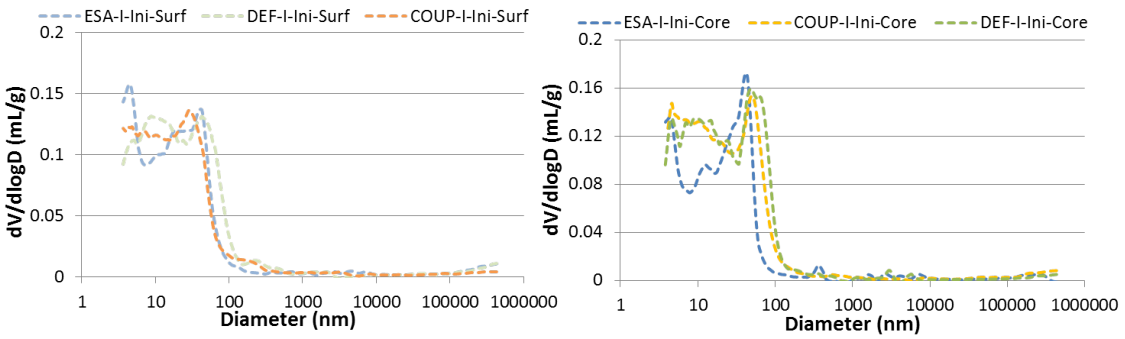

(a) Comparison of pore size distribution of initial samples.

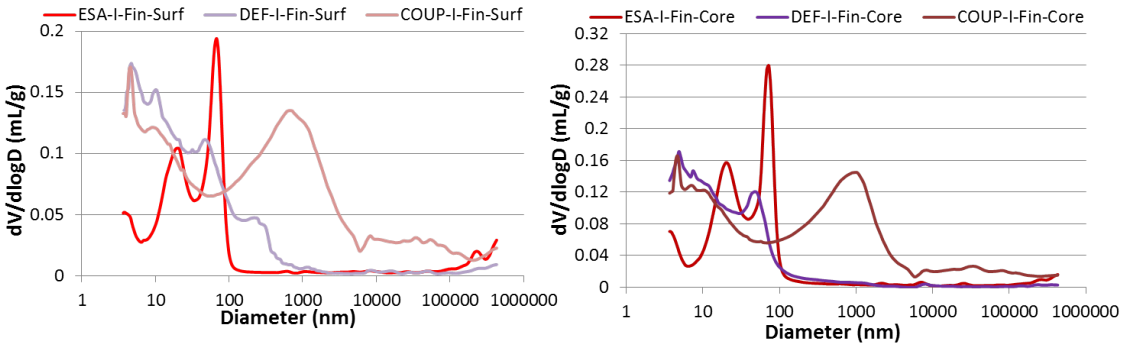

(b) Comparison of pore size distribution of final samples.

Figure 3.13 – Comparison of pore size distribution of samples from MIP.

porosity at the surface layer. A low porosity has a positive effect to resist sulfate attack from the aspects of low diffusion of aggressive ions from exterior solution and strong mechanical properties, and meanwhile a negative effect due to low space to accommodate expansive products. In this study, the low porosity presents a negative effect consistently in the case of Coupling effect and ESA. This explains the observed bending of specimens (see section 3.1.1), and the different gradients of porosity in ESA and Coup lead to the downward and upward bending, respectively. However, the bending did not happen in the case of DEF, which is probably due to a limited expansion of 0.5%.

Table 3.2 – Porosity of initial $2 \times 2 \times 12$ cm^3 at surface and core layers

	ESA-I-Ini	DEF-I-Ini	Coup-I-Ini
Surface layer	25.87%	28.23%	25.52%
Core layer	23.39%	29.58%	26.42%

Secondly, the final pore size distributions of specimens are affected by exposure conditions. In the pore range of 3.7-50 nm at the surface layer and between 3.7-20 nm at the core layer, ESA samples show more reduced pore volume than the other two

cases, and the coupling samples show a similar pore size distribution as DEF samples in this range. Although provided with more sulfate ions from the aggressive solution in the case of coupling effect, ettringite preferentially precipitates in the cracks that appeared soon after the immersion, which leads to a further degradation, as observed in Fig. 3.2. A similar situation was found in the case of ESA, Nielsen found that the ettringite existed in cracks after stored in the sodium sulfate solution. It appeared to have been deposited after the crack had been formed [266]. In addition, this crystal formed in the cracks may also be gypsum [11].

The variations of the pore volume in different pore ranges at the core layer are summarized in Fig. 3.14. The pores are categorized according to the variation of pore volume after the attacks. First, the figure illustrates the pore range where the pore volume is decreased. For example, the decreased pore volume distributes between 3.7-50 nm for ESA-I-Core, and 9.7-100 nm in the case of DEF-I-Core. For Coup-I-Core, the occupied pores are between 5.3-80 nm. These pore ranges are consistently within the capillary and gel pores. Then, the figure illustrates increased pore volumes mainly above 80 nm, which results from the dissolution of portlandite and the occurrence of microcracks. Therefore, a first conclusion can be drawn according to the results of $2 \times 2 \times 12$ cm^3 specimens that: **Ettringite is found to be formed in capillary and gel pores both in the case of ESA and Coup, while mainly in capillary pores for DEF which has limited expansion of 0.5%.**

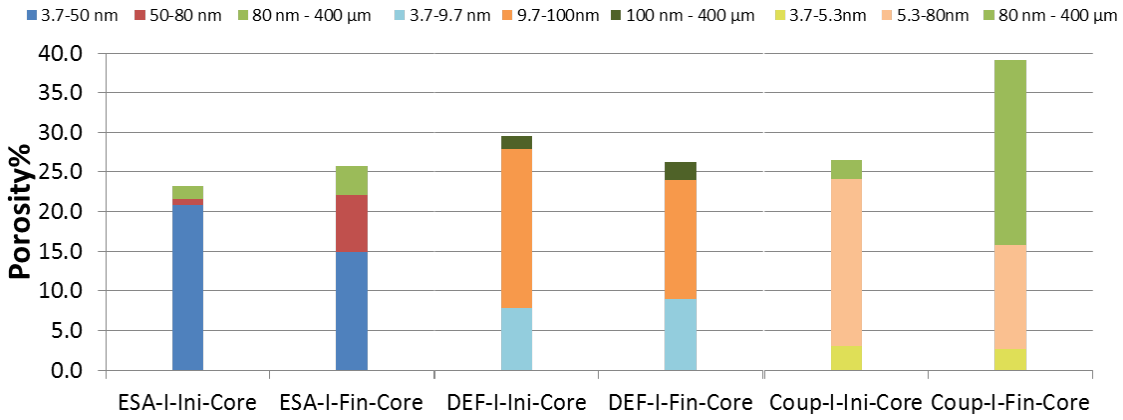

Figure 3.14 – Variation of the pore volume in different pore ranges.

3.1.3.2 Pore size distribution deduced from WVSI

First of all, the initial pore size distributions of ESA-I-Ini-Core and DEF-I-Ini-Core samples deduced from WVSI in the range of 0.3-10 nm in radius are shown in Fig. 3.15. The ESA-I-Ini-Core sample shows a higher pore volume with respect to pores between 2 and 4 nm than DEF-I-Ini-Core sample, which means that the high temperature leads to a lower porosity in this range. Kjellsen reported that the C-S-H inner product of the pastes cured at 50 °C are much denser than the corresponding phase in paste cured at 5 °C possibly due to the closer mixing of CH with the C-S-H [151]. In addition, the adsorption of ions on C-S-H contributes to a decrease of pore volume in C-S-H gels.

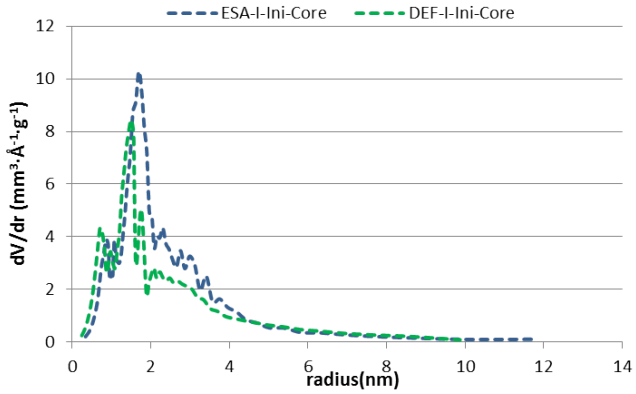

Figure 3.15 – Pore size distribution of the initial ESA and DEF samples deduced from DVS.

Fig. 3.16 illustrates the pore size distribution of cement pastes exposed to different exposure conditions between 0.3 and 10 nm in radius deduced from WVSI. It is shown that pores between 2 and 6 nm in radius show a higher volume after the attacks, which happens in all three cases but to a different extent. As explained at the beginning of this section, the decalcification of C-S-H contributes to an increase of pore volume. In the case of ESA and Coup, the unlimited provision of sulfate ions to form ettringite which consumes the calcium ions will facilitate the dissolution of C-S-H [81] and result in more release of pore volume. However, it is not consistent with the results in this study. Although exposed to the sodium sulfate solution, Coup-I shows a smaller increase of pore volume, see Fig. 3.16(c). It means that some product is formed accompanying the dissolution of C-S-H. The occurrence of ettringite during sulfate attacks has been explained a lot in section 1.2.2.2 and 1.2.3.2. Therefore, it is concluded that ettringite forms in these pores, even though the final pore volume increases. A similar case happens for ESA-I. A quantitative

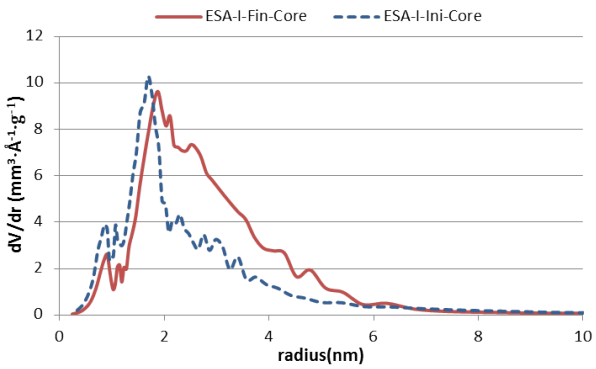

(a) Pore size distribution of ESA from DVS

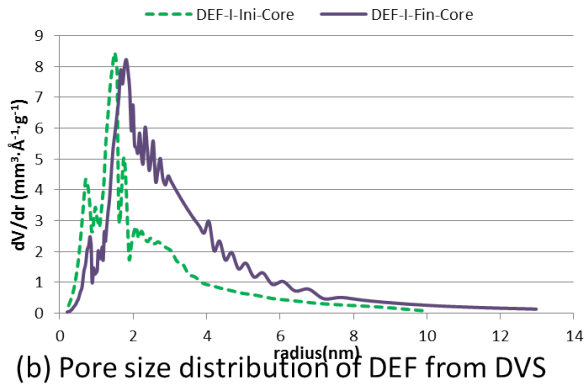

(b) Pore size distribution of DEF from DVS

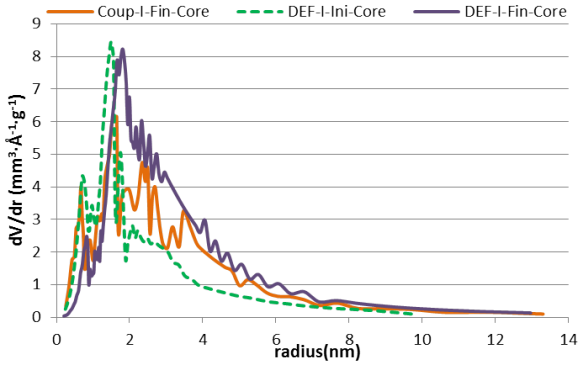

(C) Pore size distribution of Coupling from DVS

Figure 3.16 – Pore size distribution of the samples deduced from DVS.

comparison of total pore volume increase in this range is shown in Table 3.3. It presents the change of pore volume per gram after the degradation in the three attacks considered in this work. A much smaller increase of pore volume is found in the case of ESA-I and Coup-I, compared to DEF-I, which confirms that ettringite forms in the gel pore range when exposed to sulfate solutions. Coup-I shows a smaller increase rate of 21% compared to ESA-I with 33%, which means that less ettringite is formed in the case of Coup-I. This finding is consistent with the results in Fig. 3.13 that even with more sulfate ions provided by the aggressive solution, ettringite

Table 3.3 – Pore volume ranging between 0.3 and 10 nm per gram measured by DVS

Samples	Initial pore volume per gram (mL/g)	Final pore volume per gram (mL/g)	Increase ratio
ESA-I	163	217	↑ 33%
DEF-I	138	208	↑ 50.7%
Coup-I	138	167	↑ 21%

preferentially precipitates in the cracks that appeared soon after the immersion and results in a further degradation. As for DEF-I, it is difficult to conclude whether ettringite precipitates in the gel pores from these results.

3.1.3.3 Subconclusions

By analyzing the pore size distribution change of $2 \times 2 \times 12$ cm^3 specimens subjected to ESA and Coupling effect, it is concluded that ettringite forms both in the capillary and gel pores. For the $2 \times 2 \times 12$ cm^3 DEF specimens, the presence of ettringite is confirmed mainly in the capillary pores with a limited expansion of 0.5%. Meanwhile, the ettringite tends to precipitate in the new generated large voids, for example, microcracks. It further confirms that the ettringite formed in the cracks is not the reason for expansion [39], but that it could nonetheless lead to a greater level of degradation where it already happened.

3.1.4 Pore size distribution of $11 \times 11 \times 22$ cm^3 specimens

3.1.4.1 Pore size distributions along the depths of $11 \times 11 \times 22$ cm^3 specimens

According to the analyses of the $2 \times 2 \times 12$ cm^3 DEF specimens with an expansion of 0.5% after two years, it was concluded that ettringite mainly formed in the capillary pores. Then, two questions were proposed. The first one was whether the AFt would precipitate in smaller gel pores when the expansion continued. Another question was how did the pore size distribution evolve during the process of DEF for higher expansions. These two questions will be analyzed in this section.

The initiation of ESA is affected by the transport of sulfate ions to the cement

matrix and leaching of calcium ions. The transport of sulfate ions in the case of ESA has been well studied in the literature, including the measurement of the quantity of sulfate consumed from the bath solution [33, 267] and the measurement of the amount of sulfate in the cement matrix based on the profile method [32, 33, 36, 267, 268]. The results show a positive correlation between the quantity of penetrating sulfate ions and the distance from the surface. However, few studies were performed about DEF. In this section, the pore size distributions along the depths of $11 \times 11 \times 22$ cm^3 specimens subjected to DEF are presented.

For a better understanding of the results, the slicing plan for $11 \times 11 \times 22$ cm^3 specimens is recalled in Fig. 3.17. One must remind here that the DEF-I-Ini and DEF-I-Lat specimens were not cast in the same batch as DEF-I-Fin1 and DEF-I-Fin2 which may induce a difference of microstructure as presented in the previous section. This could have an impact on the analyses presented hereafter though this aspect was bared in mind; moreover, the microstructure change between the two castings of specimens was believed to be limited enough to allow comparison of the results of the corresponding parameters.

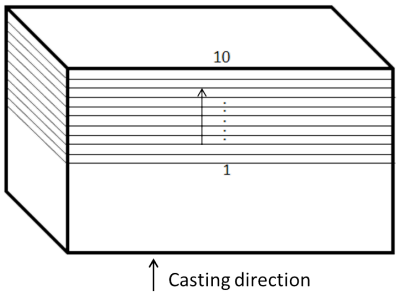

Figure 3.17 – The slicing plan for $11 \times 11 \times 22$ cm^3 specimen (layer 1 will also be denoted as core layer).

Fig. 3.18 shows the pore size distribution along the depths at the initial state. It is shown that the pore size distribution at different layers are of a similar shape with small differences. Two main peaks are shown in each pore size distribution curve where the major pore volumes are, the first one is close to 10 nm, and another one is located approximately at 100 nm. The first peak moves from 5 nm to 14 nm along the core to the surface, while the second peak stays at the same pore size with a lower amplitude once again from the core to the surface. The higher amplitude could be explained by a lower degree of hydration at the core. Fig. 3.19 (obtained by integrating the results of fig. 3.18 over the pore size range) illustrates a similar total pore volume and the pore volume in three pore ranges along the depths at the

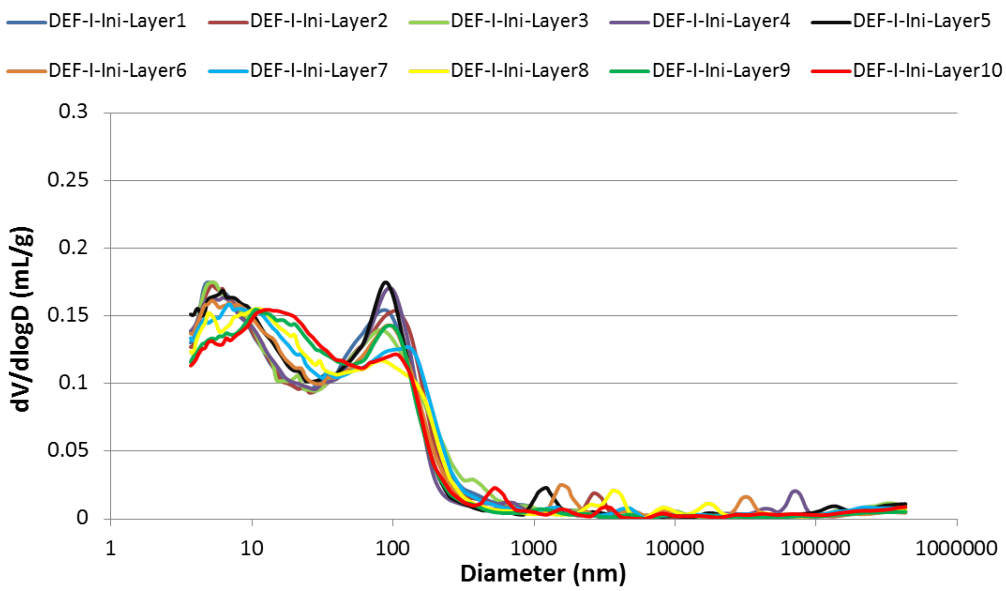

Figure 3.18 – Pore size distribution of the samples along the depths at the initial state from MIP.

initial state. In addition to the similar pore size distribution along the depths, it is concluded that the DEF $11 \times 11 \times 22$ cm^3 specimen was fabricated homogeneously.

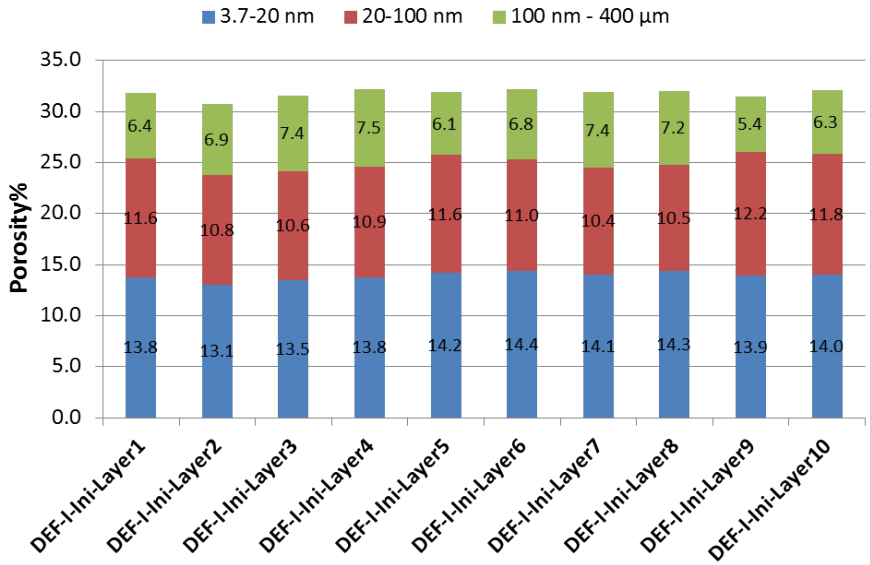

Figure 3.19 – Pore volume in different pore ranges of the $11 \times 11 \times 22$ cm^3 DEF specimen along the depths at the initial state from MIP.

Fig. 3.20 and 3.21 present the pore size distribution and pore volume along the depths of the specimen at the latent period with an expansion of 0.03%. The pore volume in the range 100 nm - 400 μm gradually increases from the core to the surface,

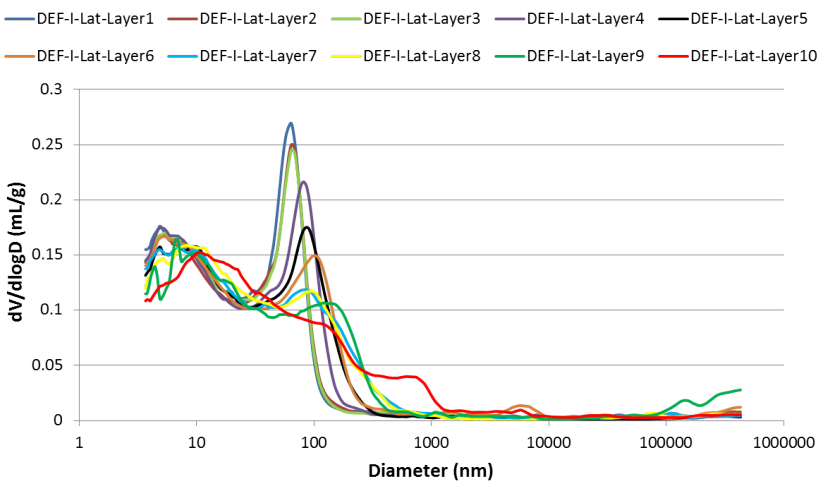

Figure 3.20 – Pore size distribution of the 11 × 11 × 22 cm^3 DEF specimen along the depths at the latent state from MIP.

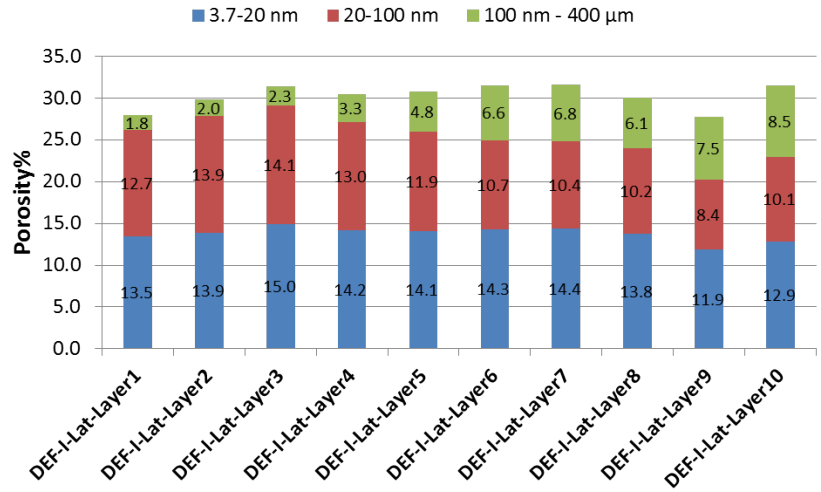

Figure 3.21 – Pore volume in different pore ranges of the 11 × 11 × 22 cm^3 DEF specimen along the depths at the latent state from MIP.

which includes the pore range corresponding to the dissolution of CH. It suggests that the surface layer is largely affected by the leaching process compared to the core layer. Therefore, studying the generation of crystals at the core layer is a better choice, which can limit the influence of calcium leaching in the interpretations.

Fig. 3.22, Fig. 3.23, Fig. 3.24, and 3.25 show the pore size distribution and pore volume along the depths at final state (specimen DEF-I-Fin1 with an expansion of 1.49% and DEF-I-Fin2 with an expansion of 1.22%). It is shown that at the final state, the first two peaks move to smaller pore size with lower valleys in the curve

along the depth from surface to core layer due to the formation of crystals, and a third peak (around 1000 nm) occurs with a high amplitude on the surface layer. This is because at the surface layer, the leaching phenomenon and microcrackings are the most serious and results in the most increase of pore volume.

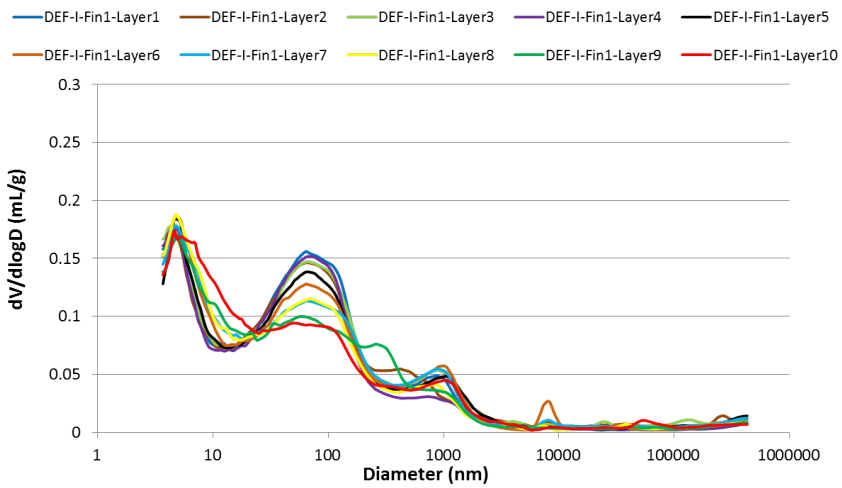

Figure 3.22 – Pore size distribution of the $11 \times 11 \times 22$ cm^3 DEF-I-Fin1 specimen along the depths at the final state from MIP.

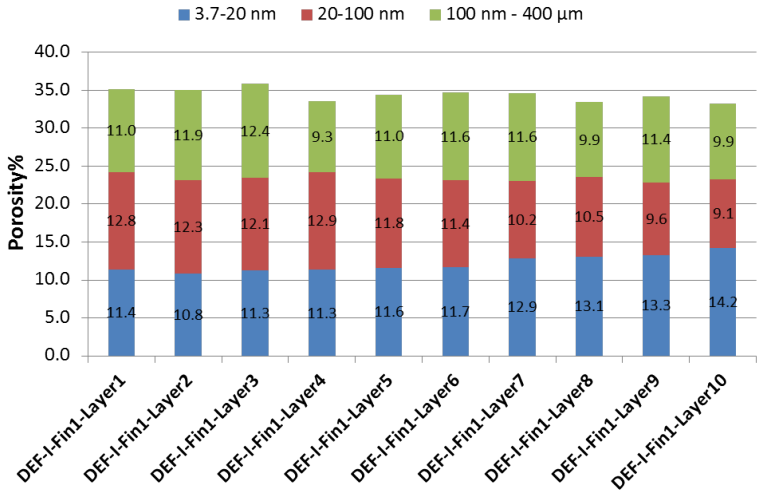

Figure 3.23 – Pore volume in different pore ranges of the $11 \times 11 \times 22$ cm^3 DEF-I-Fin1 specimen along the depths at the final state from MIP.

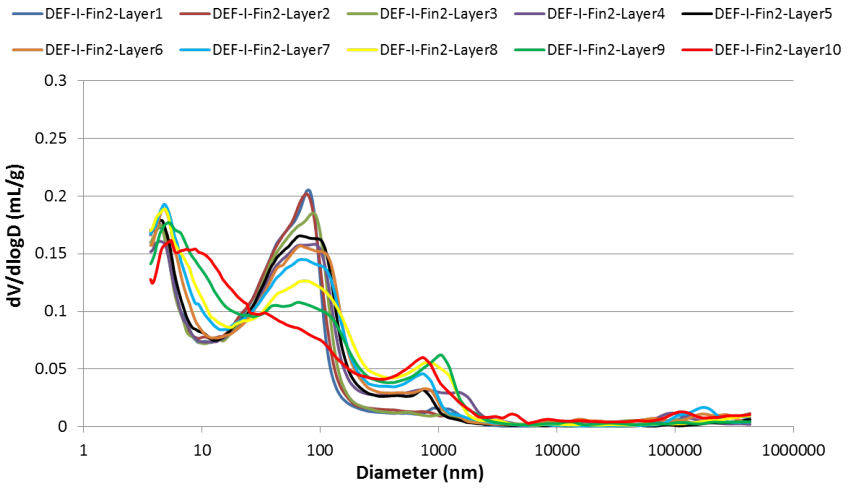

Figure 3.24 – Pore size distribution of the 11 × 11 × 22 cm^3 DEF-I-Fin2 specimen along the depths at the final state from MIP.

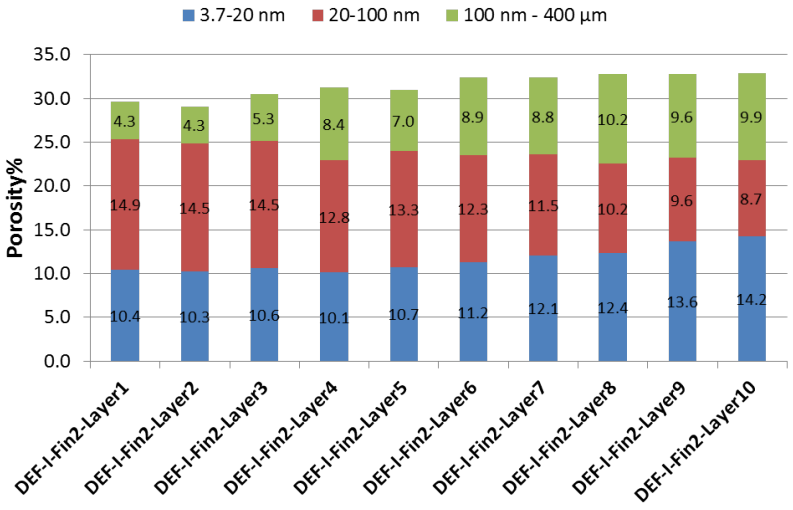

Figure 3.25 – Pore volume in different pore ranges of the 11×11×22 cm^3 DEF-I-Fin2 specimen along the depths at the final state from MIP.

3.1.4.2 Evolution of pore size distribution of $11 \times 11 \times 22$ cm^3 DEF specimens

Analysis of the expansive mechanism in the core layer The evolution of the pore size distribution of the DEF samples in the core layer is presented in Fig. 3.26. This layer has been selected because of the limited effect of calcium leaching in the core of the $11 \times 11 \times 22$ cm^3 specimens. The comparison of the DEF-I-Ini-Layer1 and DEF-I-Lat-Layer1 (expansion of 0.03%) shows that pores between 100 nm and 1 μm are filled (thus, even if voids have been created in this range, the volume of ettringite formed was higher), while pores between 10 and 100 nm are released after a 200-day immersion in water (thus, even if crystals are precipitating in this range, the volume of pores formed was higher). When the specimen DEF-I-Fin1 reaches an expansion degree of 1.49%, pores between 4 and 80 nm are occupied compared to the specimen in latent state, and pores larger than 80 nm are released. In parallel, when the specimen DEF-I-Fin2 reaches an expansion degree of 1.22%, pore volume between 3.7-20 nm and 45-75 nm is decreased after the latent state, and increased with pores larger than 75 nm. If specimen DEF-I-Fin2 is compared to DEF-I-Ini, the conclusion would be that after DEF, the pore volume of pores between 4-20 nm and 100 nm - 1 μm is decreased, while pore volume between 20-100 nm is increased. During the DEF, the pore volume in pores between 4-20 nm tends to decrease while pore volume evolution with respect to pores larger than 20 nm is variable. The latter phenomenon depends on complicated processes, including the dissolution of CH, ettringite formation and occurrence of cracks.

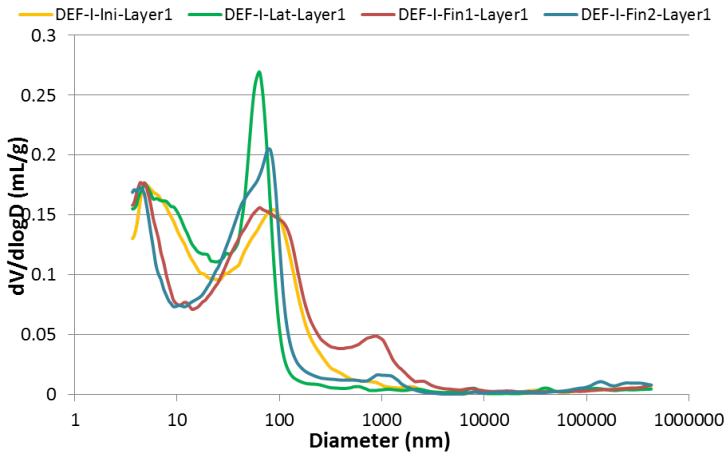

Figure 3.26 – Evolution of the pore size distribution of $11 \times 11 \times 22$ cm^3 DEF specimen from MIP at the core layer.

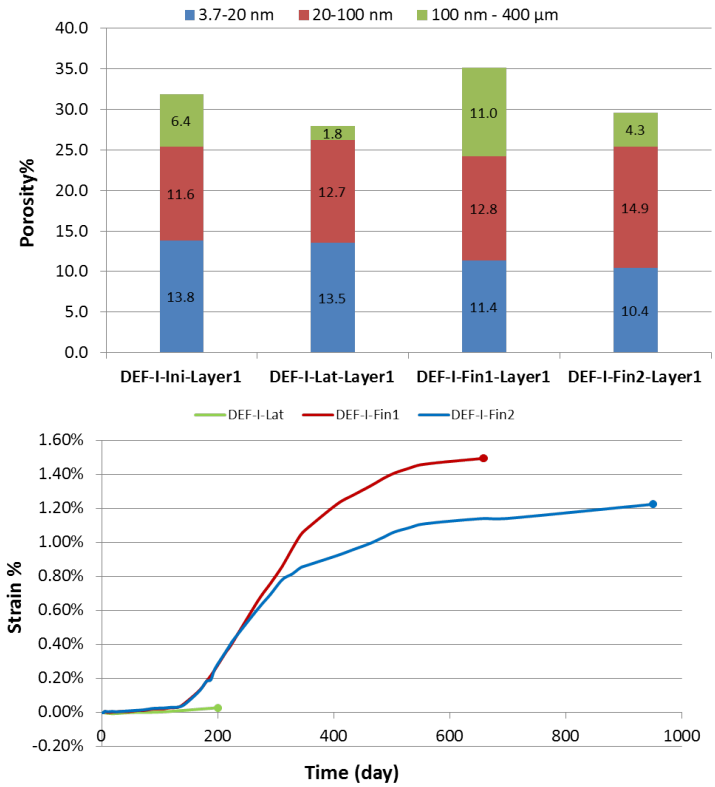

Figure 3.27 – Evolution of the pore volume in different pore ranges of $11 \times 11 \times 22$ cm^3 DEF specimen from MIP at the core layer and the recall of expansion curves.

To easily and better understand the evolution of pore structure of $11 \times 11 \times 22$ cm^3 DEF specimens, the pores are categorized into: 3.7-20 nm, 20-100 nm, and 100 nm - 400 μm based on the variations of pore size distribution which have been discussed above. Fig. 3.27 illustrates the evolution of pore volume in each category at the core layer during DEF. Firstly, compared to DEF-I-Ini-Layer1, DEF-I-Lat-Layer1 shows an obvious decrease of pore volume in the range of 100 nm - 400 μm and an increase of pore volume in the range of 20-100 nm, with the total porosity decreasing from 31.86% to 27.96%. It could be explained by the fact that calcium released from the dissolution of CH and the decalcification of C-S-H in the range of 3.7-100 nm reacts with available aluminium and sulfate ions to form ettringite, which forms in the range of 100 nm - 400 μm. However, the generated crystals in these voids do not lead to a major expansion based on the macroscopic expansion measurements. Then, in the sample DEF-I-Fin1-Layer1, a decrease of pore volume in the pores 3.7-20 nm and an increase of pore volume in the range of 100 nm - 400 μm are observed, as well as a constant pore volume in the range of 20-100 nm. The constant pore volume in red part does not mean that no crystals are generated, but a balanced process occurs between the dissolution of CH and the

precipitation of the generated crystals. In addition to a decrease of pore volume in blue part, it is concluded that the generated crystal is penetrating through the pores between 100 nm - 400 μm into smaller pores compared to DEF-I-Lat-Layer1, which corresponds to expansion. A similar phenomenon of decrease in blue part can be observed as well on sepecimen DEF-I-Fin2-Layer1, while in the red part, the pore volume released by the dissolution of CH is higher than the one occupied by generated crystals. Among these generated crystals, some may form without generating any expansion. Even though it is difficult to separate the expansive crystals from the harmless ones, it is sure that at least part of the generated crystals are the reason for expansion. Moreover, the increased pore volume with respect to pores between 100 nm - 400 μm should be attributed to the dissolution of CH and the occurrence of microcracks. In addition, the generated crystals may precipitate in newly generated cracks as well, but with a weak ability to stop the pore volume increasing. The difference on expansion degree of two final specimens may come from the different total porosity (35.16% for DEF-I-Fin1 and 29.62% for DEF-I-Fin2), if the initial porosity is assumed to be the same. To be more specific, a relatively lower occupation of generated crystals in the pores between 20-100 nm leads to less expansion in DEF-I-Fin2-Layer1, which shows a lower pore volume in the pore range of 100 nm - 400 μm. This further confirms that crystal precipitation in the capillary and gel pores is the reason for expansion, and results in cracks in the pores between 100 nm - 400 μm.

A damage mechanism can be suggested from the above analyses. **The generated crystals form in the biggest pores without generating obvious expansion during the latent period, and then penetrate into smaller capillary and gel pores from which the expansion starts to increase rapidly.** The crystallization through macro to nano pores can be explained by the fact that large crystals are more energetically favored than the small ones. As discussed at the beginning of this section, it could not be determined neither the generated crystals are ettringite or all the generated crystals lead to expansion. Nevertheless, based on the studies in the literature, it can be qualitatively concluded that the generated crystals have a high possibility to be ettringite, then the formation of ettringite in the capillary and gel pores is the reason for expansion.

Evolution of the expansive mechanism while approaching the outer solution - effect of leaching Fig. 3.28 illustrates the evolution of pore size distribution at the 5th layer, which corresponds to a depth between 2.75 and 3.3 cm.

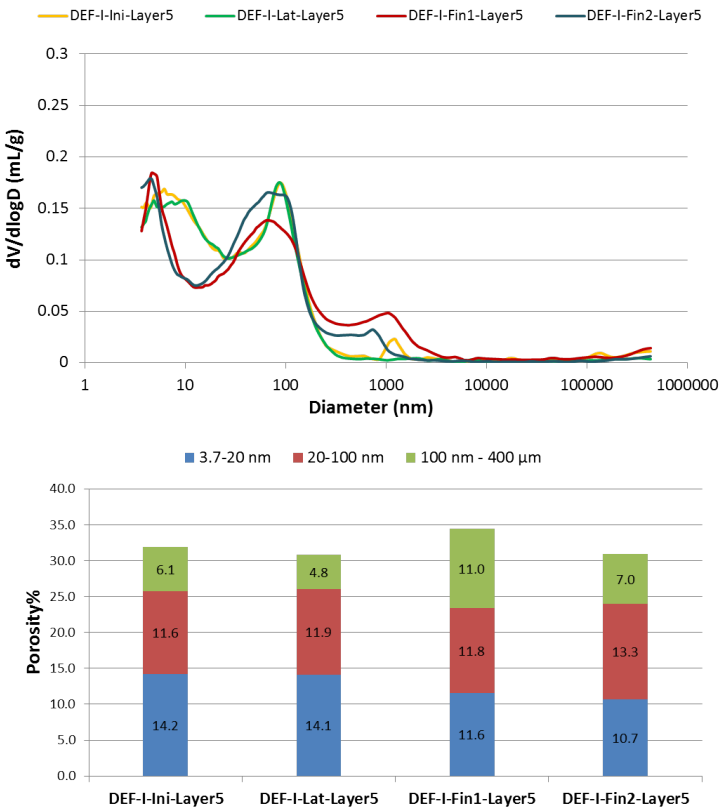

Figure 3.28 – Evolution of the pore size distribution and pore volume of DEF 11 × 11 × 22 cm^3 samples from MIP at the 5th layer.

After a 200-day immersion in water, the sample (DEF-I-Lat-Layer5) keeps a similar pore structure as the initial one (DEF-I-Ini-Layer5). Then, at the final states, pore volume of pores in the range of 8-30 nm decreases compared to samples in former two states, and pore volume in the pores larger than 110 nm increases. However, compared to DEF-I-Fin2-Layer5, DEF-I-Fin1-Layer5 shows a lower pore volume with pore diameter between 30-110 nm, and a higher pore volume with pore diameter larger than 110 nm. These observations are consistent with the observed phenomenon in the core layer showing that more crystals are formed in the capillary and gel pores of the specimen which has a higher expansion. The evolution of pore volume in three pore ranges is presented in Fig. 3.28. Similar conclusions can be drawn here. **The (at least part of the) generated crystals tend to precipitate in the pores between 100 nm - 400 μm without inducing obvious expansion, and then penetrate into smaller pores leading to expansion.** The evolution of the pore size distribution from Layer1 to Layer7 keeps the same trend (see Appendix C).

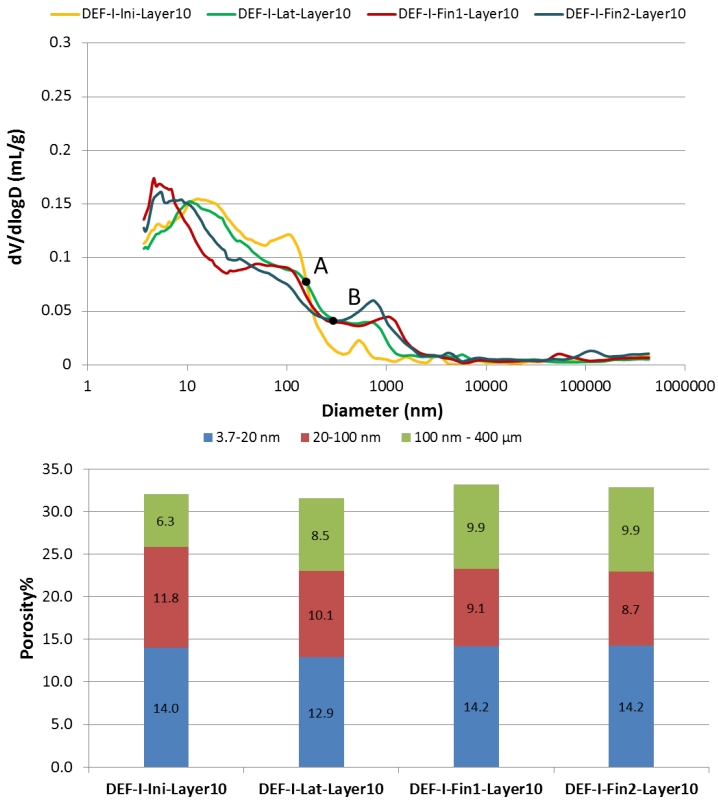

Figure 3.29 – Evolution of the pore size distribution and pore volume of 11 × 11 × 22 cm^3 DEF specimen from MIP at the surface layer.

Evolution of the expansive mechanism while approaching the outer solution - surface effect The evolution of the pore size distribution at the 8th (at a depth between 1.1 and 1.65 cm), 9th (at a depth between 0.55 and 1.1 cm) and surface layer are quite different, see Fig. 3.29. First, the pore volume tends to decrease in the pore range of less than 150 nm. Then, pore positions where the pore volume starts to be released increase. For example, pore volume is increased for pores of dimensions higher than the radius corresponding to point A in Fig. 3.29 if comparing specimens DEF-I-Ini-Layer10 with DEF-I-Lat-Layer10; this critical point moves to B (around 300 nm) by comparing DEF-I-Lat-Layer10 and DEF-I-Fin1-Layer10/DEF-I-Fin2-Layer10. It means that as exposure time increases, the balance between pores filled by new crystals and the creation of empty pores leads to the generation of new bigger pores while smaller pores are occupied. The evolution of pore volume in three ranges at the surface layer shows differences compared to Layer1 to Layer7. Pore volume with respect to pores between 100 nm - 400 μm tend to increase and pore volume of medium pores (20-100 nm) decreases, while pore space of the smallest pores (3.7-20 nm) decrease first and then increase.

The leaching is particularly obvious at this layer, that is why it is difficult to analyze the variations of pore structure during DEF. Haga found that a remaining content of Ca at the surface layer could be decreased to 30% after 91-day exposure to deionized water, while remained almost intact at the depth of 10 cm [14]. The depth of the CH dissolved front extends to further depth as the leaching period increases. However, the surface layers are the most degraded. This explains the different trend of the evolution of the pore structure at the surface and other layers. Furthermore, the pore volume between 10 and 150 nm filled by ettringite tends to decrease, but in a lower extent compared to the core layer.

3.1.4.3 Subconclusions

The evolution of pore size distribution of the big DEF specimens can solve the questions proposed above: 1. Will AFt precipitate in smaller gel pores when the expansion continues to a higher degree? 2. How does the pore size distribution evolve during the process of DEF?

- It is concluded that ettringite forms only in the capillary pores, but also in smaller gel pores when the expansion increases from 0.5% to more than 1.0%.
- A modification of the pore size distribution during the attack is observed. The generated crystals tend to precipitate in the big voids without inducing obvious expansion, and then penetrate into capillary and gel pores which leads to swelling.

3.1.5 Comparison of the pore volumes measured by MIP and WAPT

There is no unique method that can be used to characterize pores having a wide range of sizes. The different techniques, each based on different inherent assumptions, have their own capabilities and advantages. A combination of several methods is most likely to provide a good understanding of the size and pore structure. To better understand the characteristics of the techniques, the pore volume measured by MIP and WAPT are compared. A comparison of the total porosity of $11 \times 11 \times 22$ cm^3 DEF specimens measured by WAPT and MIP (in different layers) are presented in Table 3.4.

On the one hand, the table illustrates that the total porosity obtained by WAPT increases gradually during the degradation. This increasing trend is more clearly shown in Fig. 3.30. However, the average of total porosity measured by MIP has a different trend. It tends to decrease due to a higher decreased pore volume induced by ettringite formation, comparing to other possible processes which can increase the pore volume. Then, the average total porosity increases which may be induced by the dissolution of CH and/or the occurrence of microcracks. On the other hand, the porosity measured by WAPT is consistently higher than the average values measured by MIP. The relative difference in average porosity measured by these techniques ranges from a minimum of 27% at the initial state to a maximum of 36% at the final state. A noticeable difference was also reported in the work of Ragoug [32]. The water accessible technique overestimates the porosity in samples that contains a significant amount of water soluble minerals. The dissolution of these minerals during saturation may increase the measured porosity. The creation of microcracks during process is another possibility which would result in a higher porosity than the actual one. Therefore, WAPT is not recommended to be the indicator to analyze the characterization of the pore microstructure. Even though WAPT has limitations to study the durability of cement paste in a microscopic scale, it remains an easily and rapidly performed technique. It would provide more reliable results while working on the durability of mortars and concrete, which are more concerned by engineers.

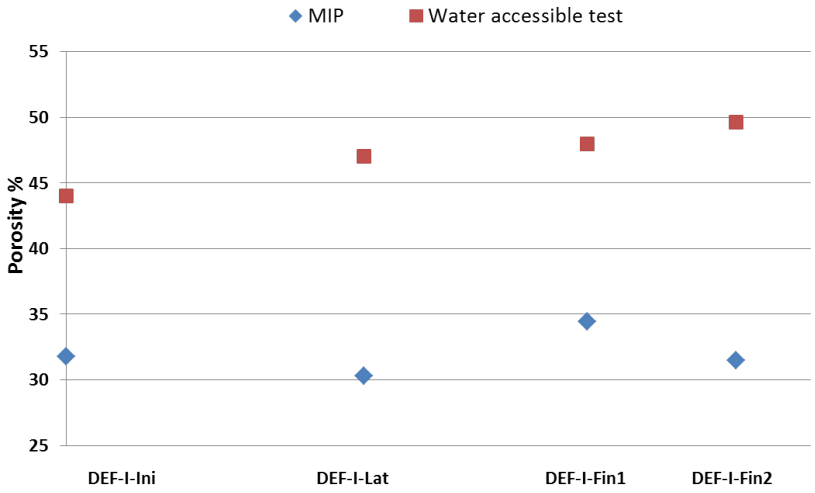

Figure 3.30 – The evolution of the total porosity measured by MIP and WAPT.

Table 3.4 – Comparisons of the pore volumes measured by MIP and WAPT.

Samples	Porosity from MIP (%)	Average (%)	Water absorption (%)	Samples	Porosity from MIP (%)	Average (%)	Water absorption (%)
DEF-Ini-Layer1	31.86	31.79	44	DEF-Fin1-Layer1	35.16	34.42	48
DEF-Ini-Layer2	30.73			DEF-Fin1-Layer2	35.06		
DEF-Ini-Layer3	31.55			DEF-Fin1-Layer3	35.85		
DEF-Ini-Layer4	32.17			DEF-Fin1-Layer4	33.54		
DEF-Ini-Layer5	31.88			DEF-Fin1-Layer5	34.42		
DEF-Ini-Layer6	32.20			DEF-Fin1-Layer6	34.68		
DEF-Ini-Layer7	31.90			DEF-Fin1-Layer7	34.65		
DEF-Ini-Layer8	32.05			DEF-Fin1-Layer8	33.42		
DEF-Ini-Layer9	31.47			DEF-Fin1-Layer9	34.23		
DEF-Ini-Layer10	32.08			DEF-Fin1-Layer10	33.21		
DEF-Lat-Layer1	27.96	30.31	47	DEF-Fin2-Layer1	29.62	31.47	49.6
DEF-Lat-Layer2	29.85			DEF-Fin2-Layer2	29.09		
DEF-Lat-Layer3	31.43			DEF-Fin2-Layer3	30.46		
DEF-Lat-Layer4	30.47			DEF-Fin2-Layer4	31.29		
DEF-Lat-Layer5	30.80			DEF-Fin2-Layer5	30.95		
DEF-Lat-Layer6	31.57			DEF-Fin2-Layer6	32.42		
DEF-Lat-Layer7	31.60			DEF-Fin2-Layer7	32.41		
DEF-Lat-Layer8	30.05			DEF-Fin2-Layer8	32.75		
DEF-Lat-Layer9	27.82			DEF-Fin2-Layer9	32.79		
DEF-Lat-Layer10	31.54			DEF-Fin2-Layer10	32.88		

3.1.6 Analyses on heat-based dissolution test results

3.1.6.1 Effect of high temperature on the microstructure

Fig. 3.31(b) presents the pore size distribution of the initial DEF sample (DEF-I-Ini) before and after a 1-day heating at 68 °C. The sample was described in detail in section 2.11.1. After the high temperature, the pore volume in pores larger than 130

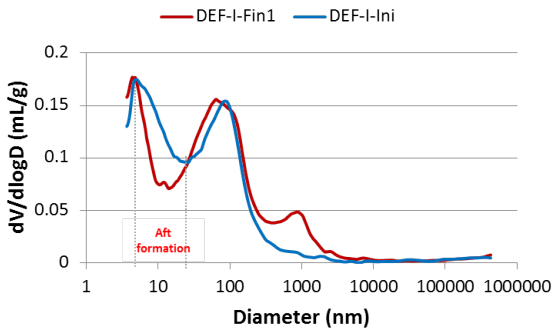

(a) Pore size distribution of sample DEF-I-Fin1 and DEF-I-Ini ;

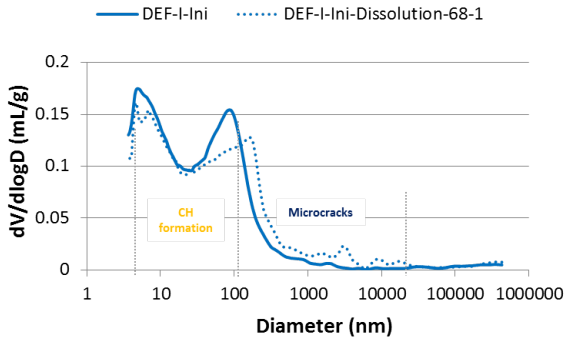

(b) Pore size distribution of sample DEF-I-Ini and DEF-I-Ini-Dissolution-68-1;

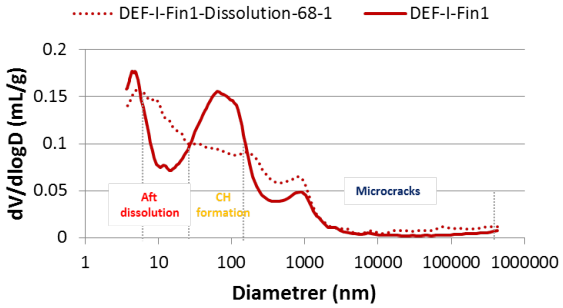

(c) Pore size distribution of sample DEF-I-Fin1 and DEF-I-Fin1-Dissolution-68-1.

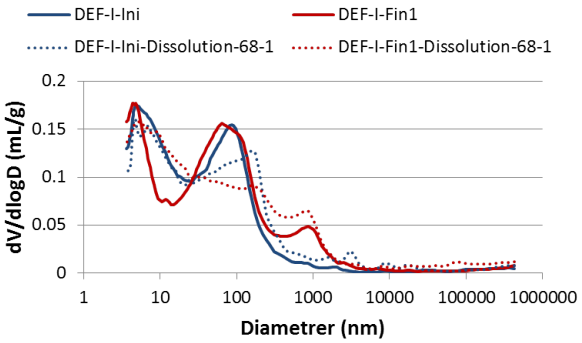

(d) Comparison of pore size distribution of sample above.

Figure 3.31 – Pore size distribution of (a) DEF-I-Fin1 & DEF-I-Ini; (b) DEF-I-Ini & DEF-I-Ini-Dissolution-68-1; (c)DEF-I-Fin1 & DEF-I-Fin1-Dissolution-68-1; and (d) all.

nm increases and pore volume with respect to diameters less than 130 nm decreases. When the cement-based material is exposed to high temperatures, the most important processes happening include chemical reactions, phase transformations and heat deformations occurring at a microscopic scale [269]. The total porosity of gel and capillary pores was found to be stable when heated up to 300°C in [270] due to the shrinkage of cement paste on the one hand [269] and on the other hand to additional hydration of unhydrated cement grains and the recrystallization of $Ca(OH)_2$. The solubility of portlandite decreases as the temperature increases. For instance, the dissolved Ca from portlandite decreases from 13.6 mmol at 100 °C to 0.506 mmol at 350 °C [271]. As specimens in this study have been kept in water for up to 1 year, the shrinkage of the cement paste and the hydration process should have been finished. Therefore, the pore size change of the cement paste in this heat-based dissolution test should be caused by the microcracks due to heating in the pores larger than 100 nm [264] and the recrystallization of $Ca(OH)_2$ [270] in the pores less than 100 nm, and maybe the dissolution of AFt.

3.1.6.2 Microstructure after the heat-based dissolution

Firstly, the pore size distribution change of the $11\times11\times22$ cm^3 DEF specimens DEF-I-Ini and DEF-I-Fin1 is recalled in Fig. 3.31(a). It has been shown that during the DEF, pores between 4 and 30 nm are filled by ettringite, and pore volume increases between 100 nm and 10 μm, which is caused by microcracks and the dissolution of portlandite. The detailed explanations have been presented previously in section 3.1.4. Then, the pore size distribution of DEF-I-Fin1 and DEF-I-Fin1-Dissolution-68-1 (sample DEF-I-Fin1 heated at 68 °C for 1 day) are shown in Fig. 3.31(c). The recrystallization of CH in the capillary pores and formation of microcracks are observed after the heat-based dissolution test. Meanwhile, pore space between 4 and 30 nm is released, which was occupied by ettringite before, as shown in (a). A general comparison of all the samples above is presented in Fig. 3.31(d). It is clearly shown that the pore size distribution between 4 and 30 nm is completely reversed to the initial state after the heat-based dissolution test.

More results of pore size distribution after heat-based dissolution exposed to different temperatures and durations are shown in Fig. 3.32 – 3.36. Based on the analyses above, we will focus only on the pore range between 4 and 30 nm and forget the rest due to portlandite formation and microcracking. The pores filled by ettringite during DEF are released after the heat-based dissolution except for 68-3, 78-3 and

88-3, and the reasons for the exception could not be explained. The differences between the curves, which are reversed to the initial state in the range of 4 and 30 nm, are not significant knowing the dispersion of the test results (see Chapter 2) and could be ignored. However, higher temperatures induce more microcracks in the material. Therefore, it is concluded that the heat-based dissolution at 68 °C for 1 day is enough and efficient to "wash" out the ettringite formed during the process of delayed ettringite formation, which in turn proves that the crystals formed in the range between 4 and 30 nm during DEF are ettringite crystals.

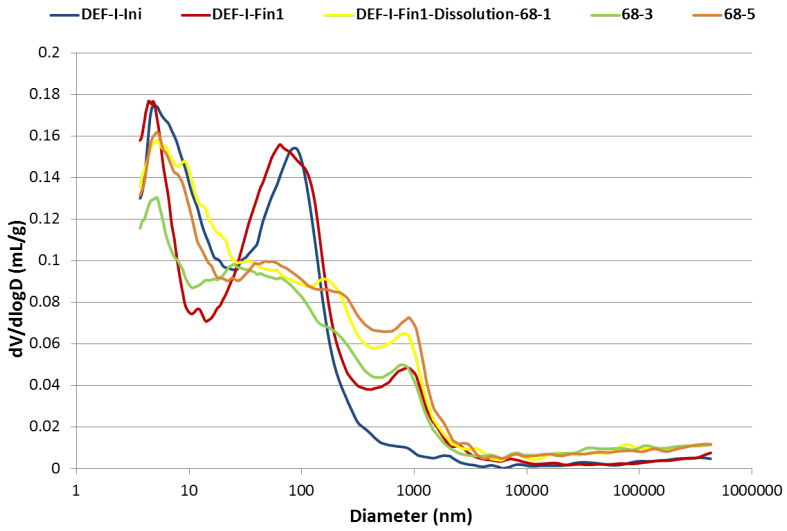

Figure 3.32 – Pore size distribution measured from MIP after the heat-based dissoluion test at 68 °C (I)

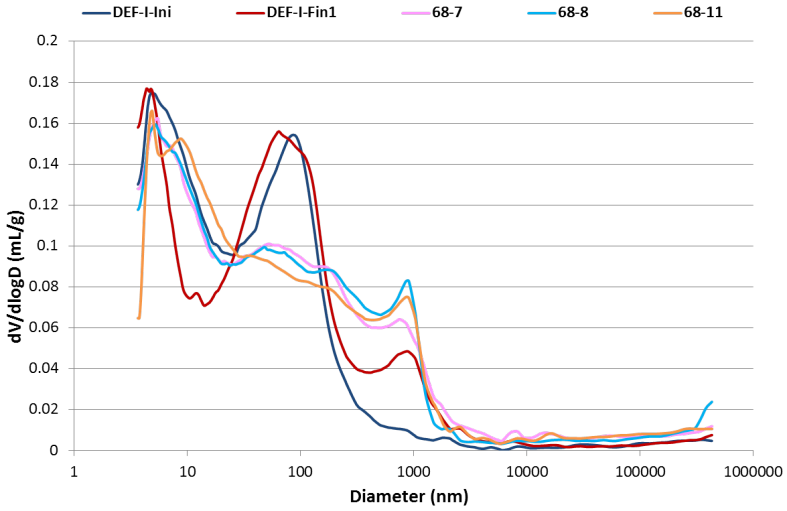

Figure 3.33 – Pore size distribution measured from MIP after the heat-based dissoluion test at 68 °C (II)

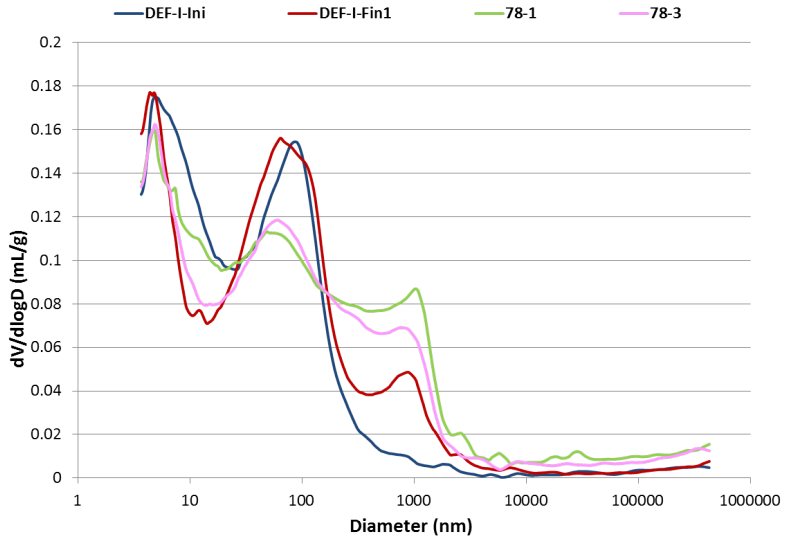

Figure 3.34 – Pore size distribution measured from MIP after the heat-based dissoluion test at 78 °C

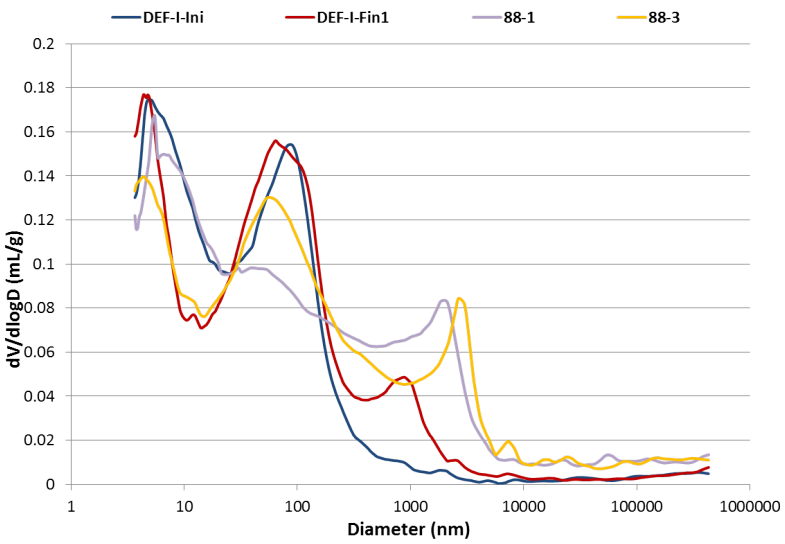

Figure 3.35 – Pore size distribution measured from MIP after the heat-based dissoluion test at 88 °C

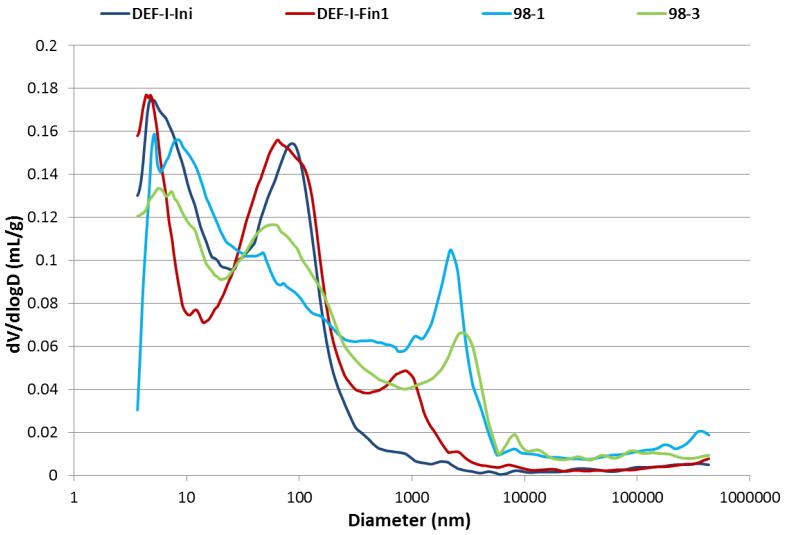

Figure 3.36 – Pore size distribution measured from MIP after the heat-based dissoluion test at 98 °C

3.2 Cement III samples

As compared to the CEM I specimens, none of the specimens fabricated with CEM III showed a major increase of expansion and mass after a 7-month exposure to sulfate attack conditions (ESA, DEF and Coupling effect), see Fig. 3.37 – 3.39. After 220-day exposure to DEF, DEF-III-Fin (expansion of 0.008%) showed an expansion 60 times less than DEF-I-Fin (expansion of 0.5%). Meanwhile, ESA-III-Fin specimen showed an expansion almost 40 times less than ESA-I-Fin. This difference is much more obvious in the case of coupling effect. However, these expansions cannot be considered as negligible as regards the expansion threshold defined in "classical" concrete performance approaches dedicated to DEF [272, 273]. The low expansion of CEM III specimens is not only due to the low content of CaO but also to the limited content of Al_2O_3 available for formation of ettringite. Although CEM III has a higher Al_2O_3 content (8.93 %) than CEM I (4.30 %), a significant part of Al_2O_3 remains in unreacted slag particles [274]. In addition, the adsorption of aluminum on C-S-H results in a lower content available for ettringite formation [275]. However, CEM III is confirmed to have a good resistance to sulfate attacks.

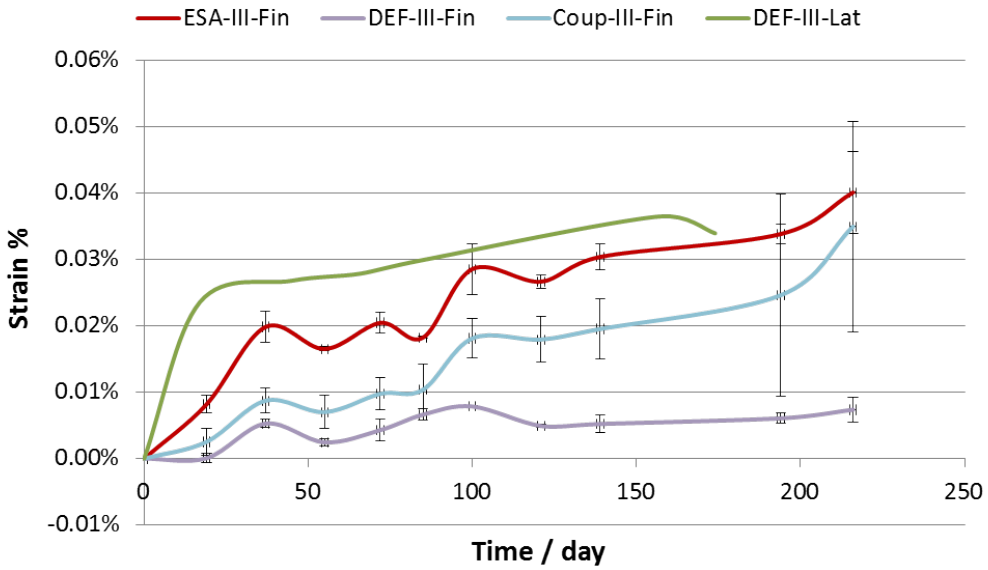

Figure 3.37 – Strain of the CEM III $2 \times 2 \times 12$ cm^3 specimens (ESA-III-Fin, DEF-III-Fin, and Coup-III-Fin) and $11 \times 11 \times 22$ cm^3 DEF specimen (DEF-III-Lat).

Some information should be recalled here. Due to the same heating treatment and curing conditions for DEF and Coup specimens, Coup-III-Ini was not fabricated. The pore size distribution of the small CEM III samples at the initial state is shown

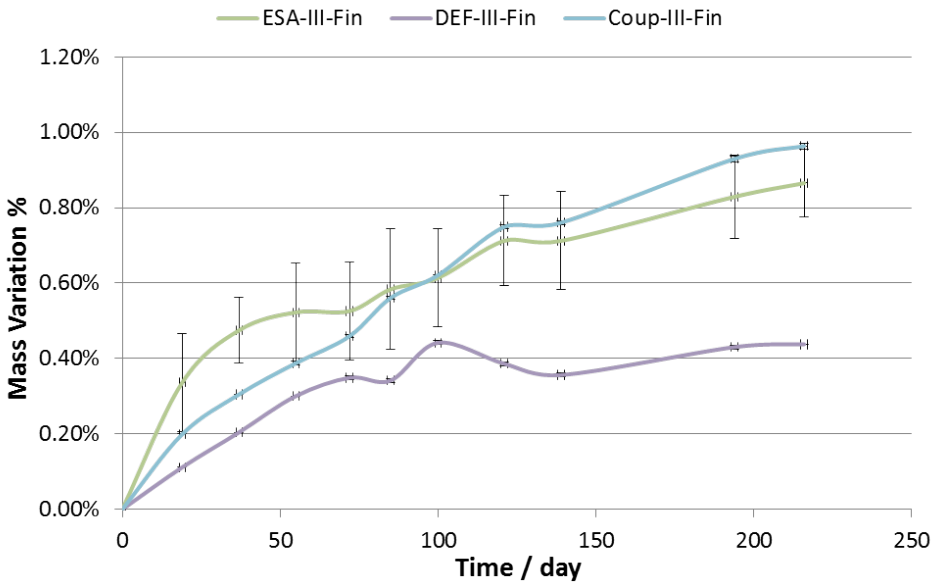

Figure 3.38 – Mass variations of the CEM III $2 \times 2 \times 12$ cm^3 specimens.

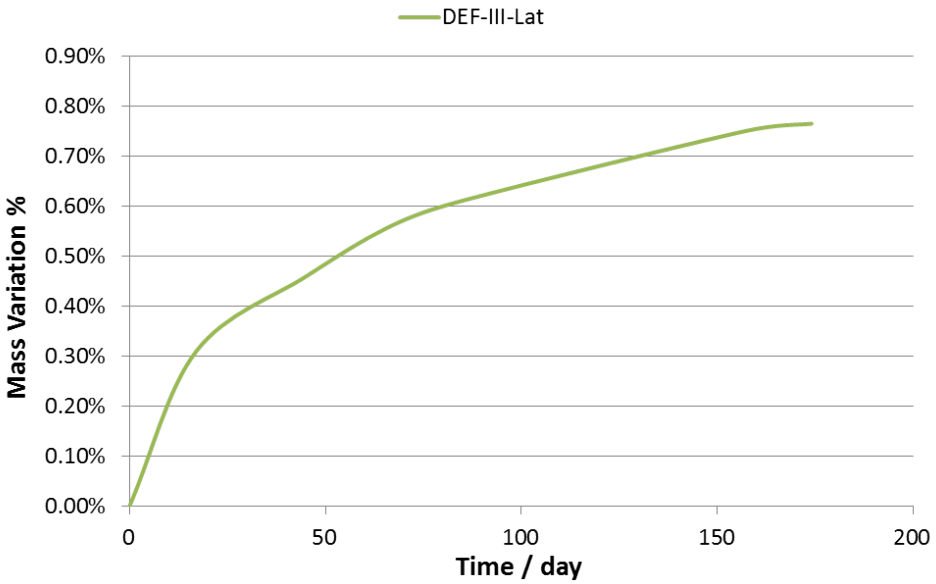

Figure 3.39 – Mass variations of the CEM III $11 \times 11 \times 22$ cm^3 specimen (DEF-III-Lat)

in Fig. 3.40. The samples show a similar pore size distribution in different layers except for the 9th and surface layer, which show a difference in the pores between 30-80 nm (see Fig. 3.43). DEF-III-Ini shows a higher pore volume between 3.7-10 nm and a lower value between 10 nm and 1 μm compared to ESA ones, especially in the core layer. The preheating on DEF specimens changes the porous structure of C-S-H, and the pore size of these pores in C-S-H (gel pores) is around 10 nm. The

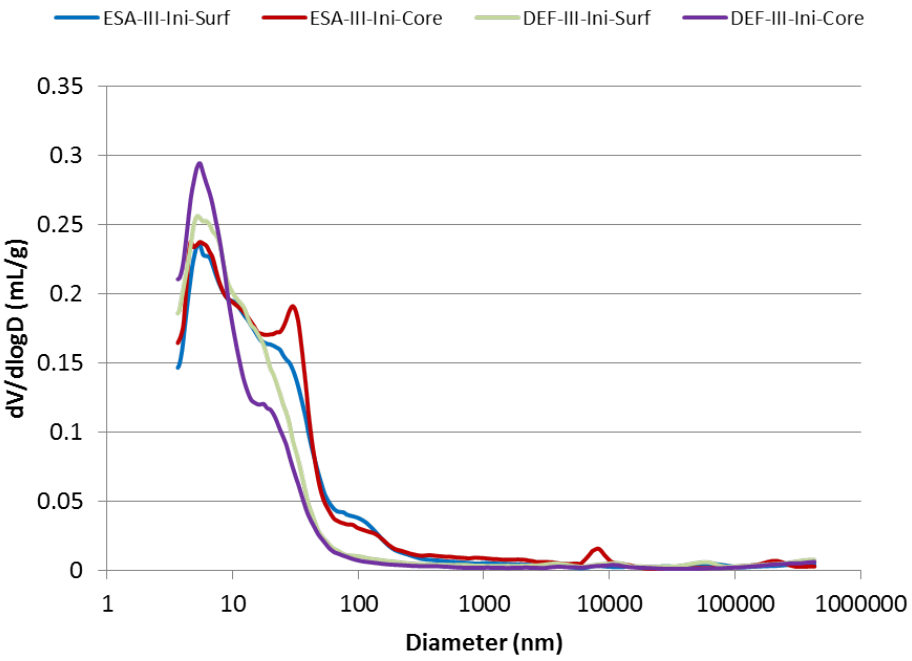

Figure 3.40 – Pore size distribution of CEM III $2 \times 2 \times 12$ cm^3 specimens.

effect of heating treatment on pore size distribution has been discussed for CEM I specimens in section 3.1.3.1.

A comparison of the pore size distribution of $2 \times 2 \times 12$ cm^3 specimens fabricated with CEM I and CEM III is presented in Fig. 3.41 and 3.42. The CEM III specimen shows a higher pore volume in the range of around less than 27 nm in the case of DEF and less than 35 nm in the case of ESA compared to the CEM I specimens. According to the analyses on small CEM I specimens in section 3.1.3.1, the formation of ettringite in the pores smaller than 50 nm for ESA and between 9.7-100 nm for DEF corresponds to expansion. The high pore volume in the range of less than around 30 nm provides a higher capacity to accommodate the expansive products, which is one more other explanation why less expansion is observed in CEM III specimens. Furthermore, the pore size distribution of $11 \times 11 \times 22$ cm^3 DEF specimen (DEF-III-Ini) at different layers are presented in Fig. 3.43. It illustrates that the microstructure along the depth are pretty similar, except for the 9th and surface layers which are affected significantly by the leaching of calcium ions and microcracks.

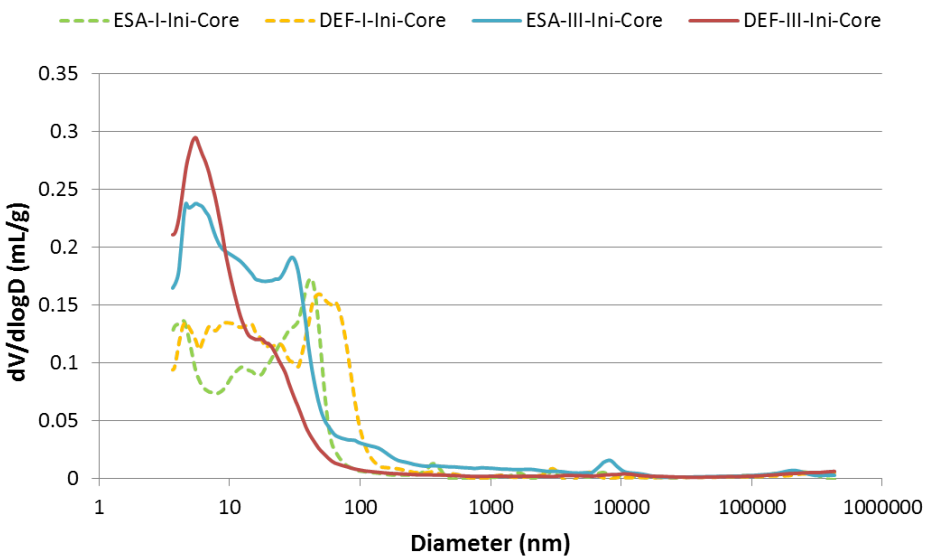

Figure 3.41 – Comparison of pore size distribution of $2 \times 2 \times 12$ cm^3 specimens between CEM I and CEM III at the core layer

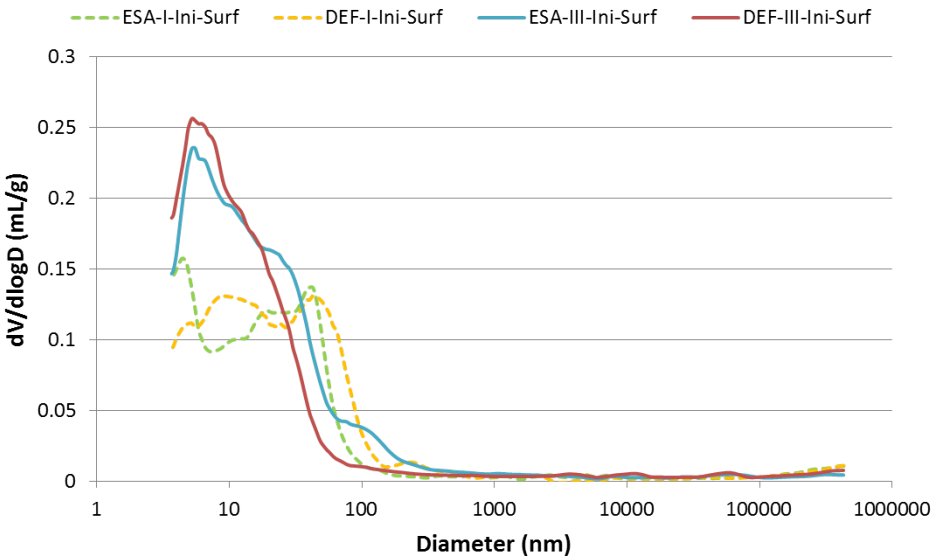

Figure 3.42 – Comparison of pore size distribution of $2 \times 2 \times 12$ cm^3 specimens between CEM I and CEM III at the surface layer

3.3 Conclusions

Small specimens ($2 \times 2 \times 12$ cm^3) fabricated with CEM I and III, which were exposed to ESA, DEF and the coupling effect of both, were monitored during the degradation process. Small specimens fabricated with CEM III showed very slow increase of length and mass variation due to limited content of CaO and Al_2O_3 available for

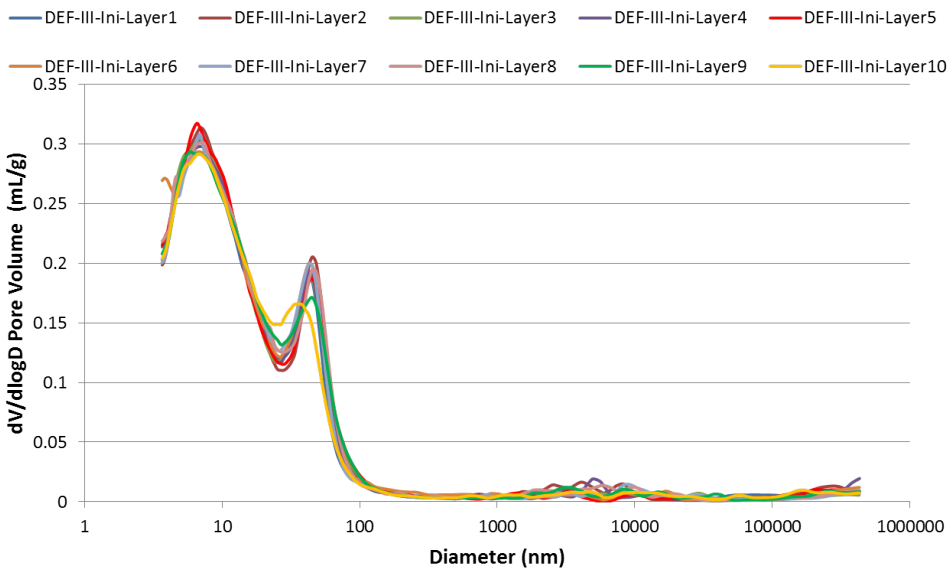

Figure 3.43 – Pore size distribution along the depths of $11 \times 11 \times 22$ cm^3 DEF specimen, DEF-III-Ini

ettringite formation. A high pore volume with respect to pores of less than around 30 nm was another reason for delay of expansion. On the contrary, CEM I specimens had high expansions. The ESA-I-Fin and Coup-I-Fin specimens showed obvious cracking in the material, while only slight cracks were seen for DEF-I-Fin specimens on the top and side surfaces with an expansion of 0.5% after two years of monitoring. In this study, the degree of swelling took an order as: DEF $<$ ESA $<$ Coupling effect, while the increase of length showed a unique linear relationship with the increase of mass in three exposure conditions at the beginning stage (elastic stage).

The measured variations of pore size distribution presented above indeed include a combination of several phenomena, for instance, the dissolution of CH, the decalcification of C-S-H, formation of ettringite (and gypsum) and the occurrence of cracks. Hence, the measured pore volume in a pore range cannot be used to quantitatively distinguish the different phenomena. However, this method provides a way to qualitatively understand the microstructure characteristics during the sulfate attack process.

The changes of the microstructure of the $2 \times 2 \times 12$ cm^3 specimens ESA-I and Coup-I measured by MIP and deduced from DVS during the sulfate attacks confirm the ettringite formation both in capillary and gel pores. However, ettringite was found to be present mainly in the capillary pores for the $2 \times 2 \times 12$ cm^3 specimen DEF-I which had an expansion of 0.5%. The continuation of the ettringite formation to gel pores

was proved on the big DEF specimens ($11 \times 11 \times 22$ cm^3): DEF-I-Fin1 (expansion of 1.49%) and DEF-I-Fin2 (expansion of 1.22%). Therefore, it was concluded that the ettringite precipitates both inside capillary and gel pores regardless of the exposure conditions. According to the evolution of pore size distribution of $11 \times 11 \times 22$ cm^3 DEF specimens, a damage mechanism is proposed: ettringite precipitates in the big voids firstly without inducing obvious expansion, and then penetrates into capillary and gel pores which leads to expansion. Meanwhile, crystals form in the generated voids with possibility to increase the damage.

With additional sulfate ions coming from the aggressive solution, the Coup specimens showed a similar pore size distribution in the pores less than 100 nm as the DEF specimens, but a much higher pore volume in the pore ranges corresponding to the microcracks. It indicates that ettringite tends to preferentially form in the new created big voids, e.g. microcracks, rather than to continue to penetrate into smaller gel pores. However, the ettringite formed in big voids is not the reason for the expansion, but it nonetheless leads to a worse degradation in the area where cracks already happened. This idea was further confirmed in the evolution of pore size distribution on DEF $11 \times 11 \times 22$ cm^3 specimens at the core layer. The pore volume between 100 nm and 1 μm was observed to be decreased after a 200 days immersion in water when the specimen showed a swelling of 0.03%. A high pore space in this range (100 nm - 1 μm) was released when the expansion increased up to 1.22%, which was higher when the specimen reached a swelling degree of 1.49%.

The pore volume measured by MIP and WAPT have been compared. The water accessible porosity technique shows an overestimated porosity, because of a great amount of water soluble minerals contained in the samples that could be dissolved during the saturation. The creation of microcracks during the process is another possible reason for the overestimation of porosity. Therefore, the total porosity measurement, water accessible porosity technique is not recommended as a unique indicator of durability for the specimens exposed to sulfate attacks in the microscopic scale. Even though MIP has limitations as well, it can provide potential information, e.g. the change of the microstructure which can confirm some explanations of the sulfate attack mechanisms discussed in the literature.

Heat-based dissolution tests were performed to "wash out" the ettringite formed during DEF. Even accompanied with microcracks and the recrystallization of CH, the ettringite formed during the DEF was proved to have been removed in the pore range of 4-30 nm after the heat-based dissolution tests. The initial pore size dis-

tribution was recovered in this range, which further confirmed that the products formed were ettringite. Moreover, this reversion was observed at different temperatures and heating durations, except for the cases of 68-3, 78-3 and 88-3. However, samples treated by the higher temperatures and longer durations showed more pore volume induced by microcracks.

Based on the damage mechanism proposed in this chapter, a poromechanical model will be established to simulate the crystallization process of ettringite and predict the corresponding expansion of specimens. In addition, the pore size distribution of specimen ESA-I-Ini (before the sulfate attack) will be used in the model to represent the pore structure of cement paste. In return, the predicted crystallization process will be compared with the MIP results of specimens after the attack.

4 Poromechanical model

In the previous chapter, it was concluded that ettringite precipitated firstly in the big voids without inducing expansion, and then penetrated into capillary and gel pores which leads to expansion. Moreover, ettringite was found to be formed both in capillary and gel pores after the degradation, regardless of the type of sulfate attacks. A poromechanical model of the cement-based material subjected to both ESA and DEF is proposed, based on surface-controlled crystal growth and other physicochemical properties. This model well explains how crystal precipitates in a porous material, and the crystal growth is believed to be controlled by the interface instead of the diffusion control. Scherer explained that if growth was under diffusion control, the crystal-liquid interface would be at the solubility limit, so no pressure could be tolerated [276]. The crystallization pressure is believed to be the driving force for the expansion, which links the crystal formation in the microstructure to the stress-strain response of the material.

4.1 Poromechanical approach

4.1.1 Effective stress

The expansion of a porous body, exposed to a supersaturated solution of a given crystal, is assumed to originate from the crystallization pressure exerted at the crystal-solid interface after crystal grows into contact with the wall of pores. The crystallization pressure, P_C, is the pressure needed to arrest the growth in a supersaturated solution and is given by the Correns' equation [22] under the form:

$$P_C - P_L = \frac{RT}{V_C} \ln(\beta_p) \tag{53}$$

where P_L is the liquid pressure, R is the ideal gas constant, T is the temperature, V_C is the molar volume of the crystal, and β_p is the saturation index of the crystal at the crystal-solid interface.

The poromechanical approach is used to model the expansion ϵ of a porous solid. As the sample is fully saturated in a solution, namely, no air is occupied in the pore space, the material is considered to be saturated by crystals and the liquid. Then, the effective stress can be expressed as:

$$\sigma^{'} = \sigma + b\ (S_C P_C + S_L P_L) \tag{54}$$

In this equation, $\sigma^{'}$ and σ are respectively the effective stress and stress responsible for the solid strain ϵ, b is the Biot's coefficient, S_C is the fraction of pore space saturated with crystals and S_L is the liquid saturation which equals to (1 - S_C). The liquid pressure, P_L, is assumed to be equal to the atmospheric pressure and will be neglected from now on. Then, in a stress-free condition, the effective stress, $\sigma^{'}$, can be simplified as:

$$\sigma^{'} = bS_C P_C \tag{55}$$

Through the effective stress $\sigma^{'}$, the proposed poromechanical model could be used to simulate the swelling of the material by coupling with any mechanical constitutive theories, such as elasticity ($\sigma^{'} = E\epsilon$), plasticity ($\sigma^{'} = E\ (\epsilon - \epsilon_p)$), damage theory ($\sigma^{'} = E(d)\epsilon$) and so on.

4.1.2 Lagrangian partial porosities filled by crystals

The volume fraction filled by crystals are split into two parts: invasion and deformation processes [277]:

$$\Phi_C = S_C \Phi_0 + \varphi_C \tag{56}$$

where Φ_C is the volume fraction of the crystal phase, Φ_0 is the initial porosity in the material prior to any deformation, S_C is the Lagrangian degree of saturation for crystals and φ_C is the porosity change due to deformation of the pores.

As shown in Eq. 56, the volume fraction of the crystal depends on the volume change caused by crystal invasion $\Phi_0 S_C$ and the pore deformation φ_C. The former one is related to the crystal content n_i formed in the pore invasion process by accretion of new crystals at the liquid-crystal interface:

$$S_C \Phi_0 = \mathrm{V_C} n_i \tag{57}$$

and the latter is related to the crystal content n_p formed during the deformation process by accretion of new crystals at the solid-crystal interface:

$$\varphi_C = \mathrm{V_C} n_p \tag{58}$$

where $\mathrm{V_C}$ is the molar volume of the crystals.

4.1.3 Volumetric isodeformation of pores

The deformation of the pores is assumed to be isotropic in the material. The change of the partial porosity, during the pore deformation process, is assumed to be related to the degree of crystal saturation S_C and the deformation of pores φ, under the form:

$$\varphi_C = S_C \varphi \tag{59}$$

The overall volumetric strain ϵ of a porous solid results from both the volumetric strain ϵ_s of its solid part, and from the change of the Lagrangian porosity, φ [202].

$$\epsilon = (1 - \phi_0)\, \epsilon_s + \varphi \tag{60}$$

The solid matrix is considered as incompressible grains so that $\epsilon_s = 0$, and Eq. 60 is simplified as:

$$\epsilon = \varphi \tag{61}$$

Combining Eqs. 59 and 61, the change of the partial porosity due to the deformation, φ_C, is:

$$\varphi_C = S_C \epsilon \tag{62}$$

Eqs. 56, 57, 58 and 62 are the main assumptions for the change of porosity induced by crystals formation.

4.1.4 Coupling with poroelasticity

The poroelasticity theory can be used to model the linear expansion in the elastic range ϵ of a sample caused by the crystallization pressure (Eq. 53) as following:

$$\epsilon = \frac{b}{E} S_C P_C \tag{63}$$

where E is the bulk modulus of the porous body, b is the Biot's coefficient and S_C is the fraction of pore space saturated with the crystal.

The poroelasticity is suitable to simulate the elastic expansion of the specimens, for example, when the specimens are in a constrained condition. However, when the stress exerted on the material is beyond its elastic range, the poroelasticity is not suitable anymore. Therefore, an extension of the poroelasticity to a damage theory or plasticity is necessary.

4.1.5 Coupling with damage model

A typical uniaxial tensile damage theory is coupled with this poromechanical model (see Fig. 4.1). It comprises two periods: elastic (0–1) and damage (1–2) ranges. A tensile damage model [278] is adopted in the second period, and a combined constitutive relation of the tensile stress and strain is shown as follows:

$$\begin{aligned} \sigma_{0-1} &= E\epsilon \\ \sigma_{1-2} &= E(d)\ \epsilon = E\epsilon_0\ \exp(-\frac{\epsilon - \epsilon_0}{\epsilon_f}) \end{aligned} \tag{64}$$

where $E(d) = E\ \frac{\epsilon_o}{\epsilon}\ \exp(-\frac{\epsilon-\epsilon_0}{\epsilon_f})$, ϵ_0 is the maximum elastic strain, ϵ_f is a damage parameter affecting the ductility of the response and related to the fracture energy ($\epsilon_f \approx 3.9 \times 10^{-3}$ in this study).

Then, the non-linear expansion coupled with a damage model can be expressed as:

$$\begin{aligned} \epsilon_{0-1} &= \frac{b}{E} S_C P_C \\ \epsilon_{1-2} &= \frac{b}{E(d)} S_C P_C \end{aligned} \tag{65}$$

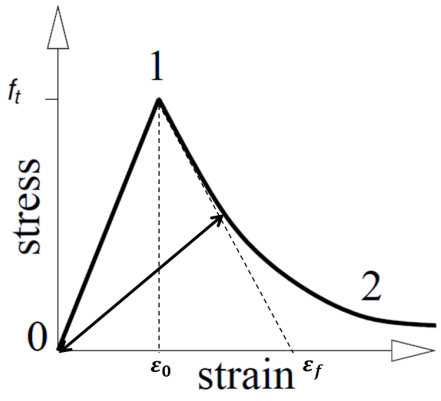

Figure 4.1 – Typical stress-strain behavior of cement-based materials.

4.2 Mechanism of crystallization-induced swelling kinetics

The mechanism of the expansion kinetics is now envisioned as follows. Consider a porous material whose pores are filled by supersaturated solution, with a saturation index of β. If a crystal nucleates on the pore wall, it will grow along radial and axial directions, by consuming the excess of the solute. It begins to exert stress on the solid matrix after it grows into contact with the opposite wall of the pore. At the crystal-solid interface, the crystal will rapidly stop growing and reach equilibrium ($\beta_p = \beta$) by exerting a stress on the wall (according to Eq. 53). However, when the material could not resist the stress, the crack occurs and a pore deformation process starts. Meanwhile, the crystal-liquid interface is out of the equilibrium and undergoes a pore invasion process. This anisotropic stress state of the crystal is shown in Fig. 4.2.

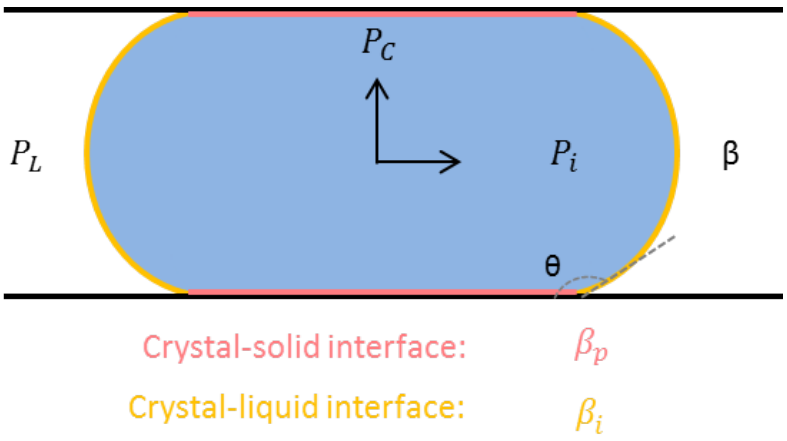

Figure 4.2 – Anisotropic stress state of crystal in a single pore

4.2.1 Crystallization process

4.2.1.1 Pore invasion process

The crystal-liquid interface will grow at a rate governed by an interface controlled growth mechanism [279] and penetrate into smaller pores with a radius of curvature predicted by the Ostwald-Freundlich equation (Eq. 66), until the crystal eventually sustains an isotropic stress state. This is called the pore invasion process. At the equilibrium state, there should be:

$$\frac{RT}{V_C}\ln(\beta) = \frac{2\gamma_{CL}}{r_{eq}} \tag{66}$$

where γ_{CL} is the surface energy of the crystal and r_{eq} is the mean radius of curvature of the crystal-liquid interface at equilibrium ($\beta_i = \beta$) i.e. after the crystal growth in the invasion process is completed. The Ostwald-Freundlich equation tells us that the solubility of the crystal increases with the inverse of its size so that a small crystal is less stable than a bigger one. The consequence is that precipitation will first occur in the biggest pores and then penetrate into ever smaller pores. During its growth, the radius of curvature of the crystal-liquid interface, $r(t)$, will then decrease and stop after reaching the limit r_{eq} given by Eq. 66.

$\beta_i(t)$, related to the radius of curvature, $r(t)$, is the saturation index of crystal at the crystal-liquid interface exhibited at the present time through the Ostwald-Freundlich equation under the form:

$$\frac{RT}{V_C}\ln(\beta_i(t)) = \frac{2\gamma_{CL}}{r(t)} \tag{67}$$

The saturation index, $\beta_i(t)$, is thus the saturation index of a theoretical solution that would be in equilibrium with the crystal-liquid interface at time t, having a radius of curvature $r(t)$. In the process of the crystal growth, this saturation index will increase from a value associated with the biggest pore and stop after having reached β. Here, for sake of simplicity and without loss of generality, the effect of contact angle (θ, see Fig. 4.2) has been neglected and so the pore radius and the interface radius of curvature have been merged.

4.2.1.2 Pore deformation process

As explained above, the crystal at the crystal-solid interface reaches equilibrium rapidly due to a high stress on the pore wall. However, this equilibrium will be broken when the cracks occur, and a pore deformation process comes. Without the constraint of the pore wall, the saturation index of the crystal at the crystal-solid interface drops quickly according to Eq. 53.

There are two possible subsequent situations:

- If the source of the reactant ions is unlimited (e.g. in the case of ESA), namely, the saturation index of crystal in pore solution is kept high and constant. Then the interface of crystal-solid will be always out of equilibrium, and results in an unlimited crystal growth;
- Another situation is when the source of the reactant ions is limited (e.g. in the case of DEF), which means that the saturation index of the crystal in pore solution will be decreased during the crystallization. Due to the decrease of the β, the equilibrium at the crystal-solid interface may be obtained again, when crystals stop growing and the swelling reaches a plateau.

During this process, the strain increases fast, the kinetics of which is assumed to be governed by an interface controlled mechanism.

4.2.2 Kinetic of crystal growth

It is assumed that the growth rate is governed by an interface controlled mechanism [279] given by:

$$\frac{d}{dt}(n) = a_v \left(1 - \exp(-\frac{\Delta G_r}{RT})\right) \tag{68}$$

where n is the crystal content, a_v is a parameter and ΔG_r is the reaction Gibbs energy of the crystal dissolution reaction, i.e $\Delta G_r = \sum_i \nu_i \mu_i - \mu_{\mathrm{C}}$ where μ_i is the chemical potential of ions in solution, ν_i is the stoichiometric coefficients and μ_{C} is the chemical potential of the solid crystal at the curved crystal-liquid interface, which can be related to that of a flat interface through the Gibbs-Thomson equation, $\mu_{\mathrm{C}} = \mu_{\mathrm{C}}^{\infty} + 2\gamma_{\mathrm{CL}} V_{\mathrm{C}}/r$. It turns out that ΔG_r can be expressed as $\Delta G_r = RT \ln(\beta/\beta_i)$

at the crystal-liquid interface, so that a kinetic law for crystallization can be written as:

$$\frac{d}{dt}(n_i) = a_m\ (1 - \frac{\beta_i}{\beta}) \tag{69}$$

where n_i is the crystal content formed during pore invasion process and a_m is a kinetic constant, which is proportional to the surface area at the crystal-liquid interface.

A similar kinetic law is employed in the pore deformation process:

$$\frac{d}{dt}(n_p) = a_n(1 - \frac{\beta_p}{\beta}) \tag{70}$$

where n_p is the crystal content formed during pore deformation process and a_n is the corresponding kinetic constant, which is proportional to the surface area at the crystal-solid interface that has been saturated by crystals.

Combining the Eq. 57 and 69, the kinetic equation of S_C could be expressed as:

$$\frac{d}{dt}(S_C) = \frac{\mathrm{V_C}}{\Phi_o}\frac{d}{dt}(n_i) = a_i\ (1 - \frac{\beta_i}{\beta}) \tag{71}$$

with $a_i = \frac{\mathrm{V_C}}{\Phi_o}\ a_m$. When the crystal-liquid interface reaches an equilibrium ($\beta_i = \beta$), the increase rate of S_C will be 0. Then S_C will be always kept constant.

By combining the Eq. 58, 59 and 70, the kinetic of strain increase could be expressed as:

$$\frac{d}{dt}(\varepsilon) = a_p\ (1 - \frac{\beta_p}{\beta}) \tag{72}$$

with $a_p = \frac{\mathrm{V_C}}{S_C}\ a_n$.

Eqs. 53, 55, 71 and 72 are the basic equations governing the mechanism for the crystallization-induced swelling kinetics.

4.3 Modeling the ettringite formation in pores

The crystal formed in this study is ettringite. The crystal saturation should be related to the pore size distribution of the porous material, which was analyzed and

presented in Chap. 3. This crystal saturation can be characterized by a function $S(r)$ representing the volume fraction occupied by pores having a pore entry radius lower than r.

According to the experimental results presented in the Chap. 3, it was concluded that ettringite induced by both ESA and DEF crystallizes preferentially in the biggest capillary pores (if there are no cracks) and then penetrates into smaller pores later. Therefore, crystals in capillary pores will saturate the fraction of the capillary pores larger than the radius of curvature of the crystal-liquid interface r:

$$S_C = 1 - S(r) \tag{73}$$

$S(r)$ is calibrated from Van Genuchten model [280] and Eq. $P_C = \frac{2\gamma_{CL}}{r}$, with an expression as:

$$S(r) = (1 + (\frac{a}{r})^{\frac{1}{1-m}})^{-m} \tag{74}$$

where a and m are parameters determined from the pore size distribution.

As an example of the volume fraction curve, S_C, which results from the pore size distribution of specimen ESA-I-Ini measured by MIP (see section 3.1.3 and Fig. 3.12(a)), is shown in Fig. 4.3.

In addition, $S(r)$ depends on the type of the materials (concrete, mortar, and cement pastes) and the mix compositions. Three examples are shown in Table 4.1, which are calibrated from saturated fraction of crystals S_C. For example, the parameters for cement paste are calibrated from Fig. 4.3, and parameters for mortars and concrete come from unpublished results from IFSTTAR. These calibrated results are used in the following simulations.

Table 4.1 – The parameters a and m calibrated from pore size distributions of concrete, mortar and cement pastes.

Materials	Concrete	Mortar	Cement paste
a (nm)	127.86	155.82	15.979
m	0.379	0.2516	0.4388

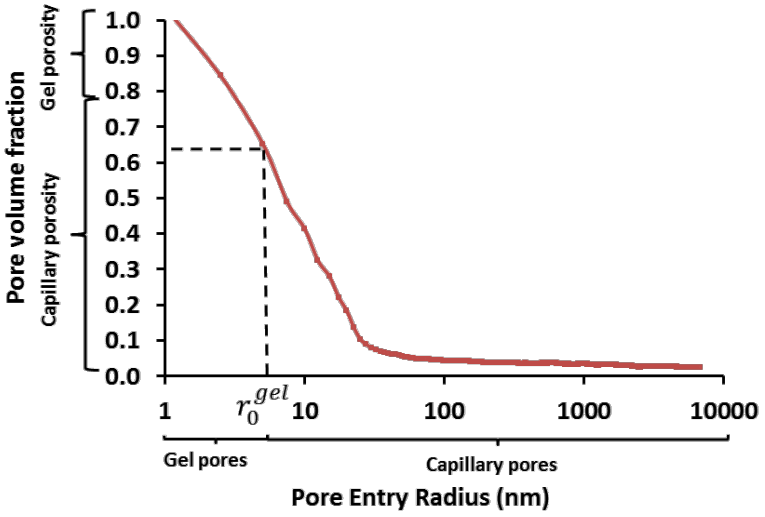

Figure 4.3 – Evolution of the pore volume fraction with the pore radius

4.4 Coupling with cement chemistry

4.4.1 Chemical assumptions for ettringite formation

It is assumed that ettringite forms from the reaction of sulfate and calcium ions with C_3A-rich hydration products and/or AFm [194, 201]. Examples of such reactions are:

$$\begin{aligned} C_3AH_6 \ + 3Ca^{2+} \ + 3SO_4^{2-} \ + 26H_2O \ &\rightarrow C_3A(C\bar{S})_3H_{32} \\ C_3A(C\bar{S})H_{12} \ + 2Ca^{2+} \ + 2SO_4^{2-} \ + 20H_2O \ &\rightarrow C_3A(C\bar{S})_3H_{32} \end{aligned} \tag{75}$$

All the calcium ions are provided by portlandite and C-S-H. It is assumed that the aluminium ions in the solution are provided by buffering agents as either hydrogarnet (C_3AH_6 is the most stable) or monosulfoaluminate (AFm) which is decomposed from the primary ettringite. Therefore, the main hydration products in cement-based materials include: CH, C-S-H (with C/Si=1.7), C_3A, and the primary ettringite. The content of these products can be predicted based on the mass balance of the mineral elements in cement, e.g. Ca, Si, Al and S. In addition, it is assumed that all the sulfur in the cement contributes to the primary AFt. Thus, the mass balance

equations in the case of ESA are expressed as:

$$\begin{aligned} n_{SiO_2} &= n_{CSH} \\ n_{CaO} &= n_{CH} + 1.7\, n_{CSH} + 3\, n_{C_3A} + 6\, n_{AFt} \\ n_{Al_2O_3} &= n_{C_3A} + n_{AFt} \\ n_{SO_3} &= 3\, n_{AFt} \end{aligned} \tag{76}$$

where n_{SiO_2}, n_{CaO}, $n_{Al_2O_3}$, and n_{SO_3} are the initial mass contents in the cement.

Then, the contents of the hydration products (n_{CSH}, n_{CH}, n_{C_3A}, and n_{AFt}) are:

$$\begin{aligned} n_{CSH} &= n_{SiO_2} \\ n_{CH} &= n_{CaO} - 1.7\, n_{SiO_2} - 3\, n_{Al_2O_3} - n_{SO_3} \\ n_{C_3A} &= n_{Al_2O_3} - \frac{1}{3}\, n_{SO_3} \\ n_{AFt} &= \frac{1}{3}\, n_{SO_3} \end{aligned} \tag{77}$$

For DEF, it is assumed that all the primary AFt is decomposed to AFm and free sulfate ions in the solution during the heating treatment. In addition, a part of the free sulfate ions in the pore solution is adsorbed on C-S-H. In this way, the initial sulfur just after the heat treatment is distributed into three parts: AFm (n_{AFm}), the free sulfate ions in pore solution ($n_{SO_4^{2-}}$), and the sulfate ions adsorbed on C-S-H ($n_{SO_4}^{ads}$).

The mass balance equations are:

$$\begin{aligned} n_{SiO_2} &= n_{CSH} \\ n_{CaO} &= n_{CH} + 1.7\, n_{CSH} + 3\, n_{C_3A} + 4\, n_{AFm} \\ n_{Al_2O_3} &= n_{C_3A} + n_{AFm} \\ n_{SO_3} &= n_{AFm} + n_{SO_4^{2-}} + n_{SO_4}^{ads} \end{aligned} \tag{78}$$

Then the solved contents of C-S-H, CH, C_3A, and AFm are:

$$\begin{aligned} n_{CSH} &= n_{SiO_2} \\ n_{CH} &= n_{CaO} - 1.7\, n_{SiO_2} - 3\, n_{Al_2O_3} - \frac{1}{3}\, n_{SO_3} \\ n_{C_3A} &= n_{Al_2O_3} - \frac{1}{3}\, n_{SO_3} \\ n_{AFm} &= \frac{1}{3}\, n_{SO_3} \\ n_{SO_4^{2-}} &= \frac{2}{3}\, n_{SO_3} - n_{SO_4}^{ads} \end{aligned} \tag{79}$$

In the model, the calcium ions are assumed to be buffered by CH, and aluminium ions are provided by C_3A (for ESA) and AFm (for DEF). Therefore, when either n_{CH} or n_{C_3A}/n_{AFm} is depleted, the formation of ettringite will be stopped.

4.4.2 Determination of the saturation index of ettringite

According to the chemical composition of ettringite, the saturation index of ettringite (β) in the pore solution is determined from the concentration of the ions: Ca^{2+}, Al^{3+}, SO_4^{2-} and OH^-. CH, C_3AH_6 and AFm are playing as buffering agents in the solution. First of all, the saturation index of AFt, CH, C_3AH_6 and AFm are presented as:

$$\begin{aligned}
&\log(\beta_{AFt}) = 6\ \log(c_{Ca^{2+}}) + 2\ \log(c_{Al^{3+}}) + 3\ \log(c_{SO_4^{2-}}) + 12\ \log(c_{OH^-}) - \log(K_{AFt});\\
&\log(\beta_{CH}) = \log(c_{Ca^{2+}}) + 2\ \log(c_{OH^-}) - \log(K_{CH});\\
&\log(\beta_{C_3AH_6}) = 2\ \log(c_{Al^{3+}}) + 3\ \log(c_{Ca^{2+}}) + 12\ \log(c_{OH^-}) - \log(K_{C_3AH_6});\\
&\log(\beta_{AFm}) = 2\ \log(c_{Al^{3+}}) + 4\ \log(c_{Ca^{2+}}) + \log(c_{SO_4^{2-}}) + 12\ \log(c_{OH^-}) - \log(K_{AFm});
\end{aligned} \tag{80}$$

where $K_{AFt} = 10^{-112}$, $K_{CH} = 10^{-5.14}$, $K_{C_3AH_6} = 10^{-20.49}$, and $K_{AFm} = 10^{-29.43}$ at 25 °C [281].

In addition, the aqueous solution is controlled by electroneutrality equation as:

$$2\ c_{Ca^{2+}} + c_{Na^+/K^+} + 3\ c_{Al^{3+}} = c_{OH^-} + 2\ c_{SO_4^{2-}} \tag{81}$$

where c_{Na^+/K^+} is the concentration of alkalis in the solution, which is assumed to be determined by the exterior solution in the case of ESA and by cement material for DEF.

Then, there are 5 equations with 8 unknowns: 4 concentrations ($c_{Ca^{2+}}$, $c_{Al^{3+}}$, $c_{SO_4^{2-}}$ and c_{OH^-}) and 4 saturation indexes (β_{AFt}, β_{CH}, $\beta_{C_3AH_6}$ and β_{AFm}). In addition, it is assumed that the portlandite is at the solubility limit, namely $\beta_{CH} = 1$ as long as portlandite is not depleted. So it ends up with 5 equations and 7 unknowns: 4 concentrations ($c_{Ca^{2+}}, c_{Al^{3+}}, c_{SO_4^{2-}}$, and c_{OH^-}) and 3 saturation indexes ($\beta_{AFt}, \beta_{C_3AH_6}$ and β_{AFm}). Then, 2 more equations are needed.

For ESA, it is assumed that $\beta_{C_3AH_6} = 1$, and $c_{SO_4^{2-}}$ is an input determined by the exterior solution used in the experiments.

In the case of DEF, the saturation index of AFm is assumed to be 1 and the content of sulfate ions is given. The alkalis provided by cement material are assumed to be dissolved all in the solution, then the concentration of alkalis can be predicted. The initial content of free sulfate ions in the pore solution is determined as (see section 4.4.1):

$$n_{SO_4^{2-}} = \frac{2}{3} n_{SO_3} - n_{SO_4}^{ads} \tag{82}$$

where the first part on the right is the total amount of the free sulfate ions decomposed from the primary ettringite, and $n_{SO_4}^{ads}$ is the amount of sulfate ions adsorbed on C-S-H.

In the literature, plotting the quantity of sulfate ions adsorbed on C-S-H vs. the sulfate concentration at equilibrium in the solution is the most common way to represent the results of adsorption studies. The Langmuir isotherm model was found to well represent this relationship [97] as:

$$1/C_b = 1/(kC_{bm})\ 1/C + 1/C_{bm} \tag{83}$$

where k is the affinity constant, C is the concentration at equilibrium, C_b is the quantity adsorbed per gram of the C-S-H, and C_{bm} is the quantity adsorbed when the surface is saturated. Then, the content of sulfate ions that adsorbed on C-S-H can be predicted as:

$$n_{SO_4}^{ads} = C_b \times n_{CSH} \times M_{CSH} \tag{84}$$

where n_{CSH} is the content of C-S-H, which equals to n_{SiO_2}, M_{CSH} is the molar mass of C-S-H. In the experiments of [97], 3.4 g C-S-H was added into a 250 mL mixed solution of NaOH and Na_2SO_4. Then the quantity of adsorbed sulfate ions was measured, and a relationship between the quantity of adsorbed sulfate ions and the equilibrium concentration was found. In order to simulate a pH value of around 13, the experimental results of the mixed solution with a concentration of NaOH around 0.1 mol/L are chosen. Then the calibrated results are: $k = 1.149$ L/mol, and $C_{bm} = 13.6$ mmol per gram of the C-S-H. This model is used to simulate the amount of sulfate ions adsorbed on C-S-H in this study.

During DEF, the formation of ettringite consumes sulfate ions. Thus the content of sulfate ions in the solution is decreased. Then, at a given time, t, the content of sulfate ions in the solution can be determined with an expression as:

$$n_{\mathrm{SO}_4^{2-}}(t) = \frac{2}{3}\, n_{\mathrm{SO}_3} - n^{ads}_{\mathrm{SO}_4}(t) - 2\, n_{\mathrm{AFt}}(t) \tag{85}$$

where $n^{ads}_{\mathrm{SO}_4}(t)$ is the content of sulfate ions adsorbed on C-S-H at time t, which depends on the concentration of sulfate ions in pore solution. $n_{\mathrm{AFt}}(t)$ is the content of ettringite formed at time t, which increases with time. When all the free sulfate ions in the solution are completed, the formation of ettringite will be stopped, as well as the expansion.

4.5 Summary of the constitutive laws

The swelling strain as predicted by Eq. 63 and 65 depends on several factors:
(1) the mechanical properties: Young's modulus E and Biot's coefficient b. These two parameters are determined by the specimens. In this study, E is assumed to be 20 GPa, and b=1.
(2) the property of the microstructure presented through the volume fraction occupied by ettringite: S_C.
(3) two kinetic constants: a_i and a_p for the crystal growth in the pore invasion and deformation processes, which should be calibrated respectively.
(4) the saturation index of ettringite: β, which results from the ion compositions of the pore solution.

4.6 Sensitivity analyses

A process of the crystallization in a porous material has been explained above, and the input β, two kinetic constants a_i and a_p have been introduced in the model. Then, the effect of these variables on the S_C, elastic and damage strain will be analyzed in this part.

4.6.1 Sensitivity of the evolution of S_C (Eq. 71) and the elastic strain (Eq. 63) with β and a_i

The Eq. 71 ($\frac{d}{dt}(S_C) = a_i\ (1 - \frac{\beta_i}{\beta})$) is solved by varying β and kinetic constant a_i. According to Fig. 4.4(a), the saturation index of crystal in pore solution, β, contributes essentially to the final crystal saturation and has a restricted effect on the kinetics at the last moment before reaching the equilibrium. The kinetic constant a_i (see Fig. 4.4(b)) has an effect on the rate only. The crystal saturation with a higher kinetic constant a_i reaches the final state faster.

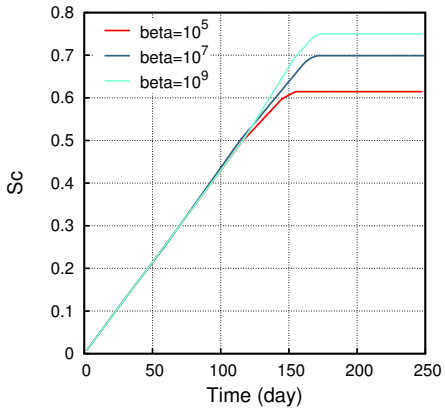

(a) Effect of β on S_C, with $a_i = 5 \times 10^{-8}$

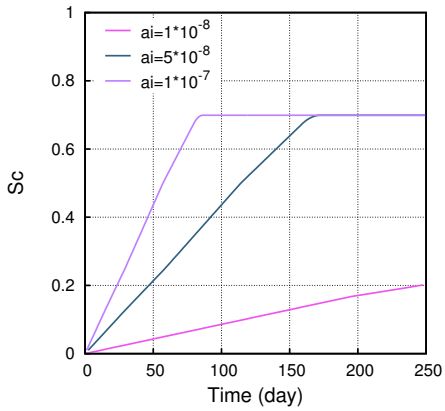

(b) Effect of kinetic constant a_i on S_C, with $\beta = 1 \times 10^7$

Figure 4.4 – Sensitivity analyses of β and a_i on S_C

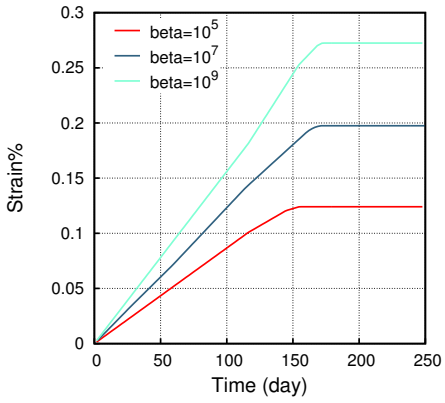

(a) Effect of β on strain% with $a_i = 5 \times 10^{-8}$, E = 20 GPa and b=1.

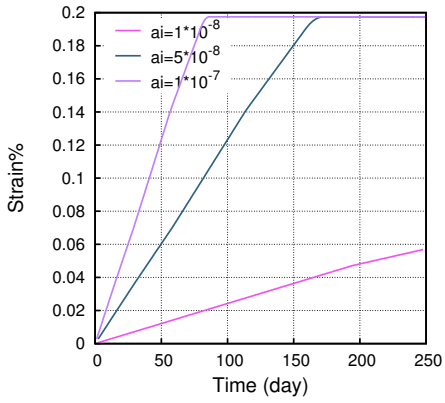

(b) Effect of kinetic constant a_i on strain% with $\beta = 1 \times 10^7$, E = 20 GPa and b=1.

Figure 4.5 – Sensitivity analyses of β and a_i on elastic strain

The effects of β and a_i on the elastic strain are analyzed in this part, see Fig. 4.5.

Eq. 63 ($\epsilon = \frac{b}{E} S_C P_C$) tells us that the effect of β on the strain not only comes from the S_C which has been explained above but also from P_C (see Eq. 53). The higher saturation index forces ettringite to form in smaller pores, which in turn increases the crystal saturation and the time required to reach equilibrium. In this way, the final expansion increases with the ettringite saturation index. However, a_i has only effect on the kinetics.

4.6.2 Sensitivity of the evolution of S_C (Eq. 71) and damage strain (Eq. 72) with constant β, a_i and a_p in the case of ESA

Eq. 71 is solved by varying the input β and two kinetic constants a_i and a_p. The effects of β and a_i on S_C have been analyzed in the previous section. Moreover, the kinetic constant a_p has no effect on the crystal saturation.

The sensitivity of input β and two kinetic constants a_i and a_p on expansion are studied by solving Eq. 72. It is shown in Fig. 4.6 (a) and (b) that the input β and kinetic constant a_i have effect only on the elastic phase (strain less than 0.02% in this analyses) and the kinetics of damage strain is only determined by the parameter a_p. Fig. 4.6 (a) illustrates that the higher β leads to shorter elastic duration. The elastic strain ($\epsilon = bS_C P_C/E$) is determined by S_C and P_C. With a higher P_C resulting from the higher β (see Eq. 53), less S_C is required to reach the elastic peak ($\epsilon_0 = 2 \times 10^{-4}$ in this part). The effect of a_i on the elastic range is obvious: less a_i takes more time to get to yield point, which leads to a longer elastic duration. Fig. 4.6 (c) illustrates that higher value for parameter a_p contributes to faster kinetics of the damage strain.

Summarizing the analyses above, it is concluded that in the case of ESA, the elastic behavior is determined by β and a_i, and the kinetics of the damage range is only controlled by the kinetic constant a_p. These observations enable us to calibrate the kinetic constants a_i and a_p from elastic and damage responses of ESA specimens during the experiments.

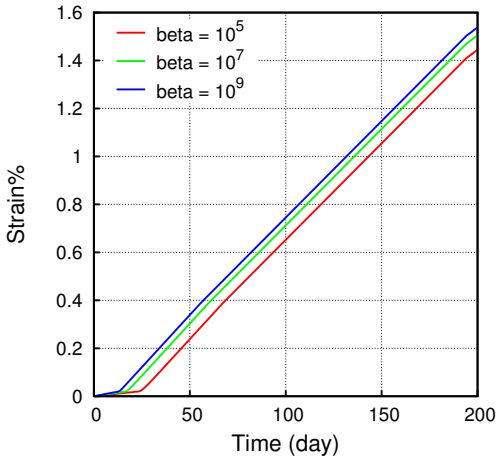

(a) Effect of β on strain% with $a_i = 5 \times 10^{-8}$, $a_p = 1 \times 10^{-9}$

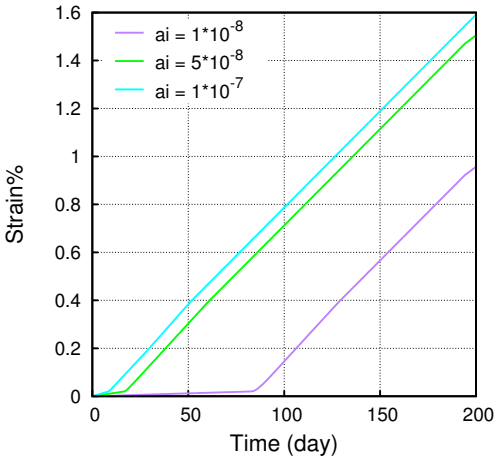

(b) Effect of kinetic constant a_i on strain% with $\beta = 1 \times 10^7$, $a_p = 1 \times 10^{-9}$

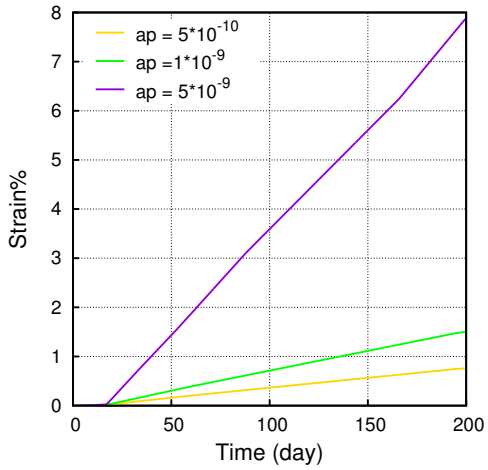

(c) Effect of kinetic constant a_p on strain% with $\beta = 1 \times 10^7$, $a_i = 5 \times 10^{-8}$

Figure 4.6 – Sensitivity analyses of β, a_i, and a_p on damage strain, with K = 20 GPa, b=1, $\epsilon_0 = 2 \times 10^{-4}$

4.6.3 Sensitivity of the evolution of S_C (Eq. 71) and damage strain (Eq. 72) with a_i, a_p, and a decreased β in the case of DEF

In the case of DEF, the initial content of sulfur, n_{SO_3}, is an input to determine the initial value for β and the amount of free sulfate ions in the pore solution, $c_{SO_4^{2-}}$. As crystals precipitate, sulfate ions are consumed. When all the SO_4^{2-} in the pore solution are completed, the crystals will stop growing. It means that the initial content of sulfur determines the total AFt formed in the material after the specimen reaches the plateau. Fig. 4.7(a) and 4.8(a) show that the β_{ini} has a positive effect on the final S_C and the final damage strain. It is easy to understand that with a higher

content of sulfate ions provided in the pore solution, more ettringite forms in both the pore invasion and deformation processes. Moreover, a higher β_{ini} contributes to a faster increase rate of damage strain. This could be explained by Eq. 72 ($\frac{d}{dt}(\varepsilon) = a_p(1-\frac{\beta_p}{\beta})$). The product of $a_p(1-\frac{\beta_p}{\beta})$ is increased with a higher β_{ini}, which leads to a faster kinetics of strain.

A complex effect of a_i and a_p on S_C and damage strain is found. According to Eq. 56 and 59, the final content of AFt formed after the expansion stops can be expressed as:

$$n_{\mathrm{AFt}} = (S_C\Phi_0 + S_C\epsilon)/V_{\mathrm{AFt}} \tag{86}$$

Provided that all the SO_4^{2-} is consumed at the end of the attack, there is a distribution of the formed AFt in the pore invasion and pore deformation process, which correspond to final S_C and strain, respectively. If less AFt formed in the pore invasion process, more crystal will be distributed in the pore deformation after the swelling stops. For example, in Fig. 4.7(b), less S_C is occupied when $a_i = 1 \times 10^{-8}$ compared to the other two cases, but much more damage strain is presented in Fig. 4.8(b). It can be concluded that a small quantity of ettringite formed in S_C contributes to a larger distribution of ettringite in the deformation process.

Based on the observations above, it is concluded that the initial content of sulfur fixes the total amount of ettringite formed in the material, and two kinetic constants determines the distribution of the ettringite in pore invasion and deformation processes. It means these two processes are in a "competition" state to gain ettringite. Therefore, the plateau value of swelling should be determined by three inputs: $n_{\mathrm{SO_3}}$, a_i and a_p, as well as the kinetics.

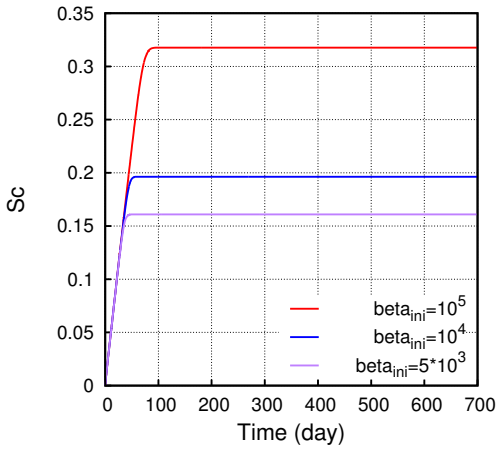

(a) Effect of β_{ini} on S_C, with $a_i = 5 \times 10^{-8}$, $a_p = 1 \times 10^{-9}$

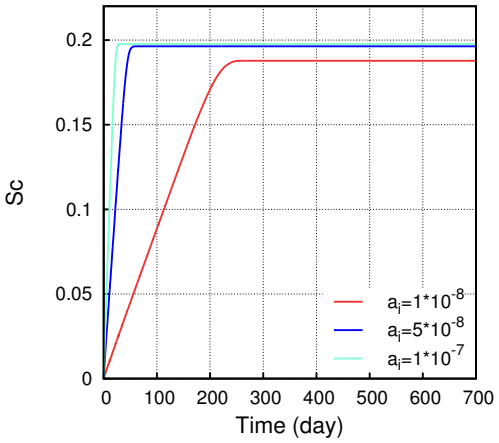

(b) Effect of the kinetic constant a_i on S_C, with $\beta_{ini} = 1 \times 10^4$, $a_p = 1 \times 10^{-9}$

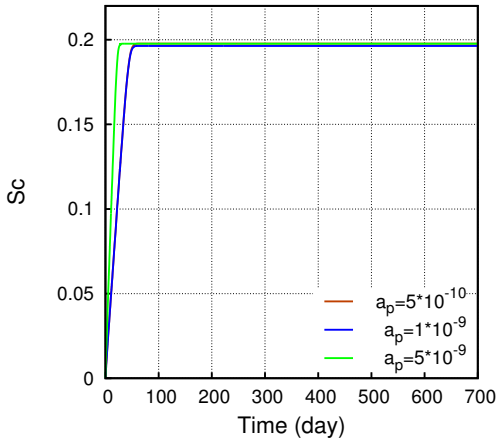

(c) Effect of the kinetic constant a_p on S_C, with $\beta_{ini} = 1 \times 10^4$, $a_i = 5 \times 10^{-8}$

Figure 4.7 – Sensitivity analyses of initial β, a_i, and a_p on S_C

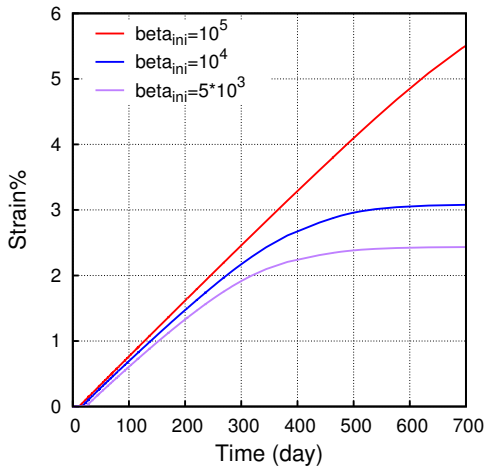

(a) Effect of β_{ini} on strain% with $a_i = 5 \times 10^{-8}$, $a_p = 1 \times 10^{-9}$, K = 20 GPa, b=1, $\epsilon_0 = 1 \times 10^{-4}$

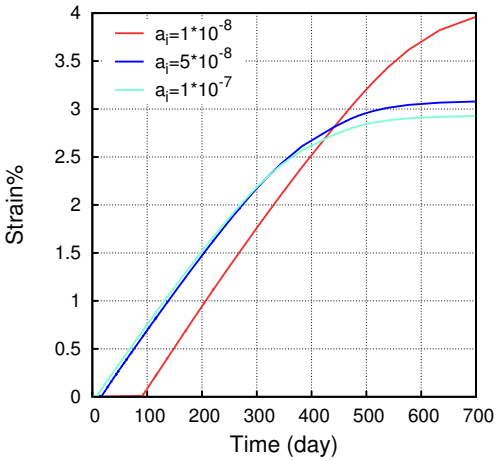

(b) Effect of the kinetic constant a_i on strain% with $\beta_{ini} = 1 \times 10^4$, $a_p = 1 \times 10^{-9}$, K = 20 GPa, b=1, $\epsilon_0 = 1 \times 10^{-4}$

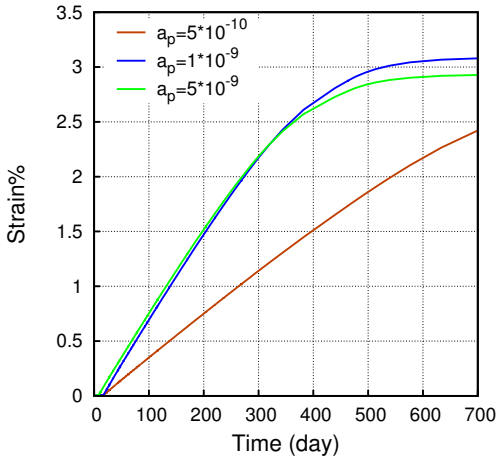

(c) Effect of the kinetic constant a_p on strain% with $\beta_{ini} = 1 \times 10^4$, $a_i = 5 \times 10^{-8}$, K = 20 GPa, b=1, $\epsilon_0 = 1 \times 10^{-4}$

Figure 4.8 – Sensitivity analyses of initial β, a_i and a_p on damage strain

4.7 Simulation of experiments of this study

In this part, the experimental studies on cement paste performed in this study are simulated and analyzed via the proposed model. First, the expansion of the specimens are simulated, which meanwhile predicts the consumption of the hydration products and the precipitation of ettringite. Further, the crystallization process is illustrated by the model, including the pore invasion and pore deformation process. In addition, the pore range where ettringite forms in the material is predicted in the model, which can be compared with the experimental results measured by MIP in section 3.1.3.1.

4.7.1 Simulation of ESA in this study

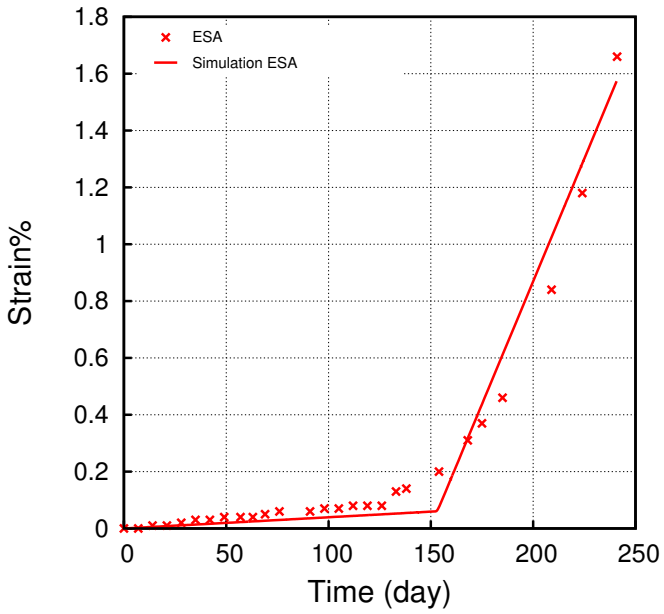

Figure 4.9 – Simulation of $2 \times 2 \times 12$ cm^3 specimen exposed to ESA in this study.

In this simulation, the initial content of products are: $n_{\mathrm{CH}} = 1.53$ mol/L, $n_{\mathrm{CSH}} = 1.393$ mol/L, $n_{\mathrm{C_3A}} = 0.114$ mol/L, and $n_{\mathrm{AFt}} = 0.059$ mol/L. The simulated expansion curve is shown in Fig. 4.9 with parameters: $a_i = 9 \times 10^{-9}$ and $a_p = 2 \times 10^{-9}$. As the sodium sulfate solution was renewed during attack with $c_{\mathrm{Na_2SO_4}} = 0.12$ mol/L, the concentration of sulfate and sodium ions are kept constant in the simulation as: $c_{\mathrm{SO_4^{2-}}} = 0.12$ mol/L and $c_{\mathrm{Na^+}} = 0.24$ mol/L. With the consumption of CH, $\mathrm{C_3AH_6}$ and sulfate ions, AFt precipitates, see Fig. 4.10. However, when any of the reactants is depleted, the formation of ettringite will be stopped.

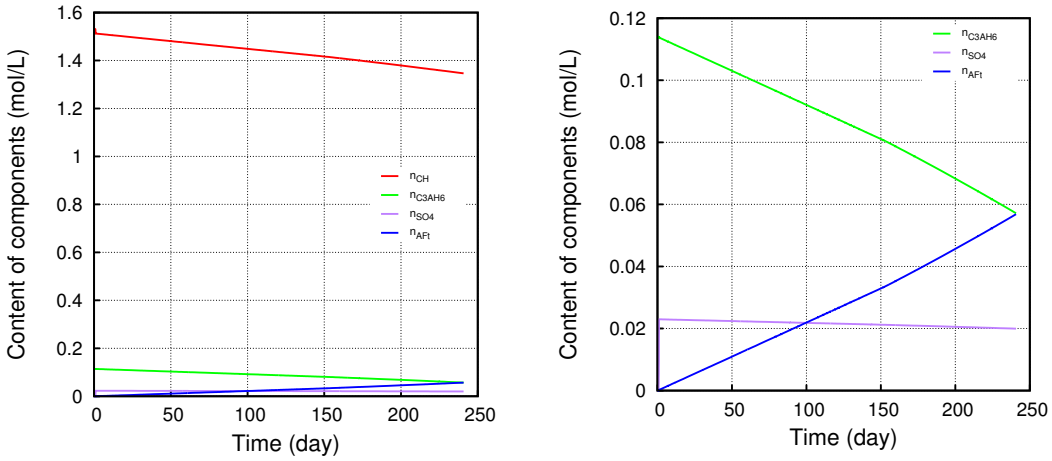

Figure 4.10 – The consumption of CH, C_3AH_6 and the precipitation of AFt in the simulation

The crystallization in the material is simulated in the model as well. As the concentration of Ca^{2+}, Al^{3+}, OH^-, and SO_4^{2-} are assumed to be constant in the pore solution, which provides a constant saturation index of ettringite in the pore solution (β), see Fig. 4.11. As ettringite forms from the largest pores and penetrates into smaller ones (see Fig. 4.12), the saturation index of ettringite at the crystal-liquid interface (β_i) increases, which results in an increase in S_C (see Fig. 4.13). β_i continues to grow until it reaches the value of β when the crystal-liquid interface is at equilibrium. Meanwhile, the saturation index of ettringite at the crystal-solid interface (β_p) increases drastically to β at the beginning of the crystallization process due to the occurrence of crystallization pressure at this interface. Then, with an increase of S_C, the effective tensile stress ($\sigma' = bS_CP_C$) grows. When material could not resist the increasing effective tensile stress, cracks occur and material comes into damage range. Without the constraint of pore wall, β_p drops rapidly and approaches to 1. The big difference between β and β_p indicates a continuous non-equilibrium at the crystal-solid interface, which means that ettringite will grow until one of the reactants is depleted.

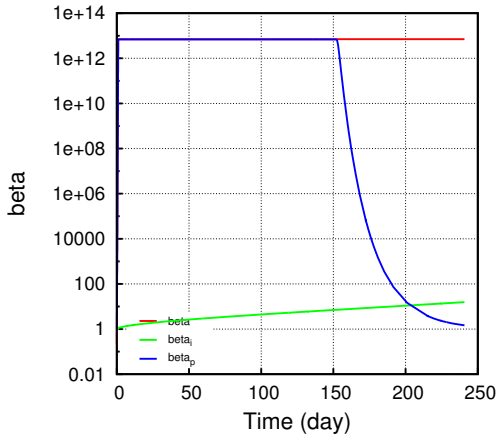

Figure 4.11 – The evolution of saturation index of ettringite in the pore solution, at the crystal-liquid and the crystal-solid interface.

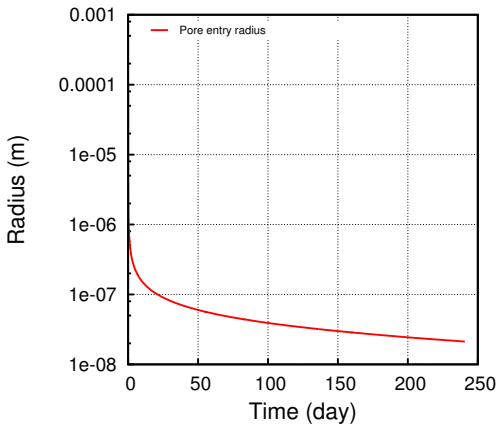

Figure 4.12 – The evolution of pore entry radius.

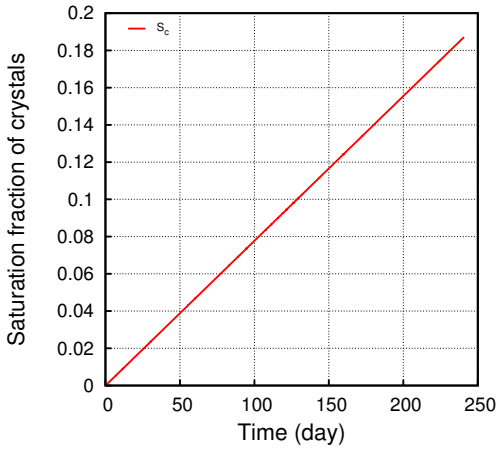

Figure 4.13 – The evolution of saturated fraction of crystals.

4.7.2 Simulation of DEF in this study

In this simulation, the initial content of products are: $n_{\mathrm{CH}} = 1.65$ mol/L, $n_{\mathrm{CSH}} = 1.393$ mol/L, $n_{\mathrm{C_3A}} = 0.114$ mol/L, and $n_{\mathrm{AFm}} = 0.059$ mol/L. The simulated expansion curve is shown in Fig. 4.14 with calibrated parameters: $a_i = 6.8 \times 10^{-9}$ and $a_p = 5.2 \times 10^{-10}$. The consumption of AFm, sulfate ions, and the precipitation of AFt are shown in Fig. 4.15. For each one mole of ettringite formed, one mole of AFm is consumed, as well as two moles of sulfate ions which come from both the pore solution and the one adsorbed on C-S-H, see Fig. 4.16. When either AFm or sulfate ions are depleted, the formation of ettringite will be stopped and the expansion will reach a plateau.

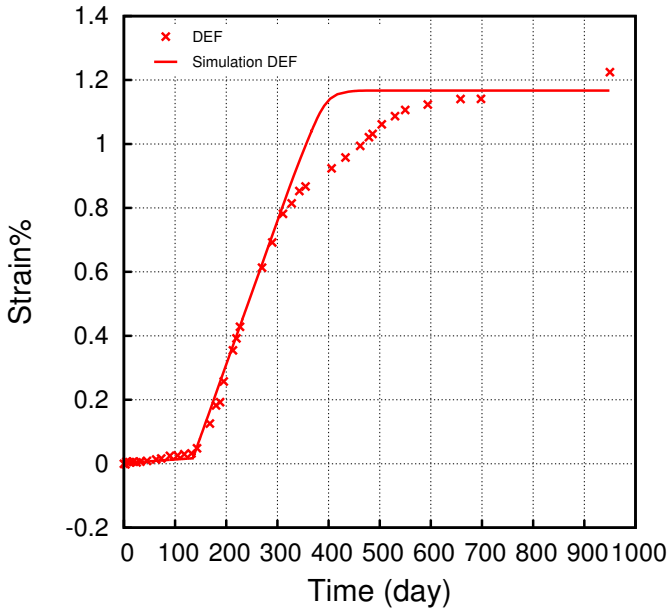

Figure 4.14 – Simulation of $11 \times 11 \times 22$ cm^3 specimen exposed to DEF in this study.

As concluded from Chap. 3, ettringite forms in the big voids firstly and then penetrates into smaller pores; it leads to a decrease of pore entry radius (see Fig. 4.17). Consequently, an increase of β_i is observed, see Fig. 4.18. Since sulfate ions in the pore solution is limited and consumed, the saturation index of ettringite in solution decreases, as shown in Fig. 4.18. An equilibrium state at the crystal-liquid interface is reached when the increasing β_i meets the decreased β, from which moment S_C reaches a plateau (see Fig. 4.19). In the following period, the equilibrium state at the crystal-liquid interface is assumed to be maintained, which means that the pore entry radius stops decreasing and S_C is kept at the plateau. In the pore deformation process, the crystal-solid interface reaches an equilibrium rapidly at the beginning

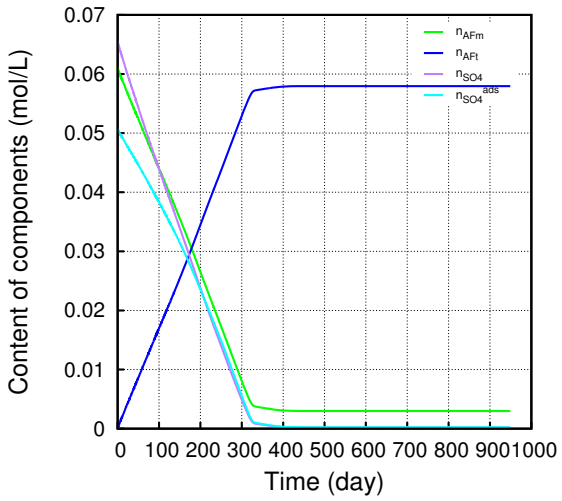

Figure 4.15 – Evolution of components in DEF.

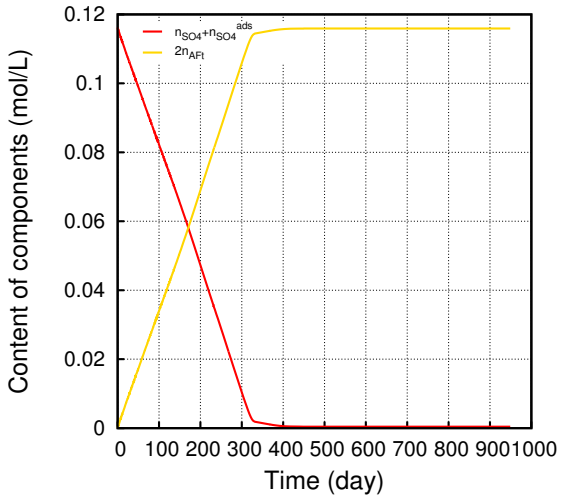

Figure 4.16 – The consumption of sulfate ions and the precipitation of AFt.

of crystallization process until cracks occur. Then β_p drops drastically to 1. At a certain moment, the equilibrium at the crystal-solid interface is regained when β is reduced to 1, which is induced by the consumption of sulfate ions. Consequently, the formation of ettringite is stopped and the expansion reaches a plateau.

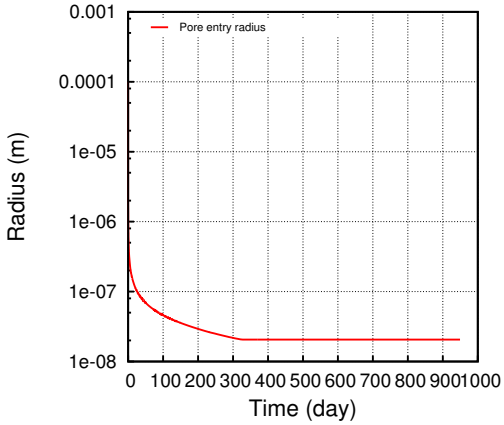

Figure 4.17 – Evolution of pore entry radius in DEF.

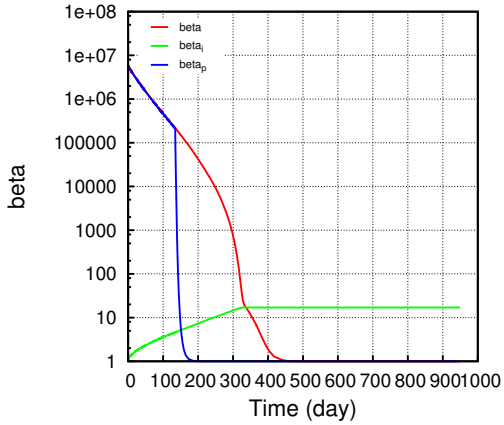

Figure 4.18 – Evolution of saturation index of ettringite in the pore solution, at the crystal-solid and crystal-liquid interface.

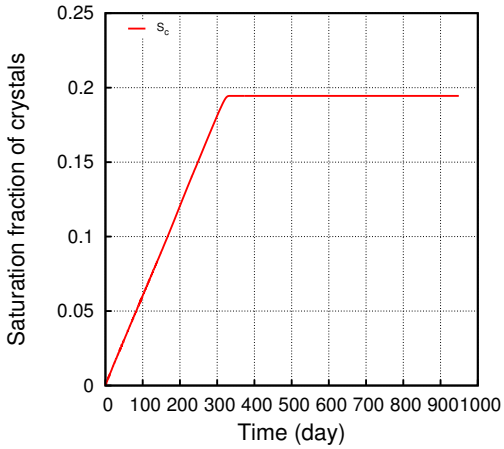

Figure 4.19 – Evolution of S_c in DEF.

As presented above, a continuous decrease of pore entry radius is predicted in the model, which stops at around 20 nm both for ESA and DEF. According to the analyses in Chap. 3, the minimum pore size where pore volume reduces is 3.7 nm for ESA-I-small specimen and 4 nm for DEF-I-big specimen. The discrepancy between experimental and modeling results should come, amongst other possibilities, from the assumption of the saturation index of ettringite in the pore solution, which has a significant effect on the crystallization process. For example, the saturation index of CH, and C_3AH_6/AFm are assumed to be 1, which provide an assumed concentration of Ca^{2+} and Al^{3+}, and may lead to the difference with the experimental results.

4.8 Simulations of experiments from the literature

4.8.1 Simulation of ESA in restrained conditions

Figure 4.20 – PVC mould and three types of restraints [282].

Ma et al. experimentally studied hollow cement paste cylinders exposed to external sulfate attack in a restraint condition. Three types of longitudinal restraints were applied on the hollow cement paste cylinders (CEM I 42.5 N) by means of a spring and steel bars (middle diameter 3 mm for low-restraint and 7 mm for high-restraint) through the specimens in order to facilitate non-, low- and high-restraint conditions. PVC moulds with stainless steel rods in the center are made to obtain the thin-walled hollow cement paste cylinders, as shown in Fig. 4.20. The thin-walled hollow cylinders were immersed in saturated limewater at 20 °C for 90 days firstly, then together with three types of restraints immersed in sodium sulfate solutions with the concentrations of 1.5 g/L and 30 g/L, respectively. Strain gauges were glued to the middle part of the stainless steel bars to measure the local restrained expansion. Then the total strain of the specimens in the axial direction, ϵ_z, was calculated in their study (see Fig. 4.21).

The specimen was in a stress-strain state as:

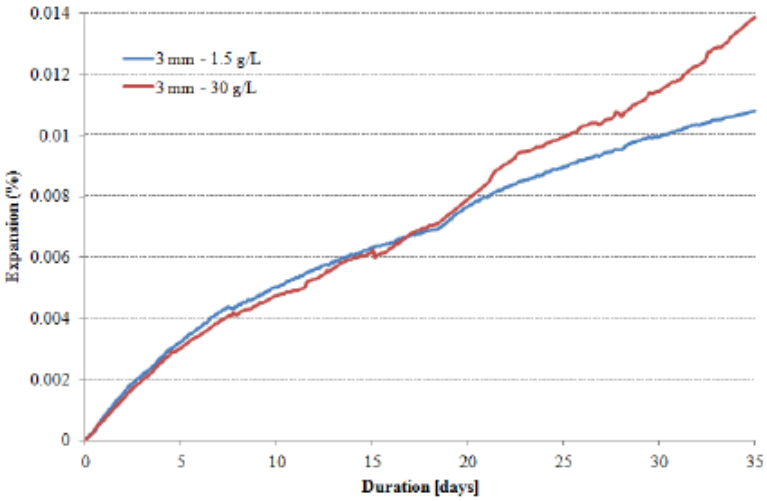

Figure 4.21 – Expansion under low-restraint

Axial stress: $\sigma_z^{'} = \sigma_z + bS_C P_C$; Axial strain: ϵ_z (see Fig. 4.21);
Radial stress: $\sigma_r^{'} = bS_C P_C$; Radial strain: ϵ_r;
Hoop stress: $\sigma_\theta^{'} = bS_C P_C$; Hoop strain: ϵ_θ.
In the axial direction, the stress-strain equation can be expressed as:

$$\sigma_z^{'} - \nu(\sigma_r^{'} + \sigma_\theta^{'}) = E\epsilon_z \tag{87}$$

where ν is the Poisson's ratio ($\nu = 0.2$ in this study).

Then, it gives:

$$\sigma_z = E\epsilon_z - (1 - 2\nu)bS_C P_C \tag{88}$$

In the model, the bulk modulus of the cement paste specimens is adopted as 20 GPa, and the Biot's coefficient b is 1. For S_C, the parameters which represent the pore structure of cement paste used in the model are: $a = 15.979$ nm and $m = 0.4388$, see Table 4.1. The initial content of the products used in the simulation (based on Table 2.3) are: $n_{\mathrm{CH}} = 1.53$ mol/L, $n_{\mathrm{CSH}} = 1.393$ mol/L, $n_{\mathrm{C_3AH_6}} = 0.114$ mol/L, and $n_{\mathrm{AFt}} = 0.06$ mol/L. The generated stress under low-restraint and the corresponding simulated results based on Eq. 88 are presented in Fig. 4.22. In this figure, the compressive axial stress is presented in positive. A kinetic constant $a_i = 2.0 \times 10^{-8}$ is calibrated from the generated stress of specimen 3mm-30g/L, in which case the diffusion process is faster and assumed completed. Then this constant is used to

predict another specimen in the case of 3mm-1.5g/L. It shows that the absolute value of predicted axial stress for 3mm-1.5g/L is quite close but lower than the actual one, which means that the predicted $bS_C P_C$ is underestimated. However, the predicted P_C may be underestimated and the parameter a_i calibrated from the higher concentration may overestimate the S_C. The product of these two variables may lead to an underestimated value.

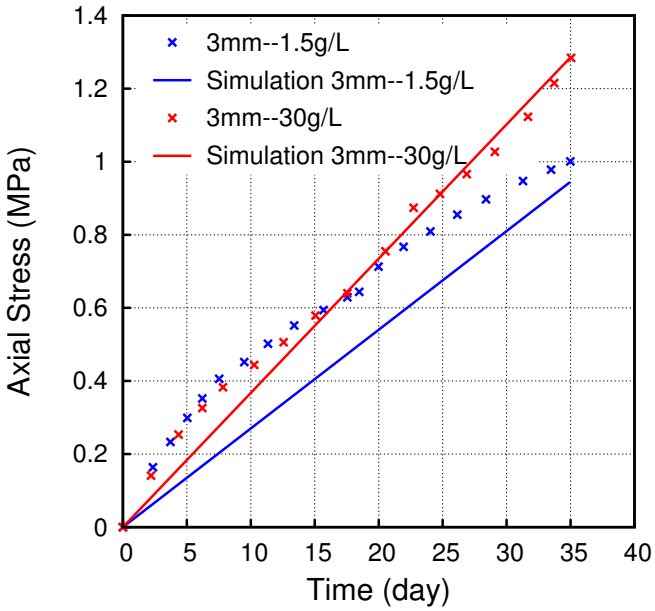

	Concentration of SO_4^{2-} (mol/L)	Concentration of Na^+ (mol/L)	a_i (s^{-1})
3mm – 1.5 g/L	0.01	0.02	2.0×10^{-8}
3mm – 30g/L	0.21	0.42	2.0×10^{-8}

Figure 4.22 – Simulation results [282].

4.8.2 Simulation of DEF in confined conditions

Burgher et al. studied the level of confining stress necessary to stop DEF [283] by Hoek cell, which was first designed by Franklin E. Hoek [284]. The typical Hoek Cell is shown in Fig. 4.23. A continual supply of water was set to allow for water to circulate to and from the ends of the concrete cylinders.

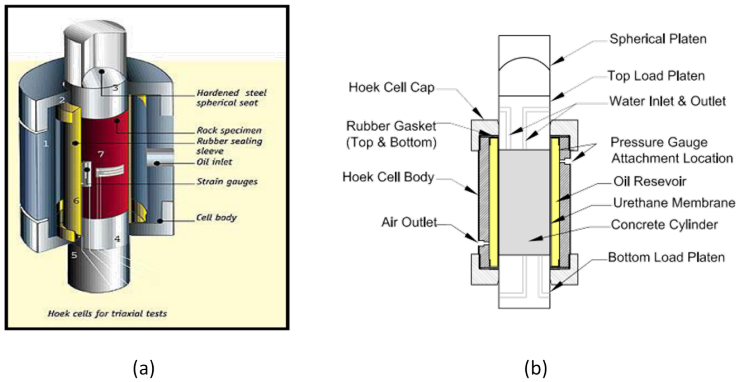

(a) (b)

Figure 4.23 – (a)Typical Hoek Tri-Axial Cell; (b) Cross-section View of Hoek Cell with concrete test cylinders and load platens shown [283]

The cylinders (8.57 cm in diameter by 17.78 cm in length) were fabricated and exposed to DEF with maximum temperature of 96 °C for 12h, at the end, cured in limewater for long-term storage at 23 °C. The experimental results of two cylinders (MC1 and MC2) are simulated in this study. These two cylinders were fabricated and cured in the same way and were removed from the limewater at approximately 110 days with expansions: 0.61% for C1 and 0.51% for C2. The cylinders were placed inside the Hoek cell, and pressures were exerted when specimens started to expand. The confining pressure of the hydraulic oil increased until it reached a level of confining pressure at which the internal stress was balanced by the external pressure (see Fig. 4.24). However, a lower degree of confining stress was exerted on specimen MC1, which was explained to be due to a suspected hydraulic oil leak by the authors.

The specimens were situated in a restrained condition with axial stress σ_z, radial stress σ_r, and hoop stress σ_θ ($\sigma_r = \sigma_\theta$ = confining stress, see Fig. 4.24). The axial strain, ϵ_z, was small and could be neglected. Then, in the axial direction:

$$\sigma_z + bS_C P_C - \nu(\sigma_r + \sigma_\theta + 2bS_C P_C) = E\epsilon_z = 0 \tag{89}$$

which gives:

$$\sigma_z = 2\nu\sigma_r - (1 - 2\nu)bS_C P_C \tag{90}$$

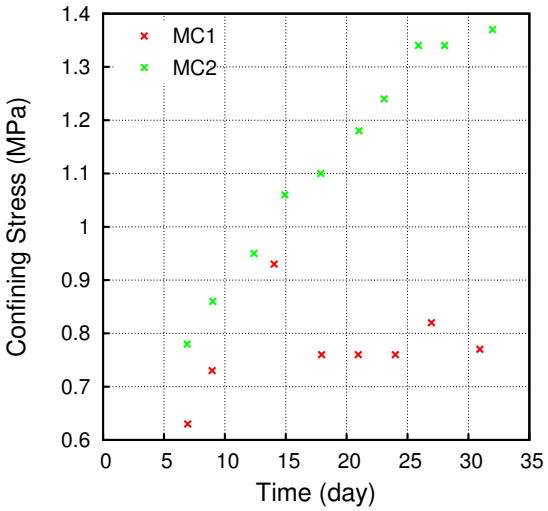

Figure 4.24 – The measured confining stresses for MC1 and MC2 according to [283].

where $\nu = 0.2$, b=1, and E=20 GPa are assumed in the simulation. The parameters used to represent the pore structure of concrete specimens are: $a = 127.86$ nm and $m = 0.379$, see Table 4.1. The initial content of products used in the simulations ((based on Table 2.3)) are: $n_{\mathrm{CH}} = 1.65$ mol/L, $n_{\mathrm{CSH}} = 1.393$ mol/L, $n_{\mathrm{C_3A}} = 0.114$ mol/L, $n_{\mathrm{AFm}} = 0.06$ mol/L, $n_{\mathrm{SO_4^{2-}}} = 0.063$ mol/L, and $n^{ads}_{\mathrm{SO_4}} = 0.05$ mol/L.

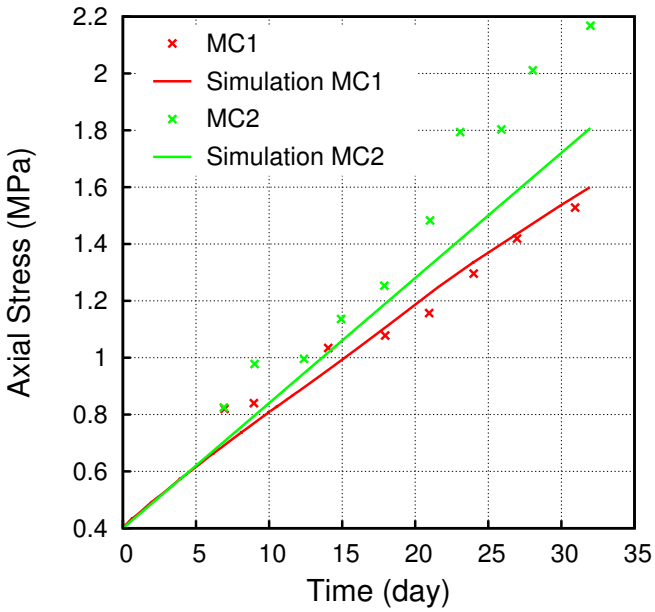

	Initial concentration of SO_4^{2-} (mol/L)	Concentration of Na^+ (mol/L)	a_i (s^{-1})
MC1	0.325	1	1.8×10^{-8}
MC2	0.325	1	1.8×10^{-8}

Figure 4.25 – Simulated axial stress of cylinders [283]

First, a kinetic constant $a_i = 1.8 \times 10^{-8}$ is calibrated from axial stress of specimen MC1 according to Eq. 90. Then, a same value of a_i is used to predict the axial stress for MC2, see Fig. 4.25. The compressive axial stress is presented in positive. The predicted axial stress for MC2 shows a quite close value with experimental data. This proves that the proposed poromechanical model works well when it is coupled with elasticity theory.

4.8.3 Simulation of ESA in free swelling

Due to the unlimited provision of sulfate ions from exterior solution, a constant β based on the experimental conditions is predicted, see section 4.4.2. It is clearly observed from the experimental swelling that the curve includes two parts: slowly increased and accelerated parts, the kinetics of which are mainly governed by two independent constants: a_i and a_p. The connection point of these two parts corresponds to the yield point in the constitutive strain-stress curve. Therefore, the yield strain point should be fixed from the swelling curves first. Then, two kinetic constants could be calibrated from the increase rate of the expansion. In addition, the bulk modulus of the porous body is adopted as 20 GPa and the Biot's coefficient b is 1.

Ferraris et al. studied the external sulfate attack by exposing mortar specimens to sodium sulfate solutions with different pH conditions and different geometries [63]. The parameters, which represent the pore structure of mortar specimens (see Tab. 4.1), are used as: $a = 155.82$ nm and $m = 0.2516$. The initial content of the products used in the simulation (based on Table 2.3) are: $n_{\mathrm{CH}} = 1.53$ mol/L, $n_{\mathrm{CSH}} = 1.393$ mol/L, $n_{\mathrm{C_3AH_6}} = 0.114$ mol/L, and $n_{\mathrm{AFt}} = 0.06$ mol/L. Some of the experimental results are selected and presented in this study. The mortar prisms ($25 \times 25 \times 276$ mm^3) were stored in pH uncontrolled and pH = 7 conditions with an initial concentration of sodium sulfate solution of 5% by weight. The initial concentration of sulfate ions and alkalis can be calculated as:

$$c_{\mathrm{SO_4^{2-}}} = \frac{5\%}{\mathrm{M_{Na_2SO_4}}} / \rho_{\mathrm{liquid}} \tag{91}$$

$$c_{\mathrm{Na^+}} = 2\, c_{\mathrm{SO_4^{2-}}} \tag{92}$$

where $\mathrm{M_{Na_2SO_4}}$ is the molar mass of Na_2SO_4, and ρ_{liquid} is the density of the liquid, which is assumed to be 1 g/mL. In this way, the calculated concentration of sulfate

ions is 0.38 mol/L, and the concentration of Na^+ is 0.76 mol/L. The solution, which was not pH controlled, was renewed each time an expansion measurement was made. The pH controlled condition was maintained by adding sulfuric acid. This method was proved to be able to fix the hydroxyl ion concentration as well as the sulfate ion concentration in solution [62]. Therefore, $c_{SO_4^{2-}}$ and c_{Na^+} are kept constant in the simulation for both conditions.

First, two kinetic constants a_i and a_p are calibrated from the expansion curve of the specimen in pH uncontrolled condition. The results are: $a_i = 9 \times 10^{-9}$ and $a_p = 1.1 \times 10^{-9}$. The pH condition simulated is shown in Fig. 4.26, which stables at around 12. The evolution of content of CH, $C\bar{S}H_2$, C_3AH_6 and ettringite are shown in Fig. 4.27. Then, these two parameters are used to predict the swelling curve of the specimen which is in a pH controlled condition at 7 (see Fig. 4.28). However, no expansion is observed. A condition of pH=7 contributes to a rapid dissolution of portlandite and the precipitation of gypsum, see Fig. 4.29. The calcium in the gypsum comes mainly from the dissolution of portlandite and the decalcification of C-S-H. However, no ettringite is formed, which is not stable at pH=7. In this model, the formation of ettringite is supposed to be the only reason for expansion. That is why the predicted curve "Simulation pH=7" does not show any expansion.

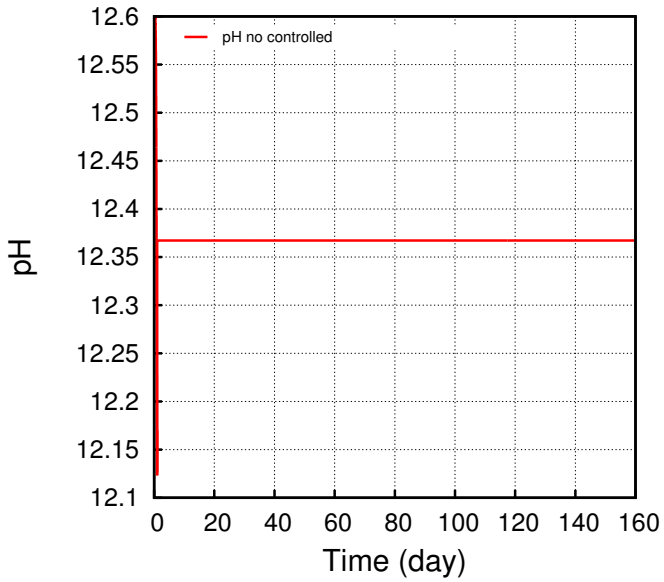

Figure 4.26 – Evolution of pH when pH is not controlled

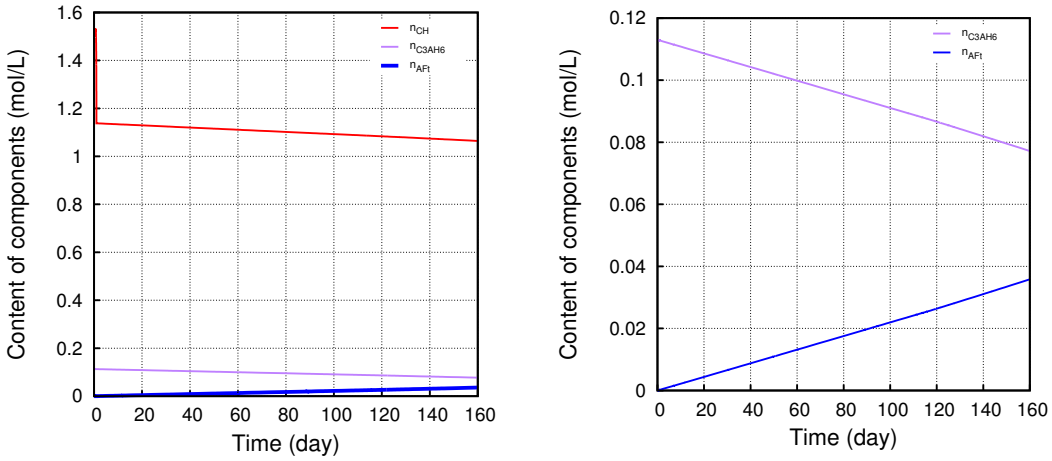

Figure 4.27 – Content of CH, CSH_2, C_3AH_6 and AFt when pH is not controlled

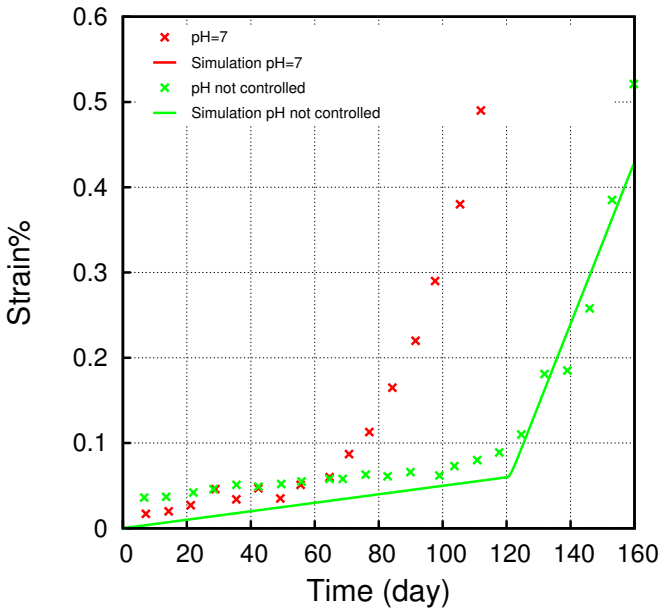

	Concentration of SO_4^{2-} (mol/L)	Concentration of Na^+ (mol/L)	ϵ_0	a_i (s^{-1})	a_p (s^{-1})
pH not controlled	0.38	0.76	6×10^{-4}	9.0×10^{-9}	1.1×10^{-9}
pH =7	0.38	0.76	6×10^{-4}	9.0×10^{-9}	1.1×10^{-9}

Figure 4.28 – Calibration of parameters for ESA [63]

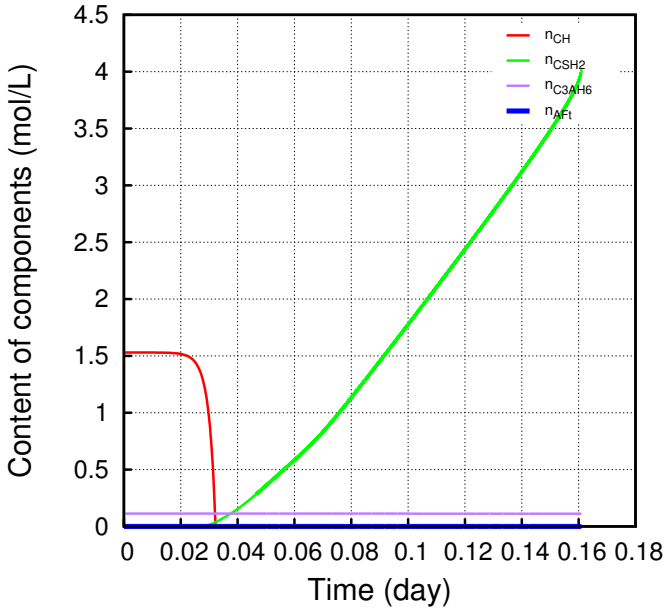

Figure 4.29 – Content of CH, gypsum, hydrogarnet and ettringite

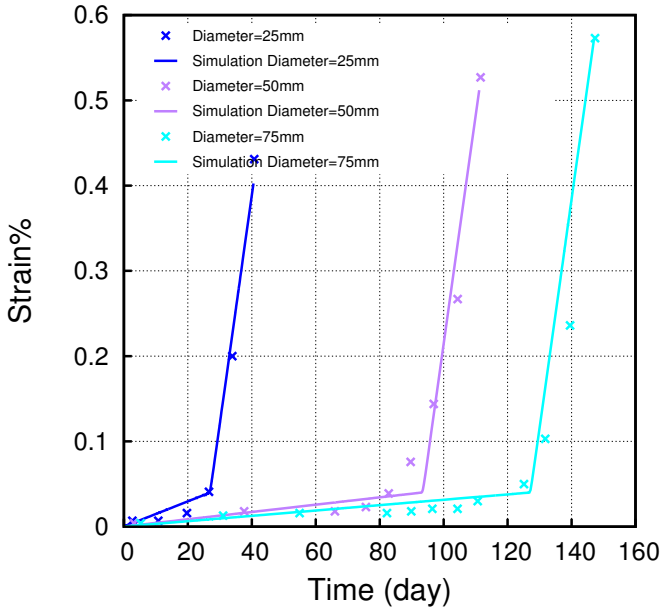

	Concentration of SO_4^{2-} (mol/L)	Concentration of Na^+ (mol/L)	Increase rate of boundary ions (mol/L/day)	ϵ_0	a_i (s^{-1})	a_p (s^{-1})
Dimension=25mm	0.38	0.76	-	4×10^{-4}	2.6×10^{-8}	3.1×10^{-9}
Dimension=50mm	0.38	0.76	1.6×10^{-3}	4×10^{-4}	2.6×10^{-8}	3.1×10^{-9}
Dimension=75mm	0.38	0.76	9.1×10^{-4}	4×10^{-4}	2.6×10^{-8}	3.1×10^{-9}

Figure 4.30 – Calibration of parameters for ESA [63]

Fig. 4.30 shows the expansion of mortar cylinders with three different diameters: 25 mm, 50 mm, and 75 mm. Small specimens start to expand earlier and faster due to the weak ability to overcome the expansive forces compared to large specimens, because specimens in different dimensions start to expand macroscopically when a similar fraction of the specimens are affected by the penetrated sulfate ions [11]. The transport of the sulfate ions depends on the diffusion process, which is indispensable when studying the effect of dimensions. Therefore, $a_i = 2.6 \times 10^{-8}$ and $a_p = 3.1 \times 10^{-9}$ are calibrated from the smallest specimen with $c_{SO_4^{2-}} = 0.38$ mol/L and $c_{Na^+} = 0.76$ mol/L. Then these two parameters are kept constant to predict the swelling of other two larger specimens with considering the diffusion of ions. As the material is assumed to be homogeneous, the content of the penetrated sulfate ions is simplified as the same along the depths but increases with time. Then the concentration of sulfate and alkali ions are simplified as to impose the $c_{SO_4^{2-}} = 0.38$ mol/L and $c_{Na^+} = 0.76$ mol/L with a single increase rate to simulate the diffusion. Fig. 4.31 shows the evolution of $c_{SO_4^{2-}}$ in the different cases. It can be seen that even when specimens have reached an expansion above 0.5%, the concentration of sulfate ions has not yet reached the value of exterior solution. However, this simplified method confirms that the elastic behavior highly depends on the diffusion process of ions.

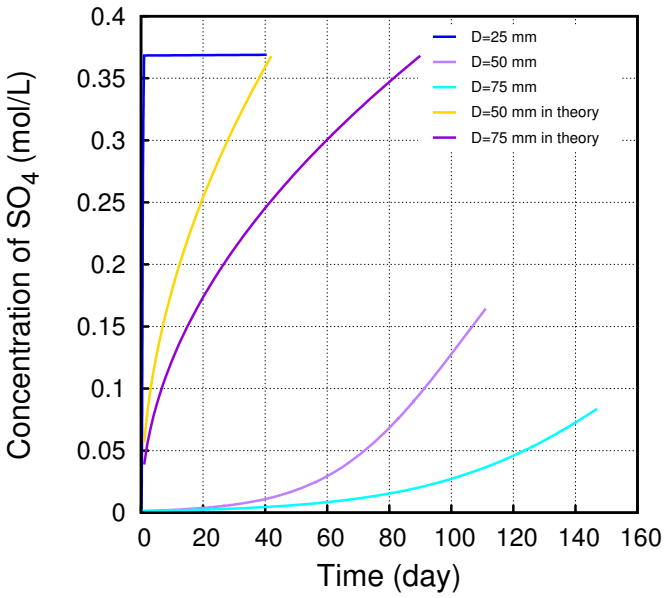

Figure 4.31 – Concentration of sulfate ions with consideration of diffusion

Theoretically, the distance that ions can diffuse through time t is: $L = \sqrt{D_{ef}\ t}$, and the corresponding area is: $A = 2\pi R\ L$. Then, the average concentration of sulfate

ions of the area πR^2 at a given time t, $c_{SO_4^{2-}}(t)$, can be predicted as:

$$c_{SO_4^{2-}}(t) = \frac{2\ R}{R^2}\ \sqrt{D_{ef}\ t}\ c_{SO_4^{2-}} \tag{93}$$

where D_{ef} is the effective diffusion coefficient of sulfate ions, which equals to 1.065×10^{-9} m^2/s [285], and R is the radius of cylinder specimen. The corresponding results are plotted in Fig. 4.31. Even though the predicted evolution of sulfate ions in theory has a differently increase trend as the one simplified above, it helps to confirm that the diffusion of sulfate ions has significant effect on elastic behavior of specimens.

4.8.4 Simulation of DEF in free swelling

The sigmoid expansion curve is the most typical kind in DEF, which is studied and simulated only in this part. It includes a latent period, an accelerated increasing phase and a plateau part (or a non-linear slowly increasing part) due to the limited source of ions. The material transforms from the elastic to damage range at the connection point of the latent and accelerated period, and this elastic limit point is determined by the physical and mechanical properties of the material. Then the strain will increase rapidly and reach a plateau when at least one of the reactants is completed. To simulate the plateau is a challenge in this work. The initial content of the sulfate ions in the pore solution ($n_{SO_4^{2-}}$) and the ones adsorbed on C-S-H ($n^{ads}_{SO_4}$), which is predicted from the amount of sulfur in cement (see section 4.4.1), determine the total amount of ettringite formed in the end. However, the distribution of the ettringite between the pore invasion and deformation processes are variable depending on the kinetic constants a_i and a_p. Therefore, the initial content of sulfur n_{SO_3} and a_i determine the kinetics of the elastic range, which together with a_p affects the kinetics of damage range and the value of plateau. In the following simulations, the yield point should be fixed from the swelling curve first. Then, two kinetic constants can be adjusted and calibrated from the increase rate of expansion based on an initial input of $n_{SO_4^{2-}}$ and $n^{ads}_{SO_4}$.

Experimental investigations were performed to study the effect of thermal history on DEF of concrete prismatic specimens ($11 \times 11 \times 22$ cm^3) in [145]. The parameters, which represent the pore structure of concrete specimens (see Table 4.1), are used as: $a = 127.86$ nm and $m = 0.379$. The bulk modulus is assumed to be 20 GPa, and Biot's coefficient is 1. According to the information of cement material in this literature, which is the same as shown in Table 2.3, the initial content of products

are: $n_{\mathrm{CH}} = 1.65$ mol/L, $n_{\mathrm{CSH}} = 1.393$ mol/L, $n_{\mathrm{C_3A}} = 0.114$ mol/L, $n_{\mathrm{AFm}} = 0.06$ mol/L, $n_{\mathrm{SO_4^{2-}}} = 0.063$ mol/L, and $n_{\mathrm{SO_4}}^{ads} = 0.05$ mol/L. Different maximum heating temperatures (61, 71 and 81 °C) with different heating durations were adopted in their study. However, concrete specimens preheated with 61 °C did not show expansions while the others did. Thus a temperature above 65 °C was considered to be the threshold temperature that DEF occurred. Moreover, a pessimum effect was found in the effective energy, which is the product of temperature above 65 °C and the heating duration. It means that as heating duration increases with a temperature above 65 °C, the expansion may decrease after the effective energy is beyond a threshold value. The expansion of specimens preheated with a maximum temperature of 71 °C and different heating durations are simulated in this section. The specimen which was heated at 71 °C for 12 days showed a maximum expansion, which is assumed that all the primary ettringite was decomposed. The specimen preheated with a short duration, 71-7days for example, showed a smaller expansion due to a lack of sufficient energy to decompose all the primary ettringite. The specimen preheated for 28 days showed a smaller expansion as well, which may be related to the definitive aluminum substitution of silica in C-S-H and resulted in a decrease in the quantity of ettringite precipitated [207]. For these cases, the total ettringite formed in the materials at the plateau phase are less than specimen 71-12days. Therefore, for a simplicity, the initial concentration of $\mathrm{SO_4^{2-}}$ in the pore solution are decreased to reduce the final amount of ettringite that could be precipitated. First, a_i and a_p are calibrated from specimen 71-12days. Then, these two parameters are kept constant to calibrate the initial concentration of sulfate ions from the plateau value of expansion.

The calibrated results from specimen 71-12days are: $a_i = 1.7 \times 10^{-8}$ and $a_p = 2.8 \times 10^{-9}$. Fig. 4.32 shows that AFm transforms to AFt with consuming sulfate ions. This reaction stops when all the available sulfate ions are depleted, at which moment the expansion reaches a plateau.

Fig. 4.33 illustrates the predicted swelling curves for other specimens with $a_i = 1.7 \times 10^{-8}$ and $a_p = 2.8 \times 10^{-9}$. For specimen 71-7days, an initial concentration of sulfate ions of 0.316 mol/L is calibrated and the simulation shows a shorter elastic duration compared to the actual one. For specimens 71-14days and 71-28days, a slower kinetic of elastic range is predicted. This may be explained by the fact that during the long-term (14 or 28 days) preheating, the microstructure of the material is modified which leads to a lower capacity to accommodate the ettringite and results in a shorter elastic range. This factor could not be illustrated in this

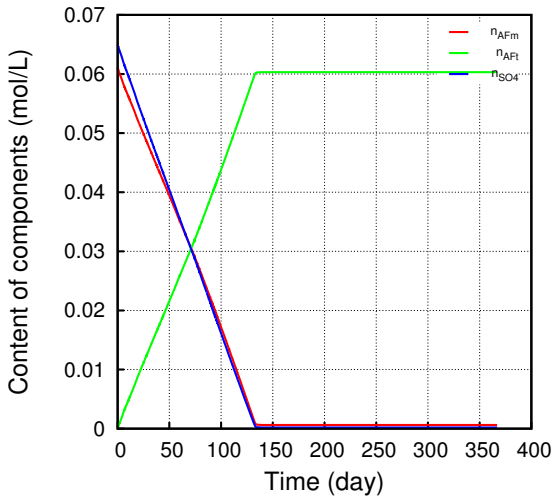

Figure 4.32 – Evolution of content of AFm and AFt, and SO_4^{2-}.

model. However, the kinetic of damage range is well predicted.

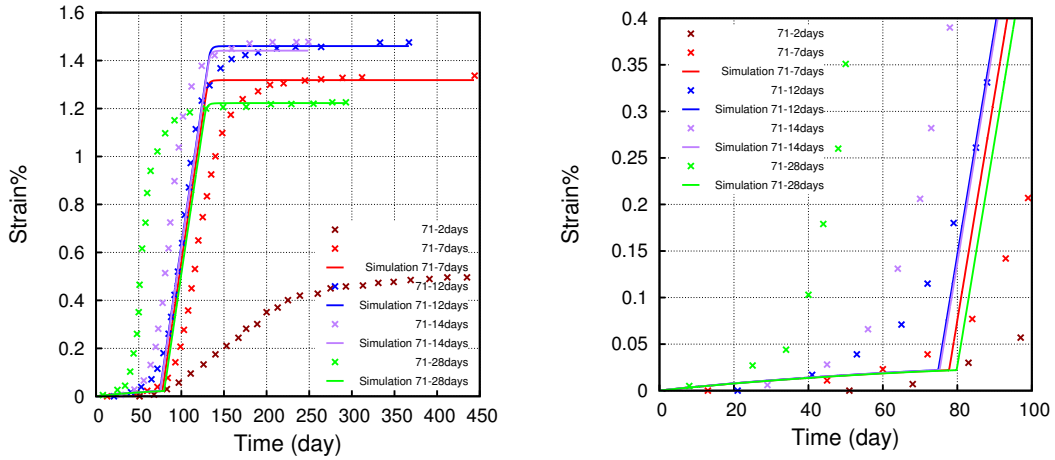

	Initial concentration of SO_4^{2-} (mol/L)	Initial content of SO_4^{2-} in pore solution (mol/L)	Initial content of SO_4^{2-} adsorbed (mol/L)	Initial content of AFm (mol/L)	Concentration of Na^+ (mol/L)	ϵ_0	a_i (s^{-1})	a_p (s^{-1})
71-7days	0.316	0.063	0.050	0.06	1	2.2×10^{-4}	1.7×10^{-8}	2.8×10^{-9}
71-12days	0.325	0.065	0.051	0.06	1	2.2×10^{-4}	1.7×10^{-8}	2.8×10^{-9}
71-14days	0.324	0.064	0.051	0.06	1	2.2×10^{-4}	1.7×10^{-8}	2.8×10^{-9}
71-28days	0.310	0.062	0.049	0.06	1	2.2×10^{-4}	1.7×10^{-8}	2.8×10^{-9}

Figure 4.33 – Calibration of parameters for DEF [145]:

The simulation of specimen 71-2days is unsatisfactory, see Fig. 4.34. As the initial concentration of SO_4^{2-} decreases from 0.2901 mol/L in simulation I to 0.2900 mol/L in simulation II, a big difference in expansion is observed. In these two simulations, the consumed amount of sulfate ions, AFm, and the precipitated content of AFt are quite similar (see Fig. 4.35). However, the distribution of AFt is different, as shown in Fig. 4.36. The figure shows a higher value of S_C in the simulation II. It means that the formed AFt is distributed only in the pore invasion process, and the

expansive stress is not sufficient to activate the damage process.

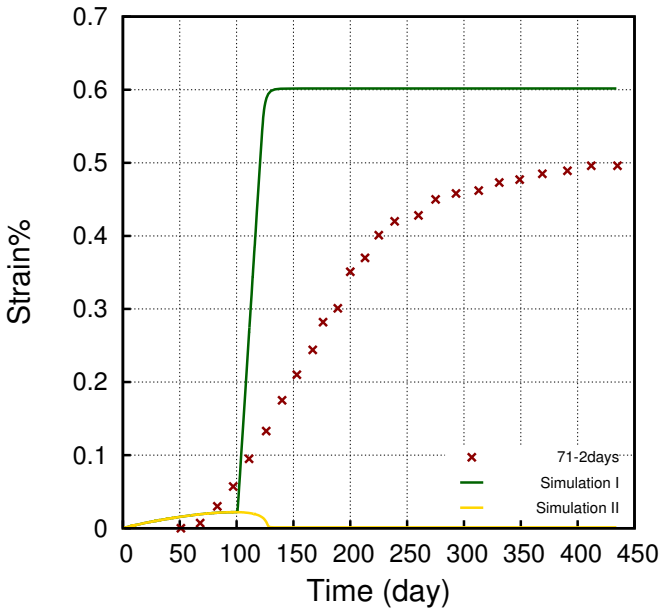

	Initial concentration of SO_4^{2-} (mol/L)	Initial content of SO_4^{2-} in pore solution (mol/L)	Initial content of SO_4^{2-} adsorbed (mol/L)	Initial content of AFm (mol/L)	Concentration of Na^+ (mol/L)	ϵ_0	a_i (s^{-1})	a_p (s^{-1})
Simulation I	0.2901	0.058	0.047	0.057	1	2.2×10^{-4}	1.7×10^{-8}	2.8×10^{-9}
Simulation II	0.2900	0.058	0.047	0.057	1	2.2×10^{-4}	1.7×10^{-8}	2.8×10^{-9}

Figure 4.34 – Calibration of parameters for specimen 71-2days [145]:

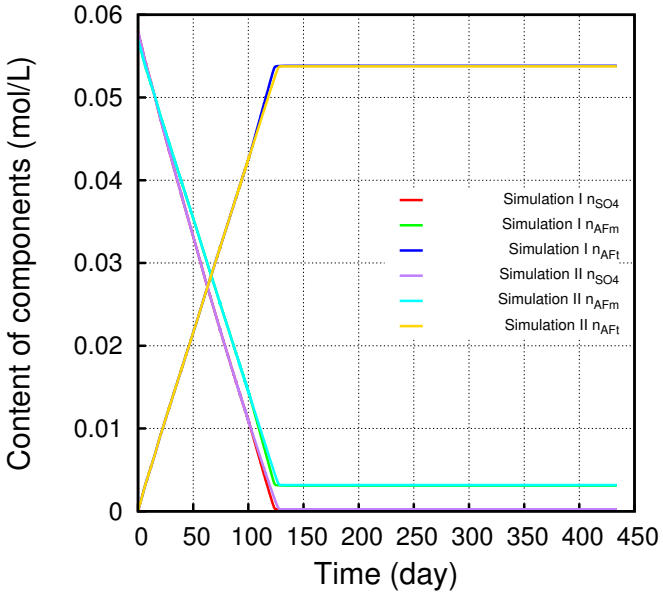

Figure 4.35 – Content of AFm, AFt and SO_4^{2-} in simulation I and II.

The simulation results shown above suggest that the proposed model can well explain the crystallization of ettringite and the expansion due to DEF, including during the latent, accelerated and the plateau period. In addition, the evolution of the

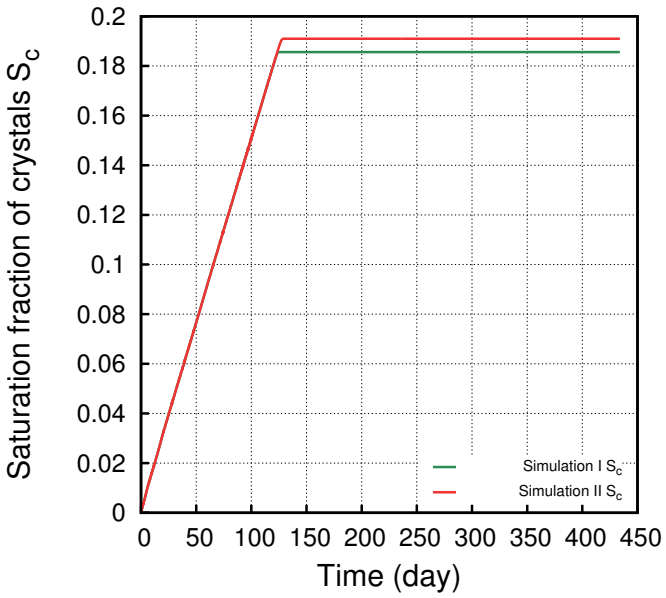

Figure 4.36 – Saturated fraction of crystals in simulation I and II.

components can be captured. However, it has limitations, for example, the effect of heating processes on the microstructure are neglected and the initial content of sulfate ions could only be predicted.

4.9 Conclusions and discussions

A poromechanical model based on the homogeneous paste expansion and surface-controlled ettringite growth mechanism is proposed in this chapter for cement-based materials submitted to sulfate attacks. This mechanism well explains the swelling of cementitious specimens induced by sulfate attacks. Based on the supersaturation pressure theory, it describes the ettringite crystallization in a porous material: the pore invasion and pore deformation process. The kinetics of these two processes are assumed to be governed by two independent constants: a_i and a_p.

In summary, the inputs required for the simulations are:
(1) the mechanical properties: bulk modulus E and Biot coefficient b;
(2) the microstructure properties through the volume fraction $S(r)$;
(3) two kinetic constants for the crystal growth: a_i and a_p, which should be calibrated from the swelling curves;
(4) the saturation index β, which is predicted from the ionic composition of the pore

solutions.

Some assumptions were used when determining the saturation index of ettringite in the pore solution. The portlandite, hydrogarnet, and monosulfate were assumed to be at equilibrium in the pore solution to determine the concentrations of Ca^{2+} and Al^{3+}. In addition, the concentration of OH^- is determined according to the principle of electroneutrality. For ESA, the concentration of sulfate ions is determined by the exterior solution, while for DEF, it is determined by the initial content of sulfur in the cement.

The advantage of this proposed poromechanics-model is that it matches with any mechanical theory, including poroelasticity, poroplasticity, damage model, etc. By analyzing the sensitivity of β, a_i and a_p in the case of ESA, it is concluded that the elastic behavior (kinetic and duration) is controlled by β and a_i, while the damage behavior is governed by a_p. However, in the case of DEF, with a decreased β, a "competition" phenomenon is observed between the pore invasion and deformation processes. The initial content of sulfur and a_i determines the kinetics of the elastic range, which, together with a_p affects the kinetics of damage range and the plateau phase. With these observations, the expansion of the specimens was simulated.

Firstly, poroelasticity theory was coupled to describe the swelling due to sulfate attacks in a restrained condition. The kinetic parameters a_i was calibrated from the axial stress of the specimens, and was then used to predict the axial stress of other specimens. The simulated results both in ESA and DEF showed a quite close value compared to the experimental results.

Secondly, a damage model was coupled with the proposed poromechanical model to simulate the expansion of specimens in a free swelling condition. In the case of ESA, a_i and a_p were calibrated from the expansion of the specimen, which was not pH controlled. Then, the calibrated parameters were used to predict the expansion of a specimen at pH=7. No expansion was observed due to the precipitation of gypsum instead of AFt. However, the formation of ettringite is considered as the only reason for expansion in the model, that is why no expansion was predicted. A simplified method was used to simulate the diffusion of ions, which imposed the boundary condition of sulfate and alkali ions with a single increase rate when predicting the expansion curves for specimens of different dimensions. The predicted expansion curves showed a good consistency with the experimental results. For DEF, a_i and a_p were calibrated from the specimen with maximum expansion, for which it was

assumed that all the primary ettringite was decomposed to AFm and free sulfate ions after the heating treatment. Then, the calibrated parameters were used to calibrate the available content of sulfate ions at the beginning from the final plateau of expansion. In the end, these parameters were adopted to predict the expansion curves. The damage behavior was well predicted, while the elastic one was not quite satisfying. This is because the effect of heating process on the microstructure was neglected, and it is difficult to determine the precise content of sulfate ions which are decomposed from the primary ettringite.

The proposed model suggests a method to explain the crystallization of ettringite and the expansion due to sulfate attacks. The minimum pores where ettringite approaches during attacks, showed a good consistency with the experimental results measured by MIP. This further proved the reliability of the proposed model. However, some of the experimental conditions were not taken into account in the model, such as the composition of concrete mix, preheating histories, curing conditions, and so on. These factors should be considered when determining the saturation index of ettringite. Furthermore, the diffusion and leaching of the ions were not considered in the simulation as well. These ideas should be modified in the model in the further studies.

Conclusions and perspectives

As emphasized in the literature review, sulfate attacks have been considered as one of the most concerned problems affecting the durability of cement-based materials. ESA and DEF have been studied separately due to different sources of sulfate ions. However, they share a lot in common, which motivated this study. Therefore, this work aimed to study the damage behavior of cement-based materials due to different types of sulfate attacks, and investigate the common phenomenon in the crystallization process.

Cement pastes fabricated with two types of cement (CEM I and CEM III) and two dimensions ($2 \times 2 \times 12$ cm^3 and $11 \times 11 \times 22$ cm^3) were exposed to three types of sulfate attack conditions (ESA, DEF, and the coupling effect of the both) in this study. CEM III specimens showed a strain of less than 0.04% after a 7-month exposure to sulfate attacks due to a low content of CaO and a limited Al_2O_3 available to form ettringite in the materials. However, CEM I specimens showed different degrees of expansion depending on the type of sulfate attacks. The multi-source of sulfate ions (Coupling effect) generated for the $2 \times 2 \times 12$ cm^3 specimen the fastest kinetics, which reached an expansion of up to 2.7% after 2.5 months. DEF $2 \times 2 \times 12$ cm^3 specimen displayed the slowest kinetics with an expansion of 0.5% after 2 years though not yet stabilized.

The comparison of the pore size distribution of cement pastes exposed to different sulfate attack conditions provided valuable insights into the pore position where expansive product forms. First, $2 \times 2 \times 12$ cm^3 specimens showed a decrease in pore volume in the pore range of 3.7-50 nm for ESA-I (expansion of 1.7%), between 9.7-100 nm for DEF-I (expansion of 0.5%), and 5.3-80 nm for Coup-I (expansion of 2.7%). These pore ranges correspond to capillary and gel pores. Then, $11 \times 11 \times 22$ cm^3 specimen DEF-I-Fin2 (expansion of 1.22%) showed a pore range occupied by generated crystals of approximately 4-20 nm, which suggested that expansive product precipitates into smaller pores leading to an increase of the expansion. To sum up, generated crystal forms both in capillary and gel pores when cement pastes are exposed to sulfate attacks, including ESA, DEF, and the coupling effect. The evolution of the pore size distribution was studied on DEF $11 \times 11 \times 22$ cm^3 specimens, which showed that: the pore volume between 100 nm - 400 μm was decreased during the latent period, which extended to capillary and gel pore ranges with the expansion increasing rapidly. The expansive crystals are assumed to be

ettringite according to the literature. Therefore, a uniform damage mechanism is proposed for cement-based materials exposed to sulfate attacks: ettringite forms in the biggest voids first without inducing any obvious expansion, then penetrates into capillary pores forwarding gel pores which leads to an accelerated swelling.

The evolution of pore size distribution of $11 \times 11 \times 22$ cm^3 DEF specimens illustrated a variable pore structure during the degradation, which was affected by the dissolution of CH, the decalcification of C-S-H, ettringite formation and the occurrence of microcracks. The pore structure is indeed governed by competing mechanisms. For example, if the increased pore volume δV_1 induced by microcracks is higher than the decreased one δV_2 due to ettringite formation, the accumulated pore volume $\delta V_1 - \delta V_2$ shows an increase, which means an increase in pore volume in total. This observation suggested that characterizing the pore structure provided a qualitative method to study ettringite formation instead of a quantitative one. Therefore, to confirm these processes quantitatively, it seems necessary in the future to carry out additional tests on chemical analyses, which can provide more information about the content of each species.

A poromechanical model was proposed based on the surface-controlled mechanism and ettringite crystallization. The model well explained the process of ettringite crystallization in the pores, which was divided into two processes: pore invasion and pore deformation. The precipitation of ettringite in the pore invasion process is governed by the interface of the crystal-liquid. Ettringite stops growing in this direction when the interface reaches an equilibrium, which accumulates a volume fraction occupied by crystals of S_C. A constant, a_i, is proposed to represent the kinetic of S_C. The deformation process is governed by the interface of crystal-solid where ettringite keeps growing until the interface reaches an equilibrium, with a kinetic constant a_p. a_i and a_p are two parameters needed to be calibrated from the swelling curves. During the degradation of ESA, the kinetics of the swelling is governed by a_i when the material is within the elastic range, while the damage expansion is governed by a_p. In the simulation of DEF, all the sulfur in the cement is assumed to contribute to the primary ettringite, which is totally decomposed to AFm and free sulfate ions during the heating treatment. The limited amount of sulfur in cement contributes to a certain content of AFt that could be formed during DEF. This means that a "competition" would happen between the pore invasion and deformation processes, which affects the expansion degree. Therefore, in the case of DEF, the kinetics of elastic and damage range depend on a_i, a_p, and the initial content of sulfur as well.

Except for these two parameters a_i an a_p, the other important input is the saturation index of ettringite in the pore solution, β. It is determined by the component ions in the pore solution, including ions of Ca^{2+}, Al^{3+}, OH^- and SO_4^{2-}. The difference between ESA and DEF is reflected by β in this model. For ESA, the exterior solution provides unlimited sulfate ions into the pore solution, which keeps β constant and high. However, in the case of DEF, the sulfate ions in the pore solution is consumed as ettringite precipitates. Therefore, the expansion reaches a plateau when one of the reactants is completed. In this study, the initial content of hydration products were predicted according to the mass balance from cement materials, and the saturation index of CH, C_3AH_6 (for ESA), AFm (for DEF) in the pore solution were assumed to be 1. However, this would be more precise if the experimental factors are considered, such as the concrete mix, the curing conditions, the exposure conditions and so on.

The proposed poromechanical model well explained the crystallization process and predicted the expansion. First, the minimum pore entry radius of experiments in this study that predicted by the model (20 nm both for ESA-I-Fin and DEF-I-Fin) is quite close to the experimental results from MIP (3.7 nm for ESA-I-Fin and 9.7 nm for DEF-I-Fin). Secondly, the calibrated kinetic constants are of a similar magnitude around 10^{-8} and 10^{-9}, respectively. Furthermore, for the same specimen materials, the damage behavior is well predicted, while the elastic behavior could be improved by considering the diffusion, the effect of the heating history on the decomposition of the primary ettringite, the modification of microstructure and so on.

The final goal of this study is dedicated to optimize the performance of cement-based materials against sulfate attacks, and predict the service-life of concrete strucures. In order to be better applied in the engineering field, the current model could be modified and improved. In the following, some perspectives are proposed.

Perspectives

In order to complete and improve this study on sulfate attacks, some aspects could be taken into considerations in further studies:

- The microstructure of cement-based materials due to sulfate attacks was studied qualitatively through an analysis of the pore size distribution. It would be interesting to extend this study with chemical analyses, in particular to distinguish the effect of calcium leaching and crystals

precipitation on the variation of pore volume. This would provide an analysis quantitatively, which would allow a better understanding of the consequences of each process. Additionally, performing the heat based dissolution test developed in this work at various stages of the reactions would confirm some of the assumptions put forward in this work regarding the evolution of the pore size distribution.

• During the degradation, the microstructure of the material is modified, which affects the crystallization procedure, for example, the volume fraction of the crystals. In the modeling, with considering the evolution of microstructure, the harmless crystals which form in the newly generated voids could be distinguished from the expansive ones. This modification will simulate the damage more precisely.

• The precipitation of gypsum during sulfate attacks has been discussed a lot in literature. Even though it is generally accepted that the formation of gypsum occurs after the expansion, it may be the reason for the expansion, for example, when the materials are exposed to an acid environment. For this reason, it would be interesting to consider the gypsum as an expansive product in the model.

• Furthermore, the diffusion and leaching of the ions could be considered in the model in the further studies, as these have a significant effect on the elastic range. The transportation of ions may determine the latent duration of the expansion. Therefore, it would be useful to take these factors into account for the simulation.

• Finally, extending the current 1-dimension model to 2-dimensions or even 3-dimensions will be interesting and useful, which could be applied on structural elements. In this way, the model could be used by engineers to predict the stress and strain of the structures.

Bibliography

[1] W.H. Harrison. Sulphate resistance of buried concrete. *Building Research Establishment Report*.

[2] K. Scrivener and J.P. Skalny. Conclusions of the international rilem tc 186-isa workshop on internal sulfate attack and delayed ettringite formation (4–6 september 2002, villars, switzerland). *Materials and Structures*, 38(6):659–663, 2005.

[3] P. Monteiro. *Concrete: microstructure, properties, and materials*. McGraw-Hill Publishing, 2006.

[4] M. Lei, L. Peng, C. Shi, and S. Wang. Experimental study on the damage mechanism of tunnel structure suffering from sulfate attack. *Tunnelling and Underground Space Technology*, 36:5–13, 2013.

[5] Y.L. Wang and Y. Yao. Researches on key engineering concrete durability and applications. *China Building Materials, Beijing*, 2001.

[6] J. Marchand, I. Odler, and J.P. Skalny. *Sulfate attack on concrete*. CRC Press, 2003.

[7] C. Ouyang, A. Nanni, and W.F. Chang. Internal and external sources of sulfate ions in portland cement mortar: two types of chemical attack. *Cement and Concrete Research*, 18(5):699–709, 1988.

[8] J.G. Wang. Sulfate attack on hardened cement paste. *Cement and Concrete Research*, 24(4):735–742, 1994.

[9] J.R. Clifton and J.M. Pommersheim. Sulfate attack of cementitious materials: volumetric relations and expansions. *National Institute of Standards and Technology IR*, 5390, 1994.

[10] P. Mehta. Sulfate attack on concrete–a critical review. *Material Science Concrete, IIIpp.*, 105, 1992.

[11] C. Yu, W. Sun, and K. Scrivener. Mechanism of expansion of mortars immersed in sodium sulfate solutions. *Cement and Concrete Research*, 43:105–111, 2013.

[12] B. Tian and M.D. Cohen. Does gypsum formation during sulfate attack on concrete lead to expansion? *Cement and Concrete Research*, 30(1):117–123, 2000.

[13] T. Van Gerven, G. Cornelis, E. Vandoren, and C. Vandecasteele. Effects of carbonation and leaching on porosity in cement-bound waste. *Waste Management*, 27(7):977–985, 2007.

[14] K. Haga, S. Sutou, M. Hironaga, S. Tanaka, and S. Nagasaki. Effects of porosity on leaching of ca from hardened ordinary portland cement paste. *Cement and Concrete Research*, 35(9):1764–1775, 2005.

[15] H. Saito and A. Deguchi. Leaching tests on different mortars using accelerated electrochemical method. *Cement and Concrete Research*, 30(11):1815–1825, 2000.

[16] M. Collepardi. A state-of-the-art review on delayed ettringite attack on concrete. *Cement and Concrete Composites*, 25(4-5):401–407, 2003.

[17] A. Neville. The confused world of sulfate attack on concrete. *Cement and Concrete Research*, 34(8):1275–1296, 2004.

[18] H. Haynes, R. O'Neill, M. Neff, and P.K. Mehta. Salt weathering distress on concrete exposed to sodium sulfate environment. *Materials Journal*, 105(1):35–43, 2008.

[19] C. Rodriguez-Navarro, E. Doehne, and E. Sebastian. How does sodium sulfate crystallize? implications for the decay and testing of building materials. *Cement and Concrete Research*, 30(10):1527–1534, 2000.

[20] G.W. Scherer. Stress from crystallization of salt. *Cement and Concrete Research*, 34(9):1613–1624, 2004.

[21] N. Thaulow and S. Sahu. Mechanism of concrete deterioration due to salt crystallization. *Materials Characterization*, 53(2):123–127, 2004.

[22] C.W. Correns. Growth and dissolution of crystals under linear pressure. *Discussions of the Faraday Society*, 5:267–271, 1949.

[23] N. Tsui, R.J. Flatt, and G.W. Scherer. Crystallization damage by sodium sulfate. *Journal of Cultural Heritage*, 4(2):109–115, 2003.

[24] R.J. Flatt. Salt damage in porous materials: how high supersaturations are generated. *Journal of Crystal Growth*, 242(3):435–454, 2002.

[25] P.S. Mangat and J.M. El-Khatib. Influence of initial curing on sulphate resistance of blended cement concrete. *Cement and Concrete Research*, 22(6):1089–1100, 1992.

[26] M. Steiger and S. Asmussen. Crystallization of sodium sulfate phases in porous materials: the phase diagram $Na_2SO_4 - H_2O$ and the generation of stress. *Geochimica et Cosmochimica Acta*, 72(17):4291–4306, 2008.

[27] E.M. Winkler and P.C. Singer. Crystallization pressure of salts in stone and concrete. *Geological Society of America Bulletin*, 83(11):3509–3514, 1972.

[28] D.G.R. Bonnell and M.E. Nottage. Studies in porous materials with special reference to building materials. i. the crystallisation of salts in porous materials. *Journal of the Society of Chemical Industry*, 58:16–21, 1939.

[29] W.G. Hime, R.A. Martinek, L.A. Backus, and S.L. Marusin. Salt hydration distress. *Concrete International*, 23(10):43–50, 2001.

[30] K.J. Folliard and P. Sandberg. Mechanisms of concrete deterioration by sodium sulfate crystallization. *Special Publication*, 145:933–946, 1994.

[31] H.F. Taylor. *Cement chemistry*. 1997.

[32] R. Ragoug. *Attaque sulfatique externe des matériaux cimentaires: Impact de différents facteurs âge, composition du liant, présence de chlorures*. PhD thesis, Paris Est, 2016.

[33] A. Chabrelie. Mechanisms of degradation of concrete by external sulfate ions under laboratory and field conditions. *École polytechnique fédérale de Lausanne, EPFL Inforscience*, 2010.

[34] P.K. Mehta. Mechanism of expansion associated with ettringite formation. *Cement and Concrete Research*, 3(1):1–6, 1973.

[35] R.S. Gollop and H.F.W. Taylor. Microstructural and microanalytical studies of sulfate attack iii. sulfate-resisting portland cement: Reactions with sodium and magnesium sulfate solutions. *Cement and Concrete Research*, 25(7):1581–1590, 1995.

[36] T. Schmidt, B. Lothenbach, M. Romer, J. Neuenschwander, and K. Scrivener. Physical and microstructural aspects of sulfate attack on ordinary and limestone blended portland cements. *Cement and Concrete Research*, 39(12):1111–1121, 2009.

[37] J. Marchand, E. Samson, Y. Maltais, and J.J. Beaudoin. Theoretical analysis of the effect of weak sodium sulfate solutions on the durability of concrete. *Cement and Concrete Composites*, 24(3):317–329, 2002.

[38] S. Yang, X. Zhongzi, and T. Mingshu. The process of sulfate attack on cement mortars. *Advanced Cement Based Materials*, 4(1):1–5, 1996.

[39] M. Santhanam, M.D. Cohen, and J. Olek. Mechanism of sulfate attack: a fresh look: part 1: summary of experimental results. *Cement and Concrete Research*, 32(6):915–921, 2002.

[40] E.F. Irassar, V.L. Bonavetti, and M. Gonzalez. Microstructural study of sulfate attack on ordinary and limestone portland cements at ambient temperature. *Cement and Concrete Research*, 33(1):31–41, 2003.

[41] S. Yang, X. Zhongzi, T. Mingshu, and B. Mather. Discussion of "the process of sulfate attack on cement mortars". *Advanced Cement Based Materials*, 5(3-4):109–110, 1997.

[42] O.S.B. Al-Amoudi. Sulfate attack and reinforcement corrosion in plain and blended cements exposed to sulfate environments. *Building and Environment*, 33(1):53–61, 1998.

[43] P.K. Mehta and O.E. Gjørv. A new test for sulfate resistance of cements. *Journal of Testing and Evaluation*, 2(6):510–515, 1974.

[44] J.W. Figg. Chemical attack on hardened concrete, effect of sulphates and chlorides. *Bulletin of the Institution of Corrosion Science and Technology*, 75:12–23, 1979.

[45] M. Santhanam, M.D. Cohen, and J. Olek. Mechanism of sulfate attack: a fresh look: Part 2. proposed mechanisms. *Cement and Concrete Research*, 33(3):341–346, 2003.

[46] K.E. Kurtis, P.J. Monteiro, and S.M. Madanat. Empirical models to predict concrete expansion caused by sulfate attack. *Materials Journal*, 97(2):156–161, 2000.

[47] O.S.B. Al-Amoudi. Performance of 15 reinforced concrete mixtures in magnesium-sodium sulphate environments. *Construction and Building Materials*, 9(3):149–158, 1995.

[48] W. Kunther, B. Lothenbach, and K.L. Scrivener. On the relevance of volume increase for the length changes of mortar bars in sulfate solutions. *Cement and Concrete Research*, 46:23–29, 2013.

[49] D. Bonen and M.D. Cohen. Magnesium sulfate attack on portland cement paste-i. microstructural analysis. *Cement and Concrete Research*, 22(1):169–180, 1992.

[50] M.D. Cohen and A. Bentur. Durability of portland cement-silica fume pastes in magnesium and sodium sulfate solutions. *Materials Journal*, 85(3):148–157, 1988.

[51] W. Kunther, B. Lothenbach, and K.L. Scrivener. Deterioration of mortar bars immersed in magnesium containing sulfate solutions. *Materials and Structures*, 46(12):2003–2011, 2013.

[52] W.R. Holden, C.L. Page, and N.R. Short. The influence of chlorides and sulphates on durability. *Corrosion of Reinforcement in Concrete Construction*, pages 143–150, 1983.

[53] S.E. Hussain and S.S. Al-Saadoun. Effect of cement composition on chloride binding and corrosion of reinforcing steel in concrete. *Cement and Concrete Research*, 21(5):777–794, 1991.

[54] O.S.B. Al-Amoudi, A.A. Rasheeduzzafar, M. Maslehuddin, and S.N. Abduljauwad. Influence of sulfate ions on chloride-induced reinforcement corrosion in portland and blended cement concretes. *Cement, Concrete and Aggregates*, 16(1):3–11, 1994.

[55] M. Maslehuddin, P.C. Rasheeduzzafar, A.I. Al-Mana, and A.J. Al-Tayyib. Effect of temperature and sulfate contamination on the chloride binding capacity of cements. In *Proceedings of the 4th International Conference on Deterioration and Repair of Reinforced Concrete in the Arabian Gulf,(GL Macmillan (ed.))*, pages 735–750, 1993.

[56] F.P. Glasser, J. Marchand, and E. Samson. Durability of concrete—degradation phenomena involving detrimental chemical reactions. *Cement and Concrete Research*, 38(2):226–246, 2008.

[57] R. El-Hachem, E. Rozière, F. Grondin, and A. Loukili. Multi-criteria analysis of the mechanism of degradation of portland cement based mortars exposed to external sulphate attack. *Cement and Concrete Research*, 42(10):1327–1335, 2012.

[58] W. Müllauer, R.E. Beddoe, and D. Heinz. Sulfate attack expansion mechanisms. *Cement and Concrete Research*, 52:208–215, 2013.

[59] E. Rozière, A. Loukili, R. El Hachem, and F. Grondin. Durability of concrete exposed to leaching and external sulphate attacks. *Cement and Concrete Research*, 39(12):1188–1198, 2009.

[60] P.K. Mehta and O.E. Gjørv. A new test for sulfate resistance of cements. *Journal of Testing and Evaluation*, 2(6):510–515, 1974.

[61] P.K. Mehta. Evaluation of sulfate-resisting cements by a new test method. In *Journal Proceedings*, volume 72, pages 573–575, 1975.

[62] P.W. Brown. An evaluation of the sulfate resistance of cements in a controlled environment. *Cement and Concrete Research*, 11(5-6):719–727, 1981.

[63] C.F. Ferraris JR, P.S. Clifton, and E. Garbocz. 22 mechanics of degradation of portland cement-based systems by sulfate attack. *Mechanisms of Chemical Degradation of Cement-based Systems*, page 185, 1997.

[64] H.T. Cao, L. Bucea, A. Ray, and S. Yozghatlian. The effect of cement composition and ph of environment on sulfate resistance of portland cements and blended cements. *Cement and Concrete Composites*, 19(2):161–171, 1997.

[65] R. El-Hachem, E. Rozière, F. Grondin, and A. Loukili. New procedure to investigate external sulphate attack on cementitious materials. *Cement and Concrete Composites*, 34(3):357–364, 2012.

[66] D. Planel, J. Sercombe, P. Le Bescop, F. Adenot, and J.M. Torrenti. Long-term performance of cement paste during combined calcium leaching–sulfate attack: kinetics and size effect. *Cement and Concrete Research*, 36(1):137–143, 2006.

[67] E. Revertegat, C. Richet, and P. Gegout. Effect of ph on the durability of cement pastes. *Cement and Concrete Research*, 22(2-3):259–272, 1992.

[68] S.U. Al-Dulaijan, M. Maslehuddin, M.M. Al-Zahrani, A.M. Sharif, M. Shameem, and M. Ibrahim. Sulfate resistance of plain and blended cements exposed to varying concentrations of sodium sulfate. *Cement and Concrete Composites*, 25(4):429–437, 2003.

[69] O.S.B. Al-Amoudi. Attack on plain and blended cements exposed to aggressive sulfate environments. *Cement and Concrete Composites*, 24(3):305–316, 2002.

[70] F.H. Dakhil, A.S. Al-Gahrani, S.S. Al-Saadoun, and M.A. Bader. Influence of cement composition on the corrosion of reinforcement and sulfate resistance of concrete. *Materials Journal*, 87(2):114–122, 1990.

[71] N.N. Naik, A.C. Jupe, S.R. Stock, A.P. Wilkinson, P.L. Lee, and K.E. Kurtis. Sulfate attack monitored by microct and edxrd: influence of cement type, water-to-cement ratio, and aggregate. *Cement and Concrete Research*, 36(1):144–159, 2006.

[72] O.S.B. Al-Amoudi and M. Maslehuddin. Rasheeduzzafar,"permeability of concrete: Influential factors,". In *Proceedings of 4th international conference on deterioration and repair of reinforced concrete in the arabian Gulf, Bahrain*, pages 717–33, 1993.

[73] Rasheeduzzafar. Influence of cement composition on concrete durability. *ACI Materials Journal*, 89(6):574–586, 1992.

[74] L. Barcelo, E. Gartner, R. Barbarulo, A. Hossack, R. Ahani, M. Thomas, D. Hooton, E. Brouard, A. Delagrave, and B. Blair. A modified astm c1012 procedure for qualifying blended cements containing limestone and scms for use in sulfate-rich environments. *Cement and Concrete Research*, 63:75–88, 2014.

[75] D.D. Higgins and N.J. Crammond. Resistance of concrete containing ggbs to the thaumasite form of sulfate attack. *Cement and Concrete Composites*, 25(8):921–929, 2003.

[76] A. Skaropoulou, K. Sotiriadis, G. Kakali, and S. Tsivilis. Use of mineral admixtures to improve the resistance of limestone cement concrete against thaumasite form of sulfate attack. *Cement and Concrete Composites*, 37:267–275, 2013.

[77] J. Bijen. Benefits of slag and fly ash. *Construction and Building Materials*, 10(5):309–314, 1996.

[78] S.T. Lee, H.Y. Moon, and R.N. Swamy. Sulfate attack and role of silica fume in resisting strength loss. *Cement and Concrete Composites*, 27(1):65–76, 2005.

[79] H.W. Song, S.W. Pack, S.H. Nam, J.C. Jang, and V. Saraswathy. Estimation of the permeability of silica fume cement concrete. *Construction and Building Materials*, 24(3):315–321, 2010.

[80] M. Mainguy, C. Tognazzi, J.M. Torrenti, and F. Adenot. Modelling of leaching in pure cement paste and mortar. *Cement and Concrete Research*, 30(1):83–90, 2000.

[81] S. Kamali, M. Moranville, and S. Leclercq. Material and environmental parameter effects on the leaching of cement pastes: experiments and modelling. *Cement and Concrete Research*, 38(4):575–585, 2008.

[82] V.H. Nguyen, H. Colina, J.M. Torrenti, C. Boulay, and B. Nedjar. Chemo-mechanical coupling behaviour of leached concrete: Part i: Experimental results. *Nuclear Engineering and Design*, 237(20):2083–2089, 2007.

[83] F.H. Heukamp, F.J. Ulm, and J.T. Germaine. Mechanical properties of calcium-leached cement pastes: triaxial stress states and the influence of the pore pressures. *Cement and Concrete Research*, 31(5):767–774, 2001.

[84] S.Y. Xie, J.F. Shao, and N. Burlion. Experimental study of mechanical behaviour of cement paste under compressive stress and chemical degradation. *Cement and Concrete Research*, 38(12):1416–1423, 2008.

[85] T.H. Wee, J. Zhu, H.T. Chua, and S.F. Wong. Resistance of blended cement pastes to leaching in distilled water at ambient and higher temperatures. *Materials Journal*, 98(2):184–193, 2001.

[86] F.H. Heukamp, F.J. Ulm, and J.T. Germaine. Poroplastic properties of calcium-leached cement-based materials. *Cement and Concrete Research*, 33(8):1155–1173, 2003.

[87] K. Haga, M. Shibata, M. Hironaga, S. Tanaka, and S. Nagasaki. Silicate anion structural change in calcium silicate hydrate gel on dissolution of hydrated cement. *Journal of Nuclear Science and Technology*, 39(5):540–547, 2002.

[88] J. Jain and N. Neithalath. Analysis of calcium leaching behavior of plain and modified cement pastes in pure water. *Cement and Concrete Composites*, 31(3):176–185, 2009.

[89] K. Haga, S. Sutou, M. Toyohara, M. Kaneko, Y. Kobayashi, and T. Kozawa. Alteration of cement hydrate by dissolution, 1. alternation test of hydrate cement paste by water-permeation using centrifugal force. *Nippon Genshiryoku Gakkai Wabun Ronbunshi*, 1(1):20–29, 2002.

[90] K.L. Scrivener, D. Damidot, and C. Famy. Possible mechanisms of expansion of concrete exposed to elevated temperatures during curing (also known as def) and implications for avoidance of field problems. *Cement, Concrete and Aggregates*, 21(1):93–101, 1999.

[91] H.F.W. Taylor, C. Famy, and K.L. Scrivener. Delayed ettringite formation. *Cement and Concrete Research*, 31(5):683–693, 2001.

[92] N. Baghdadi, J.F. Seignol, R.P. Martin, J.C. Renaud, and F. Toutlemonde. Effect of early age thermal history on the expansion due to delayed ettringite formation: experimental study and model calibration. In *Euro Mediterranean symposium on Advances in Geomaterials AGS'08*, pages 661–666, 2008.

[93] R.P. Martin. *Analyse sur structures modèles des effets mécaniques de la réaction sulfatique interne du béton.* PhD thesis, Université Paris-Est, 2010.

[94] R. Yang, C.D. Lawrence, and J.H. Sharp. Delayed ettringite formation in 4-year old cement pastes. *Cement and Concrete Research*, 26(11):1649–1659, 1996.

[95] I. Odler. Interaction between gypsum and the csh phase formed in C_3S hydration. In *7th International Congress on the Chemistry of Cement*, volume 4, pages 493–495. The Congress Paris, France, 1980.

[96] Y. Fu. *Delayed ettringite formation in Portland cement products.* University of Ottawa (Canada), 1996.

[97] L. Divet and R. Randriambololona. Delayed ettringite formation: the effect of temperature and basicity on the interaction of sulphate and csh phase. *Cement and Concrete Research*, 28(3):357–363, 1998.

[98] X. Brunetaud, R. Linder, L. Divet, D. Duragrin, and D. Damidot. Effect of curing conditions and concrete mix design on the expansion generated by delayed ettringite formation. *Materials and Structures*, 40(6):567–578, 2007.

[99] G. Escadeillas, J.E. Aubert, M. Segerer, and W. Prince. Some factors affecting delayed ettringite formation in heat-cured mortars. *Cement and Concrete Research*, 37(10):1445–1452, 2007.

[100] M.C. Lewis. *Heat curing and delayed ettringite formation in concretes*. PhD thesis, Imperial College London (University of London), 1996.

[101] Z. Zhang, J. Olek, and S. Diamond. Studies on delayed ettringite formation in early-age, heat-cured mortars: I. expansion measurements, changes in dynamic modulus of elasticity, and weight gains. *Cement and Concrete Research*, 32(11):1729–1736, 2002.

[102] D.W. Hobbs. Expansion and cracking in concrete attributed to delayed ettringite formation. *Program on "Ettringite-The Sometimes Host of Destruction"*, SP-177:151–181, 1999.

[103] K. Quillin. *Delayed ettringite formation: in-situ concrete*. CRC Press, 2001.

[104] I. Odler and M. Gasser. Mechanism of sulfate expansion in hydrated portland cement. *Journal of the American Ceramic Society*, 71(11):1015–1020, 1988.

[105] N. Leklou, J.E. Aubert, and G. Escadeillas. Microscopic observations of samples affected by delayed ettringite formation (def). *Materials and Structures*, 42(10):1369, 2009.

[106] R.L. Day. *The effect of secondary ettringite formation on the durability of concrete: a literature analysis*. Number RD108T. 1992.

[107] I. Galan, A. Elhoweris, T. Hanein, M.N. Bannerman, and F.P. Glasser. Advances in clinkering technology of calcium sulfoaluminate cement. *Advances in Cement Research*, 29(1):1–1, 2017.

[108] D. Damidot and F.P. Glasser. Thermodynamic investigation of the $CaO - Al_2O_3 - CaSO_4 - H_2O$ system at 25 °C and the influence of Na_2O. *Cement and Concrete Research*, 23(1):221–238, 1993.

[109] D. Damidot and F.P. Glasser. Thermodynamic investigation of the $CaO - Al_2O_3 - CaSO_4 - H_2O$ system at 50 °C and 85 °C. *Cement and Concrete Research*, 22(6):1179–1191, 1992.

[110] P.W. Brown and J.V. Bothe Jr. The stability of ettringite. *Advances in Cement Research*, 5(18):47–63, 1993.

[111] P. Tepponen. Damages in concrete railway sleepers in finland. *Nordic Concrete Research*, (6):199–209, 1987.

[112] E.E. Hekal and S.A. Abo-El-Enein. Effect of compression on microstructure and thermal stability of ettringite. In *Proc int conf on cement microscopy, 8th Int cement microscopy assoc. Duncanville, TX*, 1986.

[113] G.M. Darr, M. Punzet, and U. Ludwig. On the chemical and thermal stability of ettringite. In *UInU: Seminar Proceedings, Reaction of Aluminates during the setting of cements*, 1997.

[114] N.N. Skoblinskaya and K.G. Krasilnikov. Changes in crystal structure of ettringite on dehydration. 1. *Cement and Concrete Research*, 5(4):381–393, 1975.

[115] N.N. Skoblinskaya, K.G. Krasilnikov, L.V. Nikitina, and V.P. Varlamov. Changes in crystal structure of ettringite on dehydration. 2. *Cement and Concrete Research*, 5(5):419–431, 1975.

[116] N.D.M. Evans. Binding mechanisms of radionuclides to cement. *Cement and Concrete Research*, 38(4):543–553, 2008.

[117] R. Barbarulo. Comportement des matériaux cimentaires: actions des sulfates et de la température. *LMT-ENS de Cachan, France, Thèse de Doctorat*, 2002.

[118] L. Nachbaur. *Etude de l'influence d'electrolyste sur l'hydratation et la prise du silicate tricalcique, composant principal du ciment portland. Caracterisation des interactions a l'origine de la prise.* PhD thesis, Dijon, 1997.

[119] C. Famy, K.L. Scrivener, A. Atkinson, and A.R. Brough. Effects of an early or a late heat treatment on the microstructure and composition of inner csh products of portland cement mortars. *Cement and Concrete Research*, 32(2):269–278, 2002.

[120] M. Salgues, A. Sellier, S. Multon, E. Bourdarot, and E. Grimal. Def modelling based on thermodynamic equilibria and ionic transfers for structural analysis. *European Journal of Environmental and Civil Engineering*, 18(4):377–402, 2014.

[121] Y. Fu, P. Xie, P. Gu, and J.J. Beaudoin. Effect of temperature on sulphate adsorption/desorption by tricalcium silicate hydrates. *Cement and Concrete Research*, 24(8):1428–1432, 1994.

[122] R. Barbarulo, H. Peycelon, and S. Leclercq. Chemical equilibria between C-S-H and ettringite, at 20 and 85 °C. *Cement and Concrete Research*, 37(8):1176–1181, 2007.

[123] K.L. Scrivener and H.F.W. Taylor. Delayed ettringite formation: a microstructural and microanalytical study. *Advances in Cement Research*, 5(20):139–146, 1993.

[124] C. Famy, K.L. Scrivener, A. Atkinson, E. Lachowski, and A.R. Brough. Characterization of calcium-silicate-hydrate products in expansive and non-expansive heat-cured mortars-electron microscopy study. *Special Publication*, 192:385–402, 2000.

[125] H. Stade and D. Müller. On the coordination of al in ill-crystallized csh phases formed by hydration of tricalcium silicate and by precipitation reactions at ambient temperature. *Cement and Concrete Research*, 17(4):553–561, 1987.

[126] P. Faucon, A. Delagrave, J.C. Petit, C. Richet, J.M. Marchand, and H. Zanni. Aluminum incorporation in calcium silicate hydrates (C-S-H) depending on their Ca/Si ratio. *The Journal of Physical Chemistry B*, 103(37):7796–7802, 1999.

[127] D. Heinz, U. Ludwig, and I. Rüdiger. Delayed ettringite formation in heat treated mortars and concretes. *Concrete Precasting Plant and Technology*, 11:56–61, 1989.

[128] C.D. Lawrence. Mortar expansions due to delayed ettringite formation. effects of curing period and temperature. *Cement and Concrete Research*, 25(4):903–914, 1995.

[129] I. Odler and Y. Chen. Effect of cement composition on the expansion of heat-cured cement pastes. *Cement and Concrete Research*, 25(4):853–862, 1995.

[130] S. Kelham. Influence of cement composition on volume stability of mortar. *Special Publication*, 177:27–46, 1999.

[131] C.D. Lawrence. Delayed ettringite formation: an issue? *Material Science of Concrete IY.*, pages 113–154, 1995.

[132] Z. Zhang, J. Olek, and S. Diamond. Studies on delayed ettringite formation in heat-cured mortars: Ii. characteristics of cement that may be susceptible to def. *Cement and Concrete Research*, 32(11):1737–1742, 2002.

[133] M. Collepardi. Damage by delayed ettringite formation. *Concrete International*, 21(1):69–74, 1999.

[134] X. Brunetaud. *Étude de l'influence de différents paramètres et de leurs interactions sur la cinétique de l'amplitude de la réaction sulfatique interne au béton*. PhD thesis, Châtenay-Malabry, Ecole Centrale de Paris, 2005.

[135] C. Famy, K.L. Scrivener, A. Atkinson, and A.R. Brough. Influence of the storage conditions on the dimensional changes of heat-cured mortars. *Cement and Concrete Research*, 31(5):795–803, 2001.

[136] L.A. Graf. Effect of relative humidity on expansion and microstructure of heat-cured mortars. Technical report, 2007.

[137] M. Al Shamaa, S. Lavaud, L. Divet, G. Nahas, and J.M. Torrenti. Influence of relative humidity on delayed ettringite formation. *Cement and Concrete Composites*, 58:14–22, 2015.

[138] R. Yang, C.D. Lawrence, C.J. Lynsdale, and J.H. Sharp. Delayed ettringite formation in heat-cured portland cement mortars. *Cement and Concrete Research*, 29(1):17–25, 1999.

[139] C.D. Lawrence. Long-term expansion of mortars and concretes. *Special Publication*, 177:105–124, 1999.

[140] C. Famy. *Expansion of heat-cured mortars*. PhD thesis, Imperial College London (University of London), 1999.

[141] T. Ramlochan, P. Zacarias, M.D.A. Thomas, and R.D. Hooton. The effect of pozzolans and slag on the expansion of mortars cured at elevated temperature: Part i: Expansive behaviour. *Cement and Concrete Research*, 33(6):807–814, 2003.

[142] Y. Fu, J. Ding, and J.J. Beaudoin. Expansion of portland cement mortar due to internal sulfate attack. *Cement and Concrete Research*, 27(9):1299–1306, 1997.

[143] N. Baghdadi. *Modélisation du couplage chimico-mécanique d'un béton atteint d'une réaction sulfatique interne*. PhD thesis, Ecole Nationale des Ponts et Chaussées, 2008.

[144] R.P. Martin, C. Bazin, J. Billo, M. Estivin, J.C. Renaud, and F. Toutlemonde. Experimental evidence for understanding def sensitivity to early-age thermal

history. In *RILEM-JCI International Workshop on Crack Control of Mass Concrete and Related Issues Concerning Early-Age of Concrete Structures*, page 10p, 2012.

[145] B. Kchakech, R.P. Martin, O.O. Metalssi, and F. Toutlemonde. Experimental study of the influence of the temperature and duration of heat treatments at an early age on the risk of concrete expansion associated with delayed ettringite formation. In *CONCREEP 10*, pages 455–465. 2015.

[146] B. Kchakech. *Étude de l'influence de l'échauffement subi par un béton sur le risque d'expansions associées à la Réaction Sulfatique Interne*. PhD thesis, Paris Est, 2015.

[147] K.O. Kjellsen, R.J. Detwiler, and O.E. Gjørv. Backscattered electron imaging of cement pastes hydrated at different temperatures. *Cement and Concrete Research*, 20(2):308–311, 1990.

[148] Y. Cao and R.J. Detwiler. Backscattered electron imaging of cement pastes cured at elevated temperatures. *Cement and Concrete Research*, 25(3):627–638, 1995.

[149] H.H. Patel, C.H. Bland, and A.B. Poole. The microstructure of concrete cured at elevated temperatures. *Cement and Concrete Research*, 25(3):485–490, 1995.

[150] K.O. Kjellsen, R.J. Detwiler, and O.E. Gjørv. Development of microstructures in plain cement pastes hydrated at different temperatures. *Cement and Concrete Research*, 21(1):179–189, 1991.

[151] K.O. Kjellsen. Heat curing and post-heat curing regimes of high-performance concrete: influence on microstructure and csh composition. *Cement and Concrete Research*, 26(2):295–307, 1996.

[152] H.H. Patel, C.H. Bland, and A.B. Pool. The microstructure of steam-cured precast concrete. *Advances in Cement Research*, 8(29):11–19, 1996.

[153] K.L. Scrivener. The effect of heat treatment of inner product C-S-H. *Cement and Concrete Research*, 22(6):1224–1226, 1992.

[154] ACI Committee 116. 116r-00: Cement and concrete terminology. American Concrete Institute Farmington Hills, Mich., 2000.

[155] D.W. Hobbs. Expansion and cracking of concrete attributed to delayed ettringite formation. *Proceedings of a 'technical Session–Ettringite: The sometimes host of destruction, American Concrete Institute, Seattle, Washington, SP-177*, pages 151–181, 1999.

[156] L. Divet and A. Pavoine. Delayed ettringite formation in massive concrete structures: an account of some studies of degraded bridges. In *International RILEM Workshop on Internal Sulfate Attack and Delayed Ettringite Formation*, pages 98–126. RILEM Publications SARL, 2004.

[157] N. Baghdadi, J.F. Seignol, and F. Toutlemonde. Chemo-mechanical model describing the expansion due to internal sulfate attack: numerical simulation. In *International RILEM symposium on concrete modelling CONMOD*, volume 8, pages 291–298, 2008.

[158] J.F. Seignol, N. Baghdadi, and F. Toutlemonde. A macroscopic chemo-mechanical model aimed at re-assessment of delayed ettringite formation affected concrete structures. In *1 st International Conference on Computational Technologies in Concrete Structures CTCS'09*, pages 422–440, 2009.

[159] I. del Hormigón Estructural. Ehe-08. *Madrid, Ministerio de Fomento, Secretaría General Técnica*, 2008.

[160] D.R. Kester and R.M. Pytkowicx. Sodium, magnesium, and calcium sulfate ion-pairs in seawater at 25c. *Limnology and Oceanography*, 14(5):686–692, 1969.

[161] B.E. Sheetz and S. Kwan. Control of ettringite swelling. *Ashlines*, 4(1):1–10, 2003.

[162] A. Atkinson, J.A. Hearne, and C.F. Knights. Thermodynamic modelling and aqueous chemistry in the $CaO - Al_2O_3 - SiO_2 - H_2O$ system. *MRS Online Proceedings Library Archive*, 212, 1990.

[163] P.K. Mehta and F. Hu. Further evidence for expansion of ettringite by water adsorption. *Journal of the American Ceramic Society*, 61(3-4):179–181, 1978.

[164] J.L. Sagrera. Study on the durability of sulphate application of le chatelier-anstett method to an ordinary portland cement. *Cement and Concrete Research*, 2(3):253–260, 1972.

[165] M.D. Cohen. Modeling of expansive cements. *Cement and Concrete Research*, 13(4):519–528, 1983.

[166] X. Ping and J.J. Beaudoin. Mechanism of sulphate expansion i. thermodynamic principle of crystallization pressure. *Cement and Concrete Research*, 22(4):631–640, 1992.

[167] G.W. Scherer. Crystallization in pores. *Cement and Concrete Research*, 29(8):1347–1358, 1999.

[168] A.W. Adamson and A.P. Gast. Physical chemistry of surfaces. 1967.

[169] R.J. Flatt and G.W. Scherer. Thermodynamics of crystallization stresses in def. *Cement and Concrete Research*, 38(3):325–336, 2008.

[170] R.J. Flatt, M. Steiger, and G.W. Scherer. A commented translation of the paper by cw correns and w. steinborn on crystallization pressure. *Environmental Geology*, 52(2):187, 2007.

[171] M. Steiger. Crystal growth in porous materials—i: the crystallization pressure of large crystals. *Journal of Crystal Growth*, 282(3):455–469, 2005.

[172] S. Chatterji and N. Thaulow. Unambiguous demonstration of destructive crystal growth pressure. *Cement and Concrete Research*, 27(6):811–816, 1997.

[173] S. Chatterji. Aspects of generation of destructive crystal growth pressure. *Journal of Crystal Growth*, 277(1):566–577, 2005.

[174] H.Y. Ghorab, D. Heinz, U. Ludwig, T. Meskendahl, and A. Wolter. On the stability of calcium aluminate sulphate hydrates in pure systems and in cements. *Proceedings of the 7th International Congress on the Chemistry of Cement*, 4:496–503, 1980.

[175] V. Johansen, N. Thaulow, and J. Skalny. Simultaneous presence of alkali—silica gel and ettringite in concrete. *Advances in Cement Research*, 5(17):23–29, 1993.

[176] L. Yuan-Hui and S. Gregory. Diffusion of ions in sea water and in deep-sea sediments. *Geochimica et Cosmochimica Acta*, 38(5):703–714, 1974.

[177] C. Andrade. Calculation of chloride diffusion coefficients in concrete from ionic migration measurements. *Cement and Concrete Research*, 23(3):724–742, 1993.

[178] E.J. Hansen and V.E. Saouma. Numerical simulation of reinforced concrete deterioration. In *Third International Conference on Fracture Mechanics of Concrete and Concrete Structures(FRAMCOS-3)*, pages 1655–1668, 1998.

[179] P.C. Carman. Permeability of saturated sands, soils and clays. *The Journal of Agricultural Science*, 29(2):262–273, 1939.

[180] D. Mu, Z.S. Liu, C. Huang, and N. Djilali. Determination of the effective diffusion coefficient in porous media including knudsen effects. *Microfluidics and Nanofluidics*, 4(3):257–260, 2008.

[181] B. Bary and S. Béjaoui. Assessment of diffusive and mechanical properties of hardened cement pastes using a multi-coated sphere assemblage model. *Cement and Concrete Research*, 36(2):245–258, 2006.

[182] J.W. Ju, L.S. Weng, S. Mindess, and A.J. Boyd. Damage assessment and service life prediction of concrete subject to sulfate attack. *Materials Science of Concrete: Sulfate Attack Mechanisms*, 1999.

[183] M. Santhanam, M.D. Cohen, and J. Olek. Sulfate attack research—whither now? *Cement and Concrete Research*, 31(6):845–851, 2001.

[184] H.A.F. Dehwah. Effect of sulfate concentration and associated cation type on concrete deterioration and morphological changes in cement hydrates. *Construction and Building Materials*, 21(1):29–39, 2007.

[185] F. Aköz, F. Türker, S. Koral, and N. Yüzer. Effects of raised temperature of sulfate solutions on the sulfate resistance of mortars with and without silica fume. *Cement and Concrete Research*, 29(4):537–544, 1999.

[186] M. Sahmaran, T.K. Erdem, and I.O. Yaman. Sulfate resistance of plain and blended cements exposed to wetting–drying and heating–cooling environments. *Construction and Building Materials*, 21(8):1771–1778, 2007.

[187] M.A. Gonzalez and E.F. Irassar. Ettringite formation in low C_3A portland cement exposed to sodium sulfate solution. *Cement and Concrete Research*, 27(7):1061–1072, 1997.

[188] A. Atkinson, D.J. Goult, and J.A. Hearne. An assessment of the long-term durability of concrete in radioactive waste repositories. In *MRS Proceedings*, volume 50, page 239. Cambridge University Press, 1985.

[189] R. Shuman, V.C. Rogers, and R.A. Shaw. The barrier code for predicting long-term concrete performance. In *Waste Processing, Transportation, Storage and Disposal, Technical Programs and Public Education*. 1989.

[190] S.W. Li, Y.F. Wang, and S.N. Wang. Research on the prediction model of the concrete damage in the sulfate aggressive environment. *Journal of Wuhan University of Technology*, 32(14):36–44, 2010.

[191] H. Lee, M.S. Cho, J.S. Lee, and D. Kim. Prediction model of life span degradation under sulfate attack regarding diffusion rate by amount of sulfate ions in seawater. *International Journal of Materials, Mechanics and Manufacturing*, 1(3):251–255, 2013.

[192] Y. Zhou, H. Tian, H. Cui, F. Xing, and L. Sui. Model for sulfate diffusion depth in concrete under complex aggressive environments and its experimental verification. *Advances in Materials Science and Engineering*, 2015, 2015.

[193] T. Ikumi, S.H. Cavalaro, I. Segura, A. de la Fuente, and A. Aguado. Simplified methodology to evaluate the external sulfate attack in concrete structures. *Materials & Design*, 89:1147–1160, 2016.

[194] R. Tixier and B. Mobasher. Modeling of damage in cement-based materials subjected to external sulfate attack. i: Formulation. *Journal of Materials in Civil Engineering*, 15(4):305–313, 2003.

[195] B. Bary. Simplified coupled chemo-mechanical modeling of cement pastes behavior subjected to combined leaching and external sulfate attack. *International Journal for Numerical and Analytical Methods in Geomechanics*, 32(14):1791–1816, 2008.

[196] M. Basista and W. Weglewski. Micromechanical modeling of sulphate corrosion in concrete: influence of ettringite forming reaction. *Theoretical and Applied Mechanics*, 35(1-3):29–52, 2008.

[197] M. Basista and W. Weglewski. Chemically assisted damage of concrete: a model of expansion under external sulfate attack. *International Journal of Damage Mechanics*, 18(2):155–175, 2009.

[198] S. Sarkar, S. Mahadevan, J.C.L. Meeussen, H. Van der Sloot, and D.S. Kosson. Numerical simulation of cementitious materials degradation under external sulfate attack. *Cement and Concrete Composites*, 32(3):241–252, 2010.

[199] F. Schmidt-Döhl and F.S. Rostásy. A model for the calculation of combined chemical reactions and transport processes and its application to the corrosion of mineral-building materials part ii. experimental verification. *Cement and Concrete Research*, 29(7):1047–1053, 1999.

[200] M.A. Shazali, M.H. Baluch, and A.H. Al-Gadhib. Predicting residual strength in unsaturated concrete exposed to sulfate attack. *Journal of Materials in Civil Engineering*, 18(3):343–354, 2006.

[201] R. Tixier and B. Mobasher. Modeling of damage in cement-based materials subjected to external sulfate attack. ii: Comparison with experiments. *Journal of Materials in Civil Engineering*, 15(4):314–322, 2003.

[202] O. Coussy. *Poromechanics*. 2004.

[203] A.E. Idiart, C.M. López, and I. Carol. Chemo-mechanical analysis of concrete cracking and degradation due to external sulfate attack: a meso-scale model. *Cement and Concrete Composites*, 33(3):411–423, 2011.

[204] B. Bary, N. Leterrier, E. Deville, and P. Le Bescop. Coupled chemo-transport-mechanical modelling and numerical simulation of external sulfate attack in mortar. *Cement and Concrete Composites*, 49:70–83, 2014.

[205] Y. Yu, Y.X. Zhang, and A. Khennane. Numerical modelling of degradation of cement-based materials under leaching and external sulfate attack. *Computers & Structures*, 158:1–14, 2015.

[206] A. Schindler. Effect of temperature on hydration of cementitious materials. *Materials Journal*, 101(1):72–81, 2004.

[207] M. Salgues. *Modélisation des effets structuraux des réactions sulfatiques internes: application aux barrages en béton*. PhD thesis, Université de Toulouse, Université Toulouse III-Paul Sabatier, 2013.

[208] A. Sellier and S. Multon. Chemical modelling of delayed ettringite formation for assessment of affected concrete structures. *Cement and Concrete Research*, 108:72–86, 2018.

[209] A. Sellier. Model FLUENDO3D Version 20-P for Castem 2012, tentative handbook, 2015.

[210] M.C. Lewis, K.L. Scrivener, and S. Kelham. Heat curing and delayed ettringite formation. *MRS Online Proceedings Library Archive*, 370, 1994.

[211] M. Lawrence and Y. Jiang. Porosity, pore size distribution, micro-structure. In *Bio-aggregates Based Building Materials*, pages 39–71. 2017.

[212] K.K. Aligizaki. Detemination of pore structure parameters in hardened cementitious materials. *MS Thesis. The Pennsylvania State University*, 1995.

[213] M. Bertin. *L'impact du séchage au jeune àge sur la carbonatation des matériaux cimentaires avec additions minérales.* PhD thesis, Ph. D. Thesis, Paris Est, Marne-la-Vallée, France, 2007.

[214] K. Meyer, P. Lorenz, B. Böhl-Kuhn, and P. Klobes. Porous solids and their characterization methods of investigation and application. *Crystal Research and Technology*, 29(7):903–930, 1994.

[215] EN. 197-1: 2011. *Cement, Composition, Specifications and Conformity Criteria for Common Cements*, 2011.

[216] S. Messad. *Mise au point d'un essai de vieillissement accéléré de l'attaque sulfatique externe pour l'application du concept de performance équivalente dans le cadre de la norme NF EN 206-1.* PhD thesis, Ph. D. thesis, University of Toulouse, 2009.

[217] E. Rozière. *Etude de la durabilité des bétons par une approche performantielle.* PhD thesis, Nantes, 2007.

[218] J. Hema. *The effects of liquid nitrogen on concrete hydration, microstructure, and properties.* Citeseer, 2007.

[219] D.N. Winslow. The validity of high pressure mercury intrusion porosimetry. *Journal of Colloid and Interface Science*, 67(1):42–47, 1978.

[220] J. Adolphs, M.J. Setzer, and P. Heine. Changes in pore structure and mercury contact angle of hardened cement paste depending on relative humidity. *Materials and Structures*, 35(8):477–486, 2002.

[221] D.M. Roy. Relationships between permeability, porosity, diffusion and microstructure of cement pastes, mortar, and concrete at different temperatures. *MRS Online Proceedings Library Archive*, 137, 1988.

[222] R.A. Cook and K.C. Hover. Mercury porosimetry of hardened cement pastes. *Cement and Concrete Research*, 29(6):933–943, 1999.

[223] K.S. Sing. Reporting physisorption data for gas/solid systems with special reference to the determination of surface area and porosity (recommendations 1984). *Pure and Applied Chemistry*, 57(4):603–619, 1985.

[224] P.W. Winston and D.H. Bates. Saturated solutions for the control of humidity in biological research. *Ecology*, 41(1):232–237, 1960.

[225] S. Brunauer, P.H. Emmett, and E. Teller. Adsorption of gases in multimolecular layers. *Journal of the American Chemical Society*, 60(2):309–319, 1938.

[226] E.P. Barrett, L.G. Joyner, and P.P. Halenda. The determination of pore volume and area distributions in porous substances. i. computations from nitrogen isotherms. *Journal of the American Chemical Society*, 73(1):373–380, 1951.

[227] J.J. Thomas, H.M. Jennings, and A.J. Allen. The surface area of hardened cement paste as measured by various techniques. *Concrete Science and Engineering*, 1(1):45–64, 1999.

[228] J. Adolphs and M.J. Setzer. Description of gas adsorption isotherms on porous and dispersed systems with the excess surface work model. *Journal of Colloid and Interface Science*, 207(2):349–354, 1998.

[229] J. Hagymassy Jr, S. Brunauer, and R.S. Mikhail. Pore structure analysis by water vapor adsorption: I. t-curves for water vapor. *Journal of Colloid and Interface Science*, 29(3):485–491, 1969.

[230] R. Badmann, N. Stockhausen, and M.J. Setzer. The statistical thickness and the chemical potential of adsorbed water films. *Journal of Colloid and Interface Science*, 82(2):534–542, 1981.

[231] J. Baron, A. Desdevises, M. Buil, C.H. Detriche, C. Vernet, R. Duval, and T. Dumas. *La durabilité des bétons*. 1992.

[232] C.R. Clarkson, J.L. Jensen, and S. Chipperfield. Unconventional gas reservoir evaluation: what do we have to consider? *Journal of Natural Gas Science and Engineering*, 8:9–33, 2012.

[233] J.J. Beaudoin. Porosity measurement of some hydrated cementitious systems by high pressure mercury intrusion-microstructural limitations. *Cement and Concrete Research*, 9(6):771–781, 1979.

[234] H. Giesche. Mercury porosimetry: a general (practical) overview. *Particle & Particle Systems Characterization*, 23(1):9–19, 2006.

[235] S. Diamond and M.E. Leeman. Pore size distributions in hardened cement paste by sem image analysis. *MRS Online Proceedings Library Archive*, 370, 1994.

[236] N.C. Collier. Transition and decomposition temperatures of cement phases–a collection of thermal analysis data. *Ceramics-Silikaty*, 60(4), 2016.

[237] R.C. Weast and M.J. Astle. Handbook of chemistry and physics crc press. *Boca Raton (2005-2006)*, 1981.

[238] D.L. Hudson-Lamb, C.A. Strydom, and J.H. Potgieter. The thermal dehydration of natural gypsum and pure calcium sulphate dihydrate (gypsum). *Thermochimica Acta*, 282:483–492, 1996.

[239] R.C. Mackenzie. Differential thermal analysis. *Applications*, 2, 1972.

[240] K.T. Greene. Early hydration reactions of portland cement. In *Proc. 4th Intl. Congress on the Chemistry of Cements. Washington I*, volume 359, page 74, 1960.

[241] G.C. Bye. *Portland cement: composition, production and properties*. Thomas Telford, 1999.

[242] R.J. Hand. Calcium sulphate hydrates: a review. *British Ceramic Transactions*, 96(3):116–120, 1997.

[243] Y. Deutsch, Y. Nathan, and S. Sarig. Thermogravimetric evaluation of the kinetics of the gypsum-hemihydrate-soluble anhydrite transitions. *Journal of Thermal Analysis and Calorimetry*, 42(1):159–174, 1994.

[244] I. Kapralik, F. Hanic, J. Havlica, and V. Ambruz. Subsolidus phase relations in the system $CaO - Al_2O_3 - SiO_2 - Fe_2O_3 - MgO - CaSO_4 - K_2SO_4$ at 950 °C in air referred to sulphoaluminate cement clinker. *British Ceramic. Transactions and Journal*, 85:107–110, 1986.

[245] J.J. Rowe, G.W. Morey, and I.D. Hansen. The binary system $K_2SO_4 - CaSO_4$. *Journal of Inorganic and Nuclear Chemistry*, 27(1):53–58, 1965.

[246] J. Bensted and S.P. Varma. Some applications of infrared and raman spectroscopy in cement chemistry. part 3-hydration of portland cement and its constituents. *Cement Technology*, 5(5):440–445, 1974.

[247] G.L. Kalousek, C.W. Davis, and W.E. Schmertz. An investigation of hydrating cements and related hydrous solids by differential thermal analysis. In *Journal Proceedings*, volume 45, pages 693–712, 1949.

[248] V.S. Ramachandran. *Applications of differential thermal analysis in cement chemistry*. Chemical Publishing Company New York, 1969.

[249] V. Šatava and O. VepŘek. Thermal decomposition of ettringite under hydrothermal conditions. *Journal of the American Ceramic Society*, 58(7-8):357–359, 1975.

[250] S.M. Bushnell-Watson and J.H. Sharp. The application of thermal analysis to the hydration and conversion reactions of calcium aluminate cements. *Materiales de Construcción*, 42(228):13–32, 1992.

[251] C.M. George. Industrial aluminous cements. *Structure and Performance of Cements*, pages 415–470, 1983.

[252] S. Kwan, J. LaRosa, and M.W. Grutzeck. 29Si and 27Al MASNMR study of stratlingite. *Journal of the American Ceramic Society*, 78(7):1921–1926, 1995.

[253] J. Bensted. Calcium aluminate cements. *Leás Chemistry of Cement and Concrete*, 1998.

[254] E.L.I.O. Passaglia and R. Rinaldi. Katoite, a new member of the $Ca_3Al_2(SiO_4)_3 - Ca_3Al_2(OH)_{12}$ series and a new nomenclature for the hydrogrossular group of minerals. *Bull. Mineral*, 107:605–618, 1984.

[255] R.S. Alwitt. Aluminium-water systems. *Oxides and Oxide Films*, 4:169–250, 1976.

[256] R.C. Mackenzie. The oxides of iron, aluminium and manganese. *The Differential Thermal Investigation of Clays*, pages 229–238, 1957.

[257] R. Gabrovšek, T. Vuk, and V. Kaučič. Evaluation of the hydration of portland cement containing various carbonates by means of thermal analysis. *Acta Chim Slov*, 53:159–65, 2006.

[258] E.T. Stepkowska, J.M. Blanes, C. Real, and J.L. Perez-Rodriguez. Hydration products in two aged cement pastes. *Journal of Thermal Analysis and Calorimetry*, 82(3):731–739, 2005.

[259] V.S. Ramachandran, R.M. Paroli, J.J. Beaudoin, and A.H. Delgado. *Handbook of thermal analysis of construction materials*. William Andrew, 2002.

[260] Z. Šauman. Carbonization of porous concrete and its main binding components. *Cement and Concrete Research*, 1(6):645–662, 1971.

[261] L.M. Parker, N.B. Milestone, and R.H. Newman. The use of hydrotalcite as an anion absorbent. *Industrial & Engineering Chemistry Research*, 34(4):1196–1202, 1995.

[262] S. Chinchón Payá, A. Aguado de Cea, H.W. Nugteren, and S. Chinchón Yepes. External sulfate attack in dam concretes with thaumasite formation. *Materiales de Construcción*, 65(317):042, 2015.

[263] R.S. Gollop and H.F.W. Taylor. Microstructural and microanalytical studies of sulfate attack. i. ordinary portland cement paste. *Cement and Concrete Research*, 22(6):1027–1038, 1992.

[264] S. Diamond. *Microstructure of cement-based systems/Bonding and interfaces in cementitious materials*. Materials Research Society, 1995.

[265] A.C.A. Muller. Characterization of porosity & CSH in cement pastes by ^{1}H NMR. *École polytechnique fédérale de Lausanne, EPFL Inforscience*, 2014.

[266] J. Nielsen. Investigation of resistance of cement paste to sulfate attack. *Highway Research Record*, page 113, 1966.

[267] D. Planel. *Les effets couplés de la précipitation d'espèces secondaires sur le comportement mécanique et la dégradation des bétons*. PhD thesis, PhD thesis, University of Marne La Vallée, 2002.

[268] B. Lothenbach, B. Bary, P. Le Bescop, T. Schmidt, and N. Leterrier. Sulfate ingress in portland cement. *Cement and Concrete Research*, 40(8):1211–1225, 2010.

[269] Z. Sawicz and Z. Owsiak. Effect of temperatures on the hydrated cement pastes. In *Proceedings of the 5th Symposium on Science and Research in Silicate Chemistry, Brno (Czechoslovakia)*, pages 56–67, 1981.

[270] J. Piasta, Z. Sawicz, and L. Rudzinski. Changes in the structure of hardened cement paste due to high temperature. *Matériaux et Construction*, 17(4):291–296, 1984.

[271] J.S. Seewald and W.E. Seyfried Jr. Experimental determination of portlandite solubility in H_2O and acetate solutions at 100–350 c and 500 bars: constraints on calcium hydroxide and calcium acetate complex stability. *Geochimica et Cosmochimica Acta*, 55(3):659–669, 1991.

[272] B. Godart and L. Divet. Recommandations pour la prévention des désordres dus à la réaction sulfatique interne: guide technique, 2017.

[273] A. Pavoine and L. Divet. Réactivité d'un béton vis-à-vis d'une réaction sulfatique interne. *Méthode d'essai des Laboratoires des Ponts et Chaussées*, (66), 2007.

[274] W. Kunther. Investigation of sulfate attack by experimental and thermodynamic means. *École polytechnique fédérale de Lausanne, EPFL Inforscience*, 2012.

[275] R.S. Gollop and H.F.W. Taylor. Microstructural and microanalytical studies of sulfate attack. iv. reactions of a slag cement paste with sodium and magnesium sulfate solutions. *Cement and Concrete Research*, 26(7):1013–1028, 1996.

[276] G.W. Scherer. Supersaturation in porous media. In *Poromechanics V: Proceedings of the Fifth Biot Conference on Poromechanics*, pages 2290–2296, 2013.

[277] O. Coussy. Revisiting the constitutive equations of unsaturated porous solids using a lagrangian saturation concept. *International Journal for Numerical and Analytical Methods in Geomechanics*, 31(15):1675–1694, 2007.

[278] M. Jirásek and B. Patzák. Consistent tangent stiffness for nonlocal damage models. *Computers & Structures*, 80(14-15):1279–1293, 2002.

[279] R.J. Knrpnrnrcr. Crystal growth from the melt: A review. *Am Mineral*, 60:798–814, 1975.

[280] M.T. Van Genuchten. A closed-form equation for predicting the hydraulic conductivity of unsaturated soils. *Soil Science Society of America Journal*, 44(5):892–898, 1980.

[281] A. Grandclerc, P. Dangla, M. Gueguen-Minerbe, and T. Chaussadent. Modelling of the sulfuric acid attack on different types of cementitious materials. *Cement and Concrete Research*, 2018.

[282] X. MA, O. Çopuroğlu, E. Schlangen, N. HAN, and F. XING. Experimental and numerical study on cement paste degradation under external sulfate attack. In *Proceedings of 9th International Conference on Fracture Mechanics of Concrete and Concrete Structures*, 2016.

[283] B. Burgher, A. Thibonnier, K.J. Folliard, T. Ley, and M.D. Thomas. Investigation of the internal stresses caused by delayed ettringite formation in concrete. Technical report, 2008.

[284] E. Hoek and J.A. Franklin. *A simple triaxial cell for field or laboratory testing of rock*. Imperial College of Science and Technology, University of London, 1967.

[285] E. Samson, J. Marchand, and K.A. Snyder. Calculation of ionic diffusion coefficients on the basis of migration test results. *Materials and Structures*, 36(3):156–165, 2003.

Appendices

A Deduction of pore size distribution from Water Vapor Sorption Isotherms (WVSI)

An example, which presents the methods to deduce pore size distribution from Water Vapor Sorption Isotherms of sample ESA-I-Ini-Int, is illustrated here. First, WVSI is shown in Fig. A.1. The desorption curve is used to deduce pore size distribution, while the surface area is determined from adsorption curve in the range of 11-35 % according to Eq. 47. A linear relationship between RH and (1/m * 1/(1/RH - 1)) is deduced in Fig. A.2, which helps to predict the surface area in the material ($S_{\mathrm{BET}} = 1.31 \times 10^5$ m^2/kg in this example). With the predicted surface area S_{BET}, the thickness of the water film at each RH can be calculated. The details of the equations are presented in section 2.8. The BJH method is shown in Table A.1.

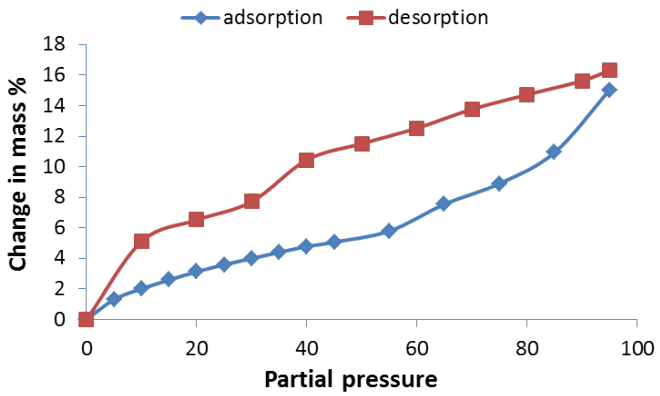

Figure A.1 – WVSI of specimen ESA-I-Ini-Int measured by DVS

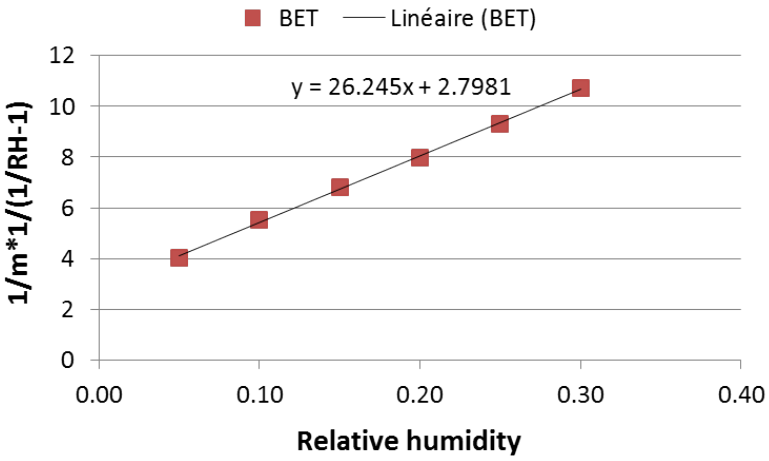

Figure A.2 – BET method to determine the surface area

Table A.1 – BJH method to deduce pore size distribution

RH	mi%	dVi(mm3/g)	ti(Å)	dti(Å)	rki(Å)	rpi(Å)	average rpi(Å)	average rpi(nm)	average rki((Å))	Ri	dVi*Ri	c	Api	c*Api	addition dVpi	dVpi(mm3/g)	∑Vpi(mm3/g)	drpi(nm)	dVpi/drpi(mm3/g/nm)
0.94	16.14		12.32		148.67	160.99				2.08									
0.92	15.90	2.42	12.14	0.18	116.70	128.84	144.91	14.49	132.78	1.19	2.87	0.77	0.04	0.03	0.00	2.87	2.87		
0.91	15.67	2.33	11.96	0.18	95.76	107.72	118.28	11.83	106.32	1.23	2.88	0.77	0.05	0.04	0.03	2.87	5.74	26.63	0.11
0.89	15.53	1.42	11.85	0.11	80.97	92.82	100.27	10.03	88.42	1.28	1.82	0.77	0.04	0.03	0.07	1.81	7.55	18.01	0.10
0.88	15.38	1.50	11.74	0.11	69.97	81.71	87.26	8.73	75.53	1.33	2.00	0.77	0.05	0.03	0.10	1.98	9.53	13.01	0.15
0.86	15.23	1.50	11.62	0.11	61.47	73.09	77.40	7.74	65.77	1.38	2.07	0.77	0.05	0.04	0.13	2.05	11.58	9.87	0.21
0.84	15.08	1.50	11.51	0.11	54.69	66.20	69.64	6.96	58.14	1.43	2.14	0.77	0.06	0.05	0.17	2.12	13.70	7.75	0.27
...																			
...																			
0.05	2.61	8.58	1.99	0.66	3.05	5.04	5.53	0.55	3.54	1.74	14.92	0.77	0.31	0.24	12.35	0.85	162.44	0.93	0.92
0.03	1.70	9.08	1.30	0.69	2.69	3.99	4.52	0.45	3.22	1.33	12.11	0.77	0.21	0.16	12.59	0.47	162.92	1.01	0.47
0.02	0.66	10.42	0.50	0.80	2.24	2.74	3.37	0.34	2.86	0.85	8.82	0.77	0.14	0.11	12.75	0.24	163.15	1.15	0.21

$dVi=\Delta mi\%\times 100/\rho$

$ti=mi\%\times 100/\rho/S_{BET}$

$rki=-4.03/\ln(RH)$

$rpi=rki+ti$

$Ri=rpi^2/(rki+dti)^2$

$Api=2\times dVp/average\ rpi$

$addition\ dVpi=sum\ c*Ap(i-1)$

$dVpi=Ri\times(dVi-dti\times addition\ dVpi)$

B Expansive curves of specimens on different faces

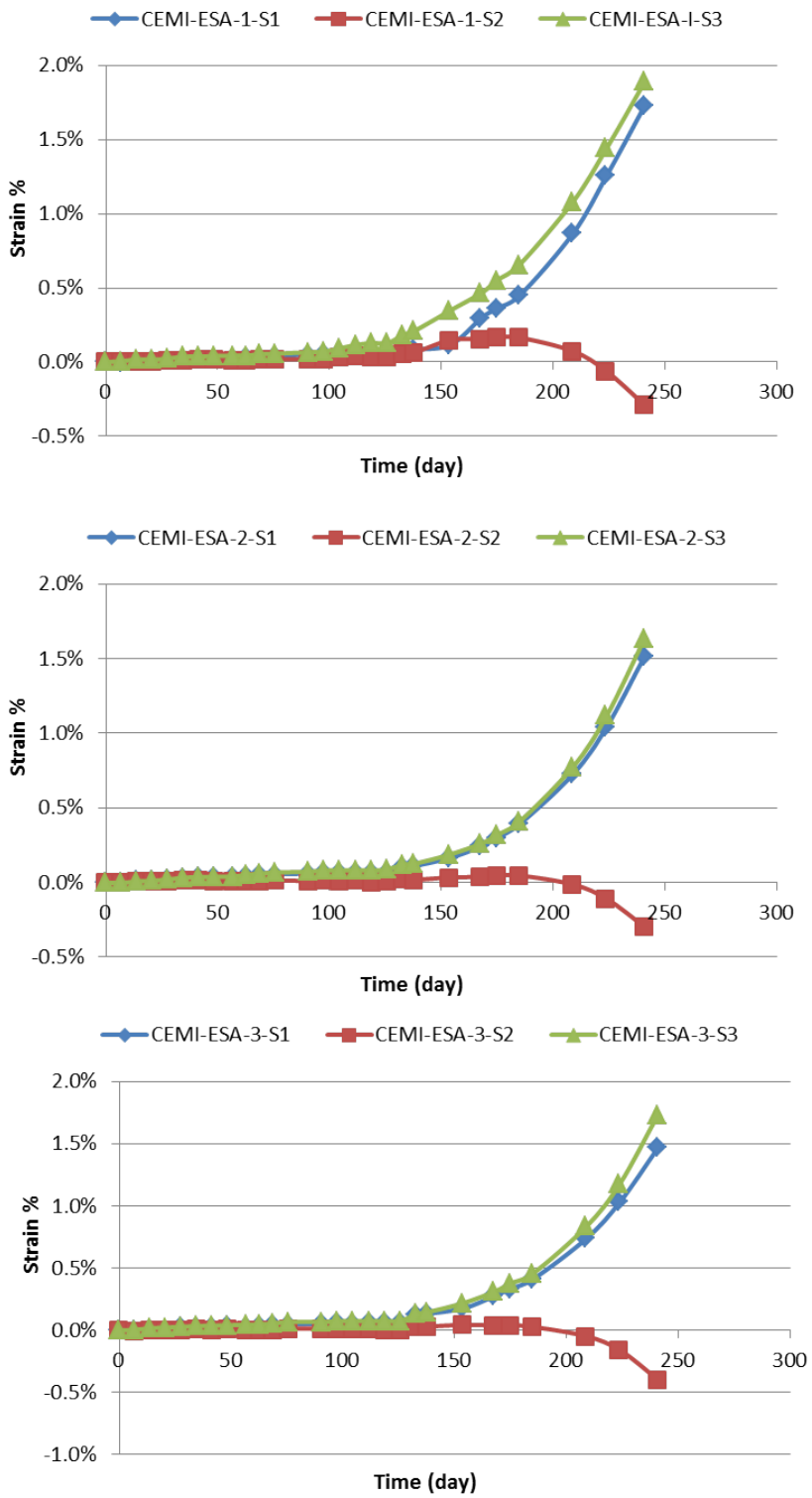

Figure B.1 – Strain of ESA-I-Fin $2 \times 2 \times 12$ cm^3 specimens on different faces

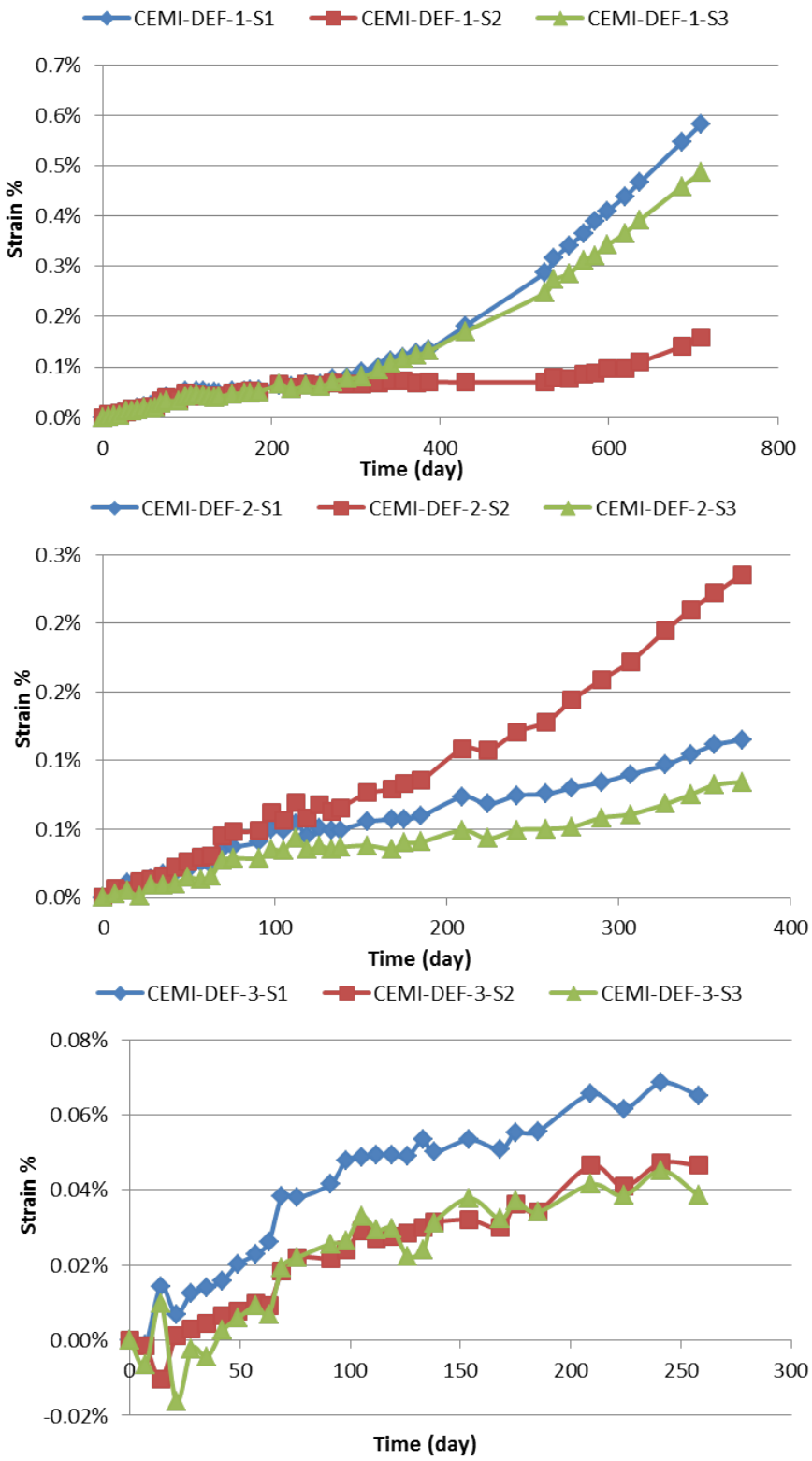

Figure B.2 – Strain of DEF-I-Fin $2 \times 2 \times 12$ cm^3 specimens on different faces

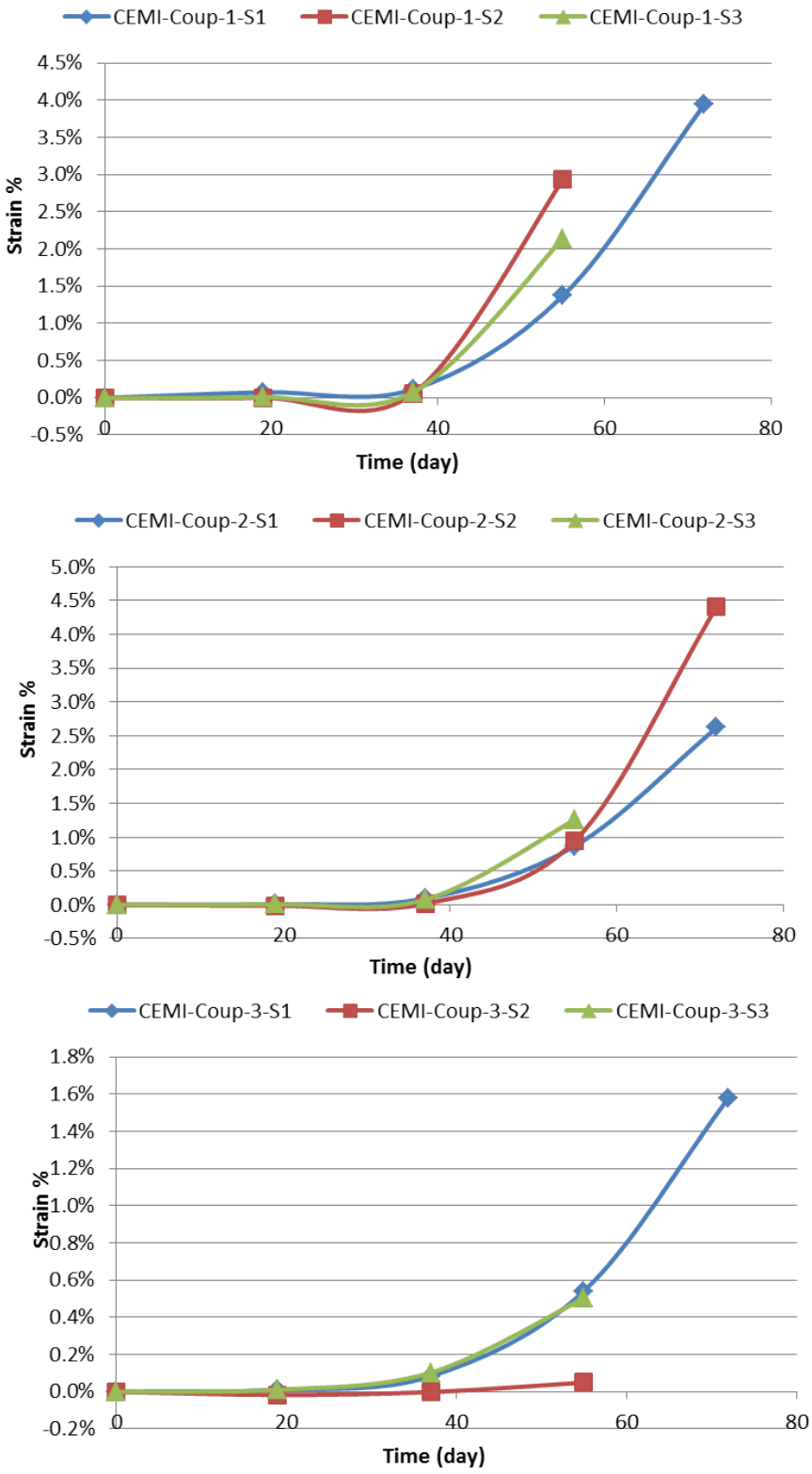

Figure B.3 – Strain of Coup-I-Fin $2 \times 2 \times 12$ cm^3 specimens on different faces

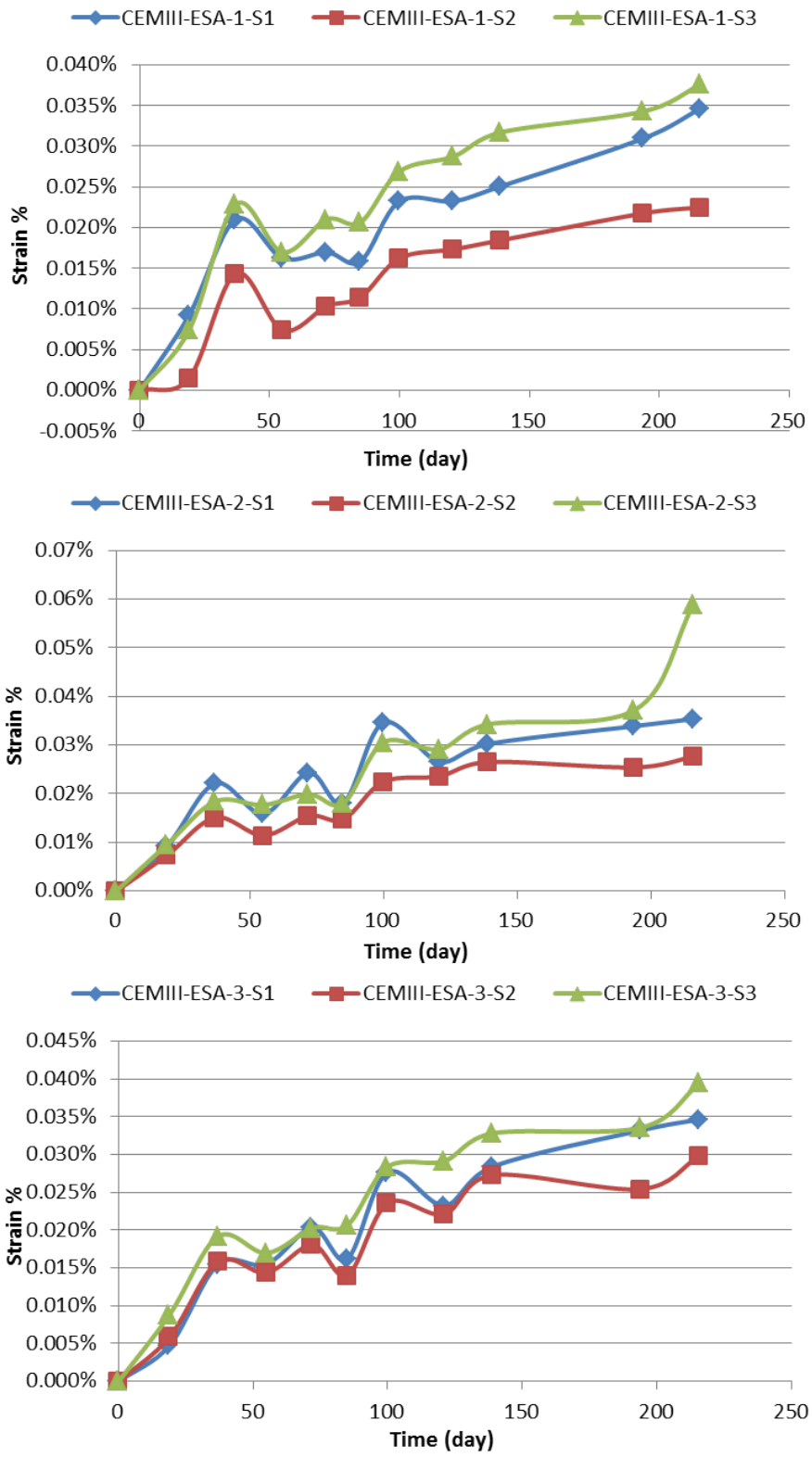

Figure B.4 – Strain of ESA-III-Fin $2 \times 2 \times 12$ cm^3 specimens on different faces

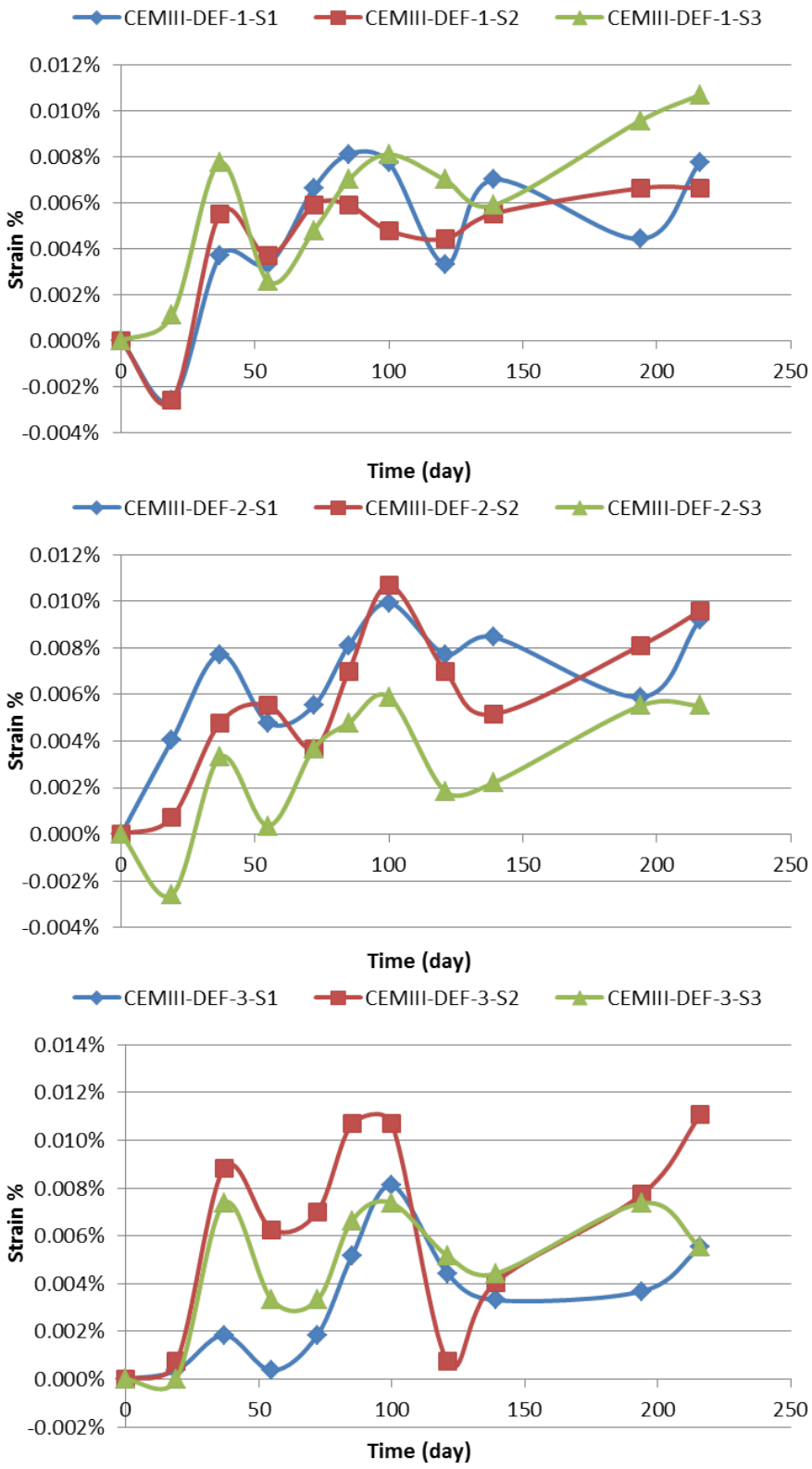

Figure B.5 – Strain of DEF-III-Fin $2 \times 2 \times 12$ cm^3 specimens on different faces

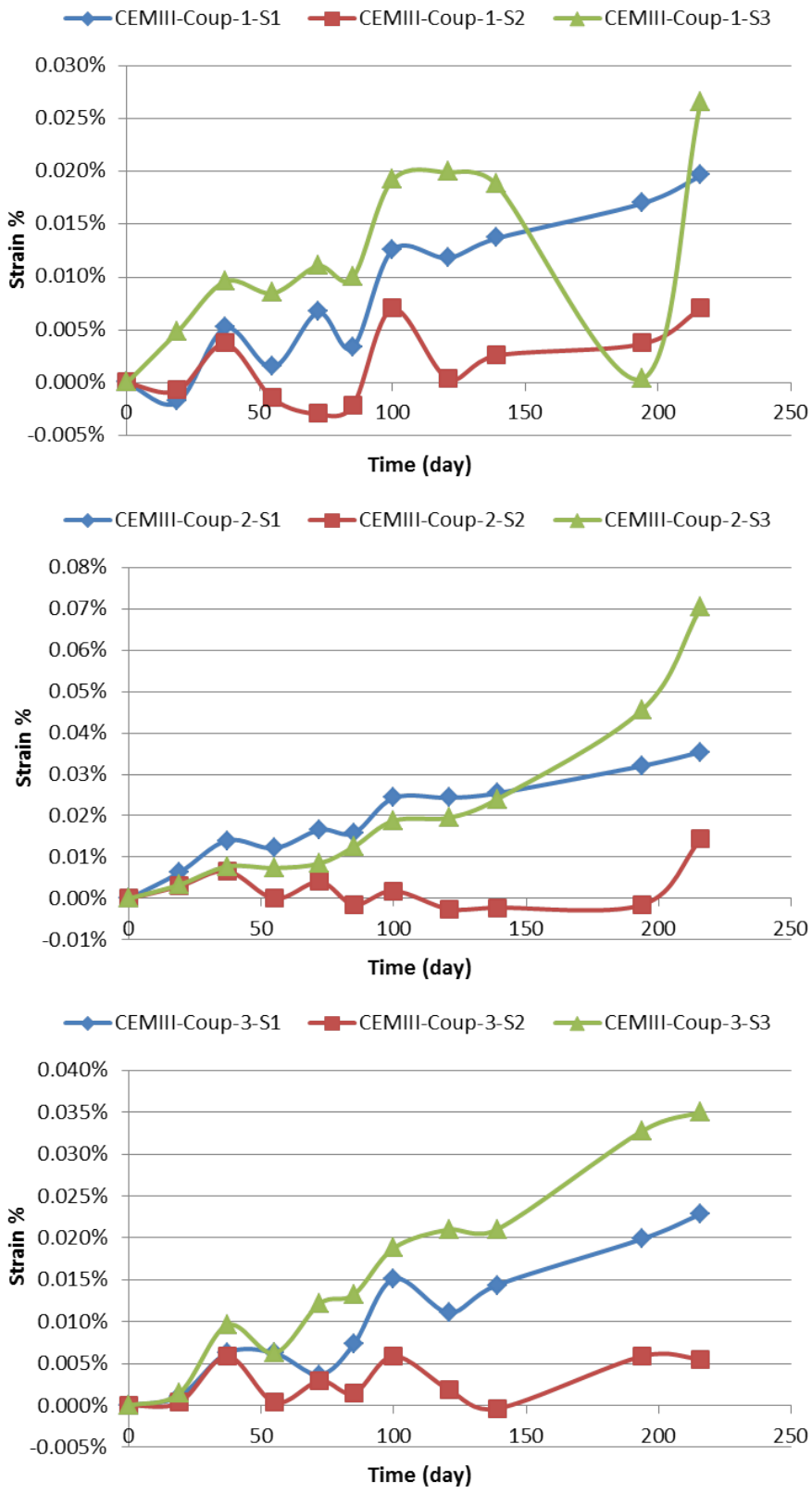

Figure B.6 – Strain of Coup-III-Fin $2 \times 2 \times 12$ cm^3 specimens on different faces

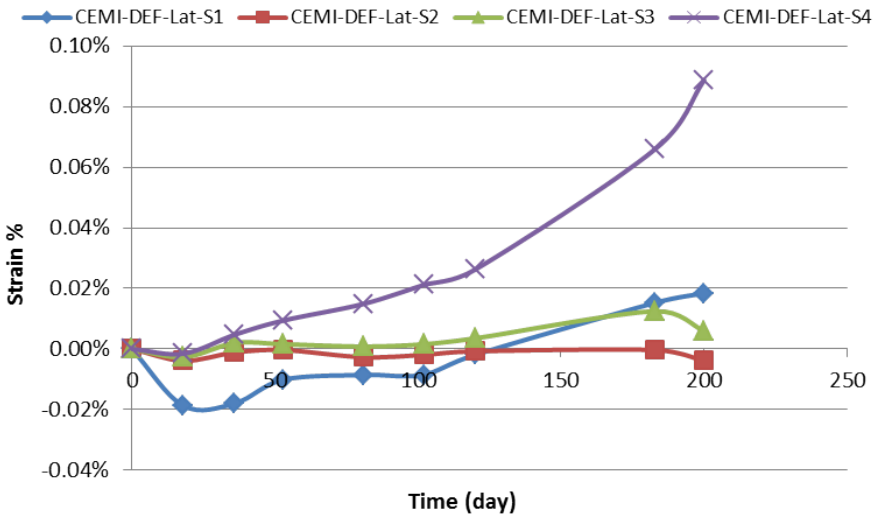

Figure B.7 – Strain of DEF-I-Lat 11 × 11 × 22 cm^3 specimens on different faces

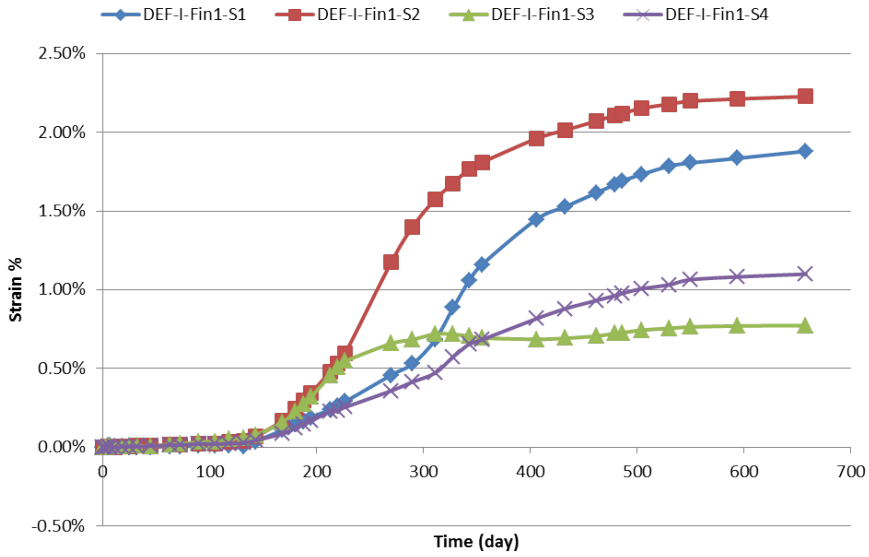

Figure B.8 – Strain of DEF-I-Fin1 11 × 11 × 22 cm^3 specimens on different faces

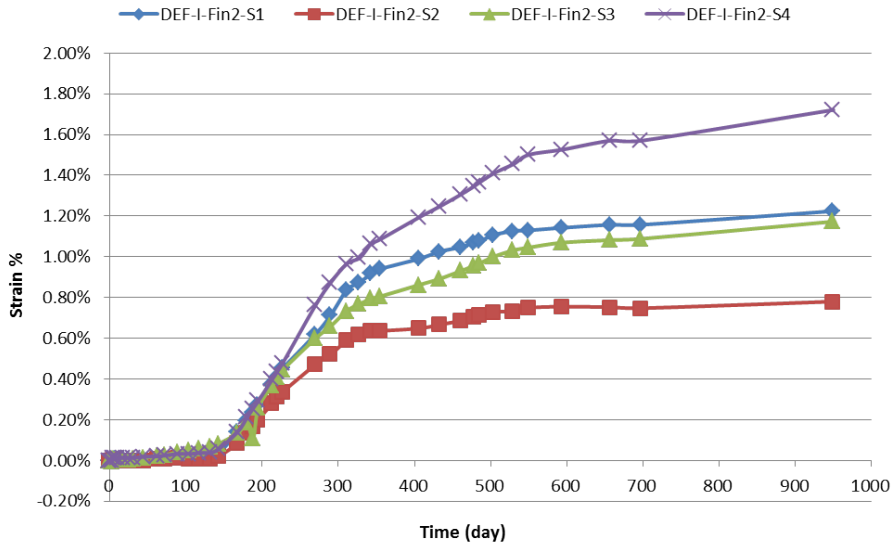

Figure B.9 – Strain of DEF-I-Fin2 $11 \times 11 \times 22$ cm^3 specimens on different faces

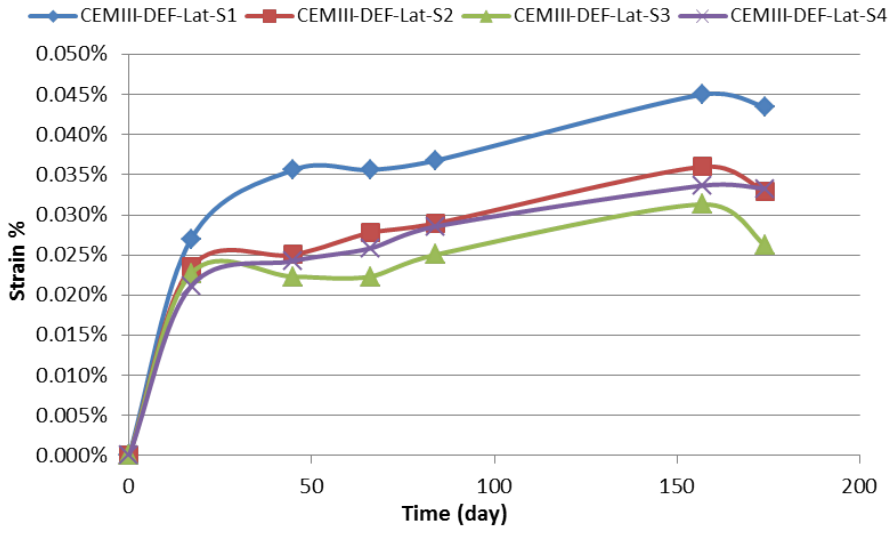

Figure B.10 – Strain of DEF-III-Lat $11 \times 11 \times 22$ cm^3 specimens on different faces

C Pore size distribution at different layers of $11 \times 11 \times 22\ \mathrm{cm}^3$ specimens

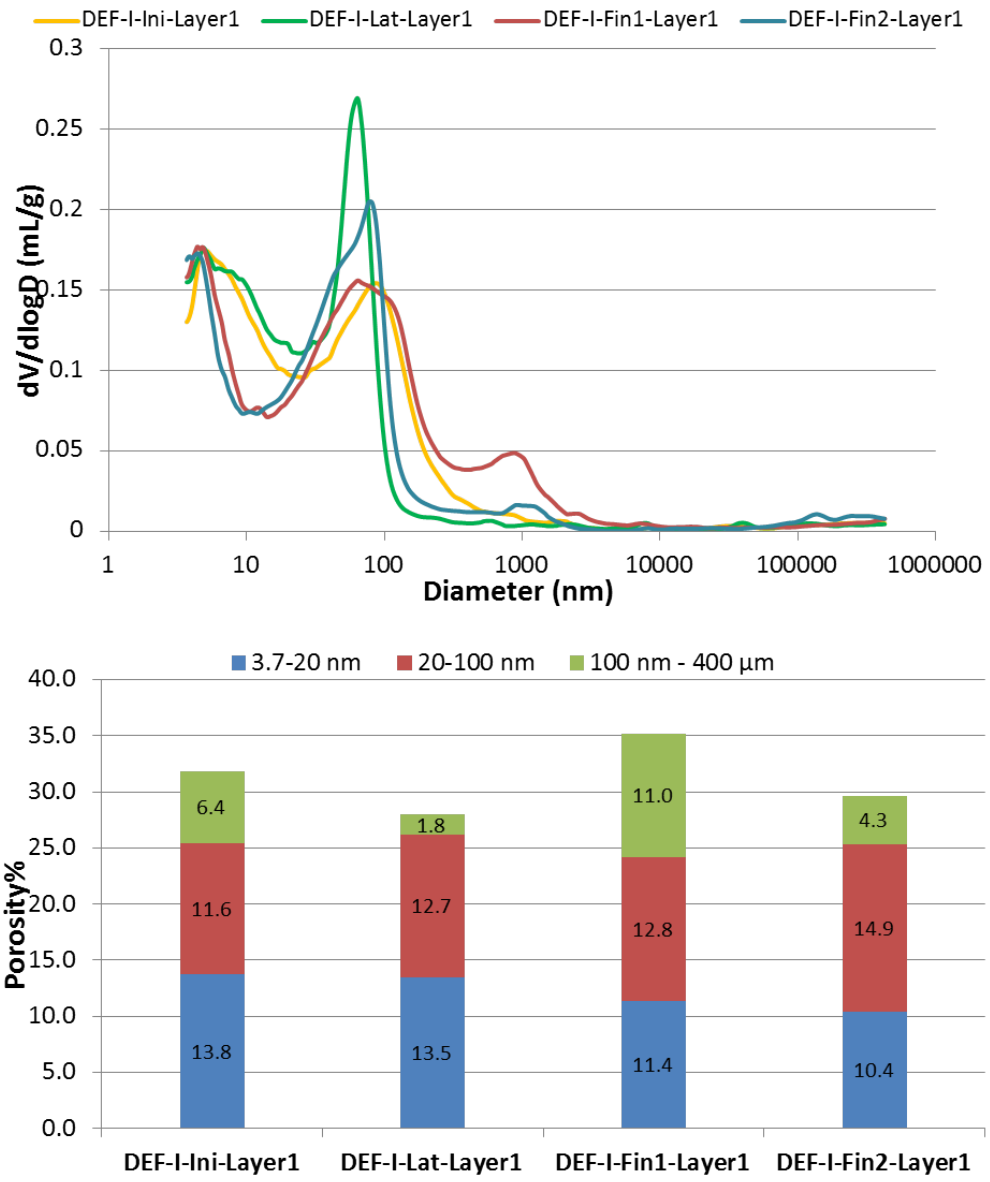

Figure C.1 – Evolution of pore size distribution of $11 \times 11 \times 22\ \mathrm{cm}^3$ DEF specimen at the core layer

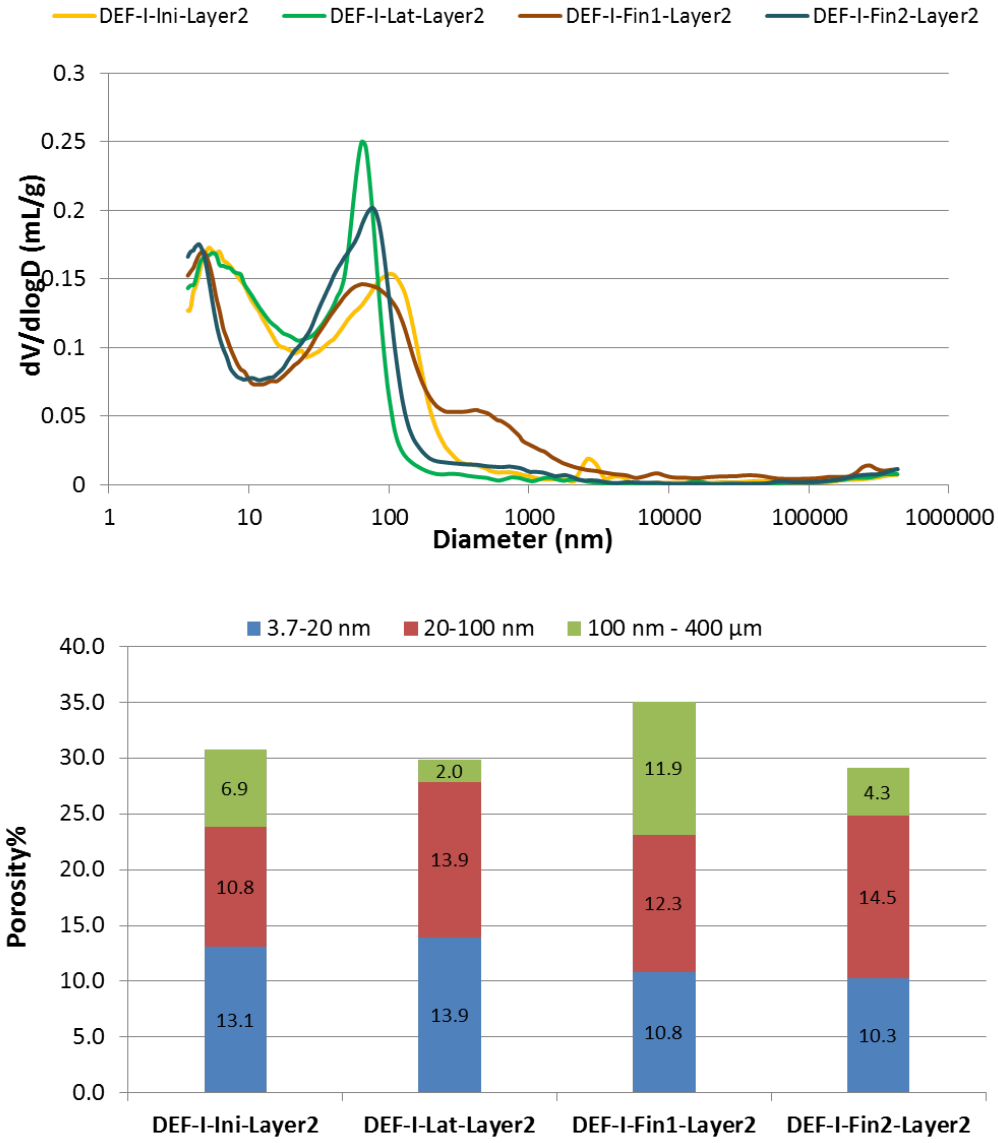

Figure C.2 – Evolution of pore size distribution of $11 \times 11 \times 22$ cm^3 DEF specimen at the 2nd layer

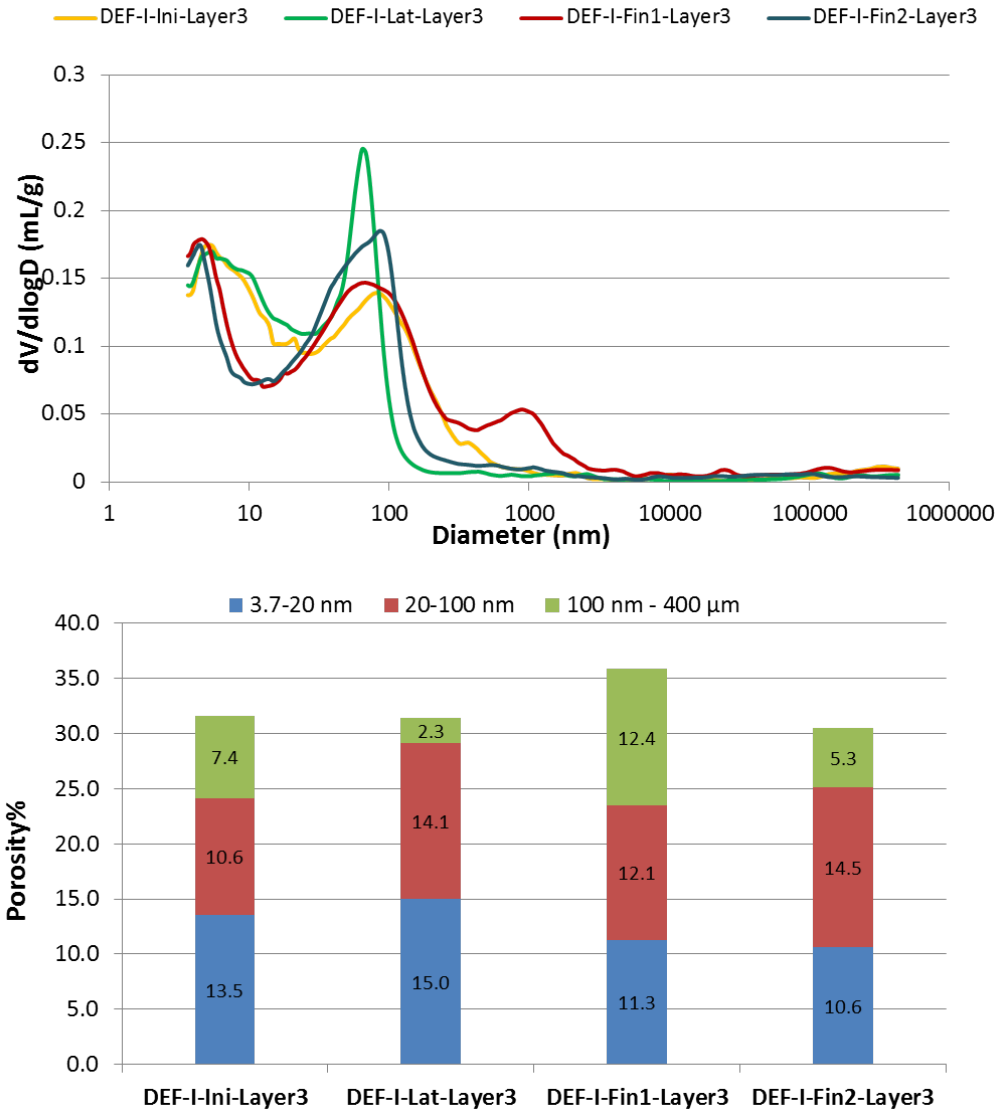

Figure C.3 – Evolution of pore size distribution of $11 \times 11 \times 22$ cm^3 DEF specimen at the 3rd layer

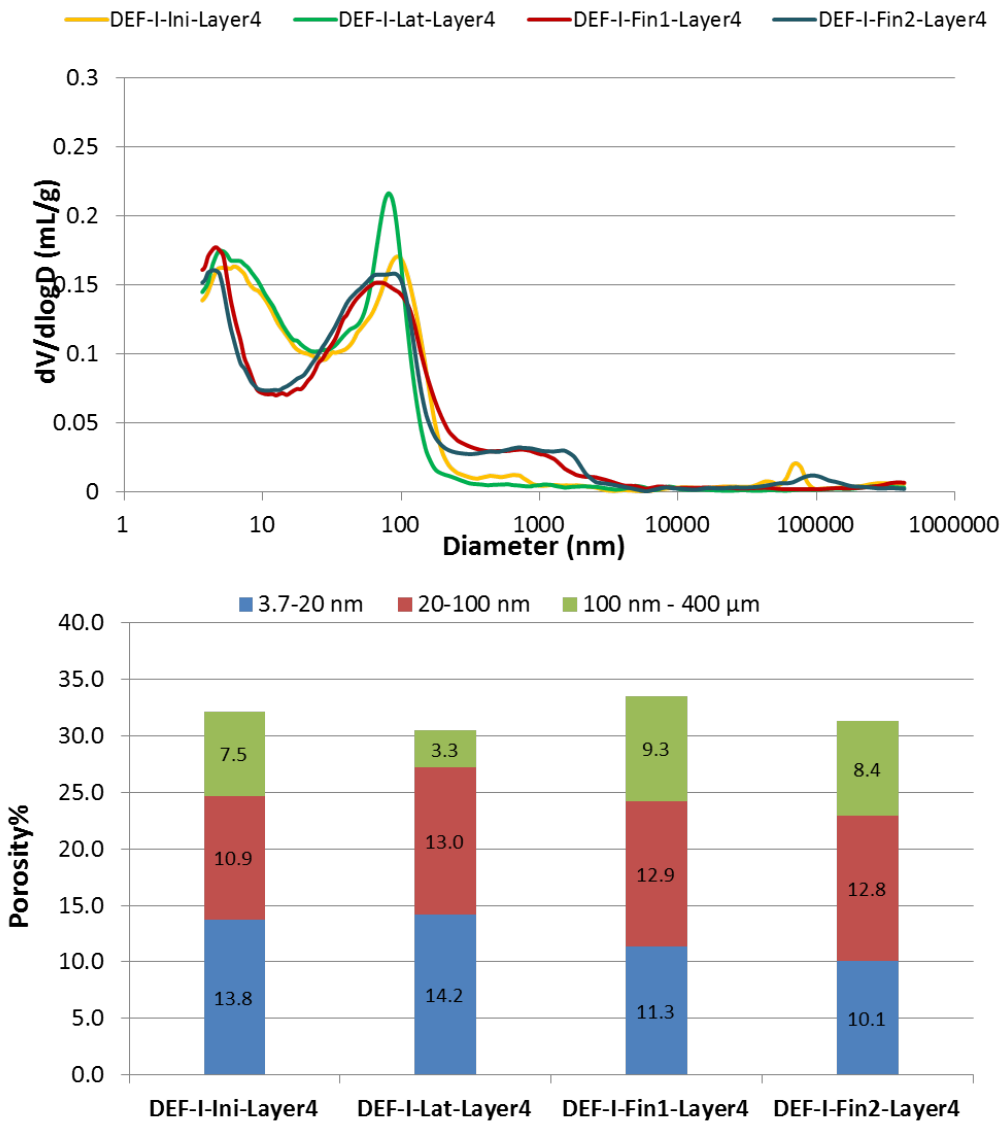

Figure C.4 – Evolution of pore size distribution of $11 \times 11 \times 22$ cm^3 DEF specimen at the 4th layer

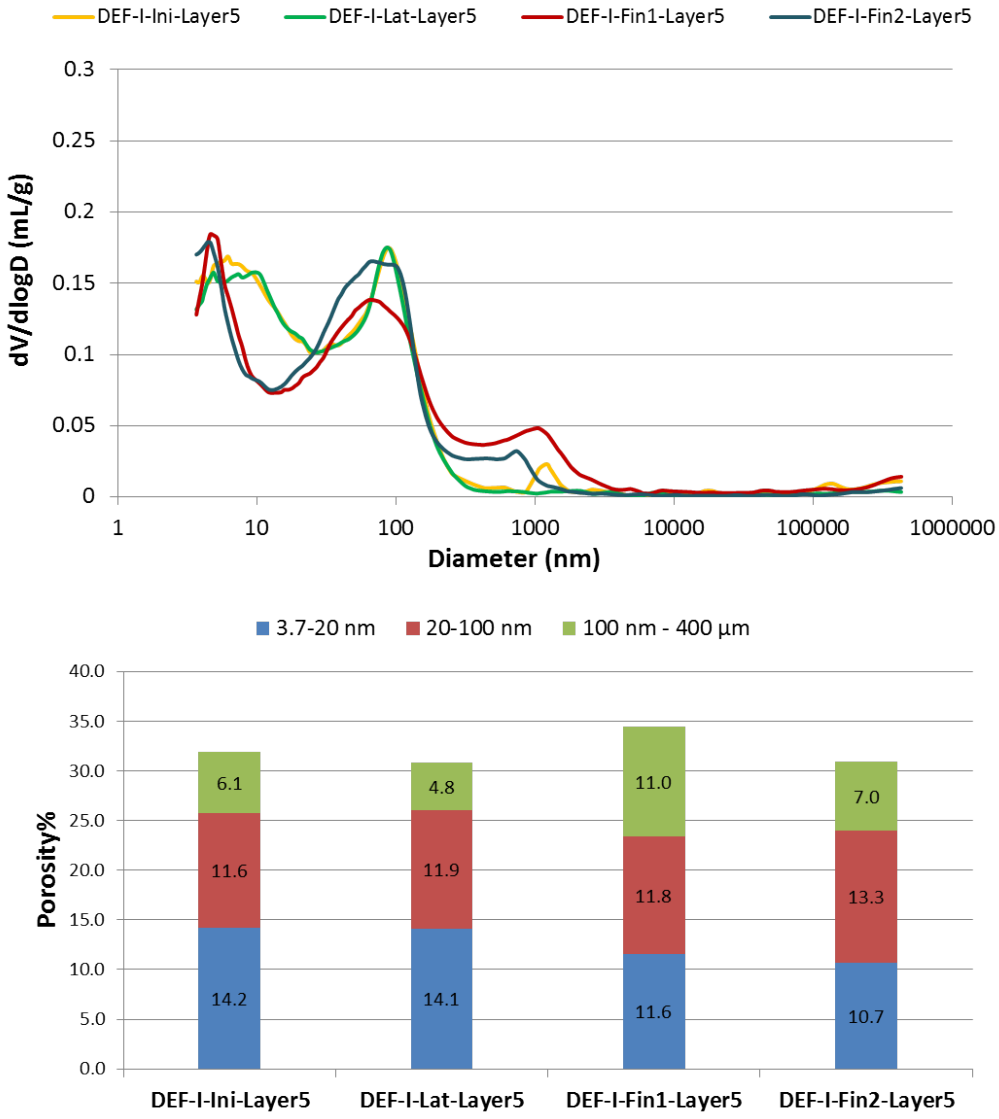

Figure C.5 – Evolution of pore size distribution of $11 \times 11 \times 22$ cm^3 DEF specimen at the 5th layer

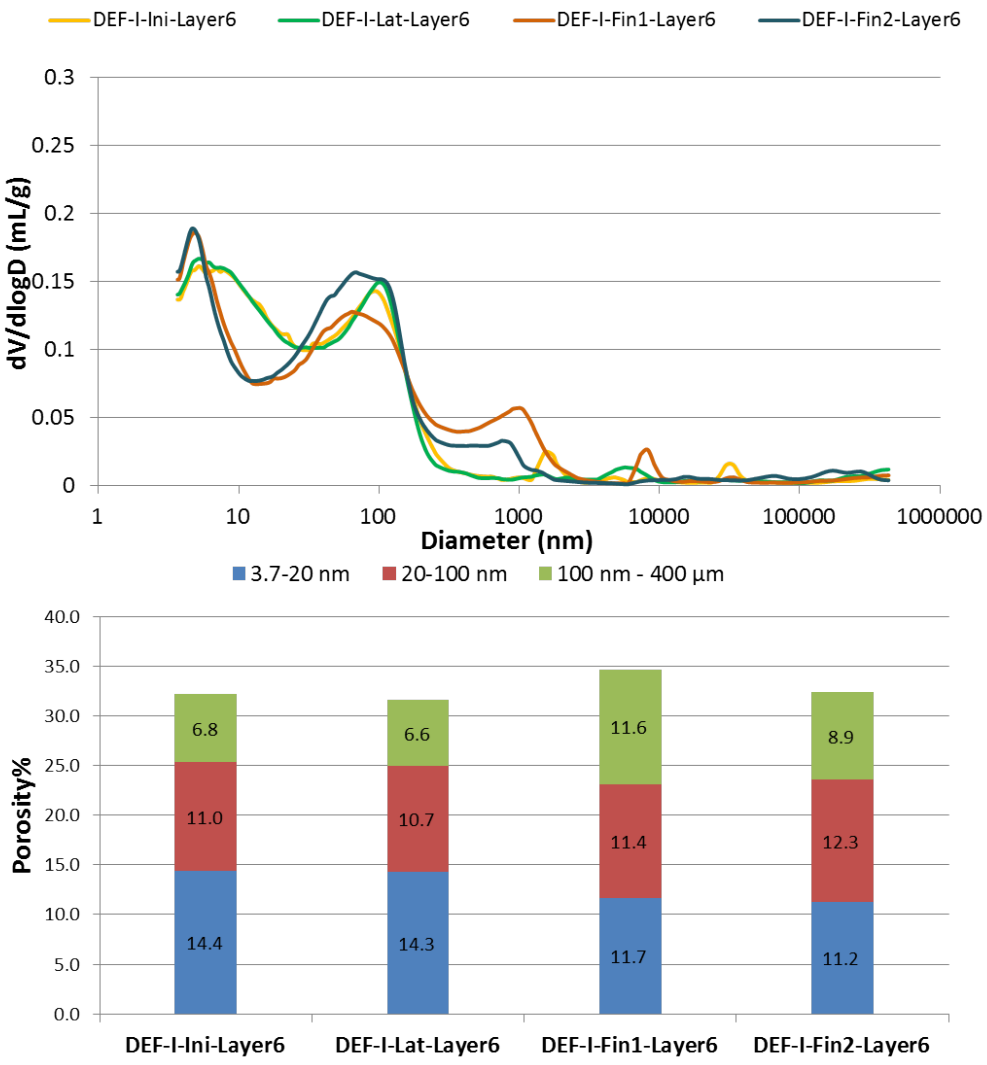

Figure C.6 – Evolution of pore size distribution of $11 \times 11 \times 22$ cm^3 DEF specimen at the 6th layer

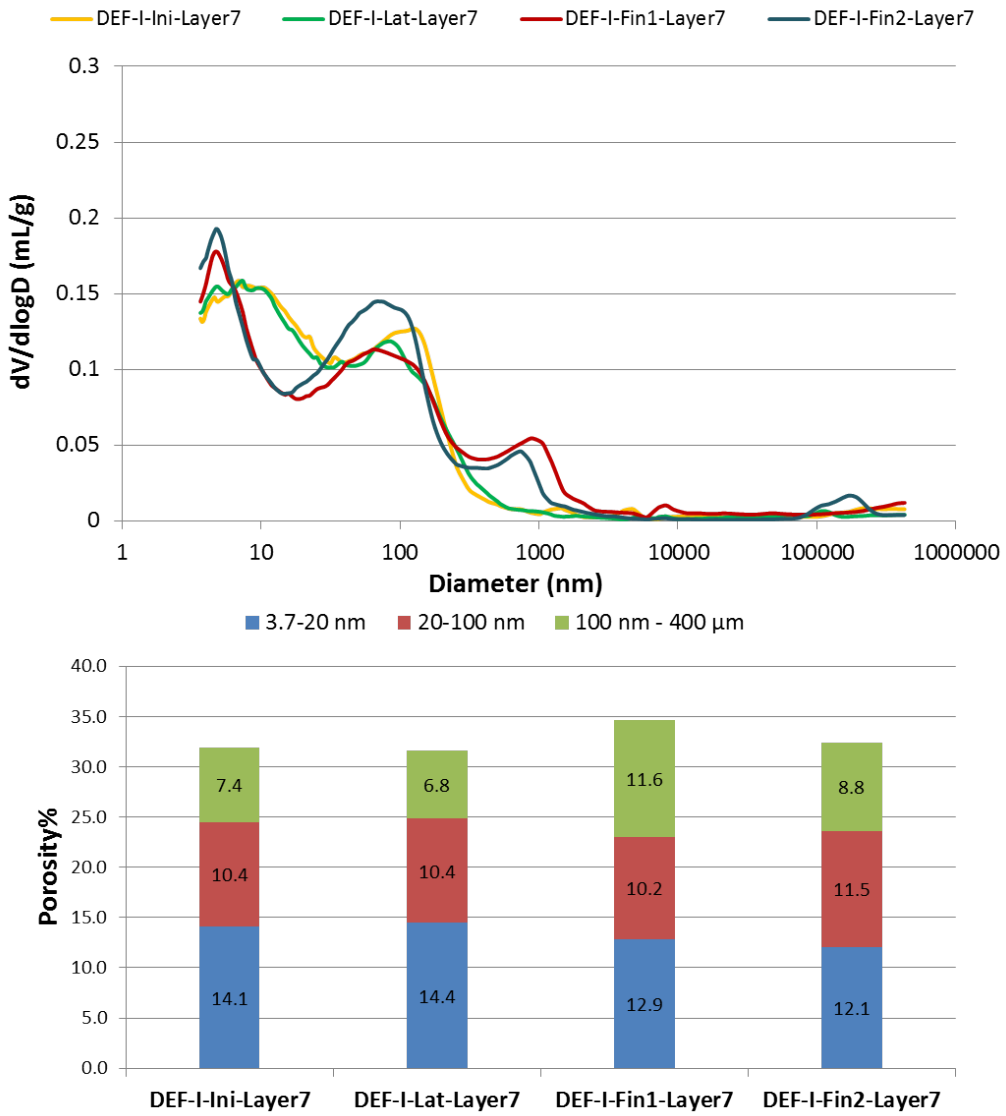

Figure C.7 – Evolution of pore size distribution of $11 \times 11 \times 22$ cm^3 DEF specimen at the 7th layer

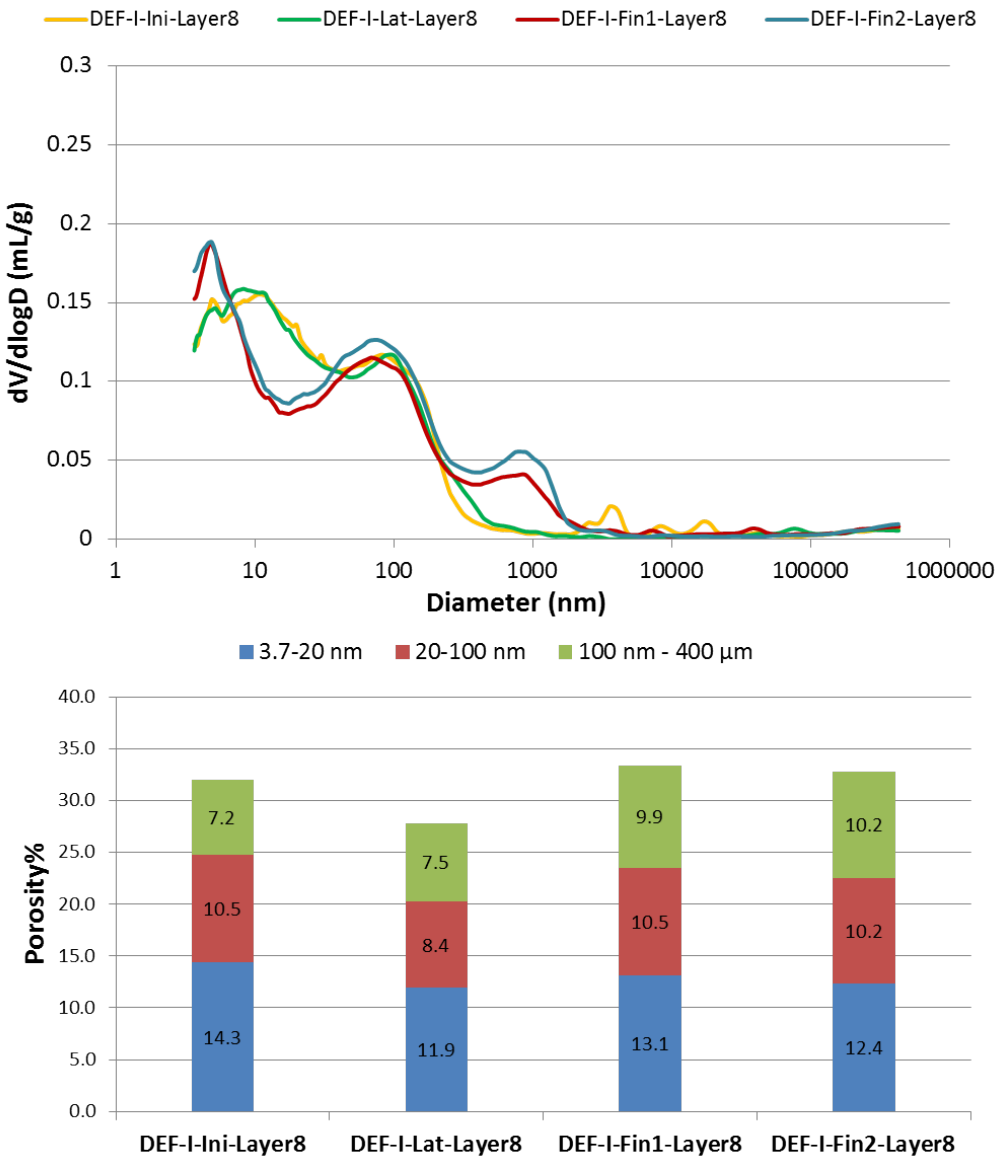

Figure C.8 – Evolution of pore size distribution of $11 \times 11 \times 22$ cm^3 DEF specimen at the 8th layer

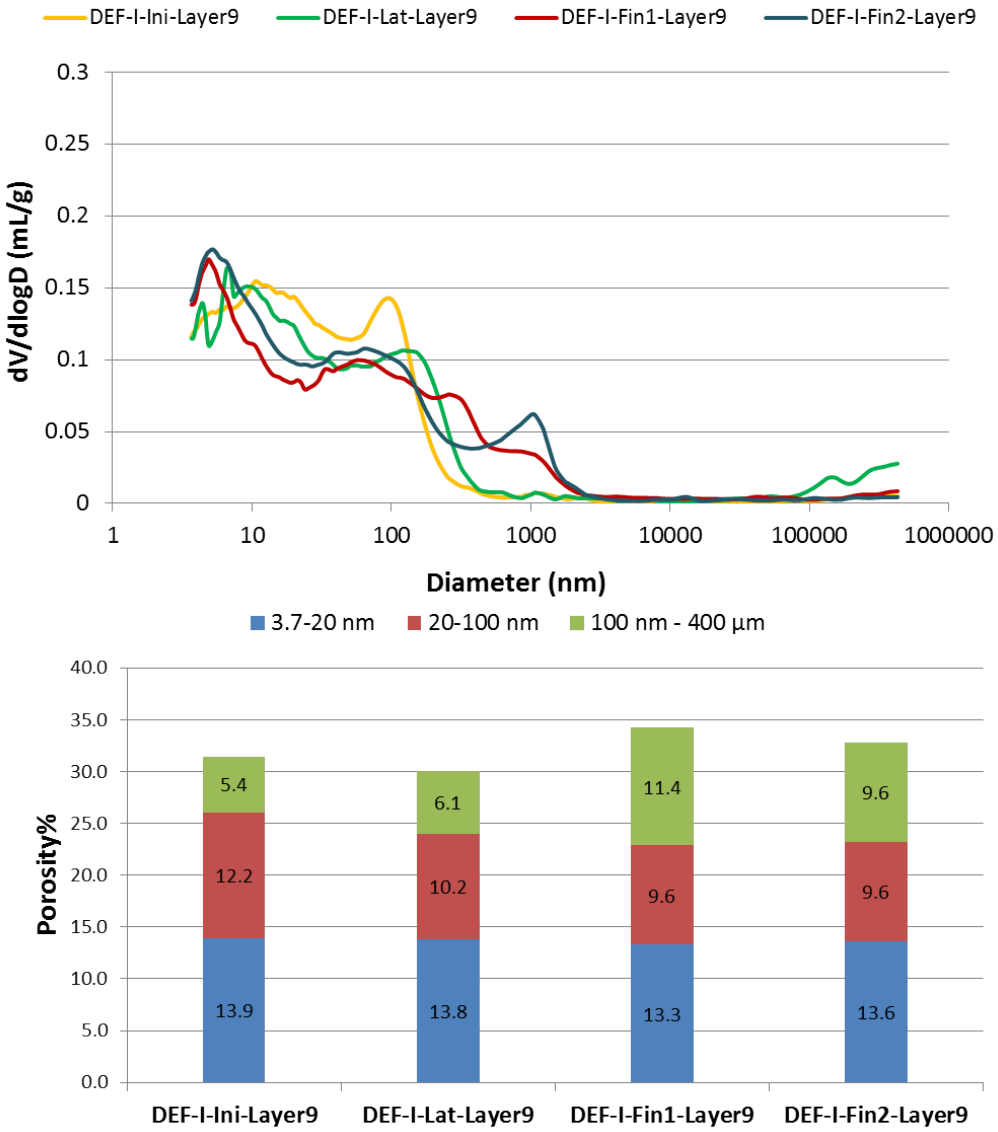

Figure C.9 – Evolution of pore size distribution of $11 \times 11 \times 22$ cm^3 DEF specimen at the 9th layer

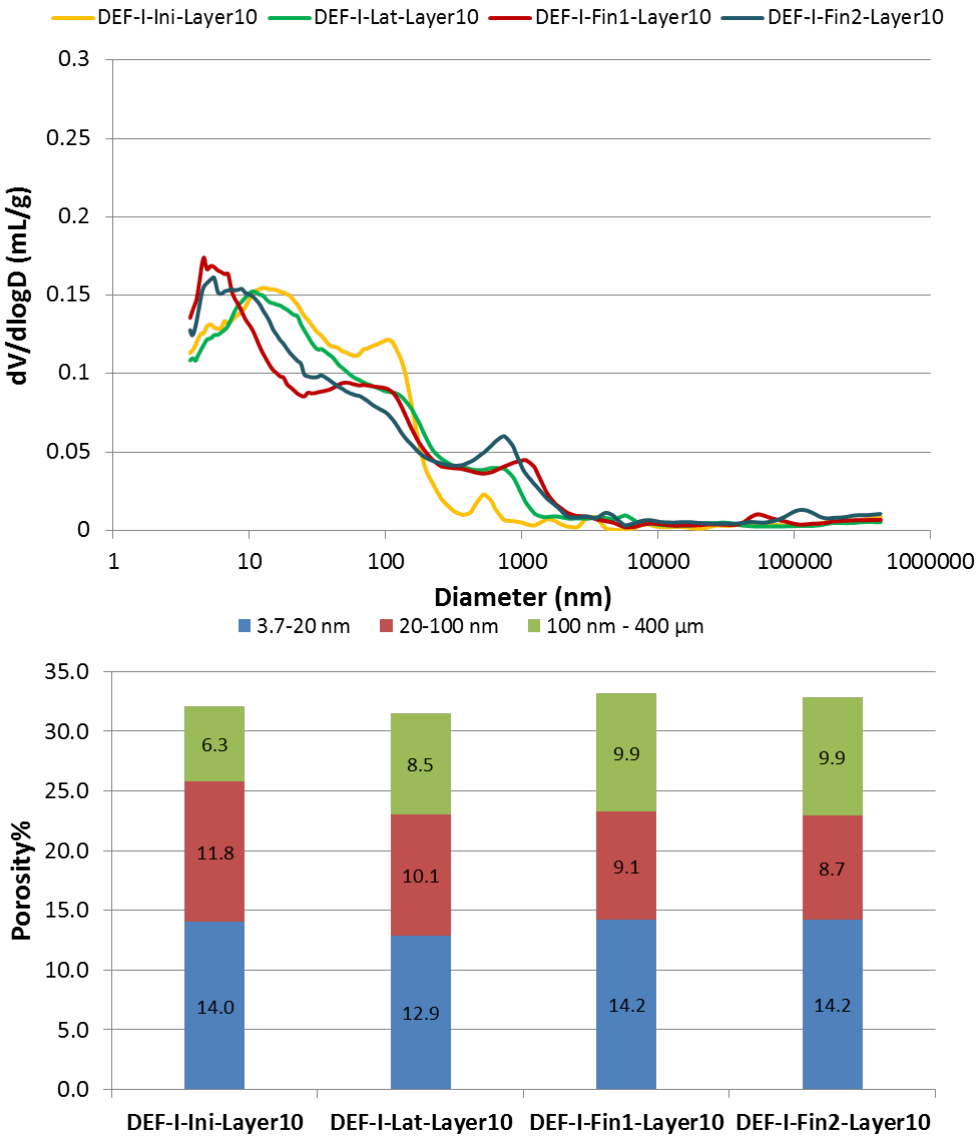

Figure C.10 – Evolution of pore size distribution of $11 \times 11 \times 22$ cm^3 DEF specimen at the surface layer